

University of Alberta

Library Release Form

Name of Author: Can Ulas Hatiboglu

Title of Thesis: Miscible and Immiscible Transfer of Liquid-Liquid and Gas-Liquid Pairs Between Matrix and Fracture Under Static Conditions

Degree: Doctor of Philosophy

Year this Degree Granted: 2007

Permission is hereby granted to the University of Alberta Library to reproduce single copies of this thesis and to lend or sell such copies for private, scholarly or scientific research purposes only.

The author reserves all other publication and other rights in association with the copyright in the thesis, and except as herein before provided, neither the thesis nor any substantial portion thereof may be printed or otherwise reproduced in any material form whatsoever without the author's prior written permission.

Signature

University of Alberta

Miscible and Immiscible Transfer of Liquid-Liquid and Gas-Liquid Pairs Between
Matrix and Fracture Under Static Conditions
by

Can Ulas Hatiboglu

A thesis submitted to the Faculty of Graduate Studies and Research
in partial fulfillment of the requirements for the degree of

Doctor of Philosophy

in

Petroleum Engineering

Department of Civil and Environmental Engineering

Edmonton, Alberta

Fall, 2007

University of Alberta

Faculty of Graduate Studies and Research

The undersigned certify that they have read, and recommend to the Faculty of Graduate Studies and Research for acceptance, a thesis entitled **Miscible and Immiscible Transfer of Liquid-Liquid and Gas-Liquid Pairs Between Matrix and Fracture Under Static Conditions** submitted by **Can Ulas Hatiboglu** in partial fulfillment of the requirements for the degree of **Doctor of Philosophy**.

Dr Tayfun Babadagli

Dr Apostolos Kantzas

Dr Ergun Kuru

Dr Jozef Szymanski

Dr Zhenghe Xu

Abstract

In this thesis work, miscible and immiscible transfers between oil or gas saturated rock matrix and fracture containing an aqueous phase or solvent are studied. This type of transfer interaction is commonly encountered during enhanced oil recovery applications, groundwater contamination, underground waste disposal, and greenhouse gas (mainly CO₂) sequestration in naturally fractured reservoirs.

The first part of the study focuses on experimental work. The recovery curves obtained from static core experiments for volumetric (immiscible interaction) and diffusive (miscible interaction) transfer ensure quantitative data. Visual analyses of the same processes on transparent 2-D sand pack models provide data for qualitative analysis. Experimental data collected from different sources, then, is blended to obtain immaculate findings on the matrix-fracture interaction process between matrix and fracture.

The effects of gravity, viscosity ratio, matrix boundary conditions (causing co- or counter-current type interaction type), wettability, rock type, interfacial tension, and temperature are tested to be able to identify the dynamics of immiscible and miscible matrix-fracture interaction process for wide variety situations. Experimental findings are explained under different sections first as separate (quantitative and qualitative data) and then, as cross comparison of core and visual experiments. The dynamics of the interaction process is clarified through this analysis in terms of the development of residual oil saturation in the matrix and the rate of recovery for various conditions.

In the second part of the dissertation, computational models are presented. For modelling miscible interaction, initially a stochastic method inspired from invasion percolation and diffusion limited aggregation algorithms are developed. This model was observed to be applicable to model the horizontal displacement. Next, the Lattice Boltzmann Method (LBM) is applied to model the experiments including the vertical displacement (miscible) cases. Another LBM model is developed to model the immiscible interaction and the results are matched to those of 2-D sand pack and micro models. The LBM models capture the experimentally observed dynamics of the process for both horizontal and vertical cases and therefore found to be a potent algorithm for modelling both miscible and immiscible fluid interaction.

Table of Contents

1	Introduction.....	1
1.1	Overview.....	1
1.2	Statement of the problem.....	4
1.3	Methodology	5
1.4	Major contributions to the literature and industry	6
2	Literature Review	8
2.1	Spontaneous imbibition (immiscible process).....	8
2.2	Diffusion-dispersion (miscible process).....	10
2.3	Visualization studies (pore scale computational and experimental).....	12
2.4	Modeling efforts	13
3	Experimental Agenda.....	17
3.1	Experiments on rock samples.....	17
3.1.1	Porous media	18
3.1.2	Immiscible processes	19
3.1.3	Miscible processes	21

3.1.4	Procedure.....	22
3.2	Visualization experiments.....	23
3.2.1	Glass bead models.....	23
3.2.2	Silicon etched micro-models.....	25
4	Immiscible matrix-fracture interaction	27
4.1	Gas-liquid interaction.....	27
4.1.1	Low temperature experiments (20°C).....	30
4.1.1.1	Berea sandstone experiments	30
4.1.1.2	Indiana limestone experiments	32
4.1.2	High temperature experiments (90°C).....	36
4.1.2.1	Berea Sandstone	36
4.1.2.2	Indiana limestone experiments	38
4.1.3	Residual gas saturation.....	40
4.1.4	Scaling of experiments.....	46
4.1.5	Observations	51
4.2	Liquid-liquid interaction	53
4.2.1	Oil-brine experiments (effect of viscosity)	56
4.2.1.1	Recovery rate	56
4.2.1.2	Scaling analysis	58
4.2.1.3	Residual oil.....	62
4.2.2	Capillary imbibition of oil-surfactant solution	65
4.2.2.1	Recovery rate and scaling analysis	65
4.2.2.2	Residual oil.....	70
4.2.3	Capillary imbibition of oil-brine (aged samples).....	72
4.2.3.1	Indiana limestone vs. aged Berea sandstone.....	72
4.2.3.2	Un-aged vs. aged Berea sandstone samples	74
4.2.3.3	Residual oil saturation	76
5	Miscible matrix-fracture interaction	79

5.1	Primary diffusion	79
5.1.1	Indiana limestone vs. Berea sandstone	80
5.1.2	Unaged vs. aged Berea sandstone samples.....	82
5.2	Secondary diffusion.....	84
5.2.1	Indiana limestone vs. Berea sandstone	85
5.2.2	Unaged vs. aged Berea sandstone samples	86
5.2.3	Residual oil saturation.....	88
5.2.4	Comparison to the crude oil experiments	92
5.2.5	Observations	94
6	Glass-bead models	96
6.1	Imbibition experiments.....	96
6.1.1	Air-water.....	97
6.1.1.1	Counter-current interaction.....	97
6.1.1.2	Co-current interaction.....	98
6.1.1.3	Matrix shape	99
6.1.2	Oil-water experiments	101
6.1.2.1	Counter-current interaction.....	101
6.1.2.2	Co-current interaction.....	103
6.1.2.3	Matrix shape	105
6.1.2.4	Aged samples.....	106
6.2	Diffusion-dispersion experiments (miscible process).....	106
6.2.1	Horizontal experiments: Counter-current interaction	107
6.2.2	Vertical experiments: Counter-current interaction.....	108
6.2.3	Vertical experiments: Co-current.....	110
6.2.4	Quantitative analysis on finger development.....	111
7	Silicon etched micro-models	113
7.1	Model preparation	114
7.2	Observations	117

8	Results and interpretations.....	121
8.1	Immiscible displacement between matrix and fracture.....	121
8.1.1	Air-water.....	122
8.1.1.1	Counter-current interaction.....	122
8.1.1.2	Co-current interaction.....	124
8.1.2	Oil-water.....	126
8.1.2.1	Counter-current interaction.....	126
8.1.2.2	Co-current interaction.....	128
8.1.2.3	Aging - wettability effect.....	131
8.2	Miscible displacement between matrix and fracture.....	133
8.2.1	Vertical experiments: Counter-current interaction.....	133
8.2.2	Vertical experiments: Co-current interaction.....	136
8.2.3	Horizontal experiments: Counter-current interaction.....	139
8.2.4	Horizontal experiments: Co-current interaction.....	140
8.2.5	Inclined experiments: Clarification on the effect of gravity.....	140
9	Modeling.....	143
9.1	Modified invasion percolation algorithm.....	143
9.1.1	Vertical Experiments: Counter-current.....	144
9.1.2	Vertical Experiments: Co-current.....	145
9.1.3	Horizontal Experiments: Counter-current.....	146
9.1.4	Horizontal Experiments: Co-current.....	147
9.1.5	Analysis of the results.....	151
9.2	Diffusion Limited Aggregation (DLA).....	157
9.3	Lattice Boltzmann Method (LBM).....	160
9.3.1	Miscible model.....	161
9.3.1.1	Simulation results.....	167
9.3.2	Immiscible Model.....	172
10	Conclusion.....	179

10.1	Accomplishments	179
10.1.1	Immiscible interaction: Core studies	180
10.1.1.1	Gas – liquid (water displacing gas in the matrix by capillary imbibition) 180	
10.1.1.2	Liquid – liquid (water displacing oil in the matrix by capillary imbibition) 181	
10.1.2	Immiscible interaction: Visualization studies	182
10.1.3	Immiscible interaction: Modeling by the Lattice Boltzmann method	183
10.1.4	Miscible interaction: Liquid-liquid pair (solvent displacing oil in the matrix by diffusion and convection)	183
10.1.4.1	Core experiments	183
10.1.4.2	Visualization study	184
10.1.4.3	Stochastic and Lattice Boltzmann models	185
10.2	Future Work	186
11	Bibliography	188
12	Appendix	196

List of Tables

Table 3-1 Properties of fluid pairs used for gas-liquid experiments.....	20
Table 3-2 Properties of fluid pairs used for liquid-liquid experiments.....	20
Table 3-3 Fluids used in miscible interaction experiments.	21
Table 3-4 Fluid pairs used in the visualization experiments.	25
Table 3-5 Micro-model properties.....	26
Table 4-1 Inventory of air-water experiments	29
Table 4-2 Rock and fluid types used in the liquid-liquid experiments.	55
Table 5-1 Miscible experiment identification according to core shape and rock type.....	80
Table 6-1 Immiscible experiment identification according to core shape and fluid type.....	97
Table 7-1 Micro-model properties.....	114
Table 7-2 Fluid pairs used in experiments.....	118
Table 8-1 Experiments conducted in this part of study. L: Length, D: Diameter.	122
Table 8-2 Updated diffusion experiment inventory.....	133

List of Figures

Figure 3.1 The sizes and shapes of the cores used in the experiments.	19
Figure 3.2 Horizontal and vertical imbibition tubes, Measurement using scales.....	19
Figure 3.3 Schematic representation of the experimental model with different boundary conditions for counter-current, and co-current interaction.	24
Figure 3.4 Experimental setup for vertical, and horizontal orientations.	24
Figure 3.5 Repetative micro-model pattern.....	26
Figure 3.6 Glass micro-model on holder.	26
Figure 4.1 Air-water imbibition recovery curves for Berea sandstone at 20° C for different diameters and lengths, vertical orientation.	31
Figure 4.2 Air-water imbibition recovery curves for Berea sandstone at 20° C for different diameters and lengths, horizontal orientation.	32
Figure 4.3 Air--water imbibition recovery curves for Indiana limestone fat 20° C for three different lengths (vertical and horizontal).....	33
Figure 4.4 Air--water imbibition recovery curves for Indiana limestone at 20° C for vertical and uncoated samples.	34

Figure 4.5 Air-water imbibition tests; comparison of different types of rocks on vertical orientation ($T= 20^{\circ} C$).....	35
Figure 4.6 Air-water imbibition tests; comparison of different types of rocks on horizontal orientation ($T= 20^{\circ} C$).....	36
Figure 4.7 Air-water imbibition tests on Berea Sandstone at $90^{\circ} C$ for three different diameters and lengths, vertical orientation.	37
Figure 4.8 Air-water imbibition tests on Berea Sandstone at $90^{\circ} C$ for three different diameters and lengths, horizontal orientation.	38
Figure 4.9 Air-water imbibition tests on Indiana limestone at $90^{\circ} C$ for three different lengths (vertical and horizontal).....	39
Figure 4.10 Air-water imbibition tests on Indiana limestone at $90^{\circ} C$ for vertical and uncoated samples.	40
Figure 4.11 Comparison of ultimate recoveries for different rocks, dimensions, temperatures ($20^{\circ}C$ and $90^{\circ}C$) and orientations.	42
Figure 4.12 Residual gas saturation (RGS) trends at $20^{\circ} C$	45
Figure 4.13 Residual gas saturation trends at $90^{\circ} C$	45
Figure 4.14 Normalized gas recovery curves of Berea sandstone.....	46
Figure 4.15 Dimensionless time (Eq.2) against normalized recovery.....	48
Figure 4.16 Estimation of P_c eff in Eq.10.....	49
Figure 4.17 Dimensionless time (Eq.6) against normalized recovery.....	50
Figure 4.18 Dimensionless time (Eq.7) against normalized recovery.....	50
Figure 4.19 Dimensionless time (Eq.9) against normalized recovery.....	51
Figure 4.20 Oil-brine imbibition tests in vertical cores.	57
Figure 4.21 Oil-brine imbibition tests in horizontal cores.	57
Figure 4.22 Scaling with the classical Mattax and Kyte equation.....	59
Figure 4.23 Scaling with the classical Mattax and Kyte equation when the new shape factor (Eq. 19) was used	61

Figure 4.24 Scaling with the Xie and Morrow equation for (a)vertical case and (b)horizontal case when the new shape factor (Eq. 19) was used.....	62
Figure 4.25 Scaling with the Li and Horne equation when the new shape factor (Eq. 19) was used.....	62
Figure 4.26 The change of residual oil saturation with the length/diameter ratio	64
Figure 4.27 The change of residual oil saturation with the dimensionless group.....	64
Figure 4.28 Same dimensionless group used in Fig 9 modified with the new shape factor....	65
Figure 4.29 Kerosene-brine and mineral oil-surfactant solution imbibition tests for the vertical case.	66
Figure 4.30 Kerosene-brine and mineral oil-surfactant solution imbibition tests for the horizontal case.	66
Figure 4.31 Scaling with the classical Mattax and KYTE equation for (a) vertical and (b) horizontal cases.....	68
Figure 4.32 Scaling with the classical Mattax and KYTE equation for horizontal case when the new shape factor (Eq. 19) was used.	69
Figure 4.33 Scaling with the Li and Horne equation for horizontal case when the new shape factor (Eq. 19) was used.....	69
Figure 4.34 Scaling with the Xie and Morrow equation for horizontal case when the new shape factor (Eq. 19) was used.....	70
Figure 4.35 The change of residual oil saturation with the length/diameter ratio.	71
Figure 4.36 The change of residual oil saturation with the dimensionless group.....	71
Figure 4.37 Proposed shape factor versus SOR plots vertical case.	72
Figure 4.38 Oil-brine capillary imbibition tests in the Indiana limestone cores.	73
Figure 4.39 Oil-brine capillary imbibition tests in the aged Berea sandstone cores.....	73
Figure 4.40 Scaling with the classical Mattax and KYTE equation.....	74
Figure 4.41 Scaling with the classical Mattax and KYTE equation for horizontal case when the new shape factor (Eq. 19) was used.	75

Figure 4.42 Scaling with the Li and Horne equation for horizontal case when the new shape factor (Eq. 19) was used.....	75
Figure 4.43 Scaling with the Xie and Morrow equation for horizontal case when the new shape factor (Eq. 19) was used.....	76
Figure 4.44 The change of residual oil saturation with the length/diameter ratio.	77
Figure 4.45 Proposed shape factor versus SOR plots vertical case.	78
Figure 5.1 Primary diffusion experiments on Indiana limestone and Berea sandstone samples.....	81
Figure 5.2 Primary diffusion experiments on Berea sandstone compared with 1-week aged samples.....	82
Figure 5.3 Primary diffusion experiments on Berea sandstone compared with 1-month aged samples.....	83
Figure 5.4 Primary imbibition followed by secondary diffusion experiments on Indiana limestone and Berea sandstone samples.	86
Figure 5.5 Primary imbibition followed by secondary diffusion experiments on Berea sandstone compared with 1-week aged samples.....	87
Figure 5.6 Primary imbibition followed by secondary diffusion experiments on Berea sandstone compared with 1-month aged samples.....	87
Figure 5.7 Change in SOR from primary diffusion experiments for different rocks and wettabilities.....	89
Figure 5.8 Change in the residual oil saturation from primary imbibition + secondary diffusion experiments for different rocks and wettabilities.	90
Figure 5.9 Comparison of the recoveries and recovery efficiencies for two processes.	91
Figure 5.10 Two methods applied to Berea sandstone saturated with crude oil.	93
Figure 5.11 Mineral oil saturated counterparts for Fig.11.....	93
Figure 6.1 Experiment aV1: Counter-current, vertical orientation, air-water pair at 20 °C. ...	98
Figure 6.2 Experiment aV2: Counter-current, vertical orientation, air-water pair at 90 °C. ...	98

Figure 6.3 Experiment aV3: Co-current, vertical orientation, air-water pair at 20 °C.....	99
Figure 6.4 Experiment aV4: Co-current, vertical orientation, air-water pair at 90 °C.....	99
Figure 6.5 Counter-current, 2:1 aspect ratio, vertical orientation, air-water pair at 20 °C.....	99
Figure 6.6 Experiment aV8: Counter-current, 2:1 aspect ratio, vertical orientation, air-water pair at 90 °C.....	100
Figure 6.7 Experiment aV9: Counter-current, 1:2 aspect ratio, vertical orientation, air-water pair at 20 °C.....	100
Figure 6.8 Experiment aV10: Counter-current, 1:2 aspect ratio, vertical orientation, air-water pair at 90 °C.....	100
Figure 6.9 Experiment OV1: Counter-current, vertical orientation, mineral oil-water pair.	102
Figure 6.10 Experiment OV2: Counter-current, vertical orientation, kerosene-water pair.	102
Figure 6.11 Experiment OV5: Counter-current, horizontal orientation, mineral oil-water pair.....	103
Figure 6.12 Experiment OV6: Counter-current, horizontal orientation, kerosene-water pair.....	103
Figure 6.13 Experiment OV3-n : Co-current, vertical orientation, mineral oil-water pair...	103
Figure 6.14 Experiment OV4-n : Co-current, vertical orientation, kerosene-water pair.....	103
Figure 6.15 Experiment OV3-t : Co-current, vertical orientation, mineral oil-water pair....	104
Figure 6.16 Experiment OV4-t : Co-current, vertical orientation, kerosene-water pair.....	104
Figure 6.17 Experiment OV7: Counter-current, 2:1 aspect ratio, vertical orientation, mineral oil-water pair.....	105
Figure 6.18 Experiment OV8: Counter-current, 1:2 aspect ratio, vertical orientation, mineral oil-water pair.....	105
Figure 6.19 Experiment OWV1: Counter-current, vertical orientation, mineral oil-water pair, aged sample.....	106
Figure 6.20 Experiment OWV3: Co-current, vertical orientation, mineral oil-water pair, aged samples.....	106

Figure 6.21 Experiment on 2-D glass bead model (kerosene).	108
Figure 6.22 Experiment on 2-D glass bead model (mineral oil).	108
Figure 6.23 Pattern captured in close-up of Fig. 6.22 at 42 min.	108
Figure 6.24 Experiment on 2-D glass bead model (kerosene).	109
Figure 6.25 Experiment on 2-D glass bead model (mineral oil).	109
Figure 6.26 Convective behaviour observed in vertical oriented experiments.	109
Figure 6.27 Experiment on 2-D glass bead model (kerosene).	110
Figure 6.28 Experiment on 2-D glass bead model (mineral oil).	110
Figure 6.29 Experiment on 2-D glass bead model (2:1 aspect ratio, mineral oil).....	111
Figure 6.30 Displacement vs. time plot of observed fingers.	112
Figure 7.1 Glass etching process.....	115
Figure 7.2 Imbibition visualization in silicon micro-model.(kerosene)	116
Figure 7.3 Imbibition visualization in silicon micro-model. (mineral oil).....	119
Figure 7.4 Visualization of spontaneous imbibition on the micro-model. image is 500 μm wide and magnified 20X.....	119
Figure 7.5 Residual oil saturation development for two different oil types on silicon model	119
Figure 7.6 Visualization experiment on micro-model with homogeneous pore structure...	120
Figure 8.1 Experiment aV2: Counter-current, vertical orientation, air-water pair at 90 °C.	123
Figure 8.2 Experiment aV4 Co-current, Vertical oriented model for air-water pair at 90°C.	125
Figure 8.3 Experiment OV2: Counter-current, vertical orientation, kerosene-water pair. ..	127
Figure 8.4 Experiment OV6: Counter-current, horizontal orientation, kerosene-water pair	128
Figure 8.5 Experiment OV4-n Co-current, Vertical oriented model for Kerosene-water pair	129

Figure 8.6 Experiment OV4-t Co-current, Vertical oriented model for Kerosene-water pair	131
Figure 8.7 Experiment OWV3 Co-current, Vertical oriented model for Mineral Oil-water pair- aged samples	132
Figure 8.8 Visualization experiment for the aged (weakly water-wet) sample (counter-current, mineral oil).....	134
Figure 8.9 Experiment V2 (counter-current, kerosene) 2D visualization experiment. (OOIP: Original Oil In Place).....	135
Figure 8.10 Experiment V4 (counter-current) 2-D visualization experiment with kerosene.	137
Figure 8.11: Comparison of the four experiments given in Figures 5 through 9. (OOIP: Original Oil In Place).....	138
Figure 8.12 Experiment V5 (mineral oil) 2D visualization experiment. (OOIP: Original Oil In Place).....	139
Figure 8.13: 2-D visualization experiment with kerosene (horizontal and counter-current case).....	140
Figure 8.14: 2-D visualization experiment with mineral oil (horizontal and co-current case).	140
Figure 8.15: 2-D visualization experiment with kerosene (horizontal and co-current case).140	
Figure 8.16: 2-D visualization experiment with mineral oil (inclined (10°) and counter-current case).....	141
Figure 8.17: 2-D visualization experiment with kerosene (inclined (10°) and counter-current case).....	141
Figure 9.1: Pentane (red) mineral oil (white) experiment (counter-current interaction, vertical orientation).....	144
Figure 9.2: Pentane (red) kerosene (white) experiment (counter-current, vertical orientation)..	144

Figure 9.3: Pentane (red) mineral oil (white) experiment on an aged model (counter-current, vertical orientation).	145
Figure 9.4: Pentane (red) mineral oil (white) experiment (co-current, vertical orientation).	146
Figure 9.5: Pentane (red) kerosene (white) experiment (co-current, vertical orientation).	146
Figure 9.6: Pentane (red) kerosene (white) experiment (counter-current, horizontal orientation).	147
Figure 9.7: Pentane (red) mineral oil (white) experiment (counter-current, horizontal orientation).	147
Figure 9.8: Pentane (red) kerosene (white) experiment (co-current, horizontal orientation).	148
Figure 9.9: Pentane (red) mineral oil (white) experiment (co-current, horizontal orientation).	148
Figure 9.10: Initial -inner- pressure distribution in the model, caused by the boundary conditions of the model	148
Figure 9.11: Invasion probability sketch for the stochastic model	149
Fig. 9.12: Timing comparison between selected simulations and experiments (countercurrent cases).	151
Fig. 9.13: Timing comparison between selected simulations and experiments (co-current cases).	151
Fig. 9.14: Fractal dimensions of fronts obtained from the simulations and experiments	152
Fig. 9.15: Fractal dimensions of fronts obtained from the simulations and experiments	153
Fig. 9.16: Simulation of kerosene – pentane diffusion (probability power=10).	154
Fig. 9.17: Simulation of kerosene – pentane diffusion (probability power=50).	154
Fig. 9.18: Simulation of kerosene - pentane diffusion (probability power=100).	154
Fig. 9.19: Mineral oil-pentane diffusion for counter-current, horizontal case and LBM simulation of the process.	155

Fig. 9.20: Simulation of kerosene - pentane diffusion (co-current, probability power=10).	156
Fig. 9.21: Simulation of kerosene - pentane diffusion (co-current, probability power=100)	156
Fig. 9.22: Simulation of mineral oil (white) pentane (red) diffusion (co-current, 200x200 matrix, probability power=10)	156
Fig. 9.23: Simulation of mineral oil (white) pentane (red) diffusion (co-current, 200x200 matrix, probability power=100).	156
Figure 9.24 Kerosene-pentane diffusion for counter-current, horizontal case.....	159
Figure 9.25 Kerosene-pentane diffusion for counter-current, vertical case.	159
Figure 9.26 Speed vectors used in the LBM simulations.	162
Figure 9.27 Flowchart of loop section.	166
Figure 9.28 Kerosene-pentane diffusion for counter-current, horizontal case and LBM simulation	167
Figure 9.29 Mineral oil-pentane diffusion for counter-current, horizontal case and LBM simulation of the process	167
Figure 9.30 Kerosene-pentane diffusion for counter-current, vertical case and LBM simulation	168
Figure 9.31 Mineral oil-pentane diffusion for counter-current, vertical case and LBM simulation.	168
Figure 9.32 Kerosene-pentane diffusion for co-current, vertical case and LBM simulation	169
Figure 9.33 Mineral oil-pentane diffusion for co-current, vertical case and LBM simulation.	169
Figure 9.34 Mineral oil-pentane diffusion for counter – current, vertical case with 2:1 aspect ratio and LBM simulation of the process.	170

Figure 9.35 Kerosene - water counter-current imbibition and simulation using LBM. (Vertical orientation).....	177
Figure 9.36 Kerosene - water counter-current imbibition and simulation using LBM. (Horizontal orientation)	177
Figure 9.37 Kerosene - water co-current imbibition a)experiment b)simulation using LBM. (Vertical orientation).....	178
Figure 9.38 Time-lapse visualization of spontaneous imbibition on the micro-model.	178
Figure 9.39 Simulation results of spontaneous imbibition at micro scale.....	178

Nomenclature

$A =$	Cross sectional area.
$A_i =$	Area of a surface open to imbibition at the i^{th} direction.
$a, b, c =$	Matrix dimensions.
$c =$	Constant.
$D =$	Matrix diameter.
$f(\theta) =$	Certain function of wettability.
$k =$	Matrix permeability.
$k_w =$	Permeability to water.
$L =$	Matrix length.
$L_H =$	Vertical height of the matrix.
$L_c =$	Modified characteristic length.
$n =$	Total number of surfaces open to imbibition.
$P_c =$	Capillary pressure.
$P_{c,eff} =$	Effective capillary pressure.
$Q =$	Imbibition rate.

S_{mi}	=	Initial water saturation.
S_{wf}	=	Water saturation at the front.
t	=	Time.
t_D	=	Dimensionless time.
V	=	Bulk volume of the matrix.
X_{Ai}	=	Distance traveled by the imbibition front from the open surface to the no-flow boundary.
ϕ	=	Porosity.
μ_o	=	Oil viscosity.
μ_w	=	Water viscosity.
μ_{gm}	=	Geometric mean of oil and water viscosities.
σ	=	Interfacial tension.
C_i	=	Pressure at cell i
ρv_c	=	New density value
R_i, B_i	=	Occupation number for Red, Blue nodes
N_i	=	Occupation number for fluid flow
Δ_i	=	Occupation number for solvent phase
x	=	Coordinates on lattice
t	=	Lattice time
c_i	=	Unit speed in i^{th} direction
λ_v	=	Relaxation parameter for kinematic viscosity
λ_D	=	Relaxation parameter for diffusion coefficient
ν	=	Kinematic viscosity
D	=	Diffusion coefficient

N_i^{neq}	Non-equilibrium distributions
ρ	Density
u	Velocity
w_i	Weight factor for i^{th} direction
F	Total external force
F_g	External force caused by gravity
F_c	External force caused by fluid-fluid cohesion
F_a	External force caused by fluid-solid adhesion
g	Gravity

Glossary

There are quite a number of terms commonly used throughout the thesis. Some of them are new and used to describe special phenomenon in this work. Some terms are common in the literature but they need to be defined for the specific case they represent in this work. For convenience, these terms are listed and defined below.

Miscible interaction: Interaction (transfer) between matrix fluid (oil) and fluid in fracture (solvent –pentane or heptane used as solvent in the experiments) under static conditions, i.e. there is no flow in fracture. The transfer process is mainly controlled by diffusion.

Immiscible interaction: Interaction (transfer) between matrix fluid (oil) and fluid in fracture (an aqueous phase, brine or surfactant solution) under static conditions, i.e. there is no flow in fracture. The transfer process is mainly controlled by spontaneous imbibition.

Counter-current Interaction: Interaction between matrix fluid and fracture fluid occurring from the same side of the model. That is modeled in the experiments by sealing all sides of the model by epoxy and leaving only one side open for the interaction.

Co-current Interaction: Interaction between matrix and fracture that is occurring from two or more sides of the model. Typically, the fluid in fracture enters to the matrix from one side(s) and displaces the oil in the matrix from the other side(s). That is achieved by sealing

the sides of the models using epoxy and keeping the top and bottom parts open to flow and/or interaction with the fluid in fracture. If all sides are open to flow (no-sealing case), the interaction is assumed (and called) co-current though it could be in counter-current throughout or certain period of the experiment depending on the size of the model and other rock properties.

Spontaneous Imbibition: The act of absorption of a liquid into matrix by capillary forces. Spontaneous term defines the case where there is no external force (viscous or gravity) applied on fluid to force displacement. In this study, however, experiments have a very small amount of hydrostatic head due to immersion of the sample into a cell filled with the aqueous phase. This force is negligible as the capillary forces are much stronger.

Capillary Imbibition: It has the same meaning as spontaneous imbibition and has been used in the text interchangeably.

t_{final} : Time required for the oil recovery curve to reach the plateau region where there is no change in the recovery anymore. This term may not define the absolute end of the process. In this case, an approximate point was selected at which the curve starts showing an asymptotic behaviour.

Primary Imbibition: Spontaneous imbibition of water phase into a 100% oil saturated media.

Primary Diffusion: Miscible interaction between 100% oil saturated samples and surrounding solvent (fluid in fracture) without any flow in fracture.

Secondary Diffusion: Miscible interaction between matrix exposed primarily to spontaneous imbibition (until the end of process) and surrounding fracture fluid (solvent).

1 Introduction

1.1 Overview

As the demand for oil, and thereby its price, has been in an increasing trend recently, it is becoming more economical to produce oil from challenging and unconventional reservoirs. Due to recent jump in oil prices, methods that were once economically unfeasible can now be employed. Hence, the techniques and resources once put aside because of infeasibility are now under research.

Despite their size and high oil storage capacity, many naturally fractured reservoirs (NFR) in the world do not show high production performance and enhanced oil recovery (EOR) techniques are very challenging. Waterflooding in such reservoirs may not be applicable if the matrix is not water-wet, very tight and heterogeneous, and oil viscosity is high. Solvent injection is an effective method in homogeneous (non-fractured) media yielding very low residual oil saturation behind. Its cost is a limiting factor and therefore applications were limited until recent rise in oil prices. Hydrocarbon solvent injection may not be feasible because of the risk of storing valuable hydrocarbon in matrix and difficulty in recovering it back. Using CO₂ as solvent is an exception if the permanent storage of CO₂ is also targeted.

In addition, there are resources which were not widely considered before. Tight gas reservoirs have never been investigated adequately as it was assumed that the gas they enclose would not be significant and the production is restricted because of extremely low

permeability. Being a very clean fossil fuel as well as its potentially efficient production by immiscible – volumetric displacement, tight gas reservoirs are very good candidates to increase gas production if the reservoir shows a degree of fracturing.

As the fossil fuels are consumed with almost exponentially increasing rates, greenhouse gases became a major issue. Global warming manipulates the delicate balance of the earth, and precautions should be taken to preserve the environment. CO₂ emissions are one of the major causes of global warming, creating an isolation chamber that lets sun in, but does not let the heat out. Continental agreements are signed to decrease CO₂ production, companies are encouraged to eliminate the excessive CO₂. The oil industry is affiliated with creating this problem, and the solution is likely to be found within the industry itself. CO₂ sequestration in subsurface reservoirs emerged with these two ideas: (1) Increasing oil production as an EOR technique, and (2) burying the excess CO₂ in underground permanently. This would require a good understanding of how naturally fractured reservoirs interact with fluids in recovering oil while storing CO₂ simultaneously.

In the light of above possible process in NFRs, this research was aimed to understand the liquid-liquid and liquid-gas interactions between matrix and fracture for immiscible and miscible conditions. More specifically, the focus of this research is to clarify the dynamics of co- and-counter-current matrix-fracture interaction (miscible and immiscible) for different liquid types, rock properties and injection conditions. Counter-current interaction is chosen to be the main focus of this dissertation. The displacement of the non-wetting phase in matrix by a wetting phase flowing in fracture (immiscible interaction) takes place from the same side of the matrix (counter-current) if the boundary conditions physically restricting the contact of wetting phase with matrix from the other sides exist or the matrix is too big. It is commonly believed that matrix-fracture interaction process in subsurface reservoirs occur in counter-current manner. To model this process in laboratory conditions, we adapted an experimental system and sealed all sides of models with epoxy and left only one part (the bottom side typically) open for interaction with fracture fluid. For practical uses, this could also be considered as the worst case scenario in modelling matrix fracture interaction and evaluating oil recovery performances as this type of representation typically yield the lowest recovery compared to other type of matrix-fracture interaction configurations.

Liquid-liquid immiscible interactions are commonly encountered in oil reservoirs. Liquid-gas interactions are critical for the energy recovery from fractured gas and geothermal reservoirs. Liquid-liquid fully miscible interaction occurs during groundwater contamination and CO₂ injection if there is enough pressure and temperature to satisfy miscibility and CO₂ is in supercritical phase.

Despite the recognition of the process for quite a long time, yet many issues are unanswered in regards to the dynamics of the spontaneous counter-current interaction between matrix and fracture. Some of these issues include the effect of the matrix shape factor, wettability (for immiscible process), and IFT (when surfactants are used as the wetting phase) on the rate of imbibition (or progress of the displacement front) and the development of residual oil saturation in both swept and unswept zones. Previous studies mostly dealt with co-current imbibition and diffusion in uncoated matrices (all surfaces open to flow).

Another restriction in producing matrix oil is wettability. For weakly water-wet or oil-wet rocks, like many carbonates, injection of heat and solvents to recover matrix oil by energy and mass transfer could be the only way to recovery matrix oil, as the spontaneous imbibition does not take place and the recovery by the gravity drainage is relatively slow process. This is more prominent in case of heavy-oil.

Understanding the matrix-fracture interaction during miscible displacement in naturally fractured reservoir is a critical task in assessing enhanced oil recovery, greenhouse gas sequestration processes and groundwater contamination. If the injected fluid flowing in fracture and original matrix fluid are miscible, the transfer between the two media occurs mainly by diffusion in NFR. This is commonly encountered in gas or liquid solvent injection processes for enhanced oil recovery or the sequestration of greenhouse gases. If multiple contact miscible fluids such as methane, CO₂, N₂ or flue gas are injected into NFRs, diffusion between matrix and fracture fluids may control the process depending on pressure and other miscibility conditions. An example case would be high pressure CO₂ flooding into light oil containing fractured reservoirs. In this case, a fully miscible process that is controlled by diffusive mass transfer between matrix and fracture takes place.

1.2 Statement of the problem

Despite tremendous effort put in the last five decades, understanding the transfer between matrix and fracture still requires more clarifications. Physical models are needed for this and more robust computational models should be developed especially, to simulate the process for complex rock and fluid properties such as unfavorable matrix boundary conditions, heavy-oil, less water-wet matrix etc. Beyond that, high oil prices and increasing demand to oil entail searching new and unconventional techniques to produce problematic matrix oil from challenging NFR's. The main mechanism to produce matrix oil is to enhance interaction between matrix and fracture. This may not be a straightforward process under unfavorable conditions such as heavy oil, high IFT and oil wet matrix. NFR characterization is another challenge and the matrix properties such as size, shape and local heterogeneity are not easy to describe deterministically. These properties strongly control the interaction type, i.e., co-or counter-current, capillary or gravity dominated, etc.

The development of residual saturation in the matrix is a critical parameter as it eventually affects the investment decision for any EOR application. Understanding matrix-fracture dynamics better will yield a clearer picture for the causes of residual oil saturation (or phase distribution in the matrix). This is a crucial task in proposing solutions to decrease the residual oil saturation by advanced EOR techniques.

Experimental work is a useful but exhaustive tool in those attempts. Its necessity is undeniable in explaining the physics behind the process, but computational works provide faster clarifications of the processes. Therefore, experimentally verified computational models that are capable of capturing the physics of the process for a various -challenging-rock and fluid properties could be extremely useful not only for the scientific studies but also for practical engineering investment decisions. Continuum models could be a solution for practical purposes but, pore scale models would be more powerful in identification of the residual saturation development and the progress of the displacement front in the matrix during the interaction process. Alternative pore scale modeling algorithms such as invasion percolation (useful for low capillary number processes) or diffusion limited aggregation (useful for high displacing/displaced phase viscosity ratios) models are highly limited for more general cases even though they are capable of incorporating the random nature of the

process, especially for miscible interaction. These limitations entail more robust pore scale models to capture the physics and random nature of the process even for wide range of rock and fluid properties, and matrix boundary conditions.

1.3 Methodology

The ultimate goal of this study was to understand the dynamics of matrix-fracture interaction in NFRs that could be of help in optimizing oil and gas production, and CO₂ sequestration processes. Modelling this type of transfer process requires a good understanding of uncertainty and fluid mechanics at pore scale. It is also important to define the transfer mechanism at small time (minute) scales.

In a naturally fractured reservoir, the system consists of oil or gas bearing matrix and complicated channel-like fracture structure. The smallest portion that represents such systems would be to a single fracture and a single matrix case. Throughout the experimental or computational modeling studies, a single matrix-single fracture system was considered for totally static conditions, i.e., no viscous force caused by the flow in fractures. The gravity effect, caused by the height of the matrix and height of the aqueous phase column in the imbibition cells, is not believed to be critical in the recovery performance. This is mainly due to negligible magnitude of the aqueous phase column height and matrix size. The rock-fluid characteristics applied in the experiments are strongly capillary dominated systems.

The study was performed at two scales: (1) core, and (2) pore. The core scale experiments were used in identifying the dynamics of the interaction through the oil recovery curves. They were then combined with equivalent 2-D sand pack models which provided only visual data. This practice was useful to clarify the uncertainties in the core experiments which were analyzed based only on the recovery curves. Two main focuses were the identification of the dynamics of the process (progress of the front) and the phase distribution in the matrix that eventually results in the development of residual oil saturation.

Both rock experiments and visualization studies (core scale studies) were limited to clarify the mechanics of the interaction process at pore scale. This is more critical in the case of

immiscible displacement process and micro models were used to visually observe the matrix-fracture interaction by spontaneous imbibitions at pore level.

Eventually, both miscible and immiscible interactions were modeled using pore scale computational models and the LBM was found to be suitable for this. It is a new technique and with modifications, the experimentally observed dynamics of the processes at core and pore scales were captured in the LBM models.

In summary, by employing core experiments, visual studies, and computational models, qualitative and quantitative analyses of miscible and immiscible matrix-fracture interaction in naturally fractured reservoirs were performed.

1.4 Major contributions to the literature and industry

Major contributions out of this dissertation can be listed as follows. The detailed and more specific contributions can be found in the “Conclusion” section.

- Dynamics of miscible and immiscible fracture-matrix interaction was scrutinized using both core scale (3D) and visual (2D) experiments for a wide range of rock and fluid properties. Quantitative data; namely trends in recovery rate and ultimate recovery obtained from the core experiments were analyzed with a support of qualitative data obtained from visual experimentation.
- The importance of the parameters such as pore architecture, matrix boundary conditions (yielding co- or counter current interaction), gravity, interfacial tension, wettability, and oil viscosity on the dynamics of immiscible interaction between matrix and fracture was identified experimentally. The effects of those parameters on the immiscible matrix-fracture interaction were also shown using the Lattice-Boltzmann method (LBM).
- Comparison of gas-liquid and air-liquid visual and core experiments provided a clear identification of immiscible interaction. It was shown that, unfavorable rock matrix types (carbonates due to their low permeability and less water-wettability) might yield

a better recovery performance than that of favorable matrix types (high permeability and strongly water wet sandstones) if the interaction type is changed. This is mainly due to entrapment of non-wetting phase controlled by the matrix boundary conditions especially for gas-liquid immiscible interaction (gas displaced by imbibing water) under the influence of gravity.

- Importance of the convective transport (buoyancy forces) in the matrix was visually shown and conditions at which this type of transfer becomes a dominating mechanism over dispersive transport were identified. This type of interaction needed more powerful computational models and the modified LBM proposed in this dissertation captured experimentally observed diffusive-convective matrix-fracture interaction for a wide range of diffusion coefficients and viscosity ratios.
- For practical purposes, optimal use of tertiary -solvent injection- techniques in naturally fractured reservoirs was defined. Conditions that yield optimal performance for waterflooding followed by solvent injection and direct application of solvent flooding without pre-waterflood were identified for different rock types.

2 Literature Review

2.1 Spontaneous imbibition (immiscible process)

Understanding the dynamics of counter-current imbibition is crucial to cure recovery problems in oil, gas, and geothermal reservoirs. The recovery rate and ultimate recovery are mainly controlled by the interaction type. Matrix shape, i.e., boundary conditions, is one of the critical parameters that is not controllable. Therefore, controllable parameters, such as the viscosity of injected fluid, IFT, temperature etc., could be adjusted based on the matrix characteristics for efficient matrix fracture interaction.

Although the capillary imbibition from a matrix with all sides open to flow has been investigated extensively, understanding the dynamics of counter-current imbibition needs more research. Frequently seen in previous studies was leaving all sides of a cylindrical core open to flow. This may or may not yield a truly counter-current displacement unless the matrix is very big. Ma et al. [1995] conducted counter-current imbibition experiments both with all surfaces open and partially coated cores. They used coated cores ranging between 4 and 6 cm in length and a fixed 1 ½ inch in diameter and were able to apply scaling equations first proposed by Mattax and KYTE [1962]. Babadagli [2000] used various configurations of matrix shape. He investigated co- and counter-current flow for surfactant and polymer solutions, and concluded that the modified form of Mattax and KYTE's scaling group is

applicable for high-IFT cases. Bourbiaux and Kalaydjian [1988] conducted counter-current imbibition experiments and estimated the relative permeabilities using numerical simulations. They observed that the relative permeabilities to the phases are smaller when compared to the ones for co-current flow. They stated that, though experimental and numerical results are consistent with the proposed theory, further investigation on counter-current interaction is needed. Schembre and Kovysek (2003) were also provided an indirect estimation technique for counter-current relative permeability. Note that it is critical to determine the end point values for a wide variety of matrix and fluid properties in deriving relative permeability correlations. This entails elaborate experimental work.

Schembre et al. [1998] performed CT scanning experiments using Berea sandstone and diatomite. Although the experiments were in counter-current manner, imbibition into Berea sandstone showed a bullet shaped water front profile. Zhou et al. [2002] observed a frontal displacement of air by water in diatomite samples due to capillary imbibition. The residual gas saturation development was sensitive to the local heterogeneity and more oil is trapped in counter-current compared to the co-current imbibition. They also observed that the counter-current imbibition is faster than co-current imbibition at early times (when the dimensionless time is less than unity). Pore structure is expected to be critical as shown by Suzanne et al. [2003] for viscous displacement as well as the matrix boundary conditions for the displacement by capillary imbibition.

Zhang et al [1996] and Ma et al [1995] observed that the counter-current imbibition recovery rate is much slower than that of co-current but eventually they all reached the same ultimate recovery for strongly water wet systems (Berea sandstone). This is in accordance with the Bourbiaux and Kalaydjian's [1988] observations. Several studies attempted to explain different aspects of matrix-fracture interaction process. Some of these issues include the effect of the matrix shape factor [Rangel-German and Kovysek, 2003; Civan and Rasmussen, 2003, 2005; Yildiz et al., 2006], wettability [Babadagli, 2002], and IFT (when surfactants are used as the wetting phase) on the rate of imbibition (progress of the front) and the development of residual oil saturation in both swept and unswept zones [Babadagli, 2001, 2002].

Li and Horne [2000], and Kantzas et al. [1997] investigated the development of residual gas saturation for capillary imbibition and the latter tested different models suggested to estimate it.

Recently, Morrow and Mason [2001] reviewed the studies published on capillary imbibition of liquid-liquid systems in the last four decades. It is agreed that the gas-liquid systems may differ from liquid-liquid systems and the approaches used to describe and formulate the phenomenon, i.e., the scaling groups, may not be applicable for gas-liquid systems mainly due to the differences in density, viscosity, surface tension, and wettabilities of the phases. Gas phase in the matrix of naturally fractured gas and geothermal reservoirs can be produced if there exists a liquid phase in fractures by capillary or gravity interaction. Mechanism is counter-current, i.e., displacement of non-wetting phase by wetting phase takes place from the same side of the matrix, if the boundary conditions physically restricting the contact of wetting phase with matrix from the other sides exist. Although the mobility ratio and wettability are more favourable in gas-liquid systems, high surface tension may cause the entrapment of non-wetting phase gas phase. This is more prominent in case of counter-current flow as the boundary effects show more restriction to flow.

2.2 Diffusion-dispersion (miscible process)

Studies on the oil recovery from matrix by injecting solvent and obtaining recovery by molecular diffusion exist in the literature. The investigation was mainly on the rock matrix with all sides open to flow. A limited number of studies focused specifically on counter-current type interaction. Stubos and Poulou [1999] studied oil recovery potential from fractured reservoirs by mass transfer processes. They investigated the oil recovery by evaporation and diffusion mechanisms through a macroscopic analysis of the flow and mass transfer phenomena. This led them to analytical expressions for evaporation, the extent of the two-phase zone in matrix, and the location of the propagating front. Morel et al. [1990] studied the diffusion effects in gas-flooded light oil (pentane) fractured reservoirs that are subjected to methane or nitrogen gas flooding. They concluded that most of the pentane in place is recovered within several weeks. Pentane recovery was twice as fast with methane as with nitrogen. Saturation profiles revealed a strong capillary end effect for nitrogen injection

with an accumulation of liquid near the fracture. Zakirov et al. [1991] investigated the miscible displacement of fluids within fractured porous reservoirs. They clarified the effects of the displacement rates and magnitude of pressure on the reservoir performance and the dynamics of the process. Le Romancer et al. [1994] studied the mechanism of oil recovery by gas diffusion in fractured reservoir in the presence of water. They examined the effect of gas diffusion in the matrix blocks of light oil fractured reservoir subjected to gas injection, and found that saturation profiles reveal a strong capillary end effect for nitrogen injection with an accumulation of oil near the fracture. They also observed that the impact of water saturation on recovery depends strongly on the nature of the diffusing gas.

A few numerical modeling studies appeared in the literature on the diffusion process in NFR's as well. Da Silva and Belery [1989] used Fick's molecular diffusion approach to present a numerical solution. They proposed a method to predict molecular diffusion and embedded their model into a dual porosity, fully implicit, fully compositional, EOS based reservoir simulator. Lenormand et al. [1998] worked on the same problem to calculate the amount of transferred component by diffusion as a function of fracture geometry, fluid velocity in the fracture, and fluid compositions in fracture and matrix. They considered the fracture as a porous block but then could not directly account for the diffusion flux as a boundary condition. The only way to model the diffusion transfer was to calculate an effective diffusion coefficient, which accounts for the diffusion transfer. LaBolle et al. [2000] generalized stochastic differential equations to the case of discontinuous coefficients and developed random-walk methods to numerically integrate these equations. Polak et al. [2003] used a medical based X-ray CT scanner to monitor the diffusion of NaI into the matrix of 20cm long, 5cm diameter artificially fractured core. Their mathematical model assumed diffusion within the matrix and a linear concentration variation through the transition layer from its value in the fracture to its time-dependent value at the transition layer/matrix interface.

2.3 Visualization studies (pore scale computational and experimental)

Wardlaw et al. [1993] conducted experiments using glass cells and showed the importance of local differences in surface roughness on the imbibition of water and brine displacing oil. Indelman and Katz [1980] analyzed the mechanics of counter-current imbibition on 2-D models numerically and observed that the amount of imbibed liquid is a linear function of the square root of time. They investigated the local heterogeneity on the process as well. Tidwell et al. [1995] studied matrix imbibition during flow in the fracture. They modeled the matrix imbibition as a linear function of the square root of time as suggested by Indelman and Katz [1980] and observed that this approach is applicable only to homogeneous matrix. They further investigated the heterogeneity effects using x-ray imaging and visualized the imbibition of water into a slab of volcanic tuff. They observed that the trend shows a linear behavior although the hydraulic conductivity of tuff varies by over four orders of magnitude. Medina et al. [2001] conducted experiments on filter papers with different shapes and showed that in rectangular strips the dynamics of the capillary imbibition yields the classical Washburn law.

Yortsos and Xu [1997] and Xu et al. [1998] developed a phase diagram of fully developed drainage in porous media using invasion percolation simulation runs. The transition between the stabilized displacement and fingering is controlled by the change of the sign of the gradient of the percolation probability (from stabilizing to destabilizing). They described the transition boundary by scaling laws. When the mobility, M is sufficiently small, the displacement can be modeled by a form of gradient percolation [Xu et al., 1998].

Studies on the diffusion-dispersion controlled displacement are limited compared to the imbibition or drainage processes, especially from the visualization point of view. The interaction type, i.e., co-current and counter-current, viscosity of the displaced fluid, matrix boundary conditions, and displacement direction affect the diffusion controlled displacement process. Wen et al. [2005] proposed an approach to estimate the diffusion coefficients using NMR. They experimentally obtained diffusion coefficient curves against time and solvent content. Both represented by exponential curves whereas diffusion coefficient curves against viscosity yielded a straight line.

Pringle et al. [2002] used Hele-Shaw experiments to capture the structural patterns of double-diffusive convection. They justified that parallel plates would also serve as an analog for flow through porous media provided that the assumptions by Wooding [1960] are satisfied.

With the advancements in micro-chip and micro-fluidics industry, 2-D glass micro models of high quality and precision were developed recently. The evolution started with etched-glass models and continued with silicon etching, which allowed to replicate pore sizes on real world scale. These models were used in various studies [George and Kavscek., 2001; Sagar and Castanier, 1997].

2.4 Modeling efforts

The invasion of wetting fluid into non-wetting fluid containing porous medium (imbibition) is controlled by the competition between different types of displacement mechanism [Blunt et al., 1992; Lenormand et al., 1993]. Pore scale modeling is a routinely used method to investigate the different flow phenomena in porous media. Hughes and Blunt [2000] proposed a pore scale model to study the effects of flow rate and contact angle on imbibitions relative permeabilities. The model they created accounts for flow in wetting layers that occupy roughness or crevices in the pore space. Fracture flow is represented in the case of two-dimensional flow. They classified the displacement patterns under five groups for different capillary numbers, contact angles and initial wetting phase saturations.

In another publication, Hughes and Blunt [2001] studied multiphase flow in fractures using network modelling. They developed a variable fracture aperture distribution as represented by a square lattice of conceptual pores connected by throats. They used similar concepts as in pore network modelling. Viscous forces were accounted for using the perturbation method and simulations were performed for horizontal flow, as well as gravity stable and gravity unstable displacements.

Stochastic models have been commonly applied to simulate different type of displacement processes in porous media. Studies in this area resulted in different displacement patterns

varying from piston like to fingering [Lenormand, 1990]. Quasi static displacement dominated by the capillary forces yields a process called invasion percolation (IP) [Wilkinson, 1984; Wagner et. al., 1999]. Diffusion limited aggregation (DLA) patterns were obtained during diffusion and viscous forces dominated processes [Lenormand 1989].

Modifications to IP and DLA algorithms were developed to better simulate the flow in pore level. Biroljev et al. [1991] took the gravity effect into account, developed the computer model and tested the model experimentally. They concluded that the front between the fluids is found to scale with the dimensionless Bond number (ratio between gravitational and capillary forces), and the fractal dimension of the profile is found to be $D_e \approx 1.34$.

In a recent study, Ferer et al. [2003] showed that the IP models are applicable to the systems in the limit of zero capillary number whereas DLA models the flow in the limit of zero-viscosity ratio. Fernandez et al. [1991] defined the crossover length from invasion percolation to diffusion limited aggregation in porous media. Interpore surface tension was neglected in their study and the invading fluid was assumed to be non-viscous.

More recently the Lattice Boltzmann (LBM) algorithm was adapted to simulate displacement in porous media. The LBM is relatively new but promising in modelling displacement process for complex matrix and fluid properties. The underlying idea of the LBM is to construct simplified kinetic models that incorporate the important physics of microscopic processes so that microscopic averaged properties obey the desired macroscopic equations.

The LBM uses cellular automata that implement rigorously simplified and highly discretized particle interactions at the micro-scale to recover Navier-Stokes fluid behavior at larger scales. The LBM evolved from lattice gas methods [Frisch et al., 1986], which track individual particles and their interactions are typically limited to two-dimensional hexagonal grids, whereas the LBM use near continuous particle distributions to avoid statistical noise associated with individual particles.

Evolution of the LBM was observed over the last decade. Research was focused on improving the algorithm to simulate fluids both miscible and immiscible, as well as more efficient algorithms to lighten the heavy computing requirements. Pioneers of the method

have published numerous valuable resources [Kadanoff, 1986; Doolen and Chen, 2001; Rothman and Zaleski, 1994; Benzi et al., 1992; Chen et al., 1996; Chen et al., 1996].

Bouzidi et al. [2001] studied the velocity boundary condition for curved boundaries in an effort to improve the simple bounce-back boundary condition. They worked on LBM boundary conditions for moving boundaries by combination of the “bounce-back” scheme and spatial interpolations of first and second order. Flekkoy [1993] was the first to introduce the Bhatnagar-Gross-Krook model for miscible fluids. He derived the convection-diffusion equation and the Navier-Stokes equation describing the macroscopic behaviour using the Chapman-Enskog expansion. Stockman et al. [1998] focused on enhancing the algorithm and making it more efficient for practical use and used the code to model dispersion in rough fractures and double-diffusive fingering.

The LBM is also useful to model immiscible fluid flow [Fernandez et al., 1991]. Introducing interfacial tension phenomena and the interface between the fluids, one can model phase separating fluids. An important topic in multiphase flow, bubble motion under gravity, was modeled by Takada et al. [2001]. They were able to obtain realistic results that can simulate bubble coalescence and bubble motion with surface tension values that can satisfy the Laplace's law.

Shan and Chen [1993] introduced a new approach known as pseudo-potential to simulate immiscible flow. The simplistic inclusion of fluid-fluid cohesion (interfacial tension) and fluid-solid adhesion (wettability) makes this model the most widely used LBM method to model immiscible displacement. The Shan-Chen model is not based on thermodynamical principles, therefore, the interfacial tension and wettability is introduced empirically. The free-energy approach [Swift et al., 1995], on the other hand, implements interfacial thermodynamics, and therefore allow viscosity and interfacial tension to be specified a-priori. Despite these advantages over the pseudo potential model, free-energy model is computationally more demanding and has certain drawbacks [Hazi et al., 2002; Nourgaliev et al., 2003]

Studies related to porous media among others include investigations of fluid interface configurations [Sukop and Or, 2004], capillary rise [Rasikinmaki et al., 2002], and solute transport [Zhang et al., 2002].

Scaling or model parameter calibration arises as a major topic in LBM development. Christensen et al. [2006] successfully calibrated the LBM for their needs. However the relation between physical and lattice time (which involves viscosity) is largely ignored due to the assumption that viscous forces are negligible compared to capillary forces.

3 Experimental Agenda

The experimental part of this research is decided to be a combination of qualitative and quantitative data. For quantitative data, real rock samples are used. The qualitative data is obtained from visualized 2D sand packs and micro models. Observations obtained from both studies are used to scrutinize the interaction process between matrix and fracture for different conditions.

3.1 Experiments on rock samples

In the first part of the research (section 4.1) immiscible processes are studied experimentally for the effects of the matrix shape factor, wettability, oil viscosity and interfacial tension on the rate of capillary imbibition and development of residual non-wetting phase saturation. In the second part (section 4.2), miscible process as usually encountered in enhanced oil recovery (EOR) application are analyzed as secondary oil recovery by diffusion of a solvent from the samples exposed to capillary imbibition first. Primary diffusion experiments are also performed (oil saturated samples are exposed directly to solvent phase without pre-waterflood) on selected core sizes for comparison.

3.1.1 Porous media

Cores used were Berea sandstone and Indiana limestone samples with 3 different diameters: ½, 1, and 2 inches. Each diameter was available in 3 different lengths; 2, 4 and 6 inches (Fig. 3-1). The average values of porosity and permeability of the samples are 21% and 500mD, for Berea sandstone and 16% and 15 mD for Indiana limestone, respectively. According to desired interaction type, each sample was coated with epoxy (carbolite 9085), leaving only one side (counter-current) or 2 sides (co-current) open to imbibition. Special attention was given to make sure that the impregnation of epoxy into core was minimal during the coating process. To assure this, a thin coat of epoxy first was applied onto the surface and waited for curing. Then a second -thicker- layer was applied to ensure perfect coating with minimal impregnation of epoxy into the core. Additionally, selected sizes of uncoated cores were used to serve as reference cases.

Prepared cores were saturated with mineral or crude oil in the vacuum chamber for 48 hours and pore volumes were determined from the weight difference. Pore volume and porosity values for each sample were measured. Additionally, for each rock type, wettability was calculated using the procedure proposed by Babadagli [1996] based on Handy's effective capillary pressure measurement approach [1960]. Vertically positioned cores were exposed to either solvent or brine for diffusion or imbibition processes, respectively. Some samples were exposed to aging for one week and one month to alter the wettability.

The rock samples were used for only one experiment to avoid any wettability change due to the core cleaning process. Fig. 3-2 displays the experimental set-up. A table that lists the core characteristics is included in the beginning of each related section (4.1 Gas-liquid immiscible, 4.2 Liquid-liquid immiscible, 5.1, 5.2 Liquid liquid miscible).

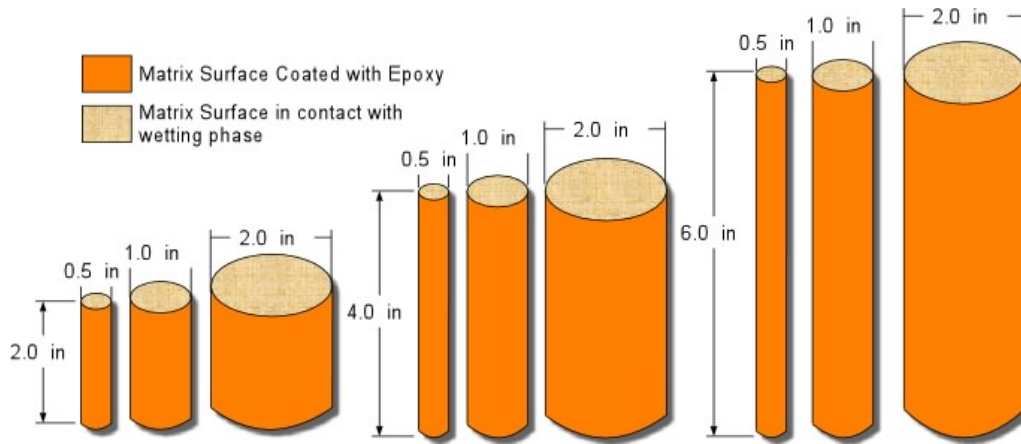


Figure 3.1 The sizes and shapes of the cores used in the experiments.

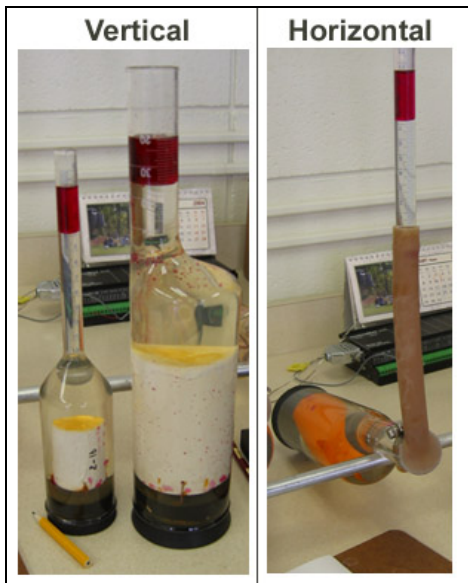


Figure 3.2 a) Horizontal and vertical imbibition tubes b) measurement using scales.

3.1.2 Immiscible processes

To study liquid-gas interaction (section 4.1), air-water pair was chosen. Experiments were performed with low (20°C) and high (90°C) temperature water. Although not particularly accurate, the higher temperature case was thought to be used in modelling the matrix-fracture interaction process in geothermal reservoirs. The properties of the fluids used and surface tensions at different temperatures are given in Table 3-1.

Table 1 Properties of fluid pairs used for gas-liquid experiments

	Wetting Phase		Non-Wetting Phase	
	Hot Water (90°)	Cold Water (20°)	Air (90°)	Air (20°)
Density (g/cc)	0.965	1	0.0009	0.001
Viscosity (cp)	0.326	1	0.210	0.182
Surface tension (dyne/cm)	60.8	72.9		

For the liquid-liquid interaction (section 4.2) oil types (non-wetting phase) used were kerosene and mineral oil and are listed in the top part of Table 3-2. The middle row of Table 3-2 lists the aqueous phase; water, brine (3% NaCl) and surfactant solutions with varying concentrations as the selected wetting phases. The properties of the fluids used and corresponding interfacial tensions (IFT) between two-phases are given in the bottom row of Table 3-2. The IFTs were measured using the ring method. Surfactant solution was prepared by mixing an anionic surfactant (2AO: Alkyldiphenyloxide Disulfonic Acid, supplied by Dow chemicals) at three different concentrations: 1%, 9% and 15%. The two values of concentrations (9 and 15%) are above the critical micelle concentration (CMC). It was observed that 1% concentration is below the CMC value.

Table 2 Properties of fluid pairs used for liquid-liquid experiments

Non-Wetting Phase	Air	Kerosene	Mineral Oil	Mineral Oil		
Density (g/cc)	0.001	0.79	0.83	0.83		
Viscosity (cp)	0.0182	2.9	36.32	36.32		
Wetting Phase	Water	Brine	Surfactant 1%	Surfactant 9%	Surfactant 15%	
Density (g/cc)	1	1.05	1	1	1	
Viscosity (cp)	1	1	1	1	1	
IFT (dyne/cm)	72.9	13.49	30.33	11.1	13.4	11.2

3.1.3 Miscible processes

Conventional practice in oil reservoirs is to flood the reservoir with water to recover matrix oil by spontaneous imbibition if the reservoir is naturally fractured. This method is efficient if the matrix is water-wet and enough supply of immiscible wetting phase exists in the fracture. This type of recovery enhancement may not be adequate if the matrix is oil wet or the displaced phase is high in viscosity. It is apparent that any type of enhanced oil recovery other than capillary imbibition would be costlier in terms of infrastructure and expenses. Due to increasing demand for oil and the requirements for CO₂ sequestration, however, miscible displacement (solvent injection) has become a serious option.

Chapter 5 of the dissertation deals with this phenomena. Experiments are grouped as two parts: (1) Primary, and (2) secondary diffusion. Oil saturated core samples are directly exposed to solvent phase to obtain primary diffusion experiments. For the secondary diffusion, a practice that would be more common in real life is applied. The samples previously subjected to oil recovery by capillary imbibition (primary imbibitions) are later exposed to diffusion (secondary diffusion) in a way to simulate tertiary recovery.

Some core samples that were previously used for capillary imbibition experiments are used to test the secondary diffusion (section 5-2). The cores used for the primary imbibition experiments (section 5-1) are identical to the secondary diffusion types. Each sample is used only once not to cause any changes on their characteristics due to cleaning process. n-Heptane is used as solvent in diffusion experiments. (Table 3-3).

Table 3 Fluids used in miscible interaction experiments.

Fluids	n-Heptane		Mineral Oil
Density (gr/cc)	0.6837@20°C	0.6795@25°C	0.83
Viscosity (cp)	0.42		36.32

3.1.4 Procedure

Static counter-current imbibition experiments were performed using imbibition tubes. Cores were coated with epoxy leaving only one side uncoated. Vertically and horizontally positioned cores were exposed to the wetting-phase.

Small and large imbibition tubes were utilized for large and small core experiments (Fig. 3-2a). The tubes are made of glass, with a graduated cylinder on top to monitor the volume imbibed. The small imbibition tubes are of 2 inches in diameter and 4 inches in length. The graduated cylinder attached has a volume of 12cc, with a 0.1cc scale. The large tube is 70mm in diameter and 7 inches in length. These tubes also have offset positioned graduated cylinders to be able to monitor the recovery for the horizontal imbibition experiments. The volume of the graduated cylinder is 50cc to accommodate the large volumes of recoveries. Small graduated cylinders may be attached to these tubes via elastic tubings to ensure precise readings as shown in Fig 3-2a.

For air-water experiments, high temperature is observed to be a concern, where evaporation was a problem. For that case, the imbibition tubes were placed in a temperature bath using a hanging line that was attached to a scale. Before doing this, the rock sample and water were preheated to 90°C. Water used in the experiments was de-aerated to avoid any gas phase coming out of it at higher temperatures. The amount of water imbibition was monitored by reading the change in the scale. Note that the vertically positioned cores have the open surface pointing downwards to allow wetting phase imbibition only against the gravity.

For the oil cases, cores were saturated with oil for 48 hours. After weighing them and calculating the pore volume of the rock (using the void and oil saturated core weight difference), they were immersed into the imbibition tube filled with the wetting-phase. The recovery was monitored against time. As in the air water case, vertically positioned cores have the open surface pointing downwards allowing wetting phase imbibition only against the gravity.

Miscible process prevents to visually identify the recovered oil. Therefore, the experiments were performed using accurate scales (Ohaus Explorer Pro series) (Fig. 3-2b). Cores that are positioned vertically were suspended to the scales using the built-in hooks under them to

monitor the weight difference. For noise reduction, the data acquired from the scales were averaged. Weight difference was translated into recovered oil using a simple material balance equation. The n-heptane level was kept constant in the tubes by continuous feeding via a pump.

3.2 Visualization experiments

3.2.1 Glass bead models

The models saturated 100% with either mineral oil or kerosene under vacuum were put into contact with pentane either horizontally or vertically. For both co- and counter-current cases, the bottom edge was immersed into pentane. For the co-current case, the top edge was open to the atmosphere whereas for the counter-current case it was sealed.

The horizontal case had its limitations; a high-intensity halogen light source had to be used to supply enough illumination since the light has to be powerful enough to be transmitted through both the model and the reservoir of the diffusing fluid. The light source was fan-cooled and computer controlled to allow automatic switch off when not in use to avoid excessive heat generation. For the horizontal case, the model was slightly tilted upwards not to have any pentane contact with the upper portion of the model. The bottom part was fully immersed into the pentane.

For the vertical cases, weaker light source was good enough to obtain good quality images as the light had to be transmitted only through the 2-D model. Time lapse photography using a 6.3 megapixel camera served to visualize the experiments. Images transferred to computer were processed using an open-source software package (ImageJ) which has multi-image stack handling capability [Rasband, W.S., 1997- 2006].

A 2-D sand pack model was prepared using two ¼ inch thick transparent acrylic sheets. The gap between the acrylic sheets (around 0.3 mm) was filled with 0.1 mm diameter glass beads. The glass beads were packed densely to assure a homogeneous distribution. A filter paper was used to prevent glass bead movement and provide a better contact of the solvent phase (pentane) with the displaced fluid (oil) at the side of the model from which the diffusing

phase was entering. The displacing phase fluid was maintained at constant level within the container using a micro-pump. This ensures that the pressure caused by hydrostatic head is kept constant throughout experimentation. Different boundary conditions (only one or two sides open to flow) were created using epoxy sealant. A suitable epoxy sealant was selected not to react with oil or solvent phases. Figs. 3-3 and 3-4 show an outlook of the models and experimental set up, respectively. **Table 3-4** provides the properties of the fluids used in the experiments.

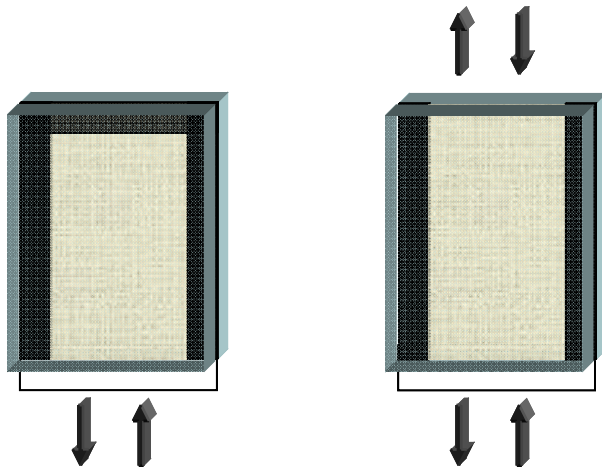


Figure 3.3 Schematic representation of the experimental model with different boundary conditions: (a) Counter-current, and (b) co-current interaction.

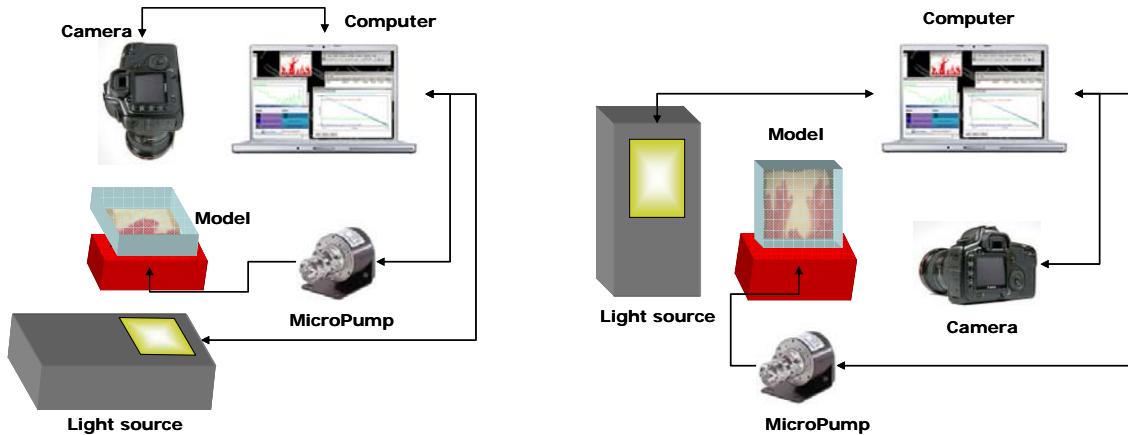


Figure 3.4 Experimental setup for (a) vertical,

(b) horizontal orientations.

Table 4 Fluid pairs used in the visualization experiments.

	Pentane	Kerosene	Mineral oil
Density (g/cc)	0.63	0.79	0.83
Viscosity (cp)	0.38	2.9	36.32

3.2.2 Silicon etched micro-models

For the micro-model study, silicon etched model is preferred over glass-etched models because of certain limiting factors. For glass-etching, acid has to be used and the reaction kinetics of acid etching enlarges the pore sizes of typical rocks by a factor of 5 to 50. In case of silicon etching, pores and throats are created photochemically resulting in 1:1 replication of a sandstone. A detailed description of the fabrication and construction process of the models used can be found in Hornbrook et al. (1992), Woody et al. (1995) and Lolomari et al. (1996). The pattern (Fig. 3-5) captured from a real sandstone thin-section is $500\mu\text{m}$ in length is repeated 10,000 times to create a 5cm^2 model. The properties of these models can be found in Table 3-5.

The model is transparent from one side only, and the ports for inlet and outlet are positioned on the opaque side. A model holder with four configurable ports is prepared using acrylic because of its flat and smooth surface (Fig. 3-6a). Two additional ports are used for vacuuming the glass model underneath so as to prevent the ports from leaking (Fig.3-6b).

The models are saturated with either kerosene or mineral oil by applying vacuum from two inlet ports. At the same time, the oleic phase is injected from the remaining two ports. Procedure is repeated around roughly 100PV oil is circulated.

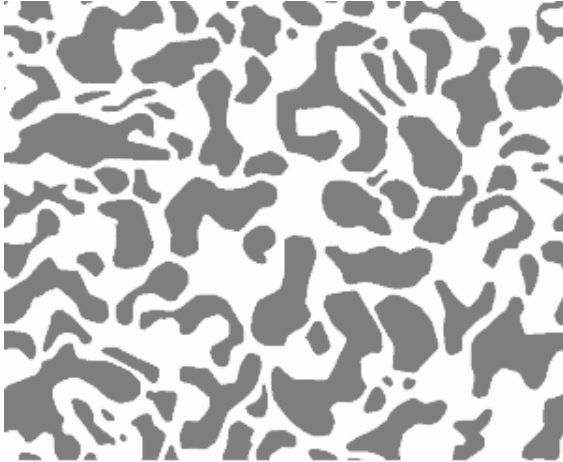


Figure 3.5 Repetative micro-model pattern.

Table 5 Micro-model properties.

Porosity	35%
Permeability	1 md
Pore Sizes	1-150 μm
Throats	0.5-10 μm
Etch Depth	15 to 35 μm

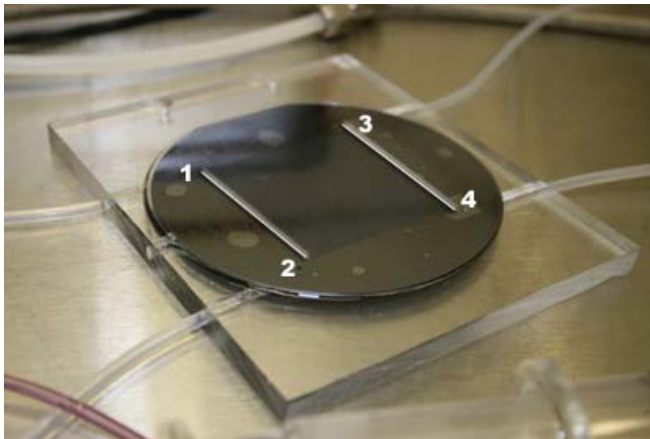


Figure 3.6 a) Glass model on holder, inlet-outlet ports connected, vacuum port disconnected. Ports on the model are marked with numbers. Ports 1&2 and 3&4 are connected with fracture which is highlighted with gray lines, b) model holder with four configurable ports and one vacuum port. Vacuum suction cups are connected to vacuum port internally.

4 Immiscible matrix-fracture interaction



















The rate and dynamics of counter-current imbibition differ depending on the contact area between fracture fluid and matrix. Rangel-German and Kovsky [2002] studied the effects “fracture filling” and “instantly filled fracture” cases on the dynamics of counter-current imbibition while there was continuous flow of water in the fracture. They observed different dynamics for the two cases. Obviously, “fracture filling” case also depends on the flow rate in the fracture [Babadagli, 2000; Babadagli and Ershaghi, 1992]. The cases we considered in the present study are totally static and therefore resemble to the “instantly filled fracture” case.

4.1 *Gas-liquid interaction*

The fluid pair chosen to test gas-liquid interaction is air-water. All available types of cores are tested for low and high temperature experiments. Repeatability tests are performed initially. The difference between the ultimate recoveries of the repeatability experiments are obtained to be within the range of 0% to 3% of the pore volume of each sample. The recovery curves followed a very similar trend in the repeatability experiments. Three-sides-sealed (counter-current) models are used with the open edge oriented to face down. Additionally, a

few Indiana limestone samples are included as well as uncoated samples to serve as reference. Air-water experiments are listed in Table 4-1

Table 6 Inventory of air-water experiments

Length (in)	Diameter (in)	Core Shape and Orientation	Cold Water Experiments			Hot Water Experiments		
			Berea Sandstone	Indiana Limestone	Uncoated (Berea Sandst. Indiana LS)	Berea Sandstone	Indiana Limestone	Uncoated (Berea Sandst. Indiana LS)
2	0.5		1			H-1		
4	0.5		2			H-2		
6	0.5		3			H-3		
2	1		4 - 4RE		25UC (Berea)	H-4		H-25UC (Berea)
4	1		5		27UC (ILS)	H-5		H-27UC (ILS)
6	1		6			H-6		
2	2		7	19		H-7	H-19	
4	2		8	20		H-8	H-20	
6	2		9	21		H-9	H-21	
2	0.5		10			H-10		
4	0.5		11			H-11		
6	0.5		12-12RE			H-12		
2	1		13			H-13		
4	1		14			H-14		
6	1		15			H-15		
2	2		16	22		H-16	H-22	
4	2		17	23		H-17	H-23	
6	2		18	24	26UC (Berea)	H-18	H-24	H-26UC (Berea)

4.1.1 Low temperature experiments (20°C).

Air-water imbibition recovery curves for the Berea sandstone and Indiana limestone experiments at 20°C are shown in **Figs. 4-1** (vertical case) and **4-2** (horizontal case) and **Fig. 4-3**, respectively. They include all different combinations of diameter, length, and orientation given in Table 4-1.

4.1.1.1 Berea sandstone experiments

Nine experiments (Exps.# 1 through 9 in Table 3-3) were conducted for vertically situated different diameter and length Berea sandstone samples. For comparison, an uncoated Berea sample gas-water imbibition experiment was also included.

Vertical samples. Small diameter Berea cores (Exps. 1, 2, and 3) yielded the most efficient displacement for the vertical cases (Fig. 4-1). They all showed a similar recovery rate and ultimate recovery regardless the aspect ratio. In other words, the matrix boundary conditions were not observed to be effective for the small diameter samples.

The 1 and 2” diameter Berea sandstone samples, however, resulted in lower displacement efficiencies, which is a sign of a “bullet profiled” water front. Boundary effects are significant especially for long (6 inches) cores. A hump in the middle of the curve is an indication of the water front reaching the no-flow boundary (see, for example, the curve Exp. 6 in Fig. 4-1). The imbibition continues laterally afterwards with a lower rate. The rate of imbibition was highly affected by the increasing diameter (or diameter/length ratio) of the core.

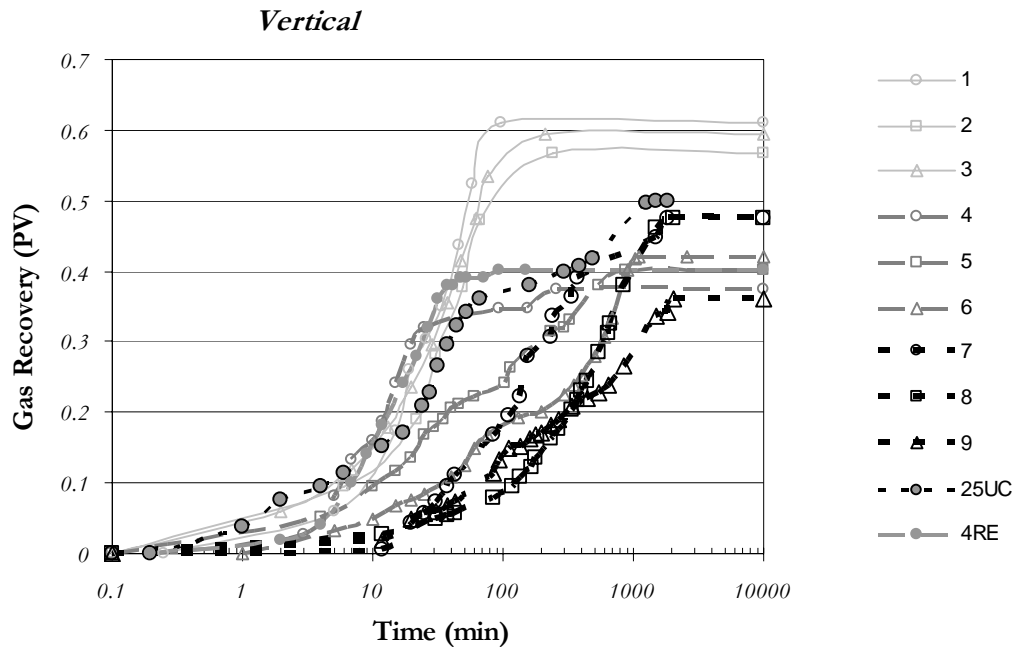


Figure 4.1 Air-water imbibition recovery curves for Berea sandstone at 20° C for different diameters and lengths, vertical orientation.

One uncoated case of vertically situated sample (Exp. 25) was included in this analysis for comparison. Exps. 25 and 4 are the same size cores with different boundary conditions. Although the recovery rates did not show a significant difference (it is even faster for the counter-current imbibition at early times), 16% higher recovery was obtained from the uncoated sample. Note that all small diameter samples yielded a faster recovery than the uncoated sample. A remarkable difference in the ultimate recoveries was also obtained between the smallest diameter samples (thin lines in Fig. 4-1) and Exp. 25. Due to the size of the sample (the longest and the largest diameter) and the difference in the densities of the phases, it is expected that the gravity effect is not negligible even if the all sides of matrix is open to flow in case of Exp. 25. The hump in the middle of the curve can be attributed to the transition from the capillary imbibition (likely to be in counter-current manner due to strong water wettability) to the gravity dominated flow (due to significant difference in the density).

Horizontal samples. Horizontally positioned cores resulted in slightly higher ultimate recovery values than those of vertical ones (Fig. 4-2). The smallest diameter samples showed a similar

behavior to the cases of vertically situated samples except the shortest one (Exp. 10). A hump caused by the front reaching the no-flow end of the core is more prominent in the horizontal cases (Exps. 16 and 17).

One uncoated case (Exp. 26) was also included in this analysis for comparison. Exps. 26 and 18 are the same size cores with different boundary conditions. Obviously, the uncoated core yielded much faster recovery than not only the same size of cores but also all the other samples. The difference in the ultimate recovery is 17% OOIP between Exp. 26 and Exp. 18. Note that the two smallest diameter samples (Exps. 11 and 12) yielded slower recovery rate but higher ultimate recovery than the uncoated samples despite the counter-current interaction type, as similar to the vertical cases shown in Fig. 4-1.

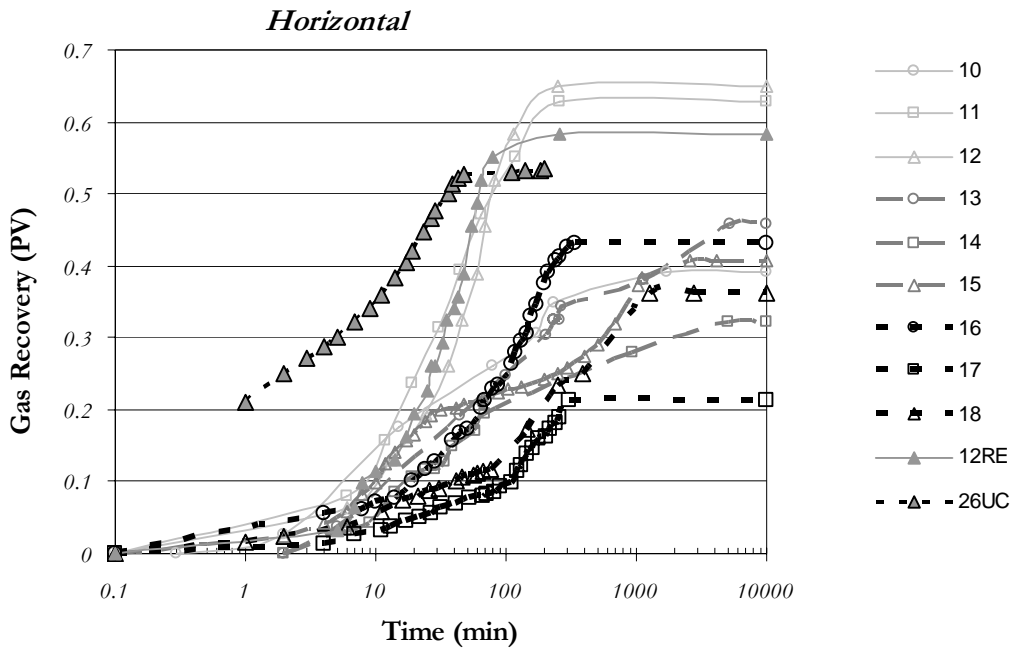


Figure 4.2 Air-water imbibition recovery curves for Berea sandstone at 20° C for different diameters and lengths, horizontal orientation.

4.1.1.2 Indiana limestone experiments

Six (three vertical, three horizontal) experiments using Indiana limestone samples were carried out at 20°C. The recovery curves are shown in Fig. 4-3. Unlike the Berea sandstone experiments of the same diameter samples (Exps. #7, 8, 9, 16, 17, and 18), the Indiana limestone samples yielded a faster recovery for horizontally situated samples. The recovery

trend, however, is similar for both rock samples, i.e., as the core length increased, the recovery rate decreased. An increasing trend in the residual gas saturation with increasing length was observed. This will be discussed later in detail.

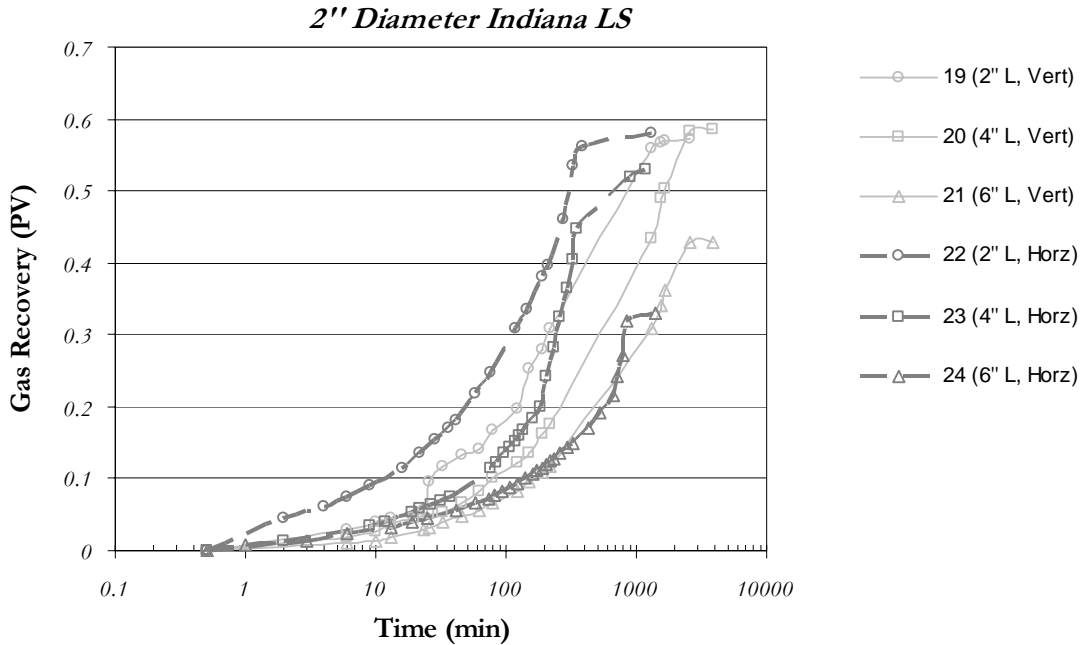


Figure 4.3 Air--water imbibition recovery curves for Indiana limestone at 20° C for three different lengths (vertical and horizontal).

For comparison, a base case uncoated Indiana limestone experiment was included in Fig. 4-4. The differences in the ultimate recovery and recovery rate are significant.

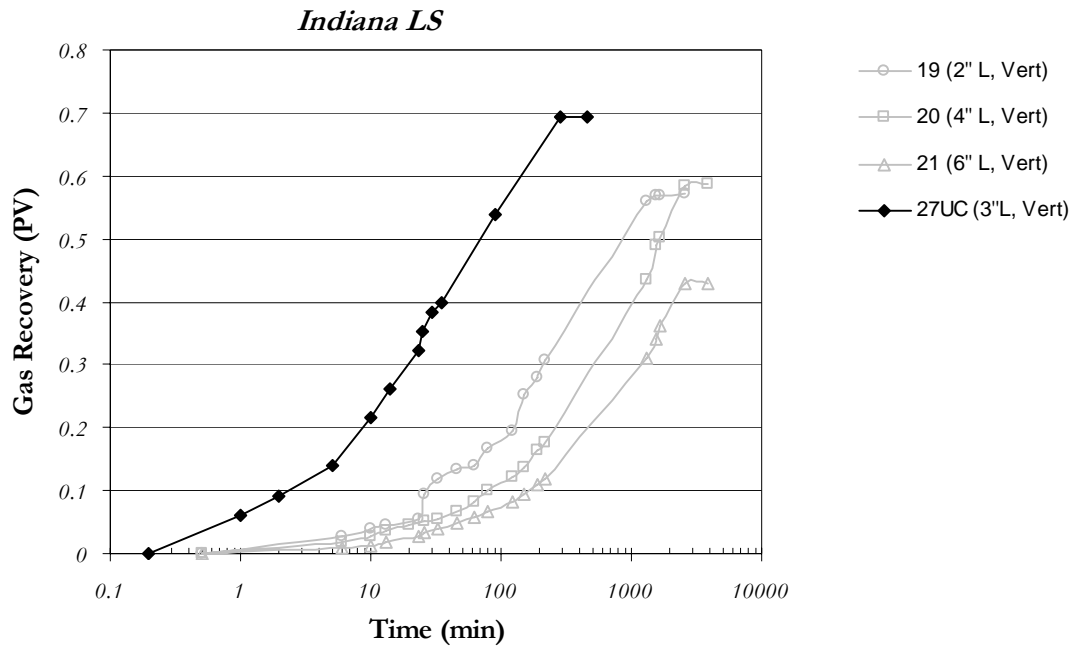


Figure 4.4 Air-water imbibition recovery curves for Indiana limestone at 20° C for vertical and uncoated samples.

Berea sandstone and Indiana limestone cases were compared in Figs. 4-5 and 4-6. Surprisingly, a very similar trend was followed for all different diameter samples of the vertical case (Fig. 4-5). The residual gas saturations for all cases are notably smaller for Berea sandstone experiments.

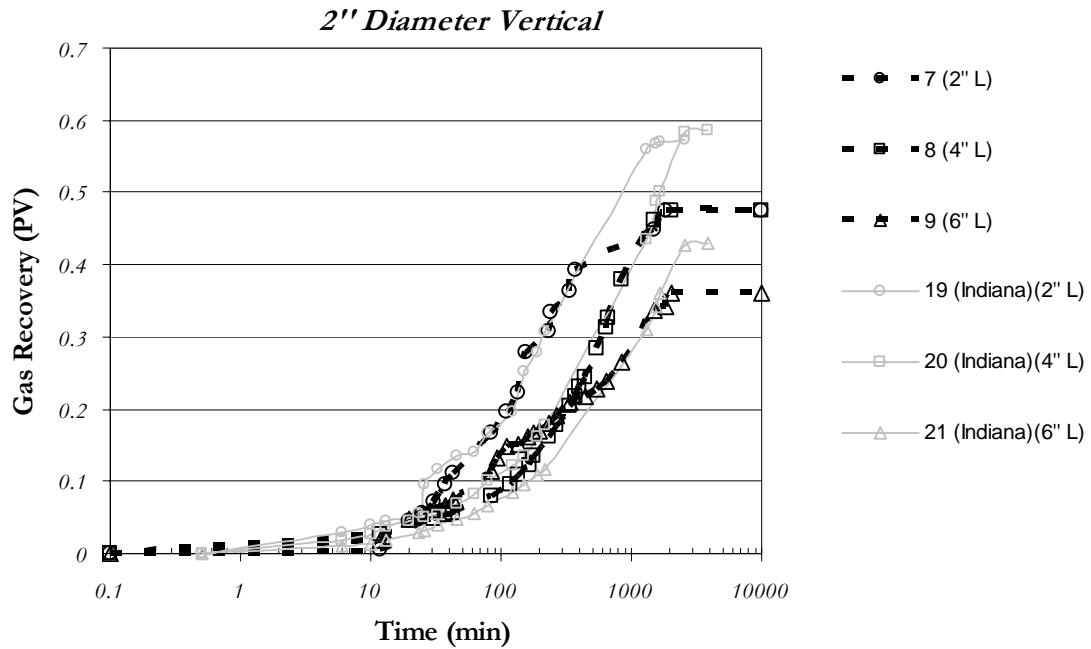


Figure 4.5 Air-water imbibition tests; comparison of different types of rocks on vertical orientation (T= 20° C).

The same observation is valid for the horizontal case as well (Fig. 4-6). This can be attributed to the pore structure of two different rock types, as the wettability characteristics of two rocks are similar as indicated by the initial stage of the experiments. The size of the residual gas bubble as non-wetting phase is larger due to the bigger pores in Berea sandstone and this hinders further displacement of gas when the water imbibed flow back due to gravity after reaching the end of the sample which is close to flow.

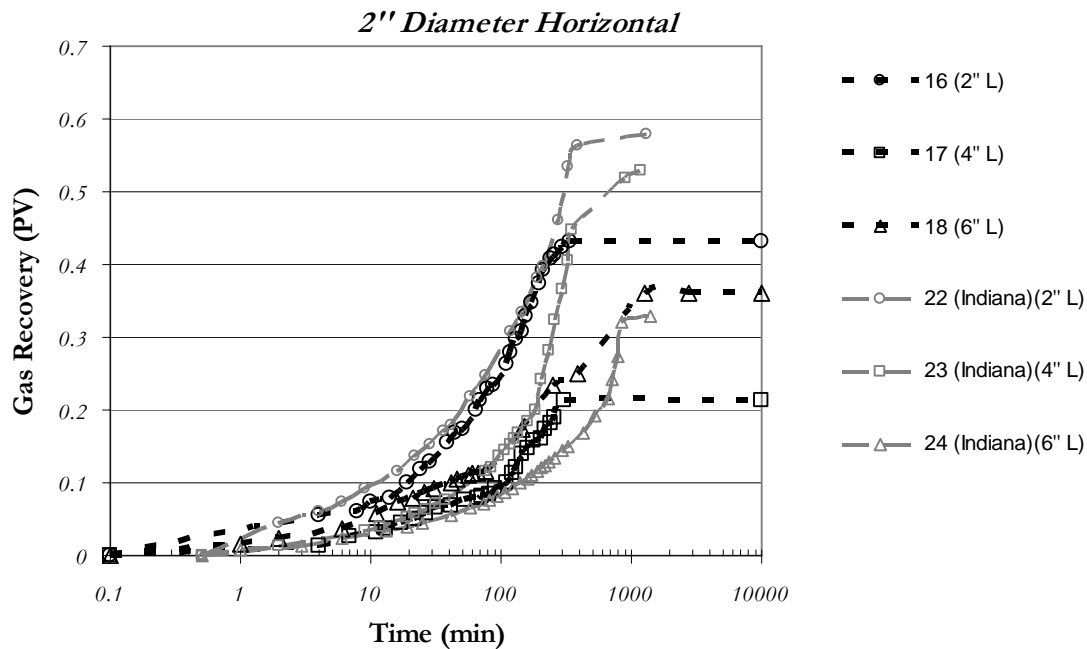


Figure 4.6 Air-water imbibition tests; comparison of different types of rocks on horizontal orientation ($T=20^{\circ}\text{C}$).

4.1.2 High temperature experiments (90°C)

Air-water imbibition recovery curves for Berea sandstone and Indiana limestone experiments at higher temperatures (90°C) are shown in Figs. 4-7 to 4-12. They include all different combinations of diameter, length, and orientation given in Table 4-1.

4.1.2.1 Berea Sandstone

Both vertical and horizontal cases showed different behavior at elevated temperatures compared to the experiments conducted at 20°C . The improvement in the recovery rate was obtained for all the samples at elevated temperature and this can be attributed to the lowered viscosity of water and IFT (Table 4-1).

Vertical samples. A faster recovery is more notable for shorter samples (Fig. 4-7). Humps on the curves were observed for higher length/diameter samples, i.e., Exps. H-3 and H-6. Note that these humps were observed for all 1 and 2" diameter cases of low temperature vertical experiments as well (Fig. 4-3). An interesting point is the low recovery with the smallest

sample (Exp. H-1) for the vertical case. When compared to the low temperature case (Exp. 1 in Fig 4-7), remarkable difference in the ultimate recovery was observed (13% pore volume).

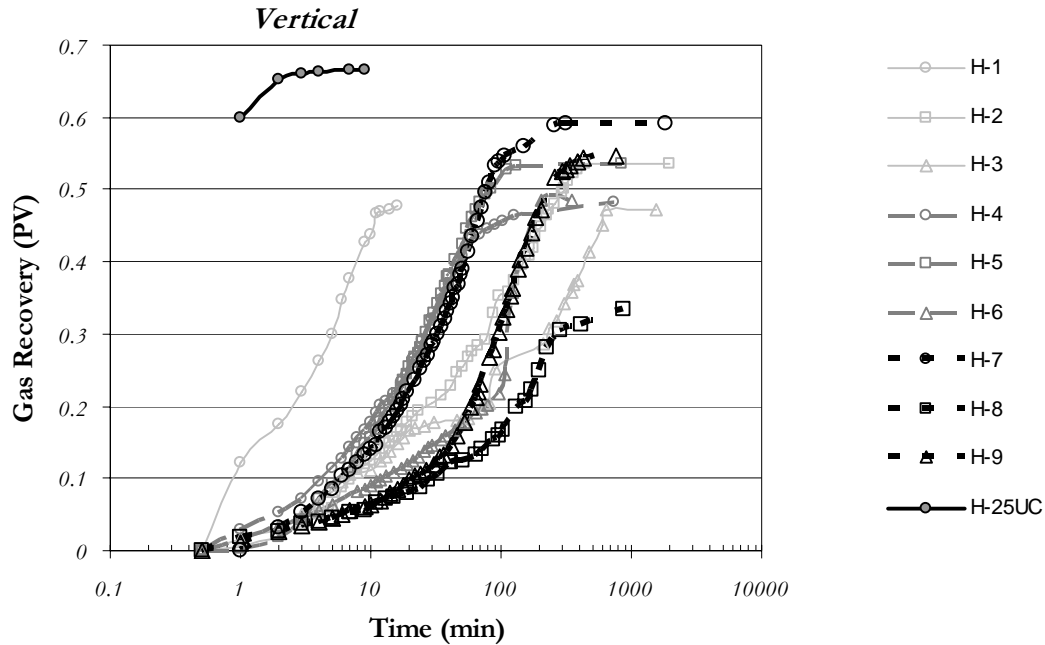


Figure 4.7 Air-water imbibition tests on Berea Sandstone at 90° C for three different diameters and lengths, vertical orientation.

Horizontal samples. The horizontal experiments showed a typical trend: The smaller the length, the faster the recovery for any given diameter (Fig. 4-8). A significant improvement in ultimate recovery was obtained with increasing temperature especially for 2” diameter samples. The uncoated sample (Exp. H-26) recovered the same amount of oil as the coated sample (Exp. H-1) of the same dimensions even though the latter yielded much slower recovery.

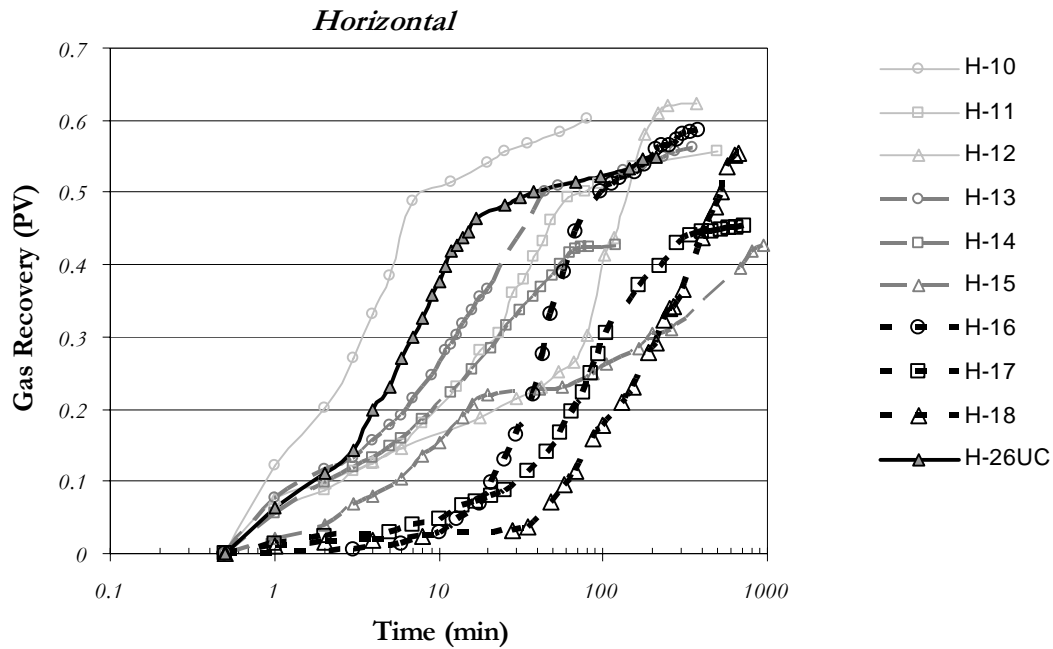


Figure 4.8 Air-water imbibition tests on Berea Sandstone at 90° C for three different diameters and lengths, horizontal orientation.

4.1.2.2 Indiana limestone experiments

Six (three vertical, three horizontal) experiments using Indiana limestone samples were carried out at 90°C. The recovery curves are shown in Fig. 4-9. The recovery trends for all cases are similar to those of cold water experiments given in Fig. 4-3. Horizontal experiments showed a faster recovery rate.

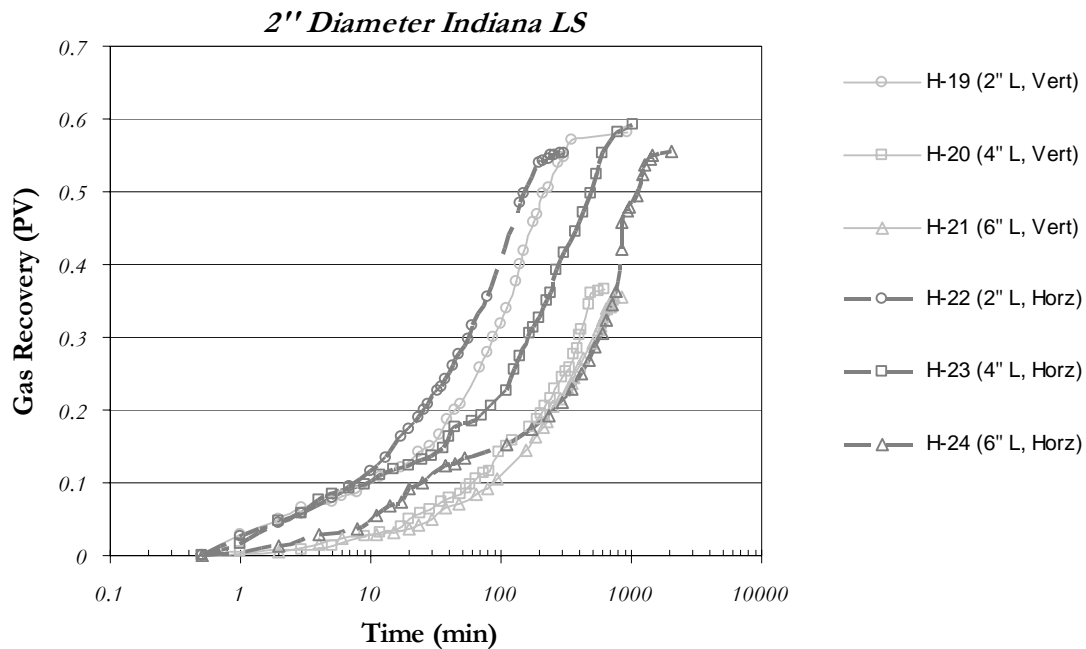


Figure 4.9 Air-water imbibition tests on Indiana limestone at 90° C for three different lengths (vertical and horizontal)

When the Berea sandstone and Indiana limestone cases for the same diameter are compared, it was observed that faster recoveries were obtained with Indiana limestone at higher temperatures (Fig. 4-10). This is opposite to the behaviour seen in the cold water experiments (Fig. 4-4). However, the difference in the residual gas saturations between both cases is lowered being close to each other. This indicates that the reduced IFT and viscosity caused less gas trapped in Berea sandstone. To clarify the effects of temperature on the residual gas saturation, high and low temperature experiments were compared for both rock types as explained in the following section.

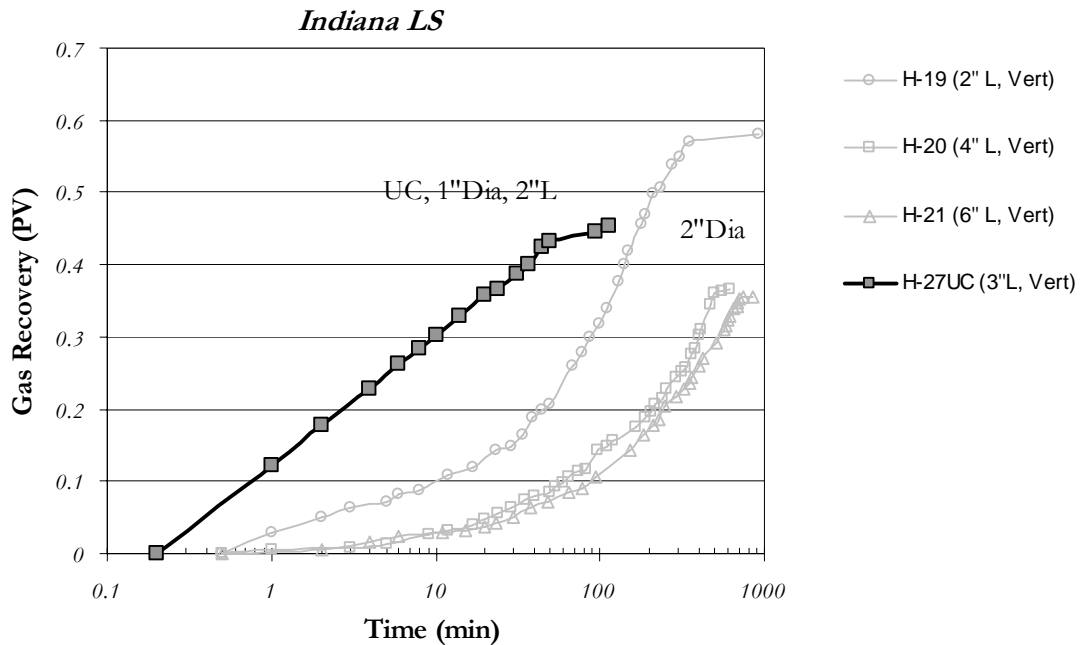


Figure 4.10 Air-water imbibition tests on Indiana limestone at 90° C for vertical and uncoated samples.

4.1.3 Residual gas saturation

It is also intended to understand the development of residual gas saturation depending on the matrix shape factor and temperature in this study. The residual gas saturations for the different temperatures and rock types are shown in **Fig. 4-10**. For 1” and 2” diameter cases of Berea sandstone, hot water imbibition yielded a higher gas recovery. For the smallest diameter cases (0.5”) no contribution to recovery due to high temperature was observed. This is also true for the larger diameter (2”) Indiana limestone experiments. For the uncoated cases, high temperature contributed to the ultimate recovery. The effect of the diameter of the core on the residual gas is more significant in the horizontal case.

The increased temperature not necessarily yielded a higher ultimate recovery. Although all the cases of horizontal samples showed an improvement in the ultimate recovery, only 1-inch diameter samples resulted in an increase in the ultimate recovery for vertical cases.

Different attempts were made to correlate the residual gas saturation to different rock and fluid characteristics such as the matrix shape factor, length to diameter ratio etc. A

dimensionless group was derived as shown below to correlate the residual gas saturation to it.

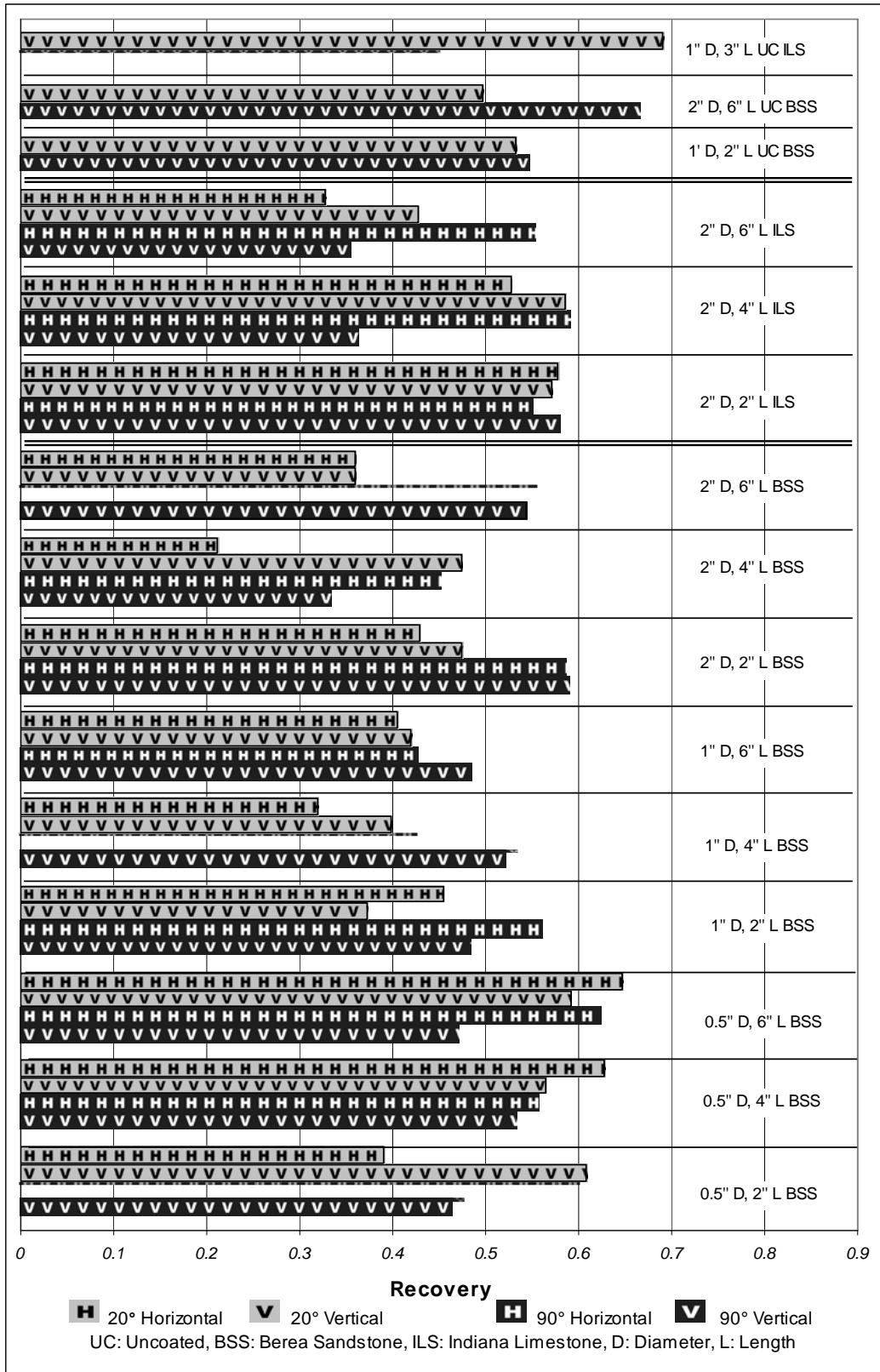


Figure 4.11 Comparison of ultimate recoveries for different rocks, dimensions, temperatures (20°C and 90°C) and orientations.

Mattax and Kyte [1962] demonstrated that the imbibition recovery of oil could be scaled by plotting normalized recovery against the following dimensionless time:

$$t_D = \left(\sqrt{\frac{k}{\phi}} \frac{\sigma}{\mu_w} \frac{1}{L_c^2} \right) t \quad \dots\dots\dots 1$$

The modified form of this equation was proposed later as follows [Zhang et al., 1996]:

$$t_D = 0.02 \left(\sqrt{\frac{k}{\phi}} \frac{\sigma}{\mu_{gm}} \frac{1}{L_c^2} \right) t \quad \dots\dots\dots 2$$

where t_D is dimensionless time, k permeability in md, ϕ fractional porosity, σ interfacial tension in dynes/cm, L_c characteristic length in cm, and t time in minutes. The term μ_{gm} represents geometric mean viscosity in cp, which, for an oil/water system, is given by:

$$\mu_{gm} = \sqrt{\mu_o \mu_w} \quad \dots\dots\dots 3$$

L_c , the characteristic length is defined as follows:

$$L_c = \sqrt{\frac{V}{\sum_{i=1}^n \frac{A_i}{X_{Ai}}}} \quad \dots\dots\dots 4$$

where V is the bulk volume of the matrix, A_i is the area open to imbibition at the i^{th} direction, and X_{Ai} is the distance traveled by the imbibition front from the open surface to the no-flow boundary.

We propose the following dimensionless group to be correlated to the residual gas phase saturation:

$$t_D = 0.02 \left(\sqrt{\frac{k}{\phi}} \frac{\sigma}{\mu_{gm}} \frac{1}{L_c^2} \right) t_{final} \quad \dots\dots\dots 5$$

For the time value in Eq. 2, the time that the imbibition reaches plateau region, i.e., the point where the ultimate recovery is reached, was used in Eq. 5 (t_{final}). Note that (t_{final}) may not be the exact point of the ultimate end of the process. It is fixed as the point where a drastic slow down is started. For consistency, the same practice was applied in selecting this point in all experiments. This dimensionless group, in a sense, represents the efficiency of the process as it considers the time needed to reach the ultimate recovery.

Fig. 4-12 displays the change of residual gas saturation with the dimensionless group defined in Eq. 5 and the length to diameter ratio for the low temperature experiments. Each diameter group was considered separately as shown in Fig. 4-12. For the vertical cases, the small (0.5”) and medium (1”) diameters followed the same trend showing the highest residual gas saturation for the medium value of the dimensionless parameter (Figs. 4-12-a and c).

When the whole data was considered, trends were captured for two cases (Fig. 4-12-b and d) as indicated by a dashed line. For example, a decreasing residual gas saturation with the t_D (Fig. 4-12-b) and a peak residual gas saturation value at $L/D=5$ were obtained for the horizontal cases (Fig. 4-12-d). These trends were represented by thick dashed lines in both plots.

No typical trend was observed for the hot water cases (**Fig. 4-13**) except the residual gas saturation change against t_D for the vertical case (Fig. 4-13-a). There exist two different trends as indicated by the thick-dashed lines. Each diameter case followed a trend showing a change with the dimensionless groups (Figs. 4-13-b, c, and d).

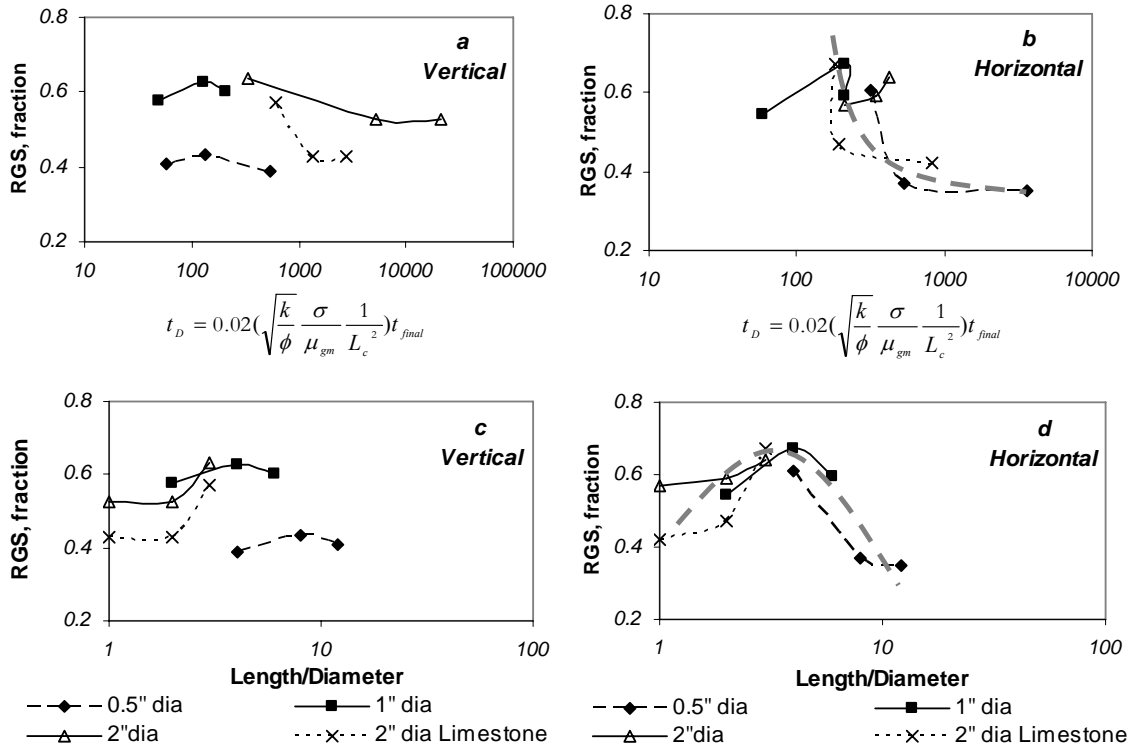


Figure 4.12 Residual gas saturation (RGS) trends at 20° C against (a) and (b) the dimensionless group in Eq.5, and (c) and (d) length to diameter ratio.

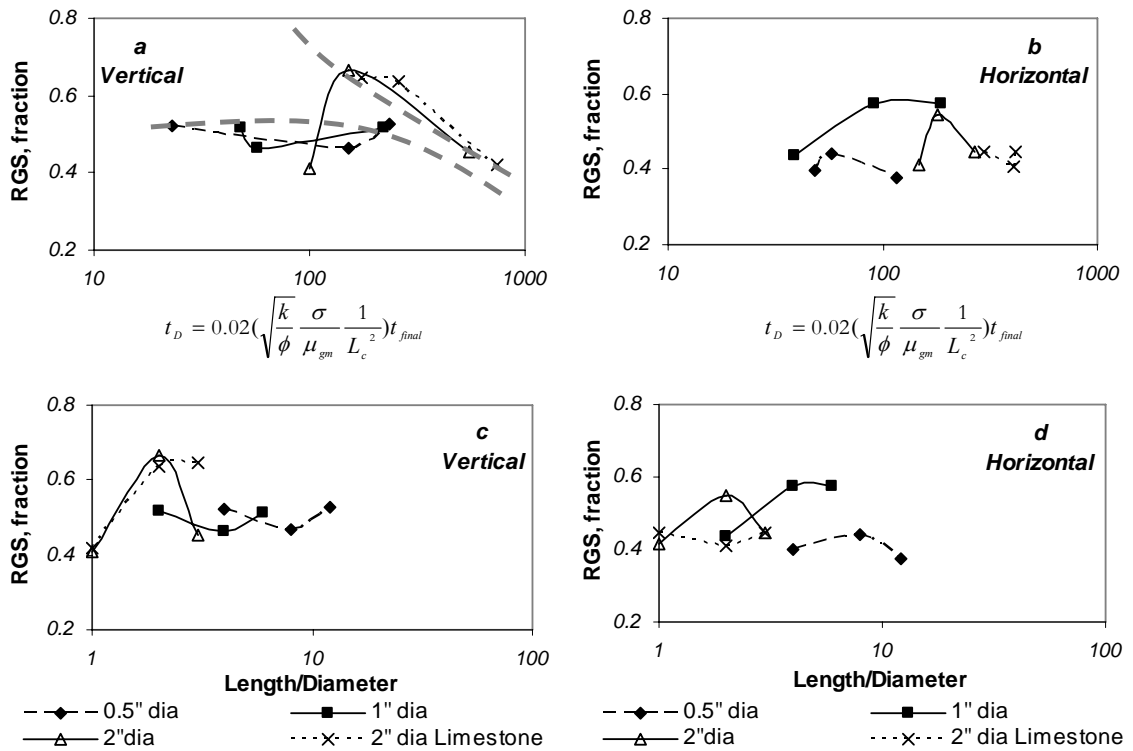


Figure 4.13 Residual gas saturation trends at 90° C against (a) and (b) the dimensionless time group in Eq.5, and (c) and (d) length to diameter ratio.

4.1.4 Scaling of experiments

The normalized recovery (recoverable gas) was plotted against several different dimensionless time groups. Fig. 4-14 shows normalized recovery vs. time for the whole data.

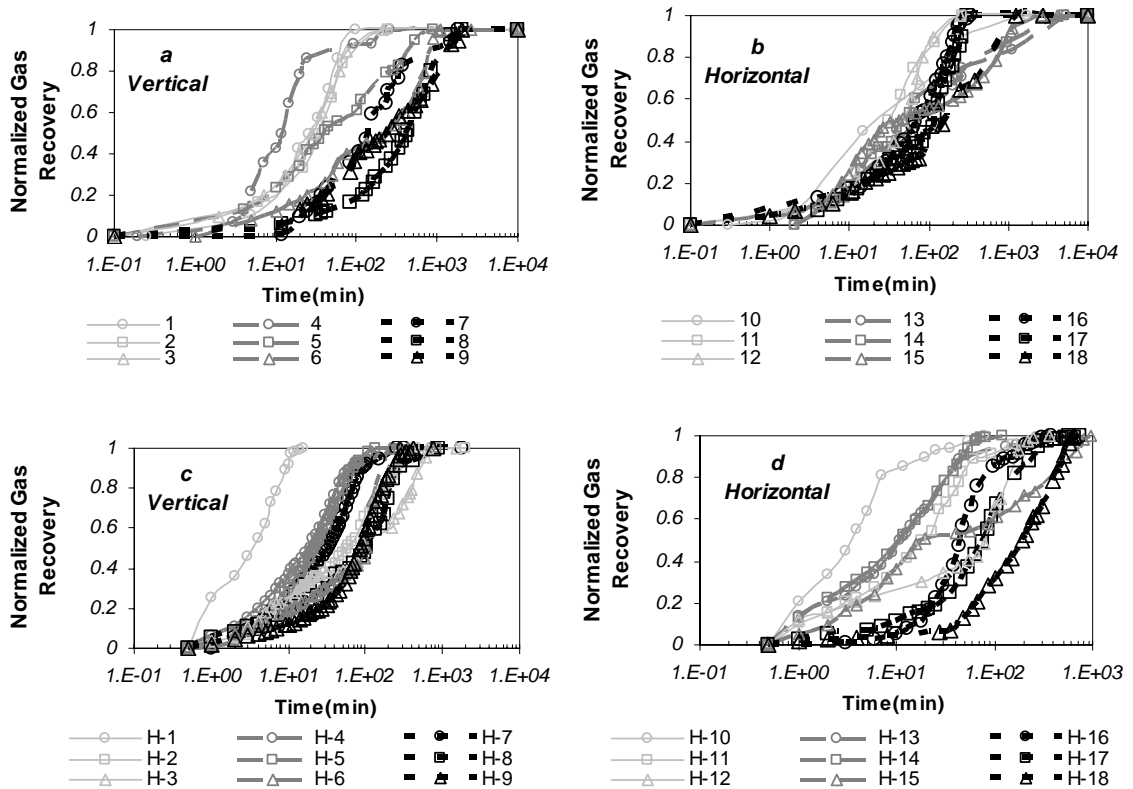


Figure 4.14 Normalized gas recovery curves of Berea sandstone for three different diameters and lengths, (a) vertical at 20°C, (b) horizontal at 20°C, (c) vertical at 90°C, and (d) horizontal at 90°C.

Different scaling equations were tested for this group of recovery curves. Eq. 5 showed a grouping for high temperature cases implying a possible scaling might exist (Figs. 4-15-c and d). No grouping was observed for low temperature cases (Figs. 4-15-a and b). Recently, Hatiboglu and Babadagli [2004] observed that the vertical case showed a possible scaling for oil-water systems of the same shape factors but not for the horizontal ones when Eq. 5 is applied at low temperature (20 °C).

The following three other scaling groups were tested as well:

$$t_D = c^2 \frac{k_w P_c (S_{wf} - S_{wi})}{\phi \mu_w L_c^2} t \quad [\text{Li and Horne, 2002}] \dots\dots\dots 6$$

$$t_D = 0.02 \left(\sqrt{\frac{k}{\phi}} \frac{\sigma}{\mu_{gm}} \frac{1}{L_c} \right) t \quad [\text{Pow et al., 1999}] \dots\dots\dots 7$$

where L_c , the characteristic length is defined as follows

$$L_c = \frac{abc}{2\sqrt{a^2b^2 + a^2c^2 + b^2c^2}} \dots\dots\dots 8$$

a, b , and, c are the dimensions of matrix.

$$t_D = \frac{k(P_c f(\theta) + \frac{\Delta \rho g L_c^2}{L_H})}{\phi \sqrt{\mu_w \mu_o} L_c^2} t \quad [\text{Xie and Morrow, 2000}] \dots\dots\dots 9$$

where P_c is a representative imbibition capillary pressure and $f(\theta)$ is a wettability factor. They were calculated following the procedure defined by Babadagli [1996] based on the following relationship proposed by Handy [1960].

$$Q^2 = \left(\frac{2P_{c,eff} k_w \phi A^2 S_w}{\mu_w} \right) t \dots\dots\dots 10$$

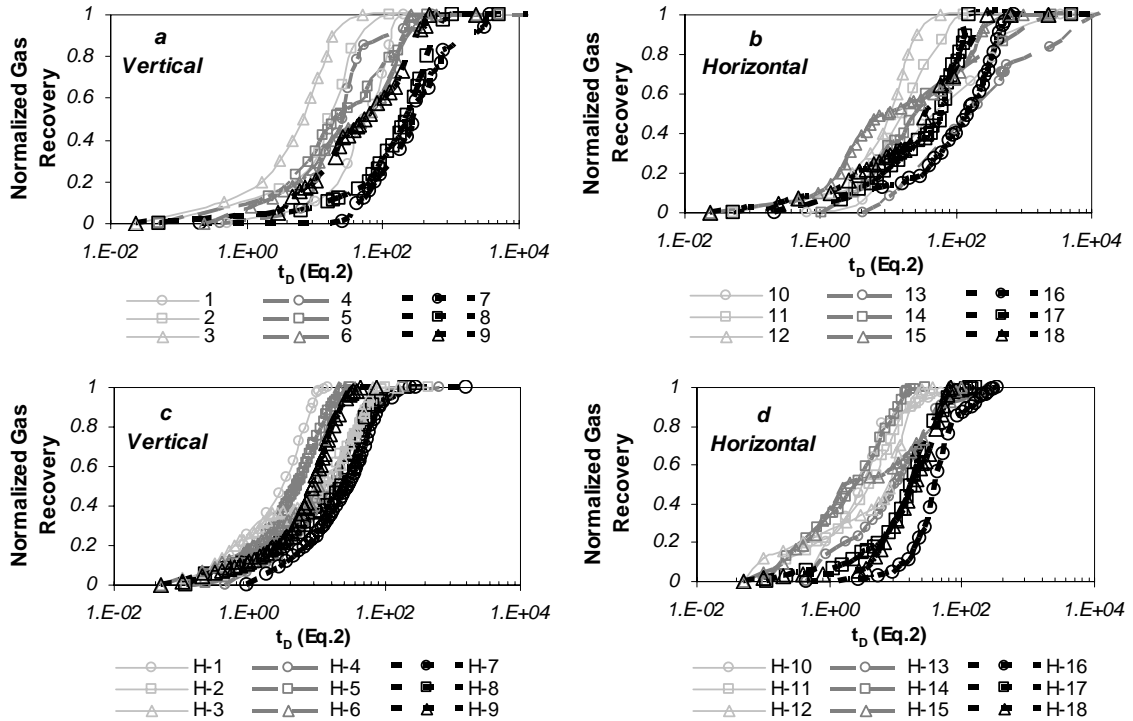


Figure 4.15 Dimensionless time (Eq.2) against normalized recovery for (a) vertical at 20°C, (b) horizontal at 20°C, (c) vertical at 90°C, and (d) horizontal at 90°C.

The t vs Q^2 plots for two rock types (uncoated) at two different temperatures are given in **Fig. 4-16**. The first portions of the plots that give a straight line were used to obtain the slope. The slopes represent the wettability of the rock corresponding to the $P_{c,eff}$ term in Eq. 10. The t_D plots for the three cases given in Eqs. 6, 7, and 9 are shown in **Figs. 4- 17, 4-18** and **4-19**, respectively.

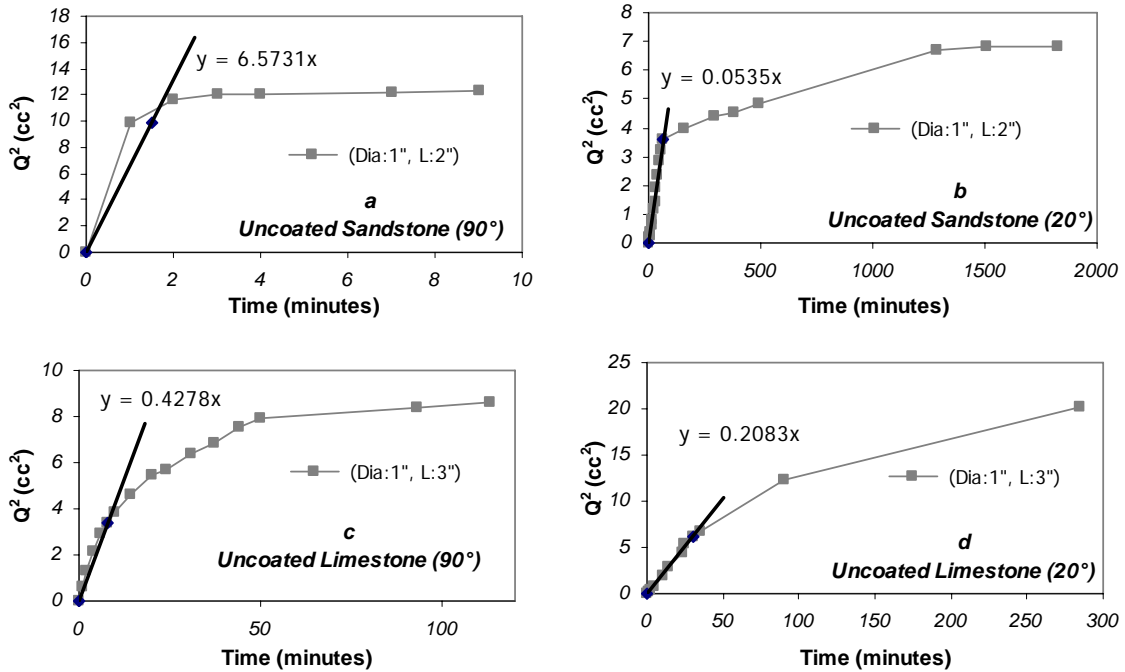


Figure 4.16 Estimation of $P_{c,eff}$ in Eq.10 for (a) Berea sandstone at 90°C, (b) Berea sandstone at 20°C, (c) Indiana limestone at 90°C, and (d) Indiana limestone at 20°C.

As opposed to the dimensionless group in given in Eq. 5, Eq. 6 showed a grouping of the curves for low temperature experiments indicating that a possible scaling exists (Figs. 4-17-a and b). No grouping was observed for high temperature cases (Figs. 4-17-c and d). Pow et al [1999] proposed a modification to the characteristic length, L_c , as given in Eq. 7. This was also tested as the matrix shape factor was the main concern in this study (Fig. 7-18). Improvement in the grouping of all curves compared to the cases shown in Fig. 4-17 was observed. This is more notable for the low temperature cases (Figs. 4-18-a and b). For the horizontal experiments of low temperature cases a good grouping was observed among the same diameters but different lengths. Intuitively, one can expect that the inclusion of the length factor would provide more improvement. Therefore, another dimensionless group proposed by Xie and Morrow [2000] also was tested. A better grouping can be seen in the low temperature horizontal cases (Fig. 4-19-b). This justifies that an improved definition of the characteristic length is needed. No improvement in the grouping of the curves was observed for the other cases (Figs. 4-19-a, c, and d) despite the change on the definition of the characteristic length by addition of the term L_{IH} . Note that the improvement by addition of the gravity term was not useful for vertical cases where the gravity is expected to play a role.

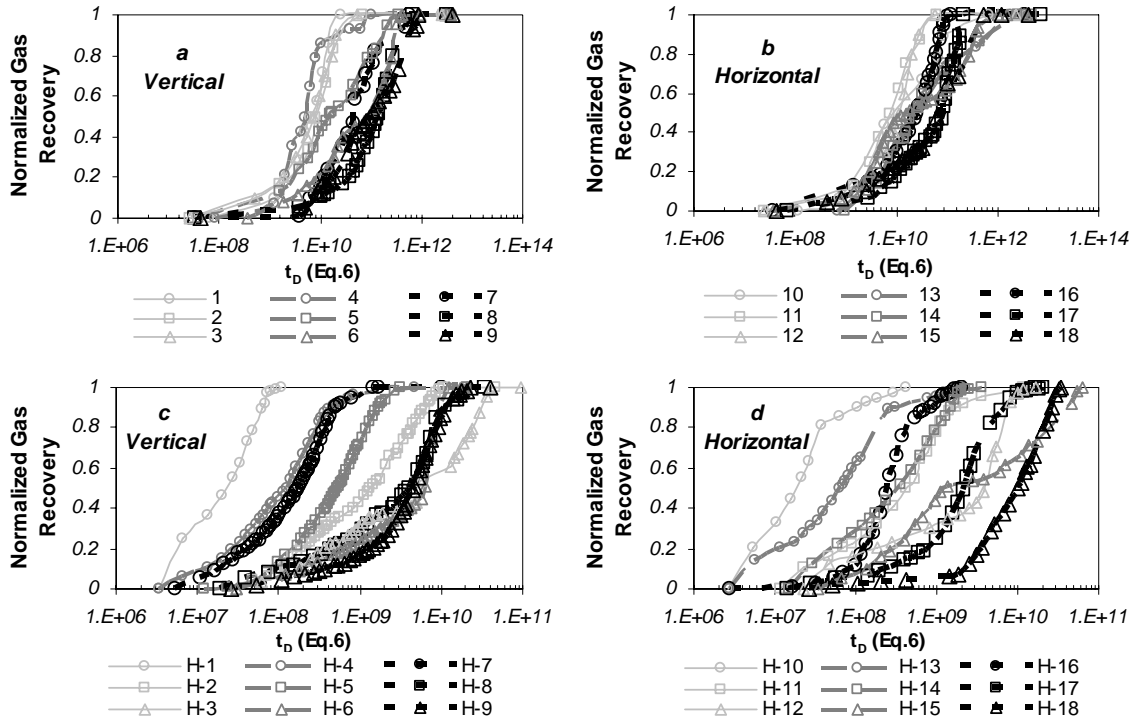


Figure 4.17 Dimensionless time (Eq.6) against normalized recovery for (a) vertical at 20°C, (b) horizontal at 20°C, (c) vertical at 90°C, and (d) horizontal at 90°C.

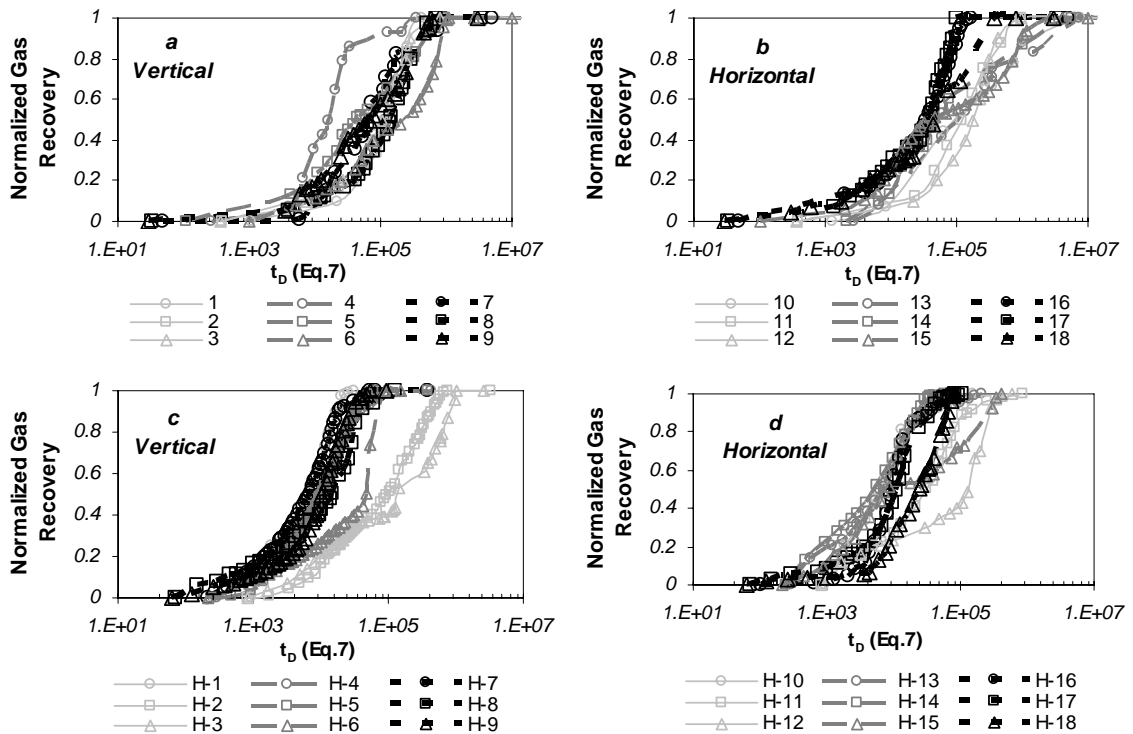


Figure 4.18 Dimensionless time (Eq.7) against normalized recovery for (a) vertical at 20°C, (b) horizontal at 20°C, (c) vertical at 90°C and (d) horizontal at 90°C.

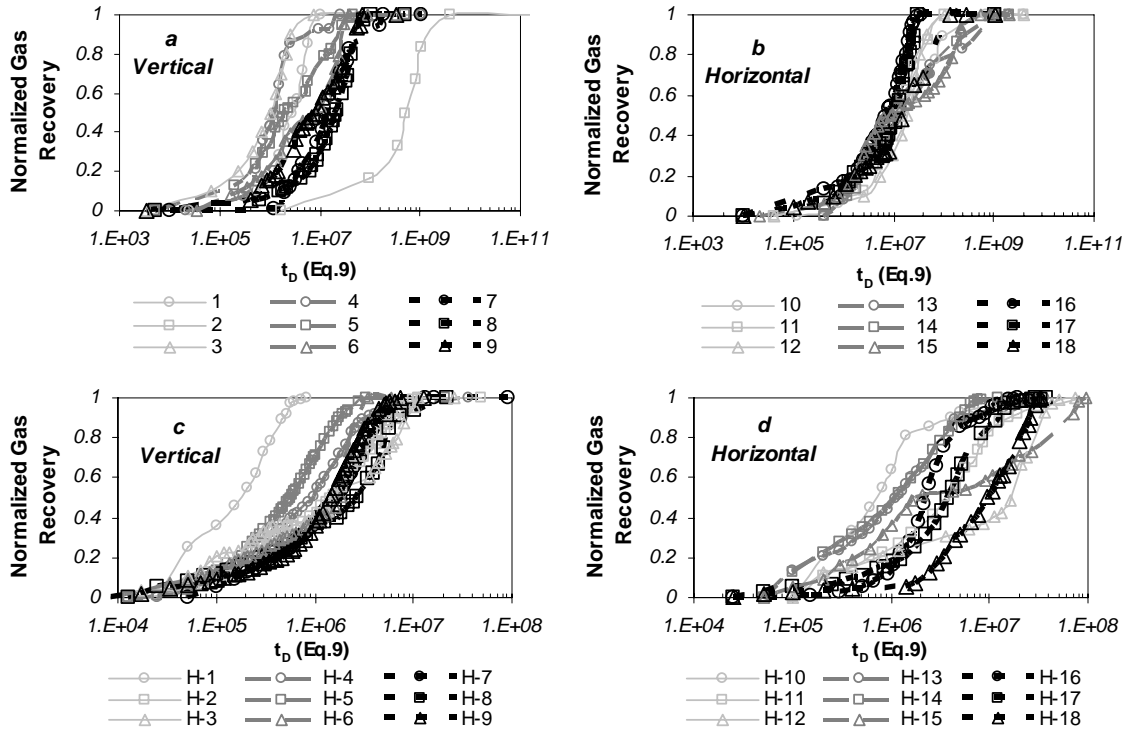


Figure 4.19 Dimensionless time (Eq.9) against normalized recovery for (a) vertical at 20°C, (b) horizontal at 20°C, (c) vertical at 90°C, and (d) horizontal at 90°C.

4.1.5 Observations

Air-water imbibition plots show high sensitivity to orientation as the gravity dominates when the cores are positioned vertically. Despite the favourable wettability and viscosity values, the air-water imbibition may take long time to fully imbibe depending on the shape of the core. Smaller cores with small diameter yield faster imbibition rates with higher ultimate recovery. A hump was observed for large and long cores, which is an indication of the bullet shaped water front. After reaching the no-flow boundary that was indicated by the hump, a slower displacement was observed. Horizontal and vertical orientations did not show much difference in the ultimate recovery.

For the low temperature experiments, residual gas saturations for air-water systems display an increasing trend with respect to the dimensionless group given in Eq. 5. A decreasing trend with respect to the elongation factor (Length/Diameter) of the cores, which is a sign of bullet shaped displacement profile, also was observed for the small diameter cores.

Typically, Length/Diameter = 4 was found to be a threshold value at which the most efficient recovery was obtained.

It is clear that the development of the residual gas phase saturation before and after the displacement front reaches the end of the core should be evaluated in details. After the displacement front reaches the end, the water imbibed would be forced to flow down by gravity displacing some more gas. This depends on the strength of the capillary forces that also cause the development of the residual gas phase. The major critical parameters are wettability and pore size. To understand the dynamics of the imbibition process for the given matrix boundary conditions causing only counter-current imbibition, separation of the recovery curves into three main zones were suggested by Babadagli et al. [2005]. For air-water cases, they observed that in the late stages of the experiments, the effect of the matrix length and diameter are significant compared to the oil-water imbibition. Zonal separation would help improve the scaling especially for low temperature horizontal cases seen in Figs. 4-18-b and 4-19-b.

Although the horizontal cases did not show any significant change in terms of the recovery - rate- trend (but showed an increase in the ultimate recovery), the vertical cases yielded different recovery rates and ultimate recoveries at elevated temperature (90°C). Reduced gas saturation was obtained only for certain core sizes (typically high diameters) with increasing temperature. That was attributed to the reduction in surface tension and water viscosities.

There are some other factors that might affect the imbibition recovery but were not investigated in this study. One of them is the initial water. Significant effects of initial water on the recovery rate and ultimate recovery was observed on the samples open to flow from all sides by Li and Horne [2002].

No phase change is expected at the given temperature range. The changes in the liquid phase existing in the rock can be an additional driving force to enhance the displacement of the gas phase [Birholzer, 2003; Udell, 1985] at higher temperatures. The change in the property of the liquid imbibition into the rock is expected to be minimal as well as the expansion of gas phase in the rock (the rock was pre-heated to the temperature) at the given temperature range. The capillary interaction was mainly controlled by the core dimensions

(or the shape factor) and the change in the surface tension and viscosity of the phases at higher temperature.

Further investigation should also focus on this area as well as the effect of temperature gradient on the capillary imbibition [Medina et al., 2003] as the higher temperatures are expected in geothermal reservoir matrix.

4.2 Liquid-liquid interaction

To study immiscible liquid-liquid interaction, oil-brine pair is chosen as the main oleic and wetting phases. The experiments are listed in Table 4.2



















Three groups of experiments were conducted. In the first group, oil saturated core samples were exposed to brine by immersing the samples into brine filled imbibition tubes. This process is called spontaneous imbibition in this thesis. The classical definition of spontaneous imbibition refers to totally capillary forces controlled process with no gravity and no viscous force contribution. Note that, in our case, a hydrostatic head over the open face of the rock would create additional pressure but this amount is highly negligible compared to capillary forces and same in all experiments. Hence, this type of process is expected not to introduce any more noise and complexity in order to achieve spontaneous imbibition. Also note that the height of the aqueous phase column was kept at the same point for all experiments. The immiscible process was represented by “oil recovery” against time plots. The second group would reflect the effect of IFT since surfactants are used to decrease the IFT between phases. Third group was designed to investigate the differences in wettability and rock type.

Overall inspected parameters can be listed as:

- (1) Interaction type: Volumetric displacement in co- and counter current manner,
- (2) Oil type: Kerosene and mineral oil,
- (3) Orientation: Horizontal and vertical (effect of gravity),

- (4) Rock type: Sandstone and limestone (different pore structures, wettabilities, and permeabilities),
- (5) Wettability of porous medium: Water wet to weakly water wet,
- (6) Matrix shape: Different aspect (length to diameter) ratios.

Table 7 Rock and fluid types used in the liquid-liquid experiments.

Length (in)	Diameter (in)	Core Shape and Orientation	Experiment Number					
			Mineral Oil – Brine (Berea Sand.)	Kerosene – Brine (Berea Sand.)	Mineral Oil – Surfactant (Berea Sand.)	M.Oil – Brine (Indiana Limestone)	M.Oil – Brine (1 week aged Berea Sand.)	M.Oil – Brine (1 month aged Berea Sand.)
2	0.5		1	19K	22-14			
4	0.5		2					
6	0.5		3					
2	1		4	20K	15-25	31-32U	36-37U	41-42U
4	1		5					
6	1		6			33	38	43
2	2		7		26-27	34	39	44
4	2		8					
6	2		9			35	40	45
2	0.5		10	21K				
4	0.5		11		28			
6	0.5		12					
2	1		13					
4	1		14		29			
6	1		15					
2	2		16					
4	2		17		30			
6	2		18					

4.2.1 Oil-brine experiments (effect of viscosity)

This section includes mineral oil–brine static imbibition tests. Fluid pair is not changed throughout this section (Exps 1 to 18). Length and diameter of the cores (shape factor) and orientation (gravity effect) are the changing variables.

4.2.1.1 Recovery rate

The recovery curves obtained from the oil-brine imbibition experiments are given in **Figs. 4-20** and **4-21**. They include all different combinations of diameter, length, and orientation given in Table 1. Gravitational forces become effective for the vertical cores causing different displacement characteristics compared to the horizontally situated samples. Generally, the longest samples resulted in the slowest recovery rate (Fig. 4-20, 4-21).

The recovery behavior of the horizontal cases is different. The boundary effects are less pronounced as many of the cases followed the same recovery trend except Exp. #14 (Fig. 4-21).

The time threshold values, i.e., the time at which the first recovery is observed, are close to 10 minutes for all cases regardless the core shape and orientation. Recoveries range between 45% and 55% of OOIP. For both horizontal and vertical cases, the 1” diameter cores, with 0.5 and 1” length, yielded the fastest recovery.

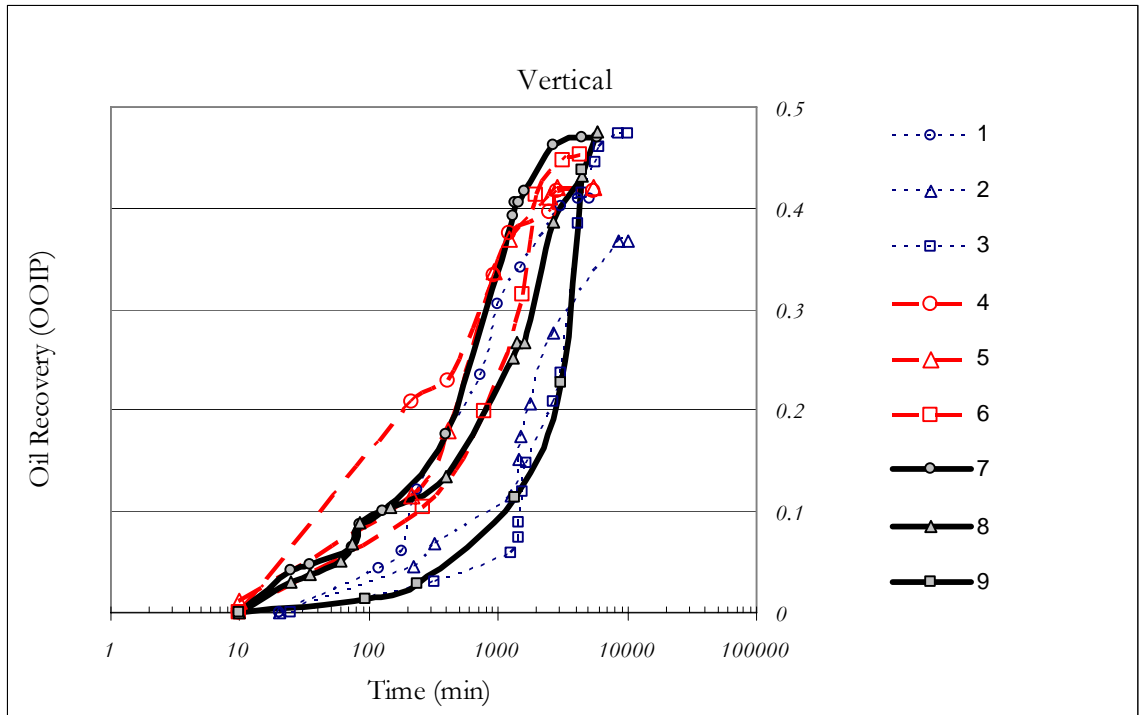


Figure 4.20 Oil-brine imbibition tests in vertical cores.

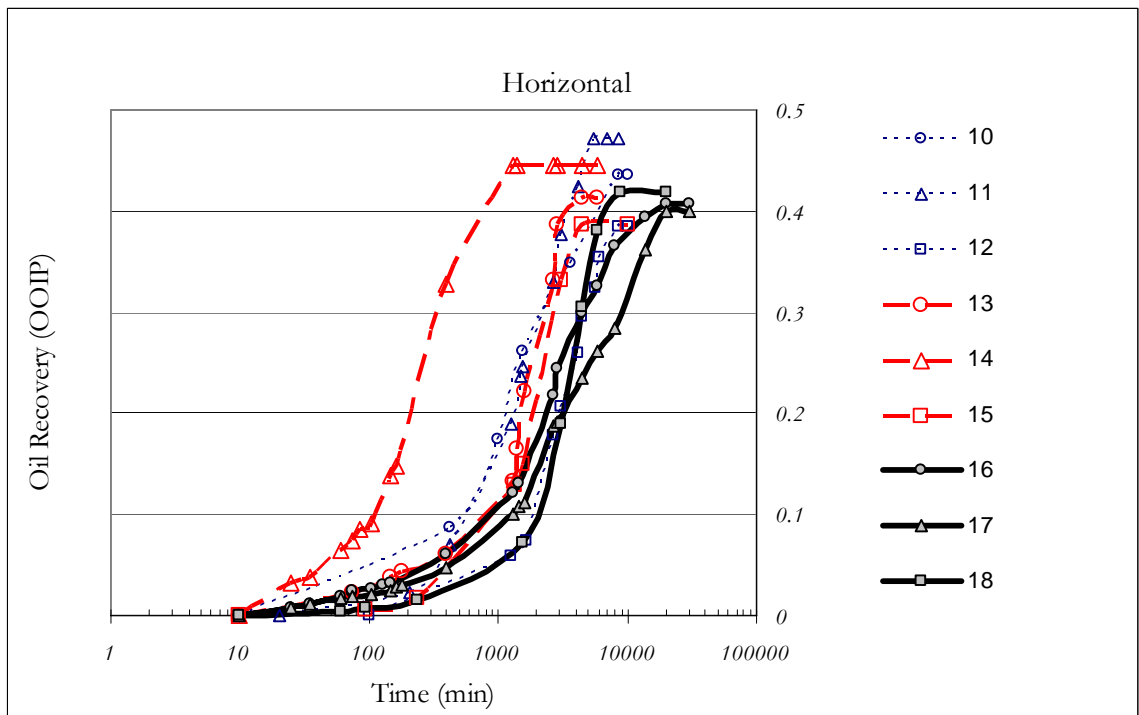


Figure 4.21 Oil-brine imbibition tests in horizontal cores.

4.2.1.2 Scaling analysis

Similar scaling groups tested in gas-liquid interaction section are also investigated in an effort to characterize liquid-liquid capillary imbibition. For readers' convenience these groups are rewritten. Mattax and KYTE [1962] demonstrated that the imbibition recovery of oil could be scaled by plotting normalized recovery against the dimensionless time, defined as:

$$t_D = 0.018849 \left(\sqrt{\frac{k}{\phi}} \frac{\sigma}{\mu_{gm}} \frac{1}{L_c^2} \right) t \dots\dots\dots 11$$

where t_D is dimensionless time, k permeability in md, ϕ fractional porosity, σ interfacial tension in dynes/cm, L_c characteristic length in cm, and t time in minutes. The term μ_{gm} represents geometric mean viscosity in cp, which, for an oil/water system, is given by:

$$\mu_{gm} = \sqrt{\mu_o \mu_w} \dots\dots\dots 12$$

L_c , the characteristic length is defined as follows [Ma et al., 1995]:

$$L_c = \sqrt{\frac{V}{\sum_{i=1}^n \frac{A_i}{X_{Ai}}}} \dots\dots\dots 13$$

where V is the bulk volume of the matrix, A_i is the area open to imbibition at the i^{th} direction, and X_{Ai} is the distance traveled by the imbibition front from the open surface to the no-flow boundary.

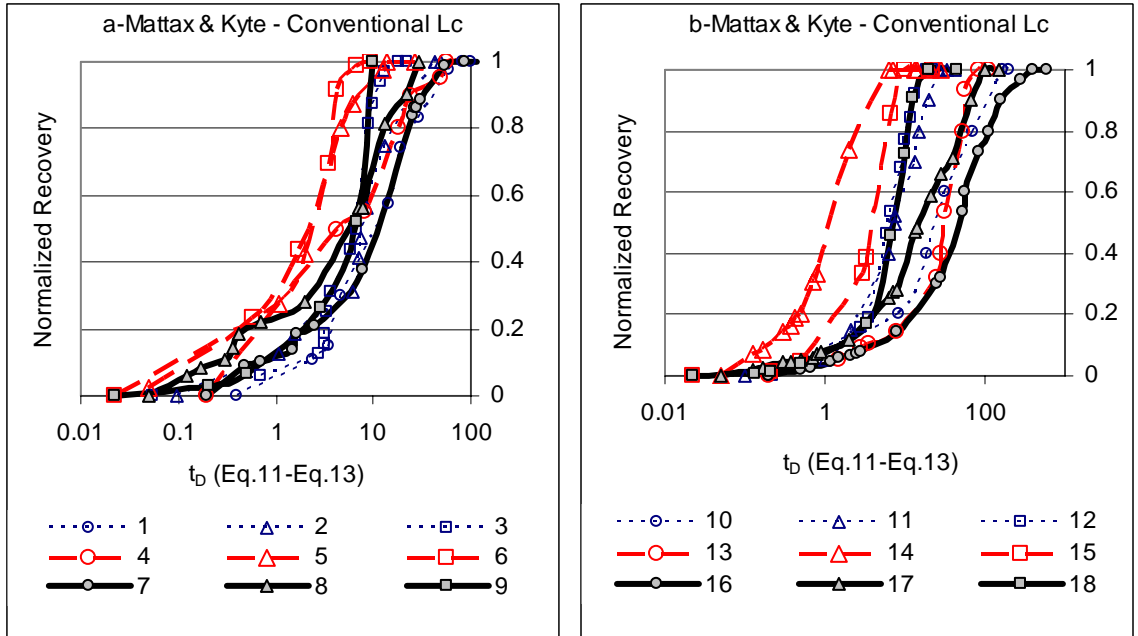


Figure 4.22 Scaling with the classical Mattax and Kyte equation for (a) vertical and (b) horizontal cases.

Classical scaling analysis was done using Eq. 11. The plots are given in **Figs. 4-22a** and **4-22b**. If the scaling law is valid for this set of curves, all the curves are expected to represent the same recovery behavior against the dimensionless time. Although two groupings were observed for the vertical case indicating the validity of the scaling group (Fig. 4-22a), no scaling for horizontal case (Fig. 4-22b) can be pronounced thus showing the effect of gravity. In fact without any dimensionless time application recovery curves show a better match.

To obtain a good match, different scaling equations were tested using the existing and newly developed characteristic length. The following equations were previously proposed to scale capillary imbibition for varying fluid pairs and different conditions.

$$t_D = \epsilon^2 \frac{k_w P_c (S_{wf} - S_{wi})}{\phi \mu_w L_c^2} t \quad [\text{Li and Horne, 2002}] \dots\dots\dots 14$$

where ϵ is the ratio of the gravity force to capillary force.

$$t_D = 0.02 \left(\sqrt{\frac{k}{\phi} \frac{\sigma}{\mu_{gm}} \frac{1}{L_c^2}} \right) t \quad [\text{Pow et al., 1999}] \dots\dots\dots 15$$

where L_c , the characteristic length is defined as follows

$$L_c = \frac{abc}{2\sqrt{a^2b^2 + a^2c^2 + b^2c^2}} \dots\dots\dots 16$$

a, b , and, c are the dimensions of matrix.

$$t_D = \frac{k(P_c f(\theta) + \frac{\Delta\rho g L_c^2}{L_H})}{\phi \sqrt{\mu_w \mu_o} L_c^2} t \quad [\text{Xie and Morrow, 2000}] \dots\dots\dots 17$$

where P_c is a representative imbibition capillary pressure and $f(\theta)$ is a wettability factor. They were calculated following the procedure defined by Babadagli [1996] based on the following relationship proposed by Handy [1960].

$$Q^2 = \left(\frac{2P_{c,eff} k_w \phi A^2 S_w}{\mu_w} \right) t \dots\dots\dots 18$$

The t vs Q^2 plots for two rock types (uncoated) at different conditions are plotted and calculated. The first portions of the plots that give a straight line were used to obtain the slope.

Having a wide range of matrix length and diameter as listed in Table 4-2, we introduced a new empirical characteristic length (or shape factor). The new characteristic length was tested against the other ones using the scaling equations listed above.

The recovery curves were carefully analyzed and it was observed that an optimum exist for 1” samples. To derive a new characteristic length, each curve was biased with a pseudo characteristic length. Then the curves were scaled for a good fit. It was observed that, the surface created by pseudo characteristic lengths resemble a parabolic surface for both horizontal and vertical orientations. The difference between vertical and horizontal

orientations is the center of axis which controls the gravity term. The derivation of the following newly defined characteristic length is given in Appendix:

$$L_c^2 = (Length - 4 \cos \theta)^2 + (Diameter - 1)^2 \dots\dots\dots 19$$

$\cos(\theta)$ term describes the direction of interaction with respect to the horizontal plane. The angle (θ) is 0° and 90° for the horizontal and vertical cases, respectively. This equation reflects an optimum around 1 inch diameter core samples. With the new characteristic length defined and applied to scaling groups, we observed that although there was improvement with the classical Mattax and Kyte approach on vertical orientation (**Fig. 4-23a**), horizontal scaling failed to group 1” diameter cores. It is apparent that once the new characteristic length is used, Mattax and Kyte [1962] and Pow et al. [1999] equations turned out to be the same equation. Therefore, no plots for the latter were included. Xie and Morrow equation gave considerably improved results especially for the horizontally positioned cores (**Fig. 4-24b**). Li and Horne approach was observed to be applicable for the vertical orientation (**Fig. 4-25a**), but not for the horizontal orientation with the new characteristic length given in Eq. 19.

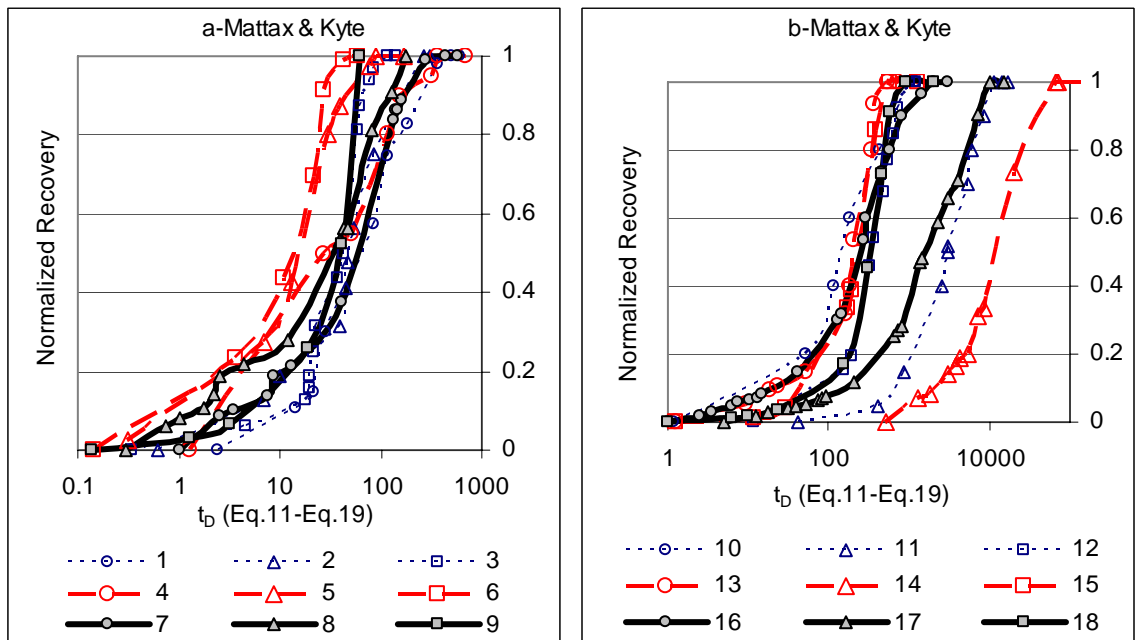


Figure 4.23 Scaling with the classical Mattax and Kyte equation for (a)vertical orientation and (b) horizontal orientation when the new shape factor (Eq. 19) was used.

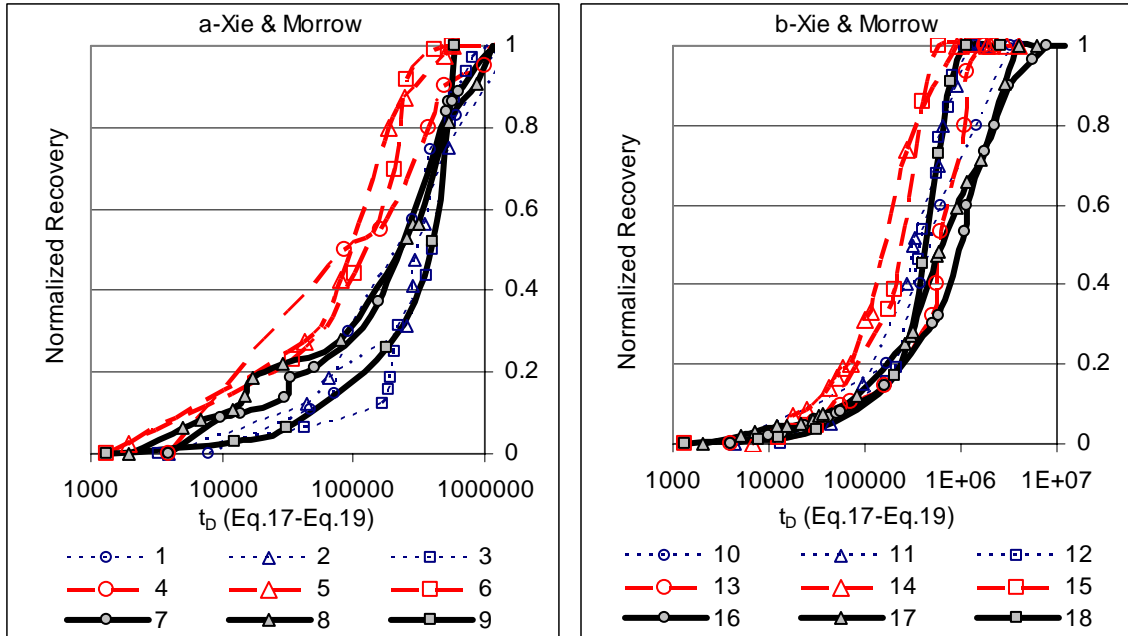


Figure 4.24 Scaling with the Xie and Morrow equation for (a)vertical case and (b)horizontal case when the new shape factor (Eq. 19) was used.

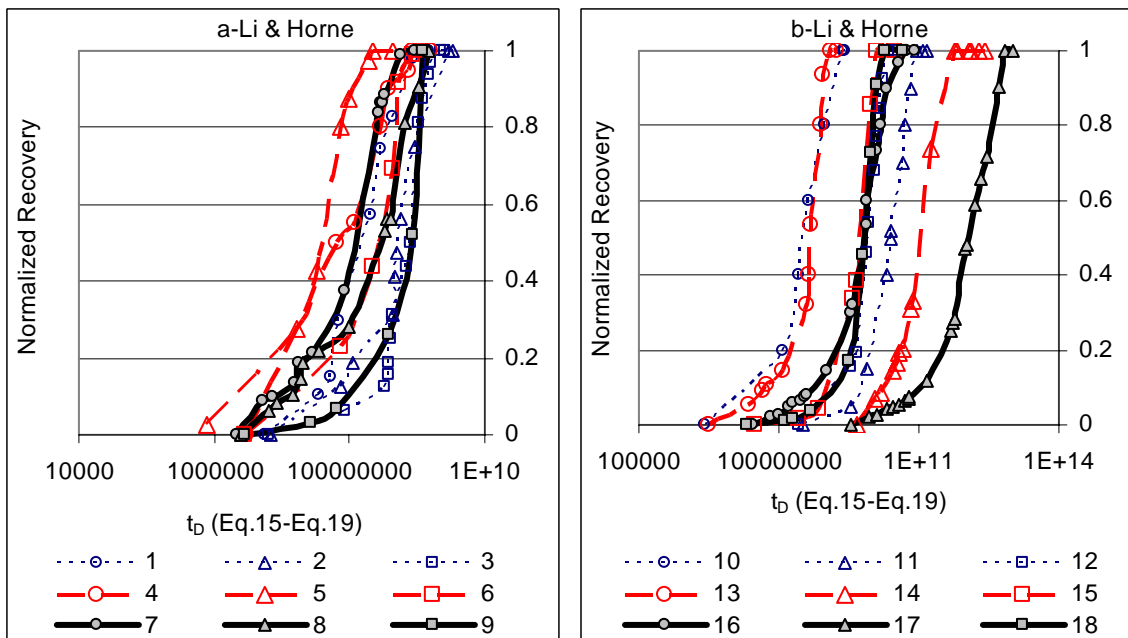


Figure 4.25 Scaling with the Li and Horne equation for (a)vertical case and (b)horizontal case when the new shape factor (Eq. 19) was used.

4.2.1.3 Residual oil

We evaluated the residual matrix oil using four different parameters: Length to diameter ratio (L/D) the newly introduced characteristic length (Eq. 19) dimensionless group

obtained by slightly modifying Eq. 11 with the conventional characteristic length (Eq. 13) and the new one (Eq. 19.). In this equation, time (t) term was replaced by t_{final} that represents the time to reach the ultimate recovery (point where the plateau region starts). Residual oil saturation shows no significant change with L/D or the conventional dimensionless group, t_D (**Figs. 4-26 and 4-27**). This is expected for strongly water-wet systems. Hamon and Vidal [1986] and Zhang et al. [1996] observed that the ultimate recoveries are the same for any possible matrix-fracture boundary conditions (all sides open, two opposite sides open, or only one side open etc.). The difference between the highest and lowest ultimate recoveries is nearly 10%. When the residual oil saturation is plotted against the t_{D^*} a threshold value, beyond which the residual oil decreases with increasing t_{D^*} was observed. Note that a strict dependency of the residual gas phase on the matrix characteristic length was observed for gas-water imbibition previously [Babadagli and Hatiboglu, 2005]. Those studies showed that the difference between the lowest and highest residual non-wetting (gas) saturations reaches 35 % when the same matrix configuration were used. It is, however, not possible to talk about optimum points when we look at the modified dimensionless time group (Eq. 11) with the new characteristic length (Eq.19) versus residual oil saturation plot (**Figs. 4-28-a and 4-28-b**). An increasing trend for vertical orientation and a decreasing trend for horizontal orientation were observed. The new characteristic length reflects itself in an opposite manner. A decreasing trend in vertical orientation and increasing trend in horizontal orientation were observed.

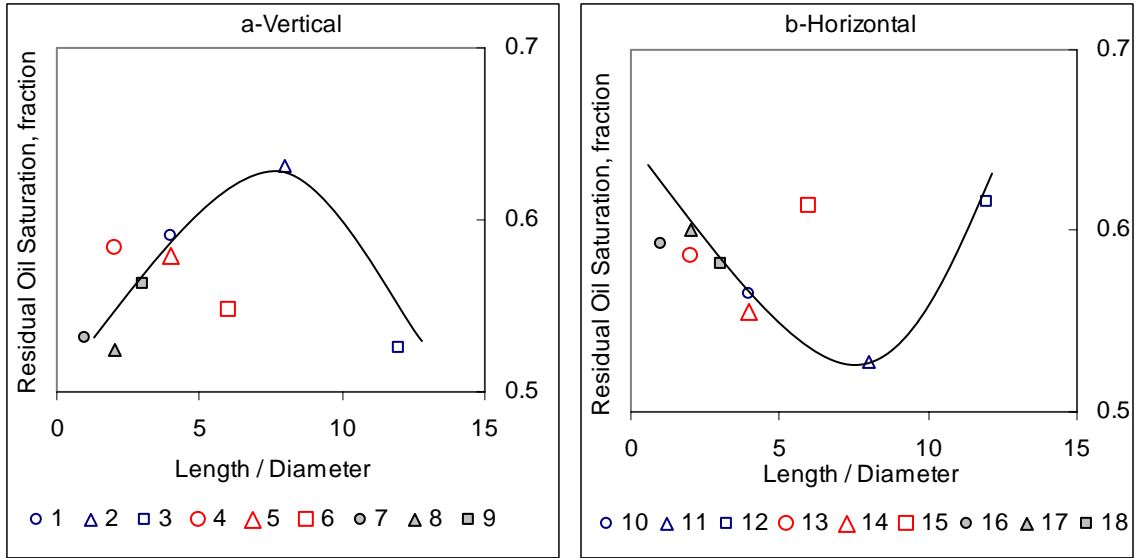


Figure 4.26 The change of residual oil saturation with the length/diameter ratio for (a)vertical case and (b)horizontal case

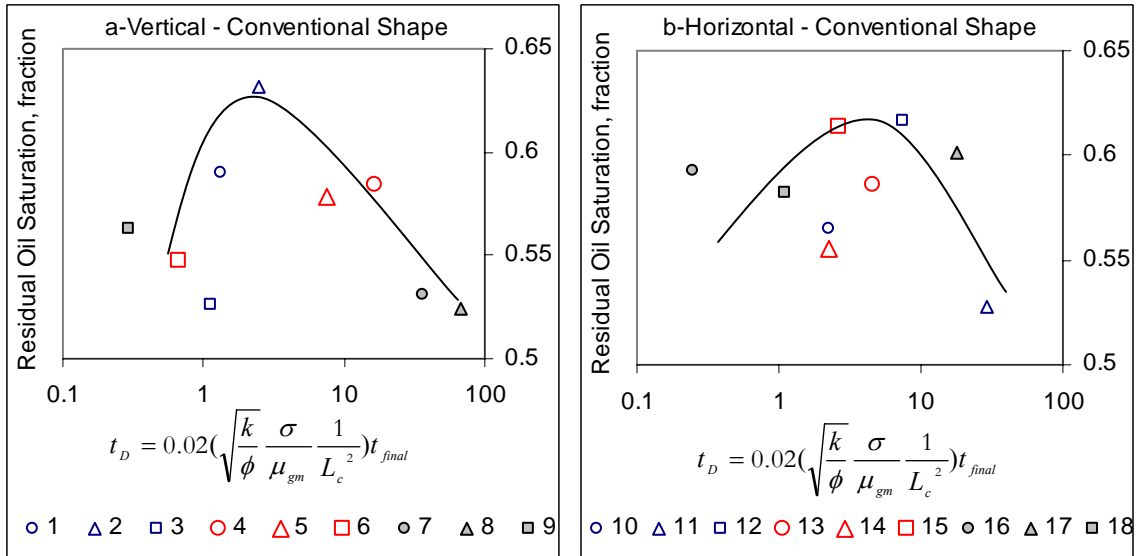


Figure 4.27 The change of residual oil saturation with the dimensionless group (t_{final} = time to reach the ultimate recovery -point where the ultimate recovery was reached) for (a)vertical case and (b)horizontal case

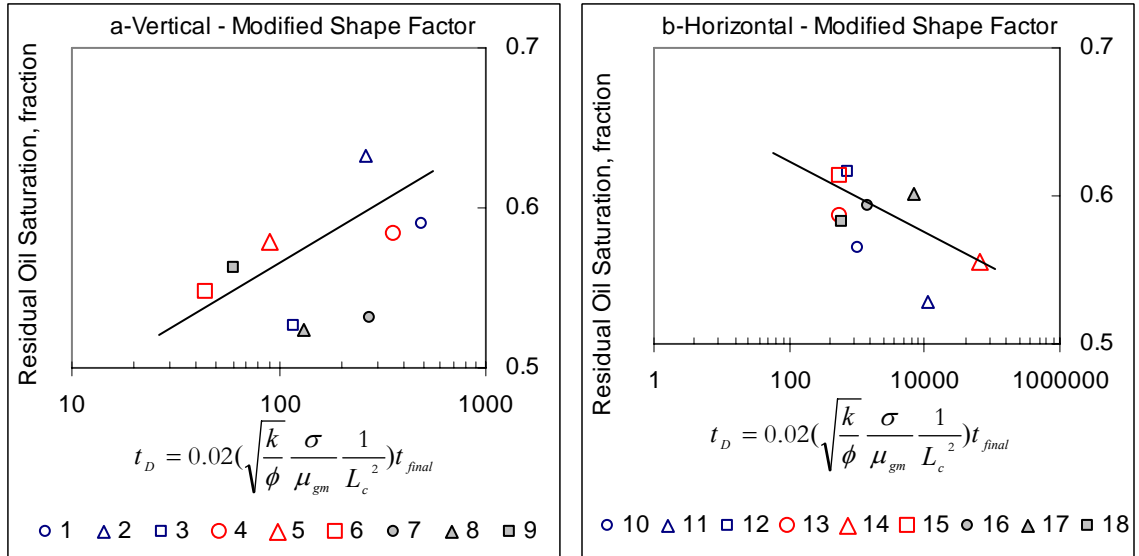


Figure 4.28 Same dimensionless group used in Fig 9 modified with the new shape factor (Eq. 9) for the (a) vertical and (b) horizontal cases.

4.2.2 Capillary imbibition of oil-surfactant solution

Capillary imbibition studies using surfactants are abundant for co-current interaction [Schechter et al., 1994; Milner and Austad, 1996; Austad and Milner, 1997; Austad et al., 1998; Standnes et al., 2002; Strand et. al., 2003; Babadagli, 2001, 2002, 2003, 2006]. A limited number of studies investigated the counter-current imbibition of surfactant solutions [Babadagli, 2001, 2002]. To understand the dynamics of the counter-current imbibition of the lowered IFT solutions several experiments were conducted. A few experiments with kerosene were also included for comparison.

4.2.2.1 Recovery rate and scaling analysis

The recovery curves are given in **Figs. 4-29** and **4-30** for the vertical and horizontal cases, respectively. As the diameter of the core increases, the recovery rate difference between the two kerosene cases becomes significant in the vertical cores (Exps. 19 and 20 in Fig. 4.29). When the two mineral oil-brine cases compared (Exps. 1 and 4 in Fig. 4.29), it can be observed that the larger diameter core yielded a faster recovery. Note that there is no significant difference in the ultimate recoveries of four different oil-brine cases (Exps. 1, 4, 19, and 20 in Fig. 4.29). However, the larger diameter cores yielded lower ultimate recoveries and this is more prominent for the higher oil viscosity cases (mineral oil).

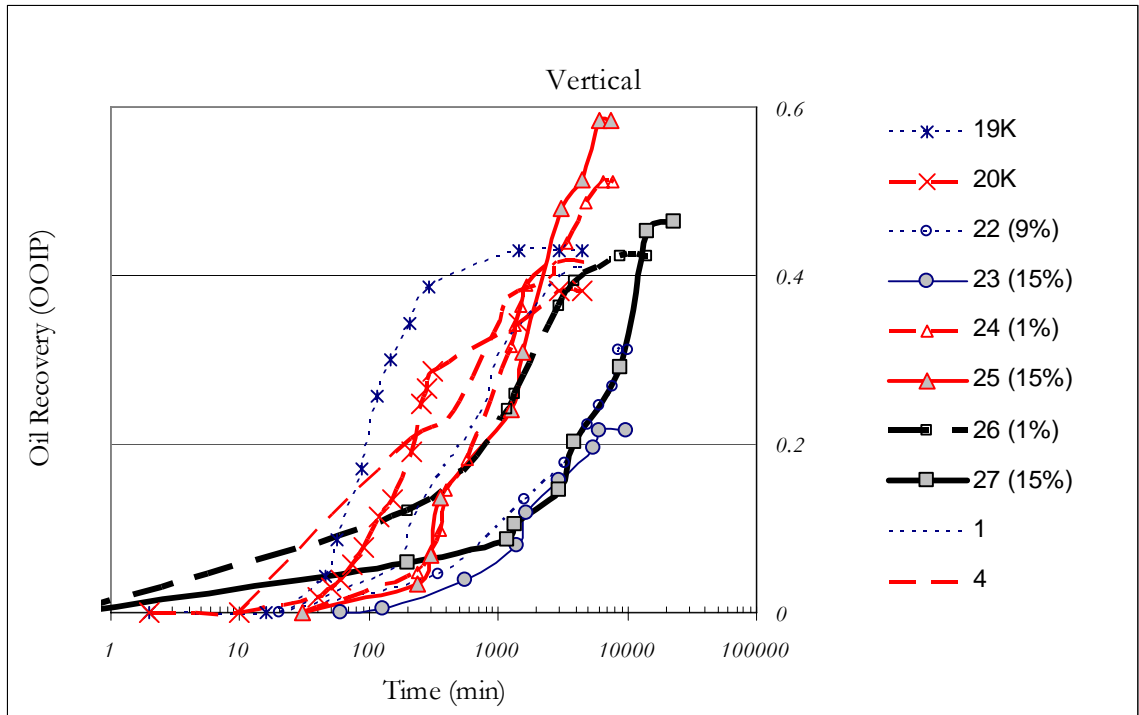


Figure 4.29 Kerosene-brine and mineral oil-surfactant solution imbibition tests for the vertical case.

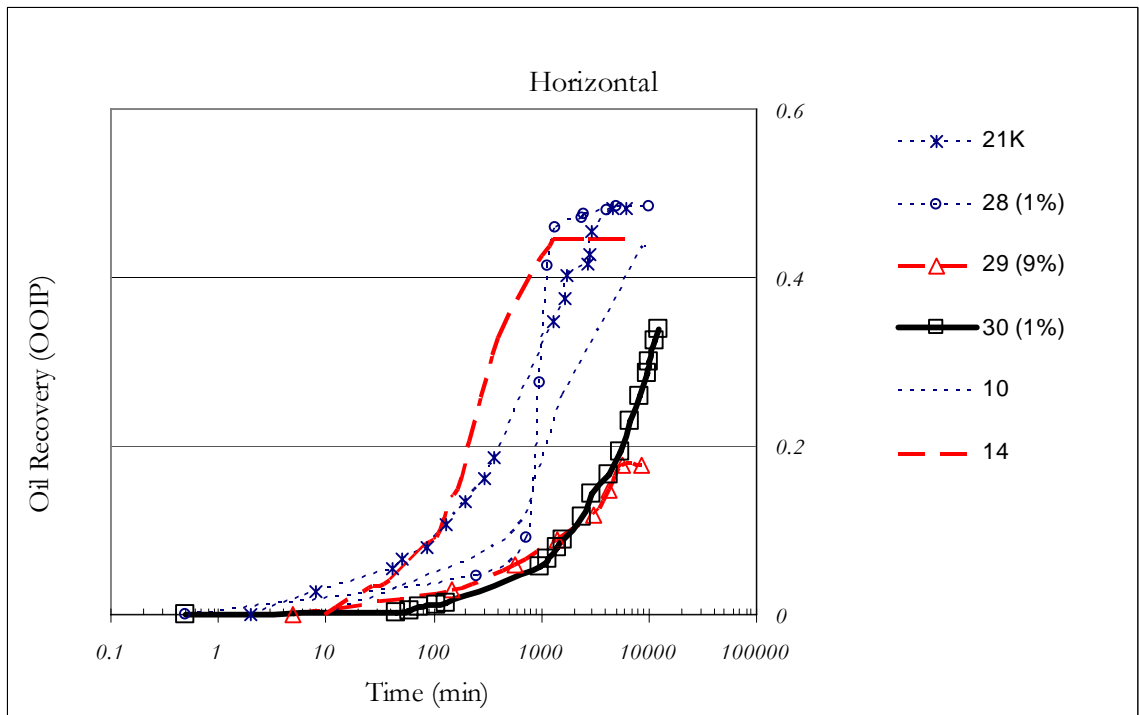


Figure 4.30 Kerosene-brine and mineral oil-surfactant solution imbibition tests for the horizontal case.

The recovery performances of low IFT solutions were also investigated. Experiments with different surfactant concentrations are included in Fig. 4.29. When the recovery behavior of the three smallest size (vertical) cores with mineral oil are compared (Exps. 1, 22, and 14),

one can observe that the high IFT case yielded the fastest recovery and the highest ultimate recovery. Lower surfactant concentration (9%) gave slightly faster recovery and higher ultimate recovery than those of high surfactant concentration (15%). Both surfactant cases exhibited similar recovery trends.

Note that the IFT values for these surfactants are above the critical micelle concentration (CMC) value. The importance of the CMC on the recovery was discussed previously. For the co-current capillary imbibition recovery of crude oil from chalk samples, surfactant concentrations above the CMC were suggested to minimize the adsorption and wettability change effects for an efficient recovery by cationic surfactants [Strand et al., 2003; Standnes et al., 2002]. For anionic surfactants, suggestion was to apply surfactant concentrations below the CMC for an efficient recovery by co-current capillary imbibition from sandstones [Babadagli, 2003] and chalks [Schechter et. al., 1994].

The micellar structure of surfactant (microemulsion) could be considered as the cause of ineffective counter-current displacement. However, the same surfactant concentration (15%) solution yielded a higher recovery rate and ultimate recovery for the larger core experiments (Exps. 25 and 27). The behavior of the surfactant solution imbibition was different for the two different core lengths. It is also interesting to note that the low surfactant concentration (1%, below the CMC) and high surfactant concentration (15%, above the CMC) showed a similar recovery trend but slightly different ultimate recoveries for shorter samples. For the shorter and larger diameter cases (Exps. 25 and 27), 15% surfactant concentration yielded a higher recovery as well.

Four cases of the horizontally situated core experiments were considered in Fig. 4.30, two additional experiments (Exps. 10 & 14) are given as reference. Despite the difference in viscosities, the larger core with the mineral oil (Exp. 14) shows slightly faster recovery than the smaller size kerosene sample. This reveals that the matrix boundary conditions dominate the recovery rate rather than the viscosity of oil. The kerosene yielded slightly lower residual oil. When the cases of two identical core samples with different oil types were considered, it was observed that the mineral oil shows slower and lower ultimate recovery than kerosene (Exps. 10 and 21). As similar to the vertical case, the 15% surfactant solution yielded much lower recovery than that of the brine (Exp. 10) and 1% surfactant

concentration cases (Exps. 28 and 30) for the small diameter cores (Exp. 29). An expected behavior is observed in Exp. 28, where ½ inch diameter sample resulted in similar recovery to that of the brine (Exp. 10) despite the difference in the length of both cases.

These observations reveal that the characteristic length dominates the recovery below certain diameter (0.5 inch) and one should select the surfactant concentrations below the CMC (Exps. 22 and 14).

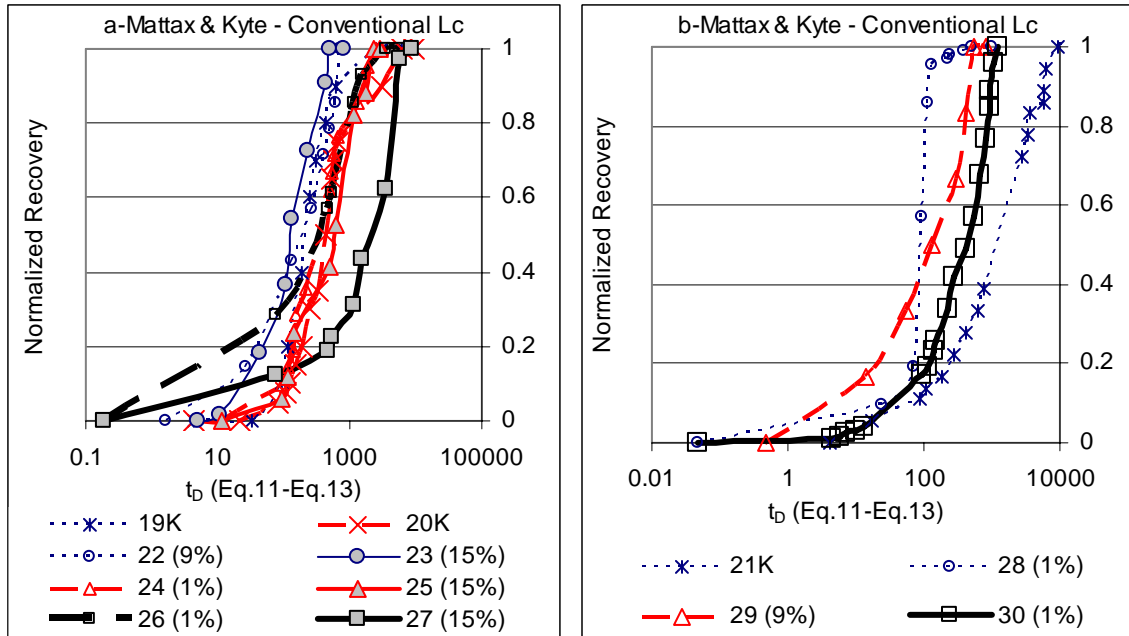


Figure 4.31 Scaling with the classical Mattax and Kyte equation for (a) vertical and (b) horizontal cases

The validity of the dimensionless group (Eq. 11) was also tested for the cases given in Figs.4.29 and 4.30. The classical scaling group plots show that possible scaling was obtained for the vertical case (**Fig. 4-31a**). No possible scaling was observed for the horizontal case (**Fig. 4-31b**). After applying the new shape factor, classical Mattax and Kyte approach for the vertical samples show similar groupings similar to the conventional shape factor. For the horizontal case, Exps. 29 and 30 are far apart from each other, and two distinct groups are observable in the plot (**Fig. 4-32b**).

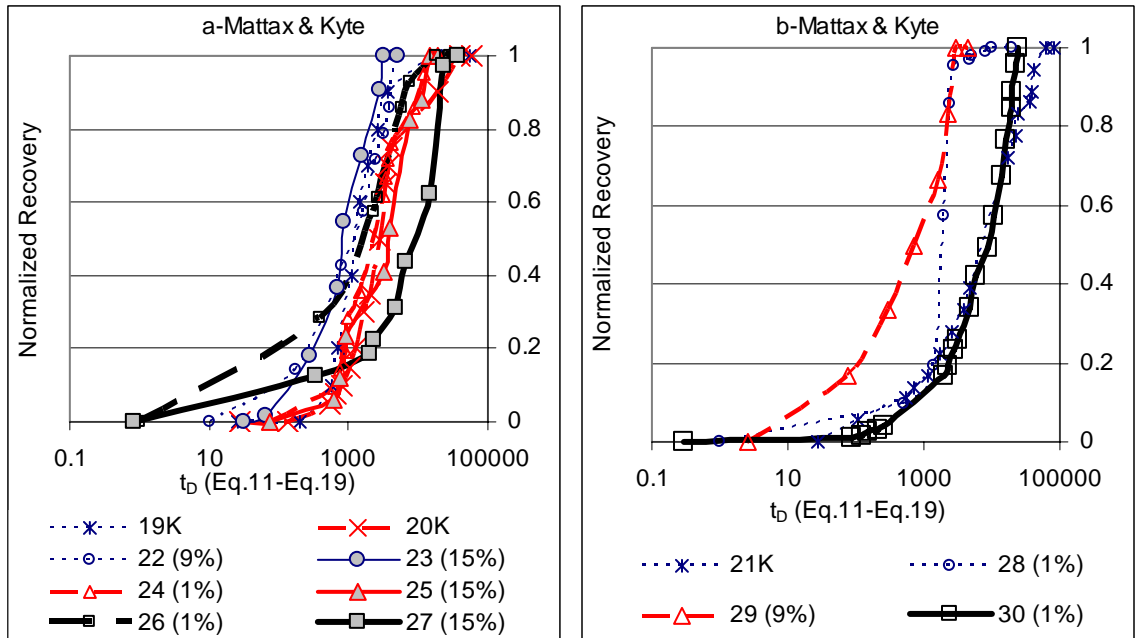


Figure 4.32 Scaling with the classical Mattax and Kyte equation for horizontal case when the new shape factor (Eq. 19) was used.

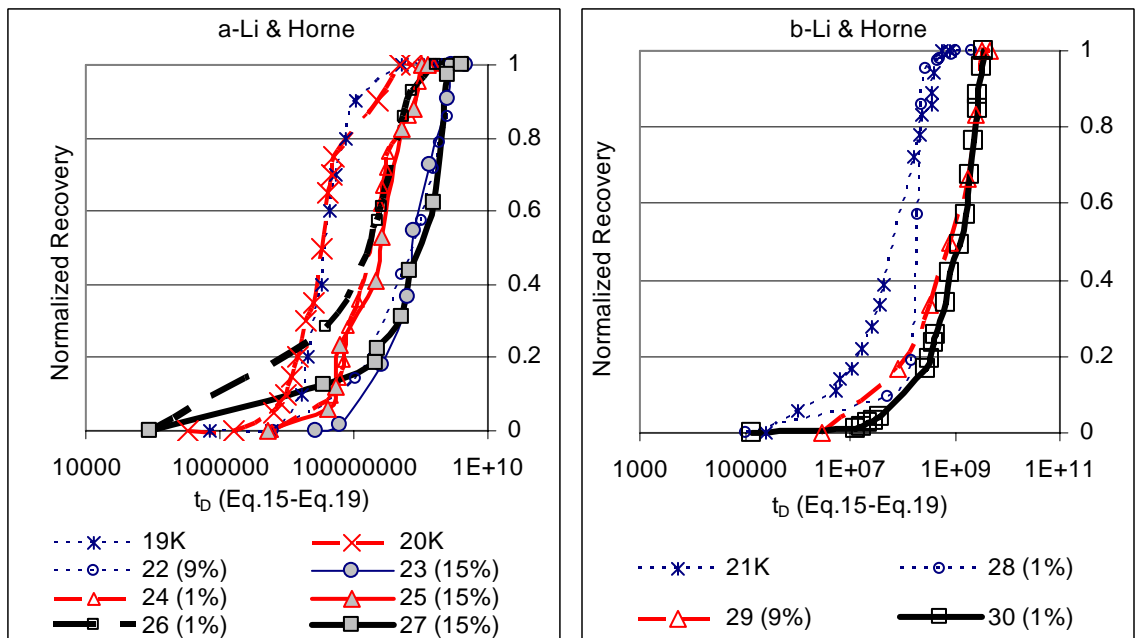


Figure 4.33 Scaling with the Li and Horne equation for horizontal case when the new shape factor (Eq. 19) was used.

Li and Horne (Fig. 4-33b), and Xie and Morrow (Fig. 4-34b) scaling groups with the new characteristic length showed a good improvement in the scaling for the horizontal orientation. The improvement in the scaling with the new characteristic length is less pronounced for the vertical orientation.

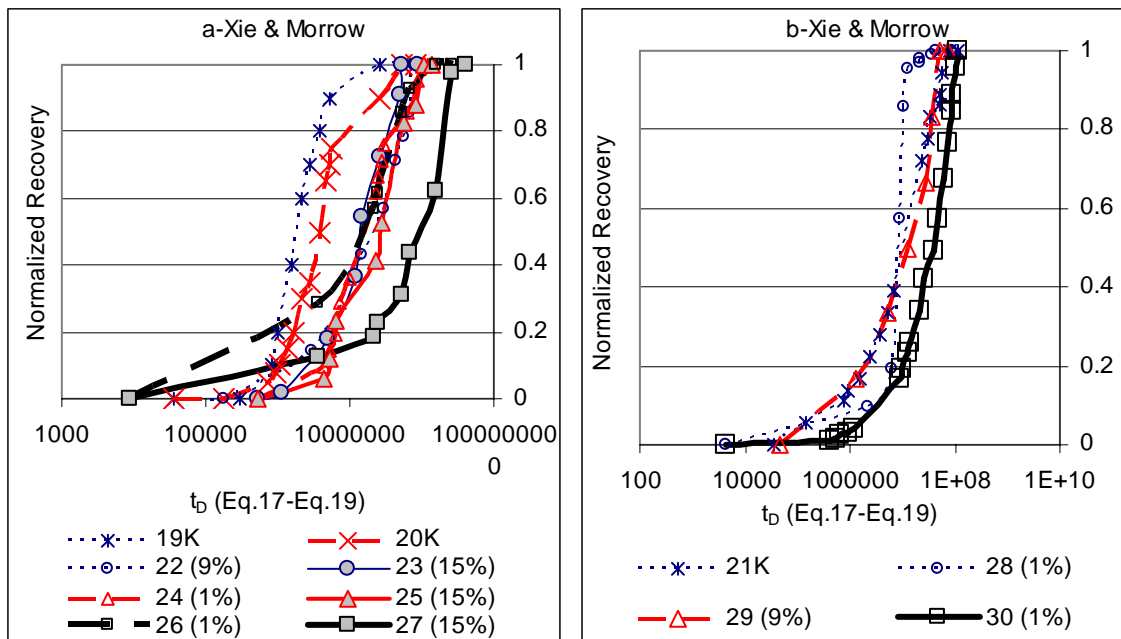


Figure 4.34 Scaling with the Xie and Morrow equation for horizontal case when the new shape factor (Eq. 19) was used.

4.2.2.2 Residual oil

Residual oil saturation analysis was done in a similar fashion to oil-brine capillary imbibition experiments. The L/D and the dimensionless time group with the conventional and newly introduced shape factor were plotted against residual oil saturation. Good correlations were obtained with these three parameters for the vertical cases (**Figs. 4.35-4.37**).

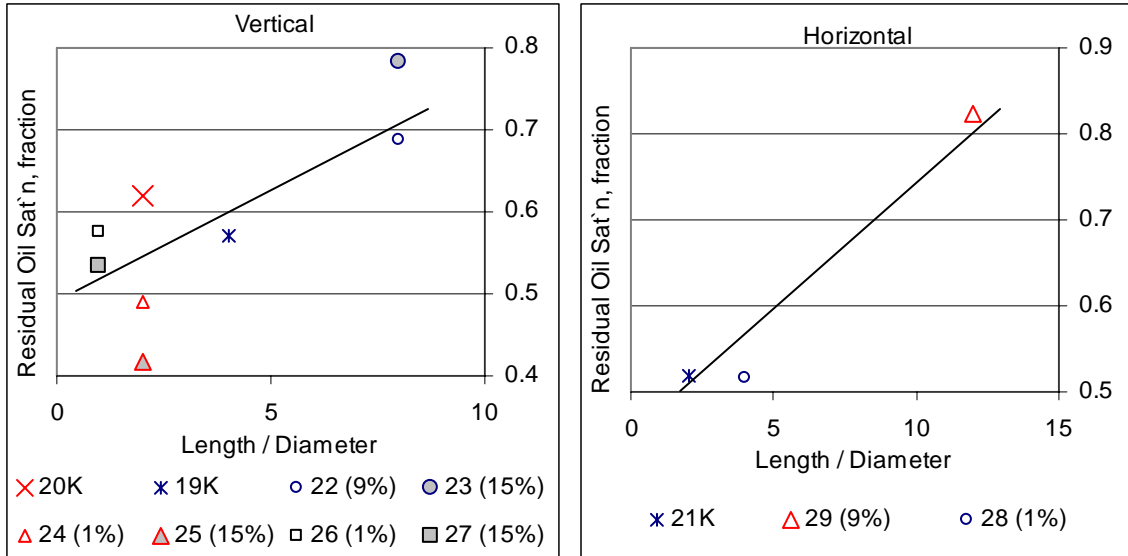


Figure 4.35 The change of residual oil saturation with the length/diameter ratio for (a) vertical case and (b) horizontal case.

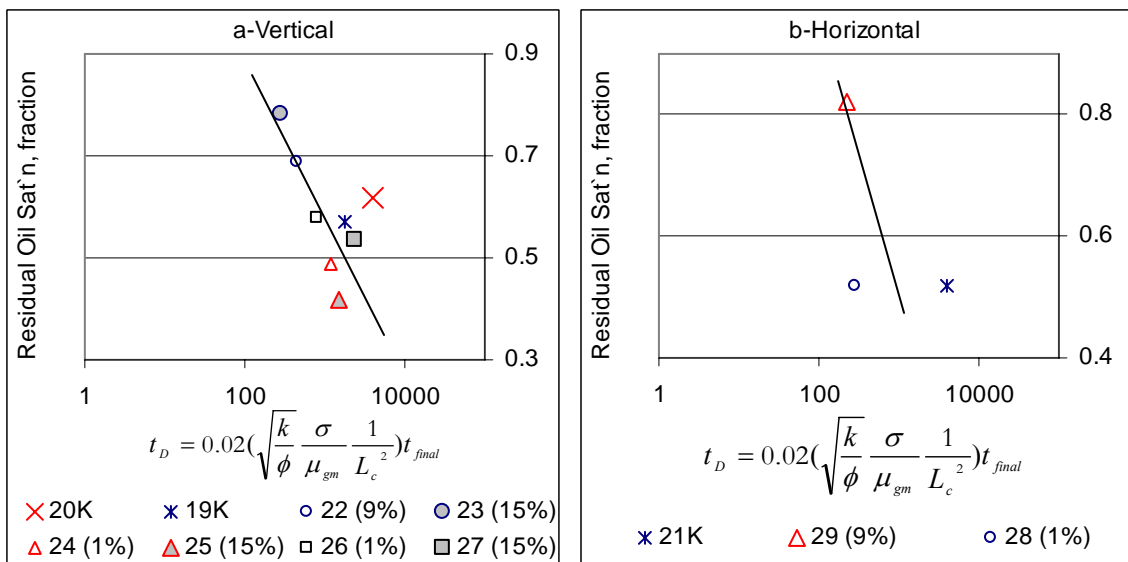


Figure 4.36 The change of residual oil saturation with the dimensionless group (t_{final} = time to reach the ultimate recovery -point where the ultimate recovery was reached for (a) vertical case and (b) horizontal case.

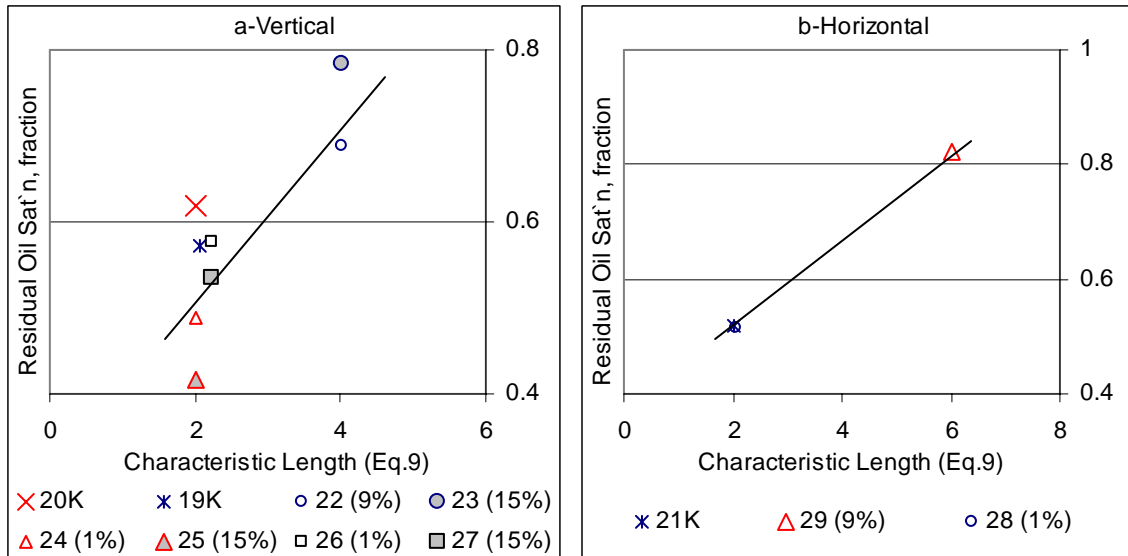


Figure 4.37 Proposed shape factor versus SOR plots vertical case.

4.2.3 Capillary imbibition of oil-brine (aged samples)

One of the critical factors in the capillary imbibition is the wettability of the rock sample. To incorporate the effect of the wettability in the scaling and residual oil saturation correlations, aged sandstone samples (1 week and 1 month) were used. The results for the aged Berea sandstone samples were compared with the Indiana limestone samples having similar wettability (weakly water wet) but different permeability and pore structure.

4.2.3.1 Indiana limestone vs. aged Berea sandstone

The recovery curves obtained from the oil-brine imbibition experiments are given in **Figs. 4.38** and **4.39**. The longest samples resulted in the slowest recovery rate (**Fig. 4.38**). Recoveries ranged between 45% and 55% OOIP. An optimum core size was observed in terms of the recovery rate. The 1" diameter cores, with 0.5 and 1" length, yielded the fastest recovery.

Average recovery is around 30% with the uncoated (Exp.32U) and largest core (Exp.35) sample giving the lowest recovery. For the rest of the cases, shorter cores resulted in slightly faster recovery, but the ultimate recoveries are around 30% OOIP.

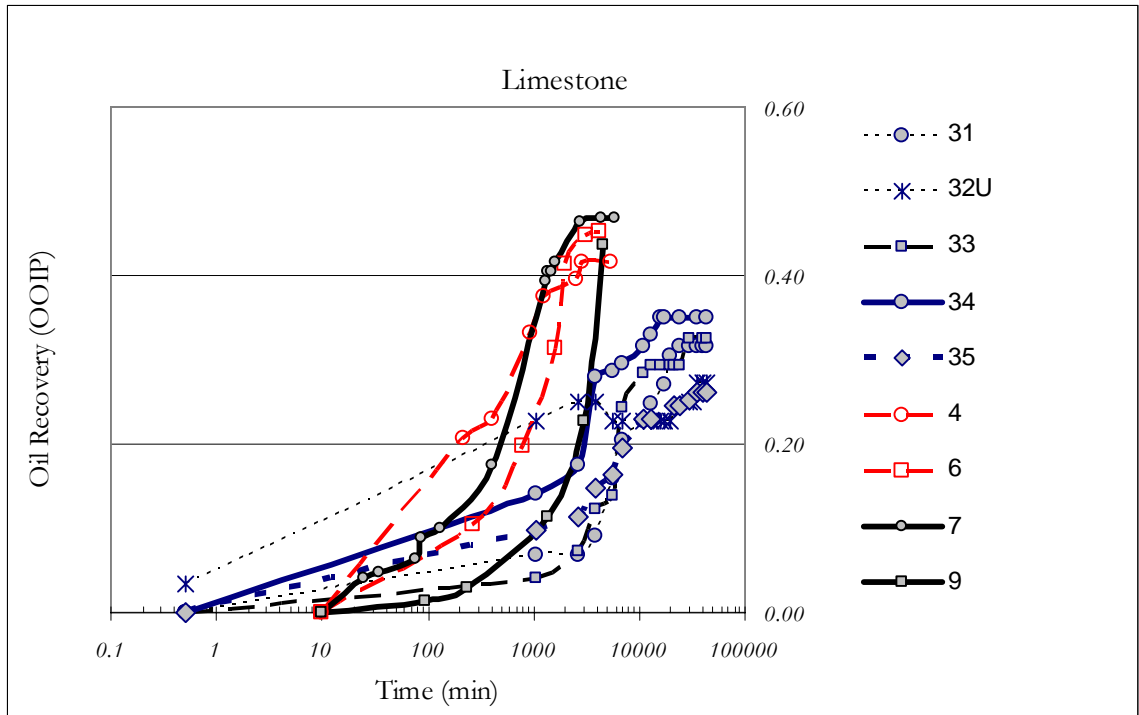


Figure 4.38 Oil-brine capillary imbibition tests in the Indiana limestone cores.

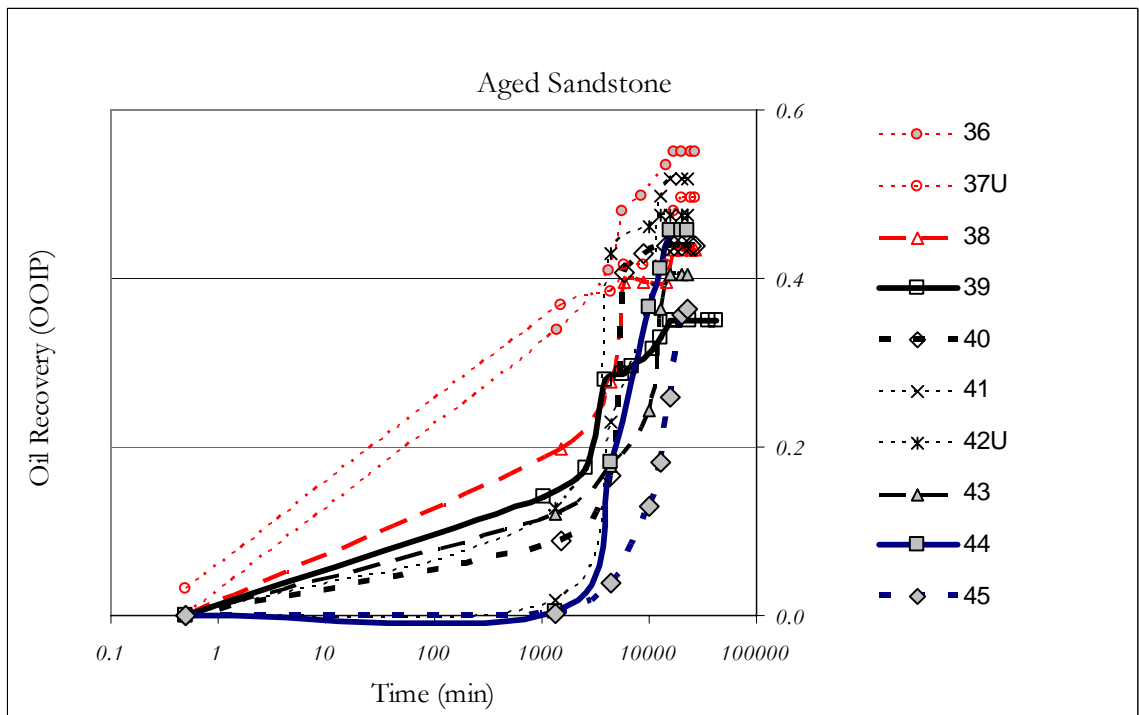


Figure 4.39 Oil-brine capillary imbibition tests in the aged Berea sandstone cores.

4.2.3.2 Un-aged vs. aged Berea sandstone samples

Consistent trend was observed among the aged samples. The difference is that the plots are shifting to right as aging process is more intensive (Fig. 4.39). In other words, wettability alteration caused a delay in the recovery. No significant effect was observed on the ultimate recoveries.

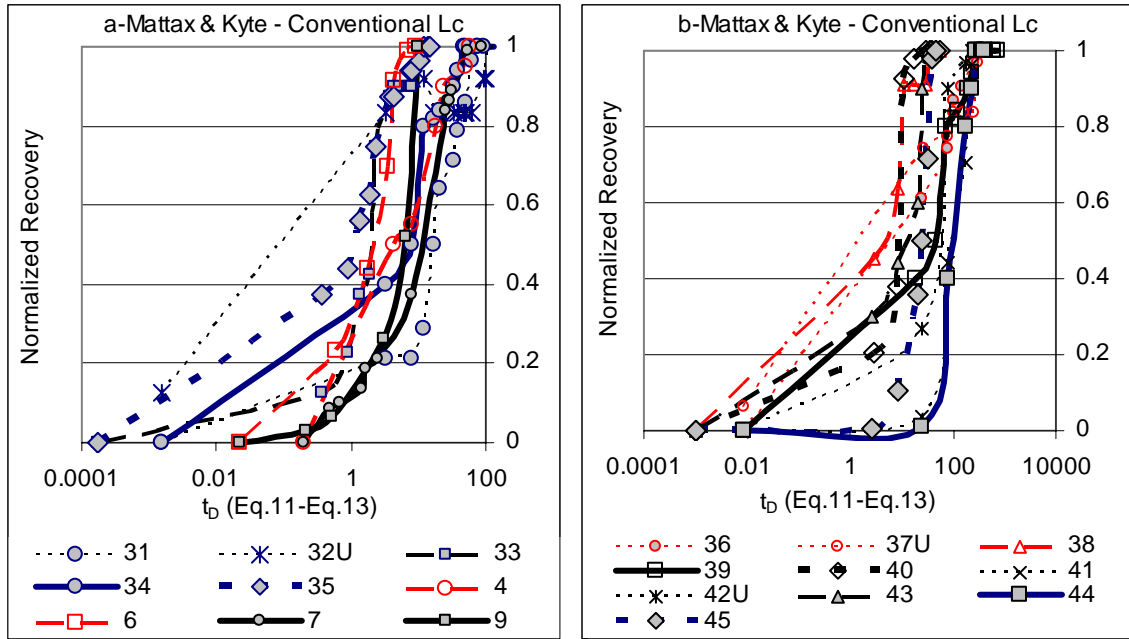


Figure 4.40 Scaling with the classical Mattax and Kyte equation for (a) vertical and (b) horizontal cases

For the 1-week aged samples (Fig. 4.39) it was observed that as the cores became larger, the recovery rate reduced, uncoated sample (Exp. 37U) giving the fastest recovery. Slightly higher recovery was observed for the smallest sample (Exp. 36) which is also the fastest among the group.

Slowest recovery amongst the aged samples was obtained from 1-month aged samples as expected (Fig. 19b). In comparison to the un-aged cases of Berea sandstone, 1-month aged samples had less ultimate recovery. Similar shaped cores had very similar ultimate recoveries at the imbibition stage of the process. The only exception is the largest size cores, where 1-month aged sample (Exp.45) delivered 35% OOIP recovery far less than the un-aged sample (Exp. 9) at 45% OOIP recovery. Interestingly, 1-month aged small diameter sample (Exp. 41) had higher recovery than its un-aged counterpart (Exp. 4).

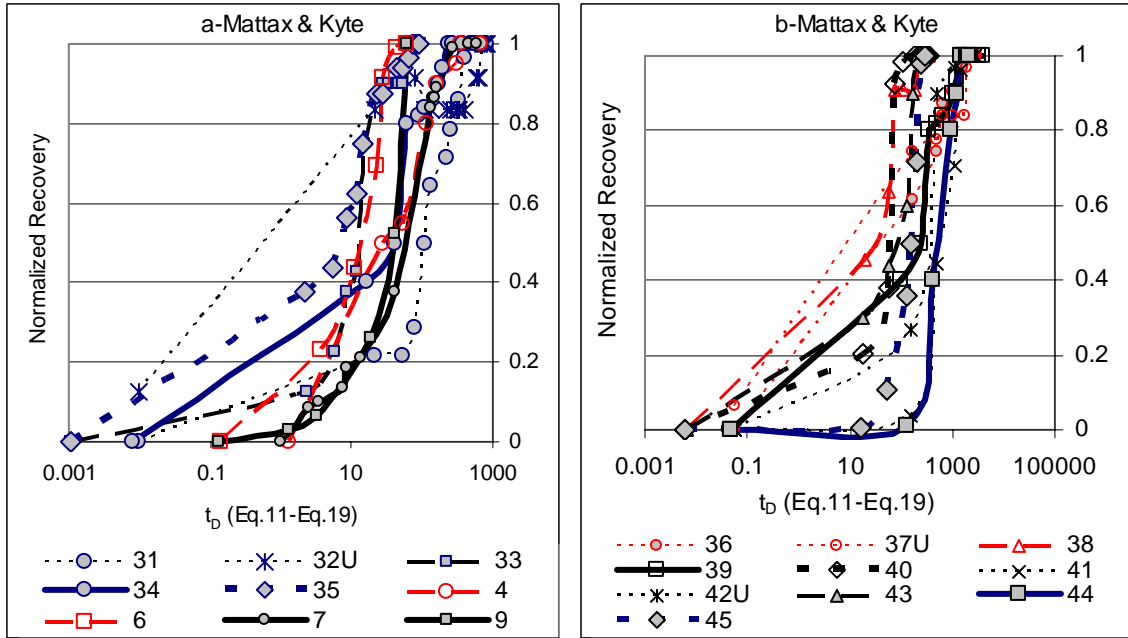


Figure 4.41 Scaling with the classical Mattax and KYTE equation for horizontal case when the new shape factor (Eq. 19) was used.

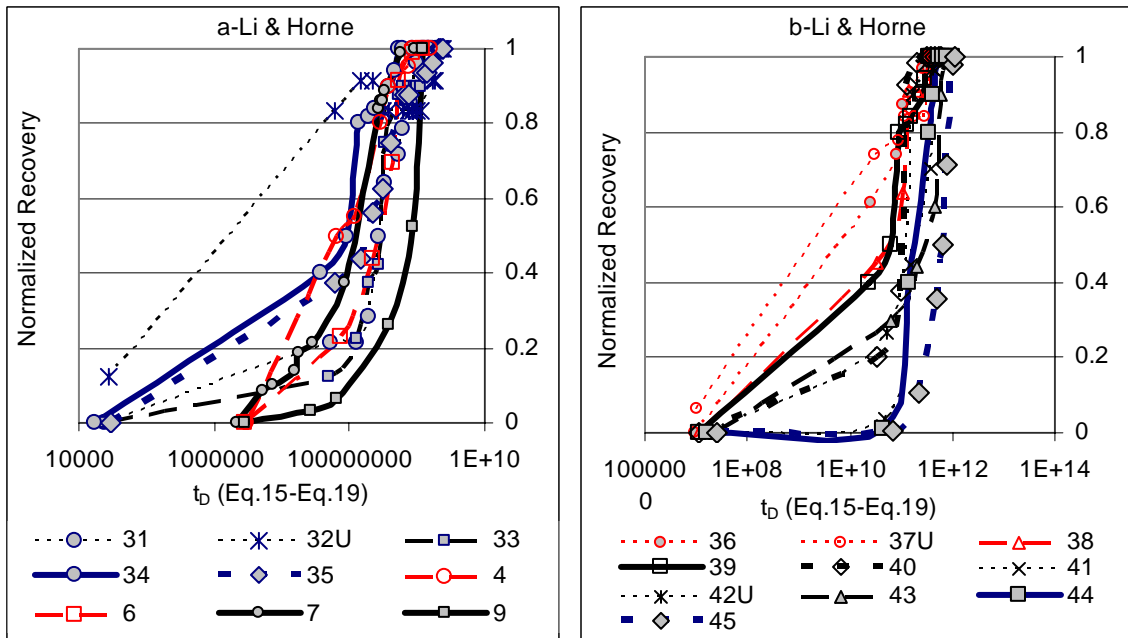


Figure 4.42 Scaling with the Li and Horne equation for horizontal case when the new shape factor (Eq. 19) was used.

In terms of the scaling, a similar behaviour to the non-aged Berea samples was observed. Since the wettability altered samples are all positioned vertically it was possible to obtain reasonable groupings using any of the scaling groups. While Li and Horne [2002] was

especially successful for scaling vertical experiments, the aged samples did not show a good scaling (Fig. 4.42a). On the other hand, Xie and Morrow [2000] group was best suited to reflect the behaviour of the horizontally positioned experiments overall and, it was possible to obtain good results for the aged samples (Figs. 4.43b).

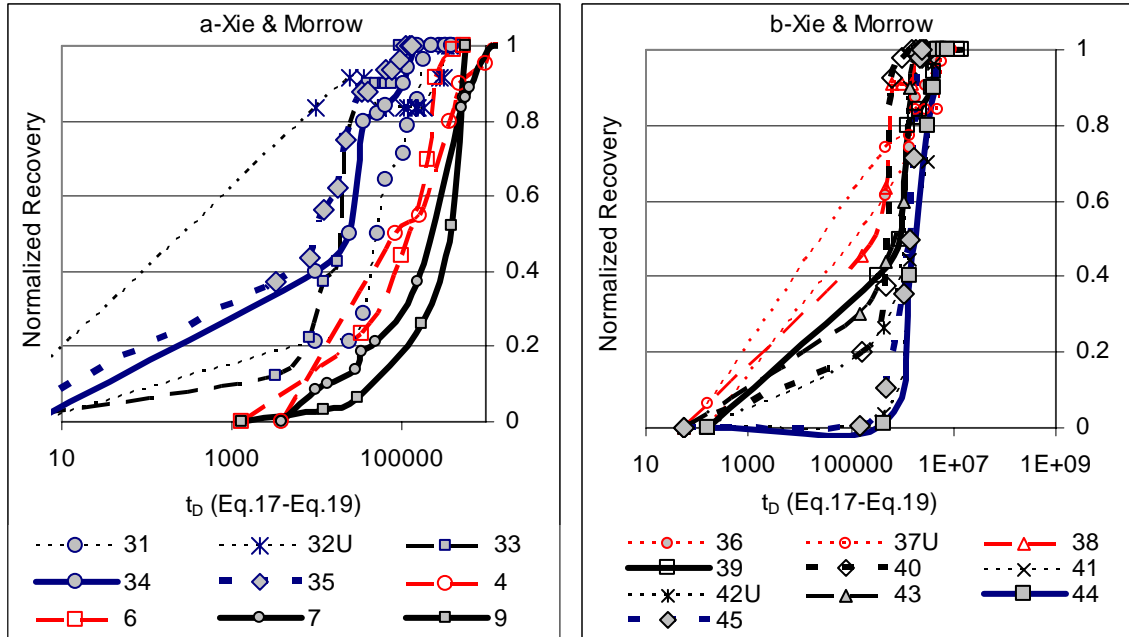


Figure 4.43 Scaling with the Xie and Morrow equation for horizontal case when the new shape factor (Eq. 19) was used.

4.2.3.3 Residual oil saturation

To clarify the effect of wettability on the process, Indiana limestone and wettability altered Berea sandstone samples were tested. The aged Berea sandstone samples showed similar trends as well as similar ultimate recoveries. Then the recovery difference between limestone and sandstone samples was attributed to different pore structures. Wettability and pore structure effect for this type of process is expected to be dominating. Regardless of the core shape, the limestone samples resulted in poorer recovery both in terms of the final amount recovered and the rate of recovery. Berea sandstone and Indiana limestone samples represent very different pore structures and wettability characteristics. To distinguish the effect of wettability and pore characteristics on the process, aged Berea samples were tested. Wettability alteration caused the rate of recovery to be slower, yet no significant difference in ultimate recoveries was observed.

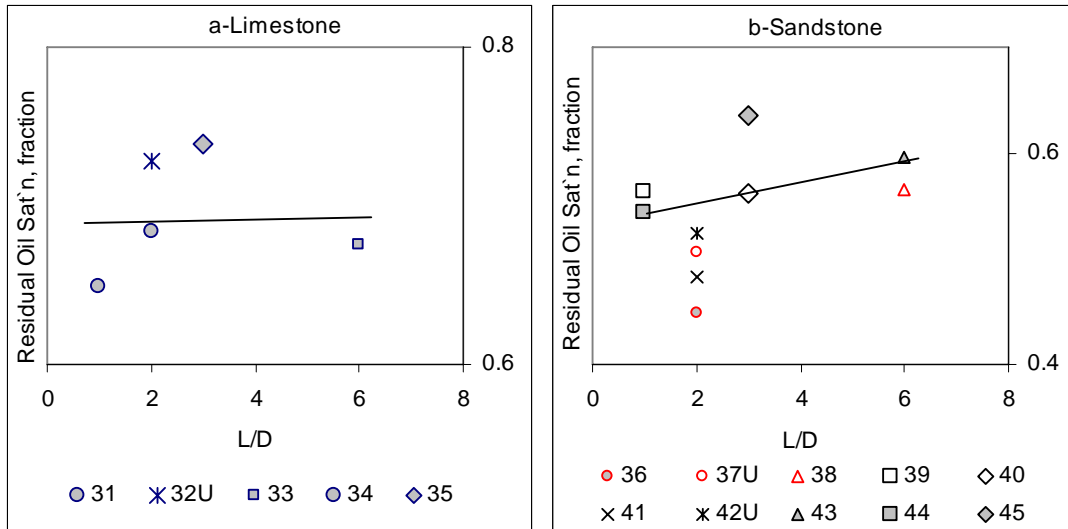


Figure 4.44 The change of residual oil saturation with the length/diameter ratio for (a) vertical case and (b) horizontal case.

When the residual oil saturation was plotted against L/D for those cases, no clear trend and relationship were observed (**Fig. 4.44b**)

Residual oil saturations with respect to the modified dimensionless group (t_D) (**Fig. 4.45b**) and shape factor showed a linear trend. Lowered interfacial tension has a significant effect in the dynamics of counter-current imbibition. However, surfactant concentration higher than CMC yielded an inefficient counter-current displacement, which could be due to adverse effects of micro-emulsive character of the wetting phase for small diameter samples (typically 0.5”).

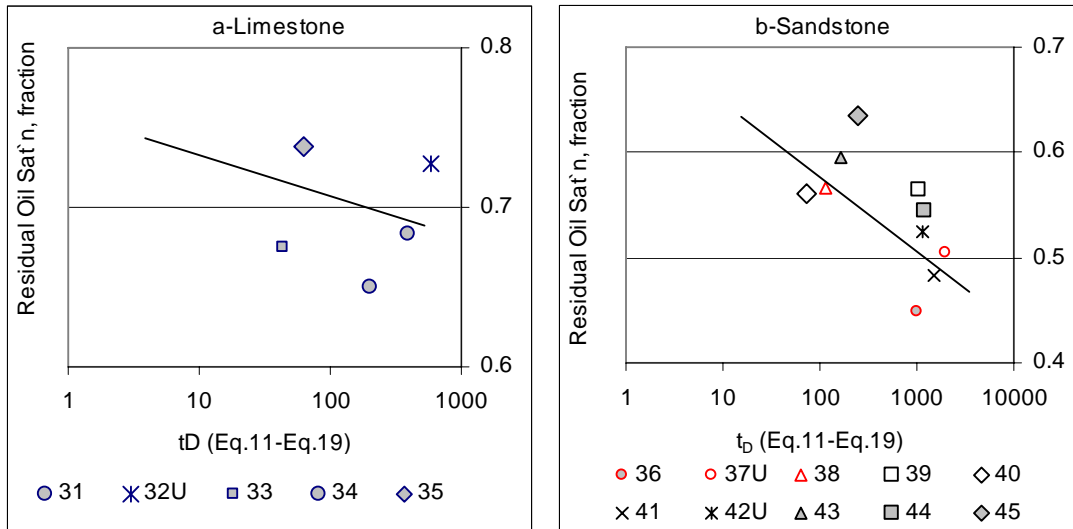


Figure 4.45 Proposed shape factor versus SOR plots vertical case.

5 Miscible matrix-fracture interaction

5.1 Primary diffusion






To simulate solvent injection into naturally fractured reservoir, a set of experiments are performed. Unlike the common practice which would utilize solvent as tertiary recovery agent, the rock samples are exposed to solvent first without any pre-flood (“primary diffusion”). Then, a more conventional method is followed and the samples were first water flooded (capillary imbibition) before solvent injection (“secondary diffusion”). The two cases are compared for different rock samples.

Different shape factors as well as wettabilities were tested and compared for two different recovery mechanisms (Table. 5.1). Wettability was altered in two different ways; either by using weakly water-wet rock (Indiana limestone) or aging the water-wet rock (Berea sandstone) for different time periods. A reference case with strongly water-wet rock sample was also included for comparison. In addition to the mineral oil experiments a few crude oil experiments were also performed with un-aged Berea rock samples.

First, the oil-saturated samples were exposed to miscible displacement by immersing them into solvent filled containers (primary diffusion). An alternate to this is pre-flushing using spontaneous imbibition (primary imbibition), then using solvent as a secondary recovery agent (secondary diffusion). In the latter case, cores that were exposed to primary imbibition were removed from imbibition tubes and immersed into solvent-filled containers.

The analysis was performed focusing on two critical issues: the recovery rate and the residual oil (ultimate recovery). In regards to the latter, a comparison chart for the two processes is presented at the end.

Table 8 Miscible experiment identification according to core shape and rock type.

	CoreShape					
	Length (inch)	2	2	6	2	6
	Diameter (inch)	1	1	1	2	2
Primary Diffusion	Berea SS	1	2U & 2UC	3	4 & 4C	5
	Indiana LST	6	7U	8	9	10
	1-week aged Berea	11	12U	13	14	15
	1-month aged Berea	16	17U	18	19	20
Primary Imbibition Secondary Diffusion	Berea SS	21	22U & 22UC	23	24 & 24C	25
	Indiana LST	26	27U	28	29	30
	1-week aged Berea	31	32U	33	34	35
	1-month aged Berea	36	37U	38	39	40

5.1.1 Indiana limestone vs. Berea sandstone

After saturation (and aging them if needed), the cores were immersed into n-heptane. The recovery curves obtained from the primary diffusion experiments are given in **Figs. 5.1, 5.2,** and **5.3.**

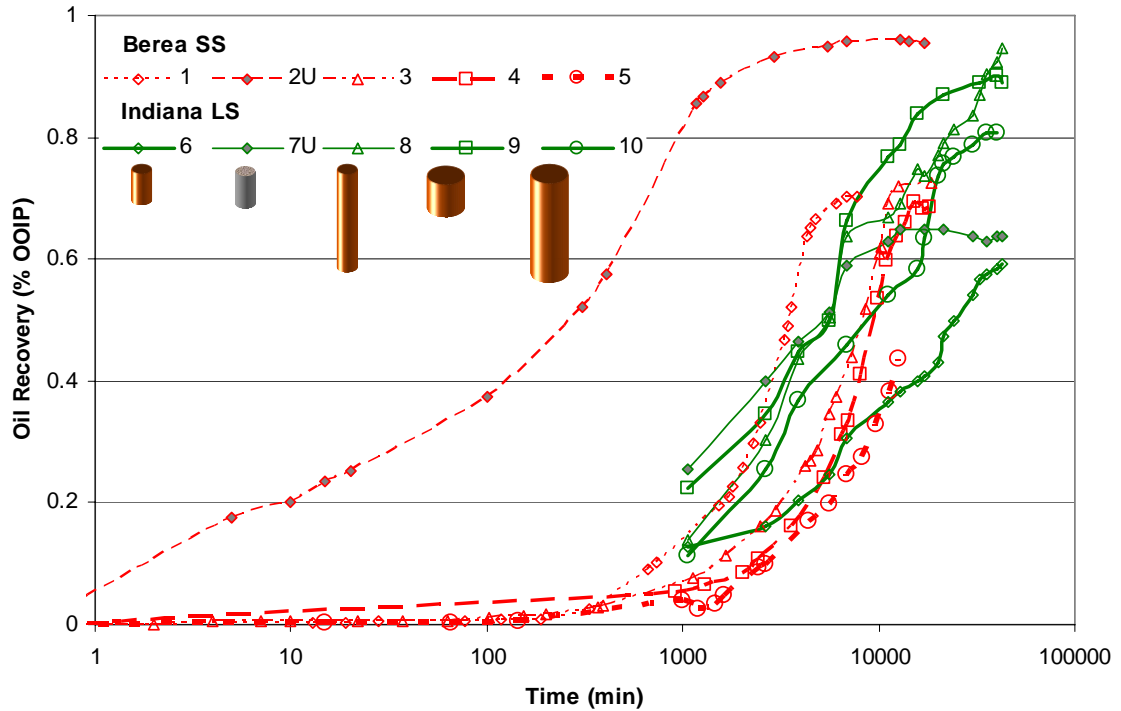


Figure 5.1 Primary diffusion experiments on Indiana limestone and Berea sandstone samples.
U: Uncoated core.

Fig. 5.1 compares limestone samples with the un-aged Berea sandstone. Uncoated samples of each rock type (Exp. 2U, 7U) had faster recoveries compared to the epoxy coated ones. With the inclusion of boundary effects, transfer dynamics were changed. Dispersive flow caused by buoyant uplift of the lighter phase was dampened through sealing the cores which greatly reduces the recovery rate. Limestone cores other than 1-inch diameter and 2-inch length ones (Exps. 8, 9 and 10) were not only faster but also higher in the ultimate recovery (around 95%) compared to the corresponding Berea sandstone experiments, which produced 70% oil (Exps. 3, 4 and 5). The small diameter limestone samples (Exps. 6 and 7U) had similar ultimate recoveries. Except for the largest sample (Exp. 5), which displayed the lowest recovery (47%), the coated Berea sandstone samples had a recovery of 70% average. The uncoated base case (Exp. 1) showed 95% recovery. The coated Indiana limestone cases (counter-current transfer) characteristically showed higher ultimate recovery than those of the Berea sandstone whereas for the uncoated case the recovery from the Berea sandstone was substantially faster and ultimate recovery was higher. The recovery rate, however, was inconsistent for limestone samples unlike Berea sandstone samples. The

recovery time increased with increasing core sizes in the Berea sandstone cases. This could be attributed to the different pore characteristics of the two rock types that eventually caused a positive effect on the oil recovery by counter-current interaction in the Indiana limestone cores.

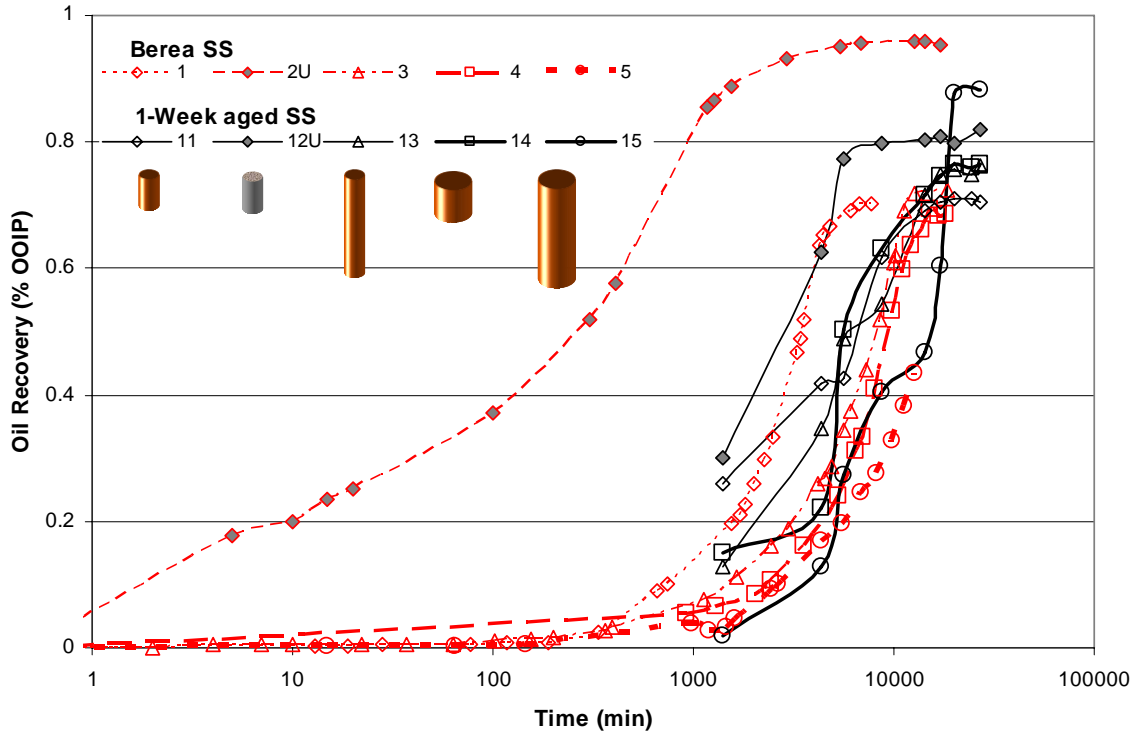


Figure 5.2 Primary diffusion experiments on Berea sandstone compared with 1-week aged samples. U: Uncoated core.

5.1.2 Unaged vs. aged Berea sandstone samples.

All experiments previously performed on Berea sandstones were repeated for the aged samples. Experiments are plotted in Figs. 5.2 and 5.3 for 1-week aged and 1-month aged samples, respectively.

Expectedly, the uncoated unaged core sample (Exp.1) yielded the fastest and highest recovery. One-week and one-month aged samples (Exps. 12U, 17U) showed very similar trend and their recoveries were both 80% OOIP. Counter-current experiments for all cases resulted in slower recovery.

Except for the largest samples (Exps. 5, 15, 20), all experiments exhibited similar trends and yielded an ultimate recovery of 80% OOIP. 2-inch diameter and 6-inch length samples showed three extreme behaviors. Unaged sample (Exp. 5) yielded the lowest recovery, which was around 45% OOIP whereas 1-week aged sample (Exp. 15) marginally had the highest recovery. 1-month aged sample (Exp. 15) was in between these two (around 60% OOIP recovery).

Observations from diffusion experiments indicate that aging has certain effects on primary diffusion process. 1-week aged and 1-month aged samples showed no difference in oil recovery, whereas the recovery from unaged samples was superior. The Berea sandstone and Indiana limestone samples represent significantly different pore structures. It was observed that diffusion process has some significant response to aging (Berea sandstone cases). Hence, the higher recovery from limestone samples could be attributed to stronger dispersive flow caused by pore characteristics where flow paths are wider.

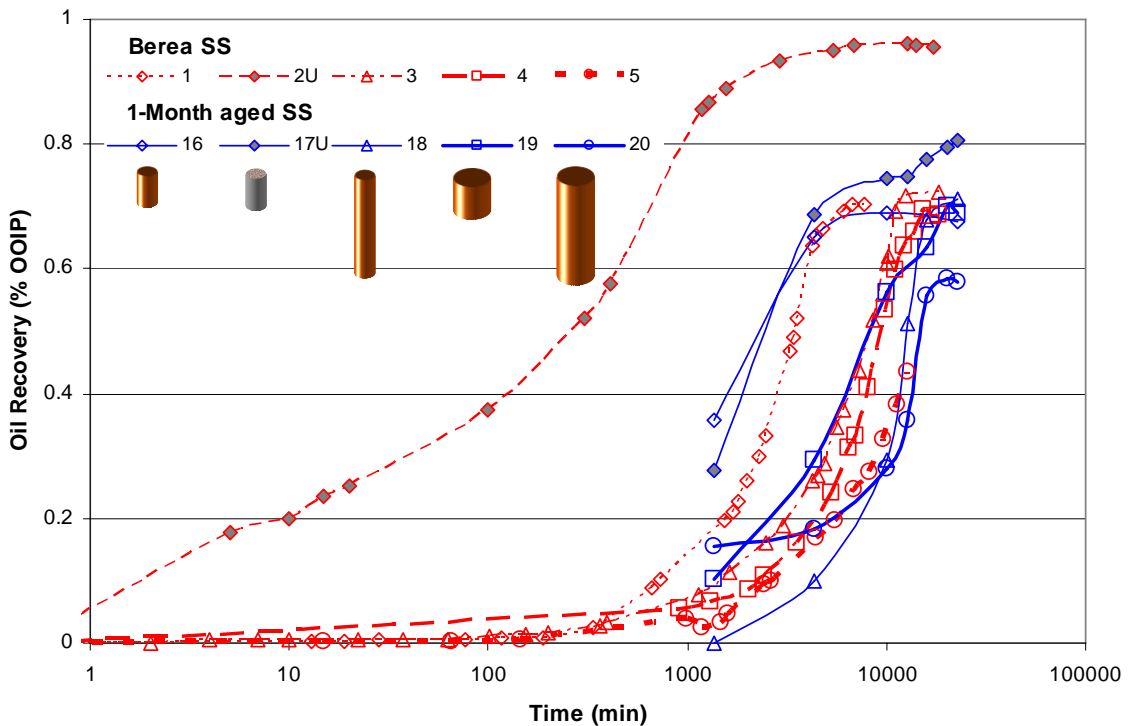


Figure 5.3 Primary diffusion experiments on Berea sandstone compared with 1-month aged samples. U: Uncoated core

5.2 Secondary diffusion

In order to simulate a water-flooding case which is common for oil reservoirs, Capillary imbibition experiments are performed first. After then, solvent is used for additional recovery (“secondary diffusion”). These experiments were analyzed in detail in section 4.2.1. A brief summary of the imbibition performance is included as reminder.

Indiana Limestone vs. Berea Sandstone. The recovery curves obtained from the oil-brine imbibition experiments are given in **Figs. 5.4, 5.5** and **5.6**. They include all different combinations of diameter and length and orientation given in Table 1. The longest samples resulted in the slowest recovery rate (Fig. 5.4). Gravity was involved as a suppressing factor since water imbibing into sample in upward direction is heavier than the oleic phase. Recoveries ranged between 45% and 55% OOIP. An optimum core size was observed in terms of the recovery rate. The 1” diameter cores, with 0.5 and 1” length, yielded the fastest recovery.

Average recovery is around 30% with the uncoated (Exp.27U) and largest core (Exp.30) sample giving the lowest recovery. For the rest of the cases, the shorter cores resulted in slightly faster recovery, but the ultimate recoveries are typically around 30%.

Unaged vs. Aged Berea Samples. Consistent trend was observed among the aged samples. The main difference is that the plots shifts to right as aging time becomes longer (Figs. 5.5 and 5.6). Wettability alteration lowered the recovery time. Although it affects the recovery rate process, it is observed that the ultimate recoveries were not influenced by aging.

For the 1-week aged samples (Fig. 5.5), the recovery decelerated as the cores became larger, uncoated sample (Exp. 32U) yielding the fastest recovery. Slightly higher ultimate recovery was observed for the smallest sample (Exp. 31) which was also the fastest among the group.

The slowest recovery among the aged samples was obtained from the 1-month aged samples as expected (Fig. 5.6). In comparison to the unaged cases of Berea sandstone, 1-month aged samples had less ultimate recovery. Similar shape cores had similar ultimate recoveries for the imbibition only. The only exception is the largest size cores, where 1-month aged sample (Exp.40) delivered 35% recovery far less than the unaged sample (Exp. 25, 45% recovery).

Interestingly, 1-month aged small diameter sample (Exp. 36) had higher recovery than its unaged counterpart (Exp.21).

Secondary diffusion is expected to recover additional oil. As the solvent phase is not soluble in the water, distribution of the oil and imbibed water in the rock would play a crucial role on the recovery from pre-waterflooded samples. This section summarizes performance assessments for different type of rocks when solvent is used as a secondary recovery agent.

5.2.1 Indiana limestone vs. Berea sandstone

After spontaneous imbibition of the samples is completed, we proceeded with secondary diffusion. Using this method, an average 10% OOIP incremental recovery was obtained from the limestone samples. Even strongly water-wet unaged Berea sandstone samples responded to the process remarkably. Especially small diameter cores (Exps. 21 and 23), where imbibition process was not very successful, resulted in 15 to 20% OOIP additional recovery. The uncoated Berea sample gave 5% OOIP additional recovery, and large diameter samples (Exps. 24 and 25) produced less.

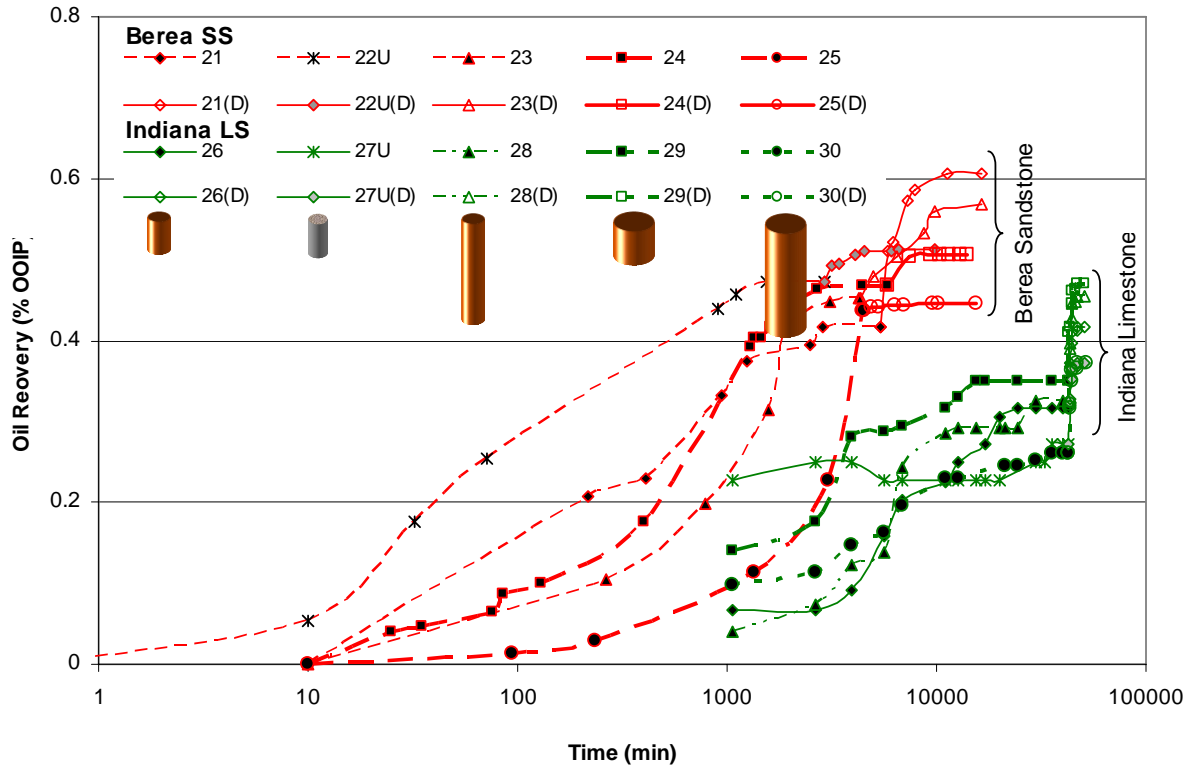


Figure 5.4 Primary imbibition followed by secondary diffusion experiments on Indiana limestone and Berea sandstone samples. U: Uncoated core D: Diffusion after imbibition experiment.

5.2.2 Unaged vs. aged Berea sandstone samples

Figs. 5.4 and 5.5 group the aged samples and display them comparing to the unaged ones. Uncoated 1-week aged Berea sample (Exp. 32U) had the highest recovery (18%). Except this case, additional recoveries range between 5% and 10% for the 1-week aged samples.

1-month aged sample had less recovery compared to unaged and 1-week aged samples. It took almost the same time for the aged samples to reach the plateau region compared to the unaged samples.

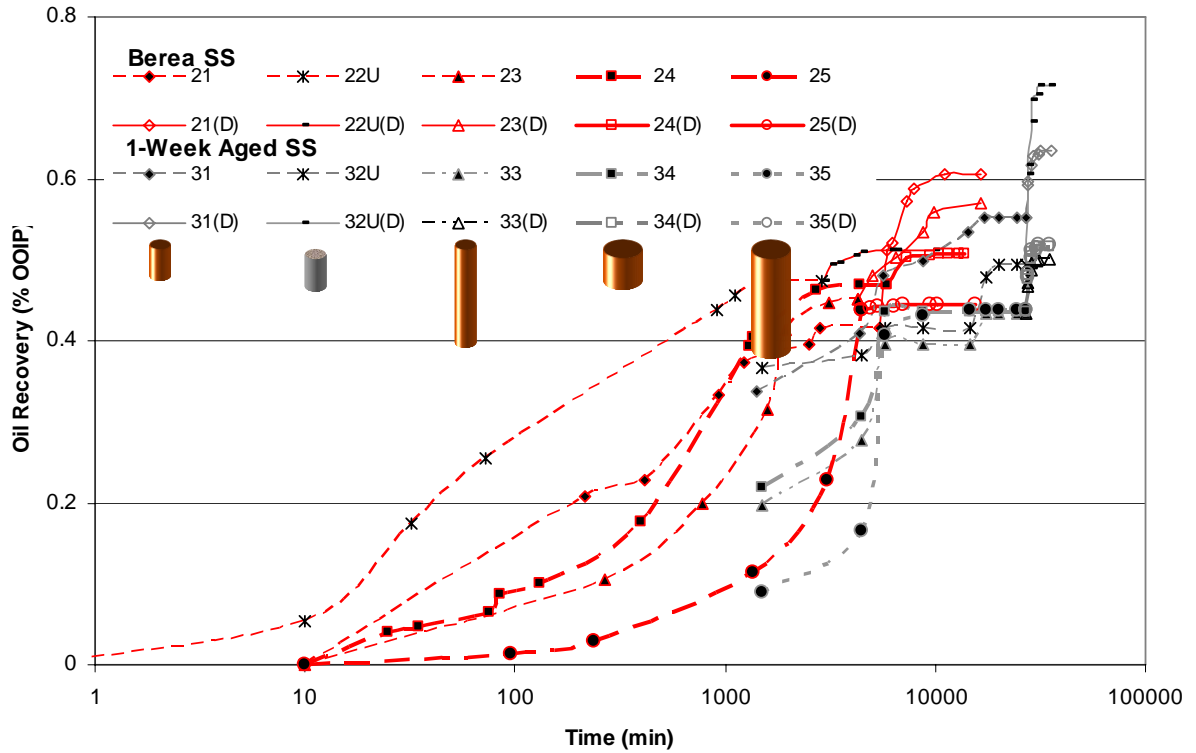


Figure 5.5 Primary imbibition followed by secondary diffusion experiments on Berea sandstone compared with 1-week aged samples. U: Uncoated core D: Diffusion after imbibition experiment.

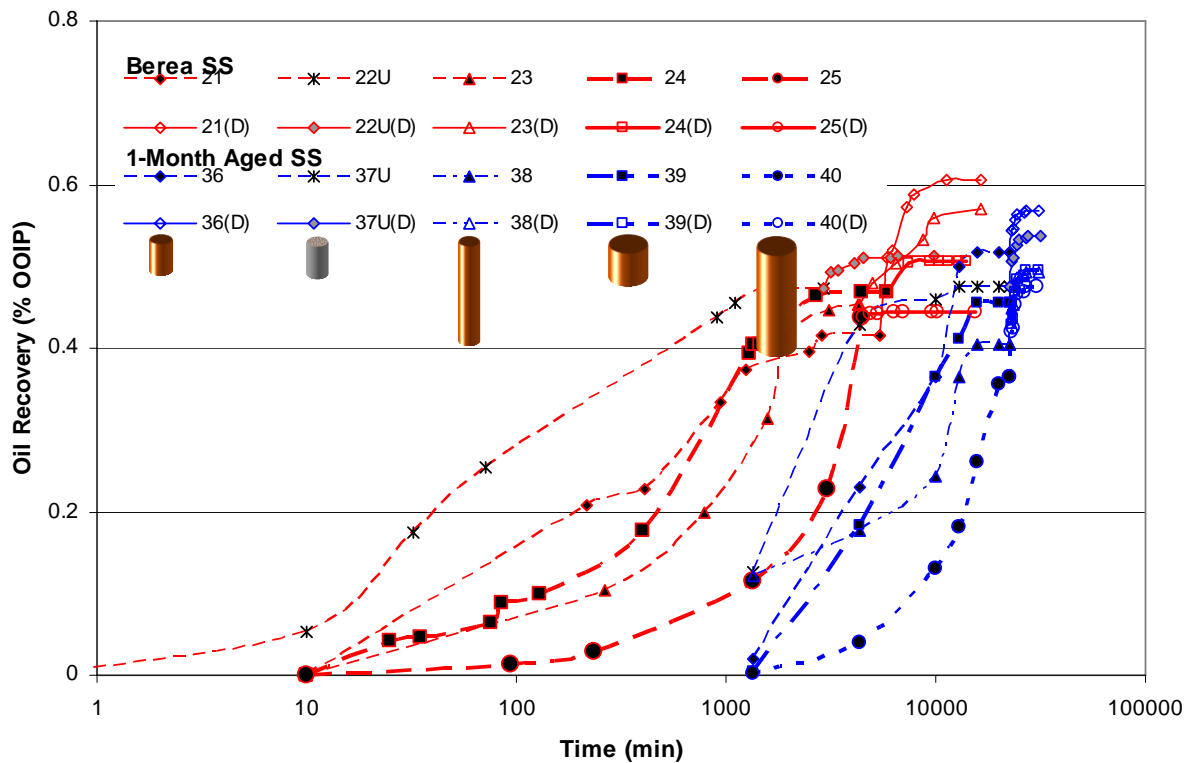


Figure 5.6 Primary imbibition followed by secondary diffusion experiments on Berea sandstone compared with 1-month aged samples. U: Uncoated core D: Diffusion after imbibition experiment.

5.2.3 Residual oil saturation

For two different processes, namely primary diffusion and primary imbibition+secondary diffusion, two separate plots were generated (Figs. 8 and 9). First, the residual oil values were plotted against Length to Diameter ratio (L/D) values for the primary diffusion cases. The red line represents the unaged Berea samples and is the reference case. No significant variation with the shape factor (L/D) was observed and the residual oil saturation was around 30% OOIP regardless the value of L/D . Uncoated sample of the same rock was able to sweep 95% of OOIP.

For the diffusion processes, aging was observed not to be critical, and the boundary conditions and gravity effect became more dominant, which was not the case for the limestone case in Fig. 5.7. Ignoring the smallest core sample (Exp. 6), the limestone gave the best recovery from the primary diffusion. This may be attributed to the different pore structure of the limestone where a more heterogeneous network with high porous channels promotes diffusion.

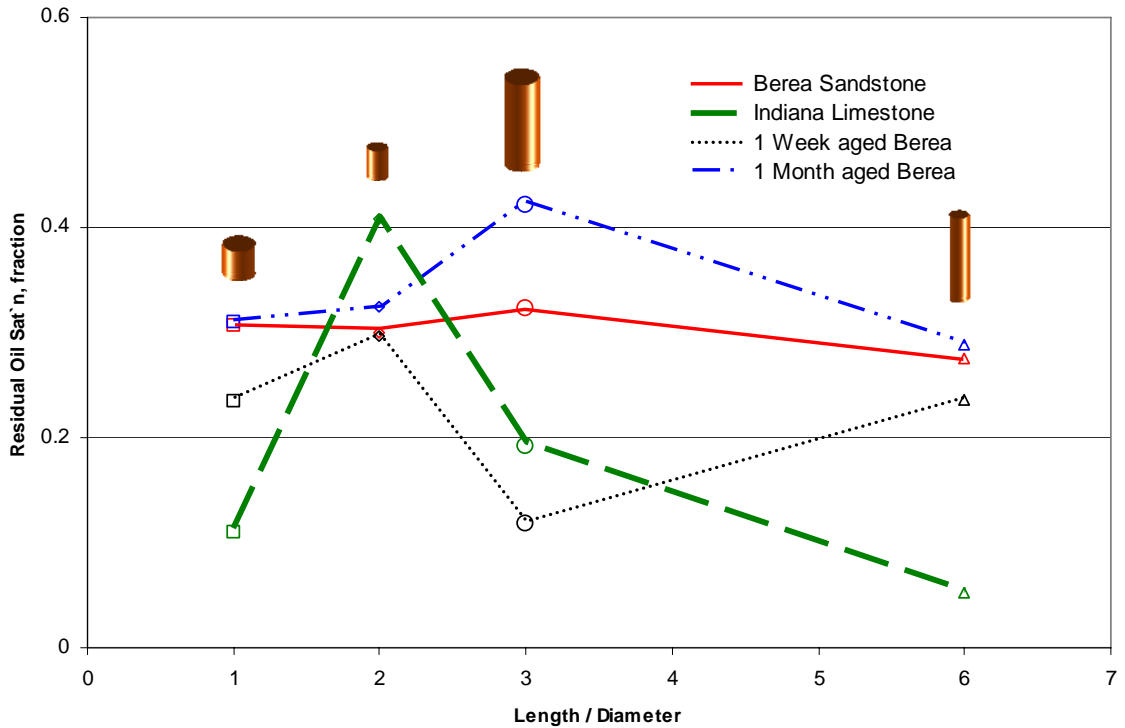


Figure 5.7 Change in SOR from primary diffusion experiments for different rocks and wettabilities.

Starting the recovery with capillary imbibition changes the picture dramatically (Fig. 5.8). The limestone recovery becomes the weakest case if we start the process with capillary imbibition. Previously imbibed water in the channels prevents the solvent to proceed further into the rock, and cause bottlenecks and inaccessible pores due to wettability (limestone is expected to be weakly-water wet) and pore space (limestone has more irregular and vugular pore structure than sandstone) characteristics.

Combining two different techniques results in a more consistent behavior for the sandstone cores. Whether aged or not, the Berea samples produced 50% of OOIP. Optimal matrix shape was observed as $L/D=2$ which corresponds to the smallest core size.

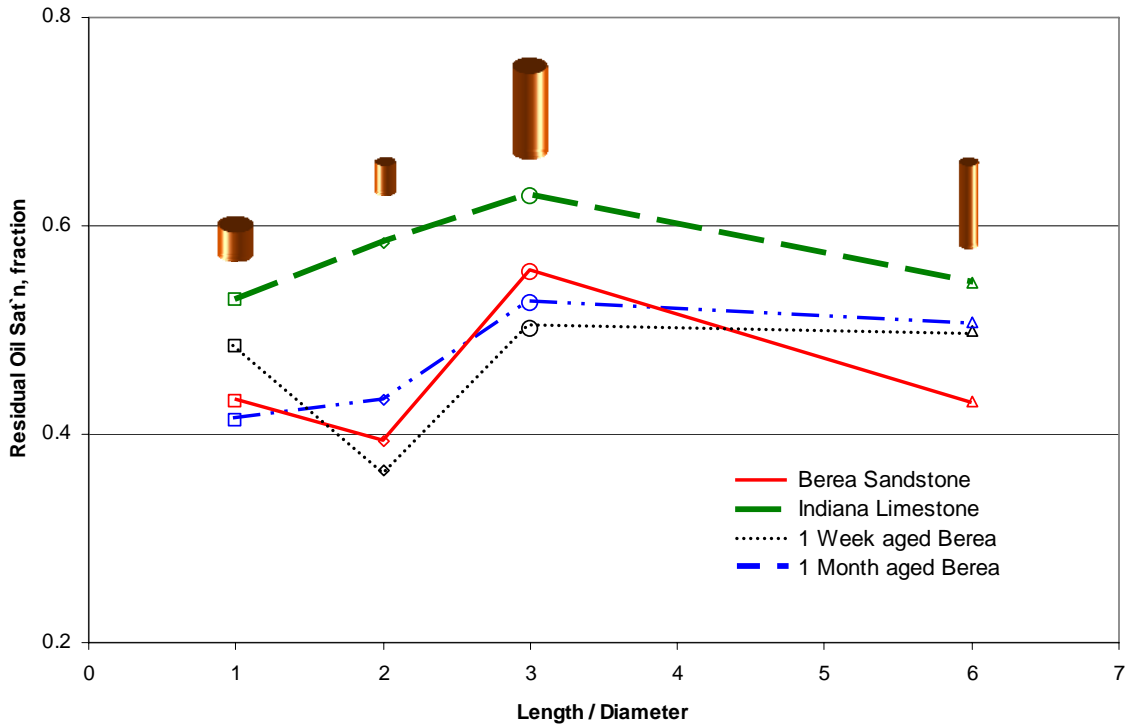


Figure 5.8 Change in the residual oil saturation from primary imbibition + secondary diffusion experiments for different rocks and wettabilities.

Finally, total recoveries by primary diffusion and primary imbibition followed by secondary diffusion are compared (Fig 5.9). Fig. 5.9-a shows the ultimate recovery for all cases. To indicate the efficiency, the ultimate recoveries were divided by the time required to complete the process (Fig. 5.9-b). As seen, -primary- diffusion is more effective for all cases, regardless of the wettability or core shape. For the limestone samples the difference is more apparent.

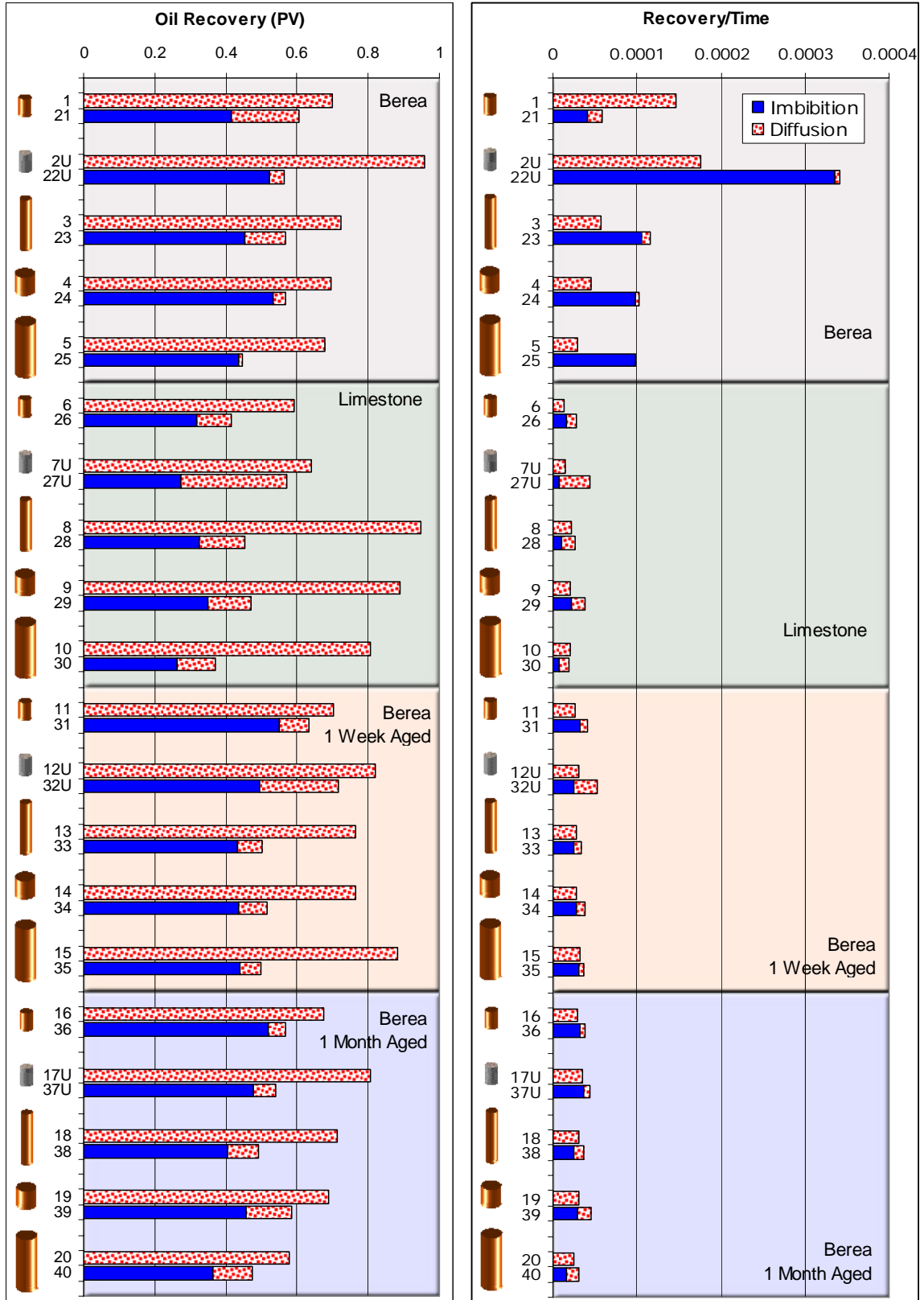


Figure 5.9 Comparison of (a) the recoveries and (b) recovery efficiencies for two processes (time: time required to reach ultimate recovery).

Although the diffusive process is more efficient in terms of ultimate recovery, the time factor should always be taken into consideration. When the ultimate recoveries are divided by the duration of the process, the primary imbibition followed by secondary diffusion becomes more feasible (Fig.5.9-b). For the unaged samples, primary diffusion is not an efficient recovery technique compared to the imbibition even though it results in higher ultimate recovery. As the wettability changes, imbibition process becomes less effective and pure diffusion should be considered. Although the limestone samples with heterogeneous pore structures generally favour primary imbibition followed by secondary diffusion (Exps. 26, 27U, 29), there are also some examples (Exps. 28, 30) that deserve a chance to start the process with diffusion.

5.2.4 Comparison to the crude oil experiments

Few sandstone samples were saturated with crude oil and experiments were repeated (**Fig. 5.10**). For each set of experiments, one uncoated and one coated sample were tested. In coordination with the previous experiments (**Fig. 5.11**), primary diffusion from uncoated sample (Exp. 2UC) gave the best recovery at 95% OOIP. Also in accordance with the mineral oil samples, the coated sample (Exp. 4C) had an ultimate recovery of 70% OOIP, which is the average value we obtained from the mineral oil saturated Berea sandstone samples.

In case of primary imbibition, crude oil saturated samples are expected to produce better than mineral oil saturated counterparts due to lower viscosity. The results show that this is true for the uncoated sample (Exp. 22UC). 70% OOIP recovery of crude oil versus 50% OOIP mineral oil from the same type of rock indicates significant difference whereas the same does not apply for the coated sample (Exp. 24C). The ultimate recovery is around 50% OOIP, which is the same as mineral oil saturated sample. This indicates that the boundary effect is dominant over fluid properties for the counter-current type interaction.

Secondary diffusion from the crude oil saturated samples is around 5% OOIP regardless of the boundary conditions. Although the same ultimate recoveries were observed from the coated and uncoated samples, the recovery rates differ remarkably. Uncoated sample (Exp. 22UC(D)) had faster recovery compared to the coated one (Exp. 24C(D)).

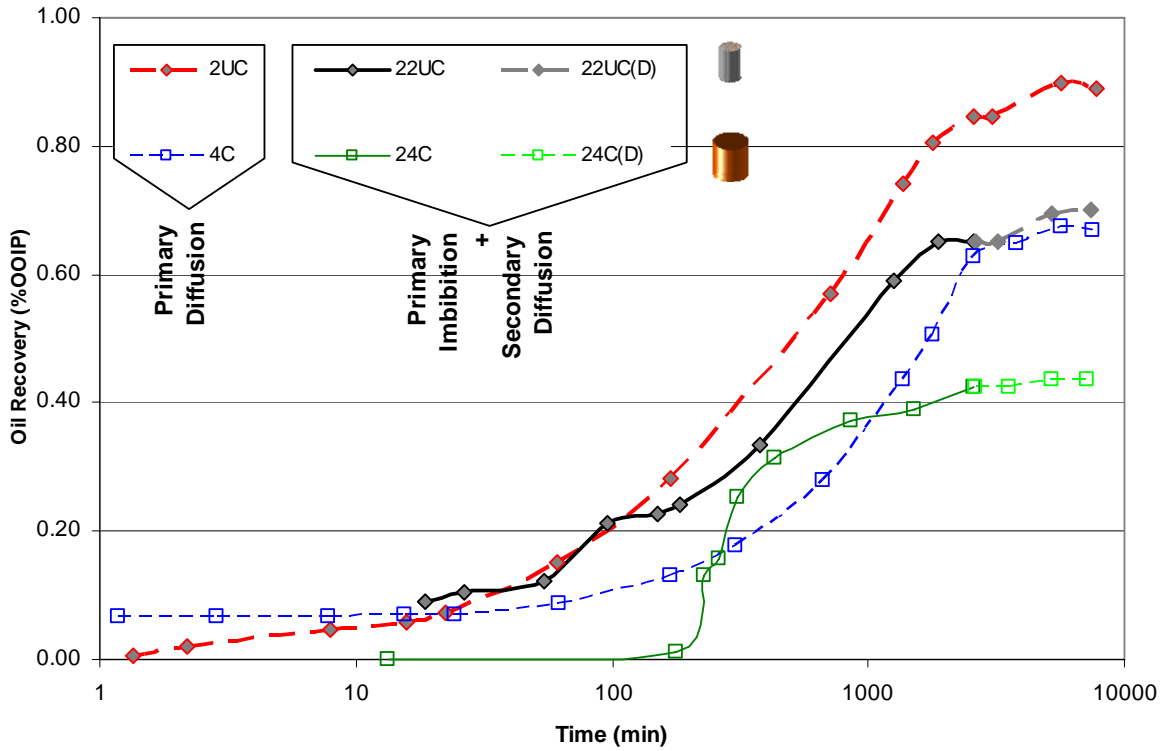


Figure 5.10 Two methods applied to Berea sandstone saturated with crude oil. U: Uncoated core C: Core saturated with crude oil D: Diffusion after imbibition experiment.

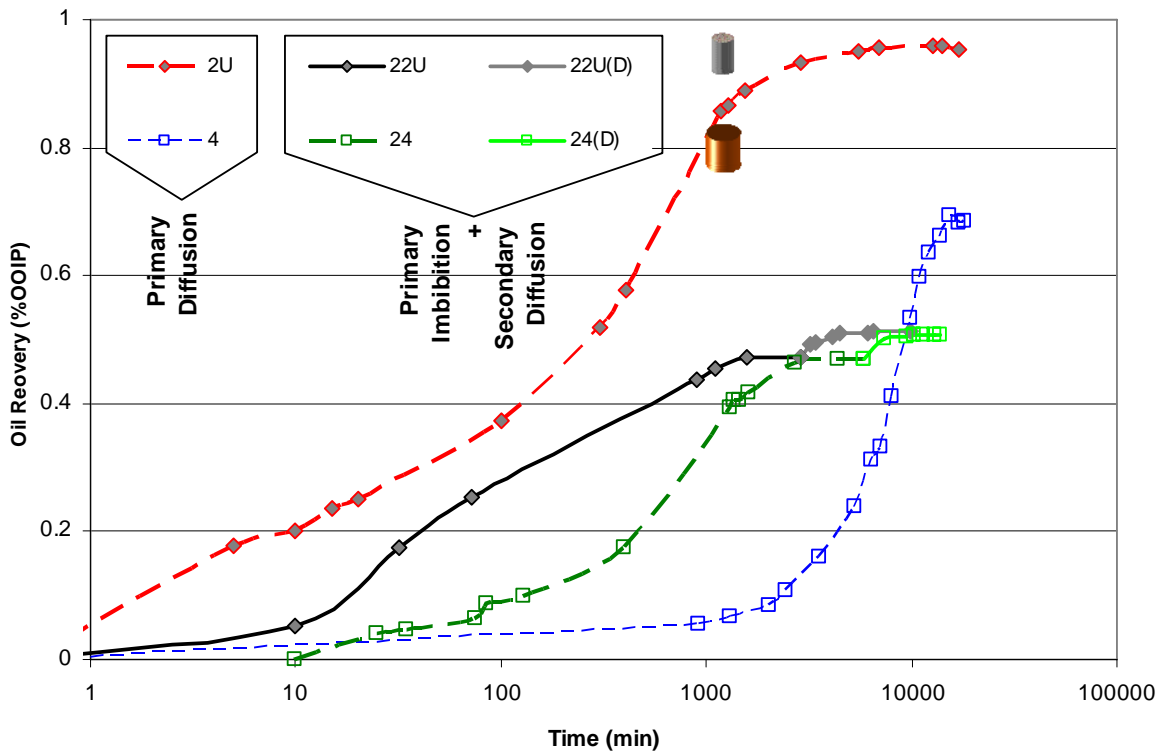


Figure 5.11 Mineral oil saturated counterparts for Fig.11. U: Uncoated core D: Diffusion after imbibition experiment.

5.2.5 Observations

Two different mechanisms were tested on two different porous media. Boundary conditions were created by coating all the surfaces of the rock except one to allow transfer in counter-current fashion. When the cores were exposed to recovery by diffusion only under fully static conditions, it was observed that for each type of rock, uncoated samples gave the fastest recovery. This was a sign of miscible dispersive flow within the core due to density difference between the original oil and oil mixed with lighter solvent. Introducing close boundaries (all sides close to flow except one) changes the transfer dynamics and limestone experiments yielded higher recovery than that of Berea sandstone for coated samples that yielded counter-current interaction. Unlike the sandstone samples with granular texture, limestone samples display vuggy structure that creates heterogeneity. Apparently, this type of architecture favored dispersive flow yielding a faster recovery and higher ultimate recovery for counter-current (coated samples) interaction in the limestone cases.

To clarify the effect of wettability on the process, wettability altered Berea samples were tested. The aged Berea samples showed similar trends as well as similar ultimate recoveries. Primary diffusion experiments indicate that miscible process was not affected by aging significantly. Then the recovery difference between limestone and sandstone samples was attributed to different pore structures; relatively larger pore channels and vugular structure of the limestone favors counter-current diffusion process.

Second mechanism tested for the same set of rocks is the primary imbibition followed by secondary diffusion. The process was started as spontaneous imbibition. Wettability effect for this type of process is expected to be dominating. Regardless of the core shape, the limestone samples resulted in poorer recovery both in terms of the final amount recovered and the rate of recovery. Berea sandstone and Indiana limestone samples represent different pore structures and wettability characteristics. To distinguish the effect of wettability and pore characteristics on the process, aged Berea samples were tested. Wettability alteration caused the rate of recovery to be slower, yet no significant difference in ultimate recoveries was observed. This indicates that the wettability effect is critical on the recovery rate and pore structure is dominant over ultimate recovery for counter-current capillary imbibition interaction. This process simulates waterflooding. After this step, solvent injection as a

secondary recovery method was tested. This is typically what is encountered in the field as a tertiary recovery process. In this case, there is more water in the system than oil and the solubility of hydrocarbon solvents in water is very low unlike other types of solvents like CO₂ and N₂. Hence, the distribution of water phase in the medium which is controlled by wettability and pore size/structure is critical on the additional oil recovery by miscible processes. Regardless the rock type and wettability, additional recovery by solvent was possible indicating that the residual oil after imbibition recovery was accessible to solvent. But the amount of additional recovery strictly depends on matrix boundary condition that causes co- or counter-current type interaction (Fig. 5.9).

Secondary diffusion resulted in significant amount of additional oil recovery from limestone samples indicating that the oil filled pores still has connection with the open-end of the core sample. Pore level investigation of this process for granular (sandstone) and vuggy-heterogeneous (limestone) structures are needed.

When the residual oil was plotted against length to diameter ratio (L/D), it was observed that the unaged base case showed no correlation. The aged Berea samples produced almost same amount of oil for any shape factor. Yet the largest samples show perversions from the linear trend. It also was observed that the limestone had generally the best recoveries regardless of the core shape.

The primary imbibition followed by secondary diffusion tests responded in different ways for the two rocks samples. The limestone cases showed much lower imbibition recovery than that of Berea sandstone. The amount of imbibed water in the limestone sample eventually caused having a weakly-wetting phase (water) in the pore channels that reduced the rate of diffusion. For the most efficient recovery from limestone, strategy should be to start with diffusion right from the beginning. For an effective and efficient recovery from the sandstone samples, diffusion yielded considerable incremental oil recovery for only the aged samples.

6 Glass-bead models




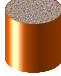




The aim of this chapter is to investigate the dynamics of the interaction between matrix and fracture visually for a miscible or immiscible displacement. Data obtained from this section will vastly be qualitative and useful to unravel the quantitative data obtained from the core experiments in previous chapters.

2D glass-bead packed transparent models, and the details about its characteristics are explained in Chapter 3. Boundary conditions are created by applying sealant on the edges of the model (3-sides-sealed for counter-current, 2-sides-sealed for co-current). The models are saturated with the desired oleic phase (kerosene or mineral oil) and immersed into the displacing phase (water for immiscible interaction, pentane for miscible interaction). Experiments are performed under static conditions where the displacing phase level in the container is kept constant using a micro-pump. Observations are captured using time-lapse photography.

6.1 *Imbibition experiments*

Aim for the experiments was to understand the dynamics of interaction between matrix and fracture. Gas-liquid and liquid-liquid interactions are studied in an agenda similar to core experiments. Table 6.1 lists the experimental program for this section.

Table 9 Immiscible experiment identification according to core shape and fluid type.

Visual Model	Corresponding core shape		L	D	Heat		Viscosity		Wettability
					Air - Water (25C)	Air - Water (90C)	M.Oil - Water	Kerosene - Water	M.Oil - Water
		counter - current Vertical	2	2	aV1	aV2	OV1	OV2	OWV1
		co-current Vertical	2	2	aV3	aV4	OV3n OV3t	OV4n OV4t	OWV3
		counter - current Horizontal	2	2			OV5	OV6	
		counter - current Vertical	2	1	aV7	aV8			
		counter - current Vertical	1	2					

6.1.1 Air-water

Air-water experiments were conducted for vertical position only because of the difficulty in visualizing the horizontally situated model experiments at higher temperatures. Both three-sides-sealed (counter-current) and two-sides-sealed (co-current) models were used. For the counter-current sample, the only open edge was oriented to face down and immersed into water and progress was recorded using time-lapse photography. Similar was applied to the co-current model, but the top edge was not in contact with the wetting phase.

6.1.1.1 Counter-current interaction

The low temperature and counter-current imbibition case is given in **Fig. 6.1**. The observations from the visual experiments indicate that fluid front shows a bullet profile. No randomness i.e., fingering at the front was observed.

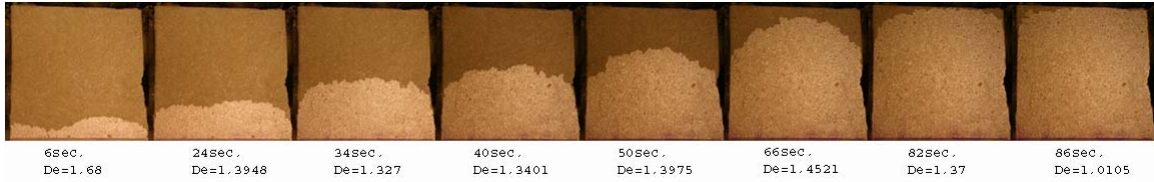


Figure 6.1 Experiment aV1: Counter-current, vertical orientation, air-water pair at 20 °C.

When the temperature increased to 90°C, displacement front (**Fig. 6.2**) shows different characteristics. The front loses its stability as indicated by more fingering compared to the low temperature case. The increase in temperature resulted in more residual saturation development behind the front. The pattern for this case (Fig. 6.2) is a reminiscent of an invasion percolation type displacement.

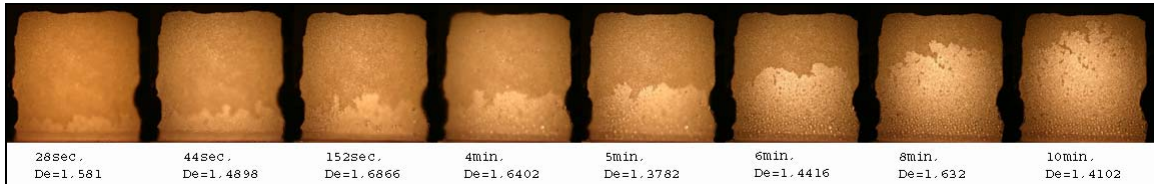


Figure 6.2 Experiment aV2: Counter-current, vertical orientation, air-water pair at 90 oC.

6.1.1.2 Co-current interaction

For the co-current model (only two-sides-sealed as in **Fig. 3. 3b**), the gas phase does not have to exit from the same edge that the liquid phase enters as the open port is open to flow. Easier water invasion translates into finger development for the co-current cases (**Fig. 6.3** and **6.4**).

Although the same type of frontal displacement and fingering were observed for both low and high temperature cases (Figs. 6.3 and 6.4) The process is faster for the high temperature case but more residual gas saturation was left behind the front.

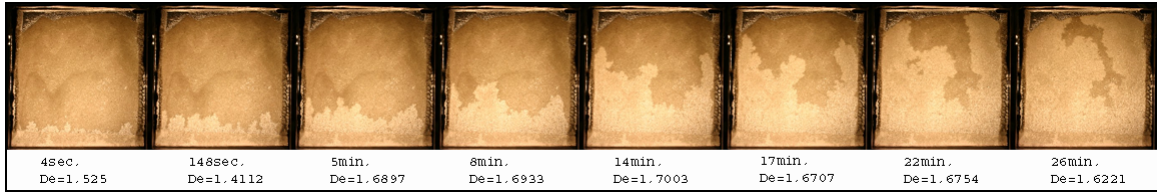


Figure 6.3 Experiment aV3: Co-current, vertical orientation, air-water pair at 20 °C.

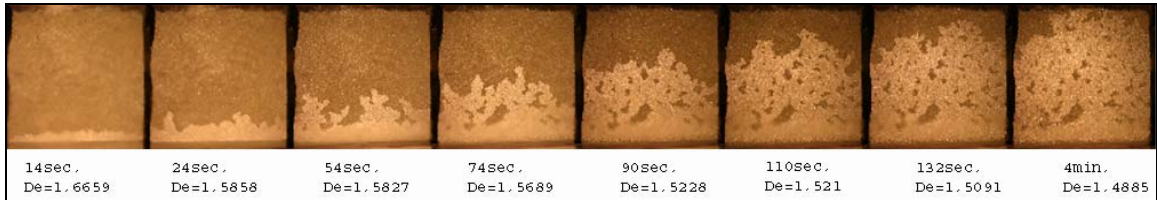


Figure 6.4 Experiment aV4: Co-current, vertical orientation, air-water pair at 90 °C.

For the high-temperature case (Fig 6.4), a similar fingering behaviour to the low temperature cases is observed. The residual gas saturation behind the front, however, drastically increases (Fig 6.4). The former is in disagreement and the latter is in full agreement with the counter-current equivalents given in Figs. 6.1 and 6.2.

6.1.1.3 Matrix shape

Experiments were conducted to observe the effect of matrix size and shape by changing width and length (aspect ratios). These experiments were to obtain qualitative data only for comparison and core representatives were not provided. Since we observed that the top-boundary has a significant effect on displacement, we conducted the experiments in counter-current manner. Four models with three-sides-sealed were prepared. Two of them have 2:1 and the other two have 1:2 aspect ratio (Table 6.1).

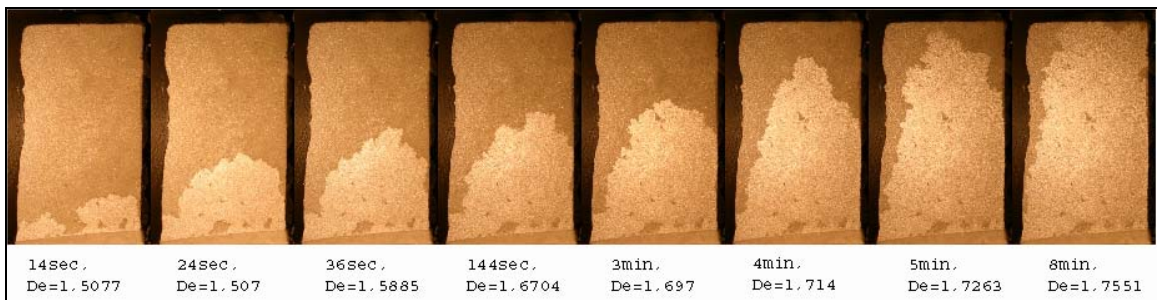


Figure 6.5 Counter-current, 2:1 aspect ratio model, vertical orientation, air-water pair at 20 °C.

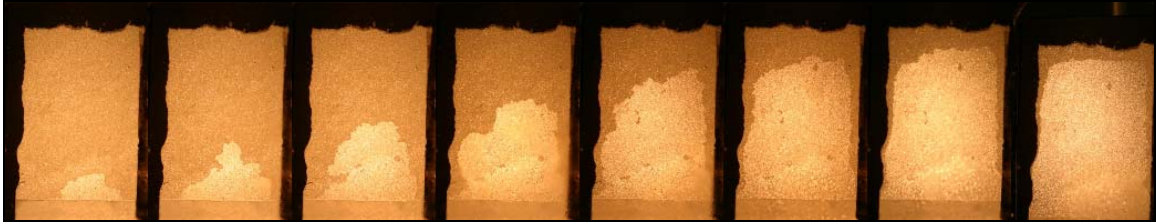


Figure 6.6 Experiment aV8: Counter-current, 2:1 aspect ratio, vertical orientation, air-water pair at 90 °C.

For the low-temperature 2:1 experiment (Fig. 6.5), a bullet shaped front was observed and the unswept region around the corners of the sample was still obvious as in the square shape model case (Figs. 6.1 and 6.2). Similar to experiment aV1, as the fluid front reached the top boundary, it started progressing laterally. More frontal sweep for the 1:2 aspect ratio model was observed (Fig. 6.7). The front shape is no longer “bullet type” and therefore, no unswept regions around the top corners were observed.

High-temperature experiments showed a similar behavior to the 1:1 aspect ratio case (Fig. 6.2). The process is faster compared to the low-temperature cases (aV7, aV9) as seen in Figs. 6.6 and 6.7. For both 2:1 and 1:2 aspect ratio models, a frontal displacement was observed. Sweep in the 1:2 aspect ratio cases are better compared to the 2:1 cases and no unswept region was observed around the top corners of the sample.

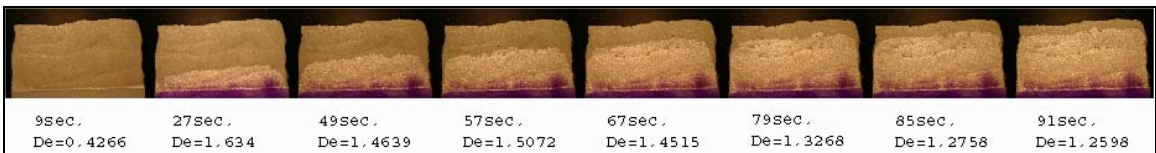


Figure 6.7 Experiment aV9: Counter-current, 1:2 aspect ratio, vertical orientation, air-water pair at 90 °C.

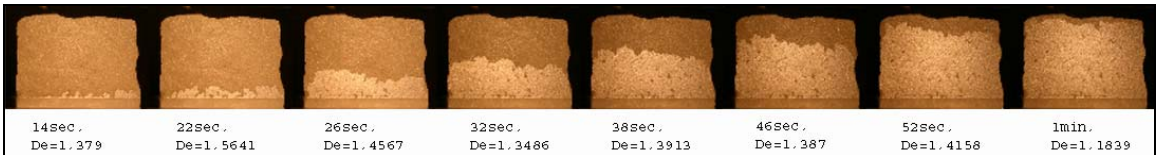


Figure 6.8 Experiment aV10: Counter-current, 1:2 aspect ratio, vertical orientation, air-water pair at 90 °C.

6.1.2 Oil-water experiments

It is expected that the dynamics of the spontaneous imbibition of liquid-liquid and gas-liquid pairs would be different as expressed in the literature. Oil-water experiments were conducted to clarify these differences emerging mainly from lower viscosity ratio and less favorable wettability in the oil-water case. A few experiments were also included to observe the matrix shape effect.

In addition to counter-current interaction, co-current oil-water experiments were studied in detail by conducting both one-side open to atmosphere, and top and bottom sides in contact with water. It was also possible to visualize experiments conducted on horizontal orientation that led us to assess the effect of gravity.

6.1.2.1 Counter-current interaction

Similar to air-water experiments, for counter-current interaction, three-sides-sealed models were prepared first. The models were saturated 100% with the oleic phase (kerosene or mineral oil). Then, the samples were immersed into water to start the capillary imbibition process. For counter-current experiments (**Figs. 6.9** and **6.10**) boundary effects were not felt since fluid front progressed in a bulk fashion regardless the type of the oleic phase for a while. Once the front reached the top part of the model, gravity starts to dominate displacing the oil downward. Less viscous kerosene was displaced faster than the mineral oil as inferred both from the visual observations and core experiments.

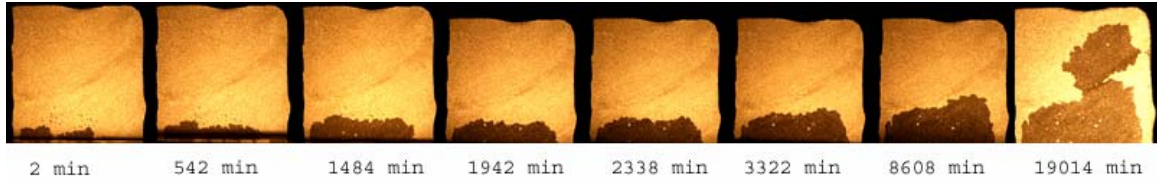


Figure 6.9 Experiment OV1: Counter-current, vertical orientation, mineral oil-water pair.

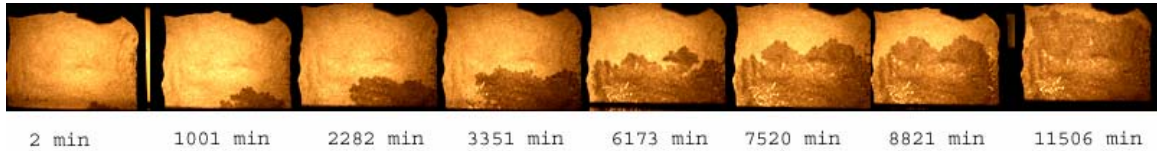


Figure 6.10 Experiment OV2: Counter-current, vertical orientation, kerosene-water pair.

The experiments were also conducted for horizontal orientation (Figs. 6.11 and 6.12) to account for the gravity effect that was critically effective in the vertical experiments. In this case a random displacement was observed (Figs. 6.11 and 6.12) as opposed to the vertical cases that exhibited more stable-frontal progress. The kerosene case (Fig. 6.12) sweep was inefficient initially, where fingers did not expand but proceed almost linearly until they reach the top boundary. It is very interesting that the imbibition started at a point and grew from this point (see the snapshot for the kerosene after 24 minutes) for both mineral oil and kerosene case. The process started from a point and the displacement was achieved by the growth of this “single finger” (Fig. 6.11) which is thicker in the mineral oil case compared to the kerosene counterpart. All other (vertical) cases, however, showed a trend of frontal progress which was identified by a uniform and frontal progress of the invading wetting phase

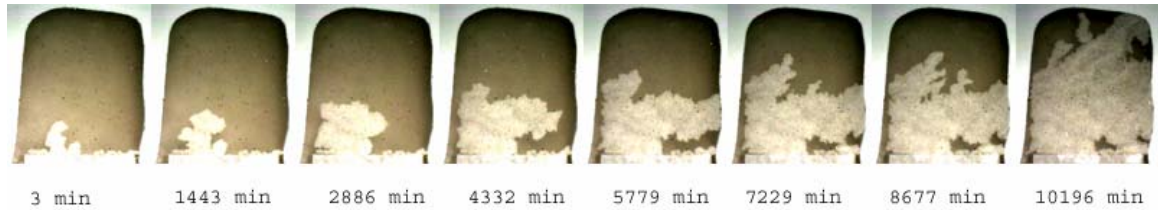


Figure 6.11 Experiment OV5: Counter-current, horizontal orientation, mineral oil-water pair.

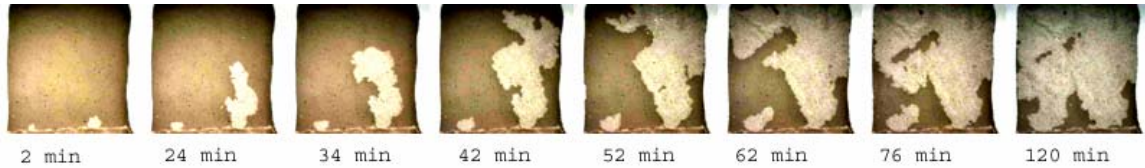


Figure 6.12 Experiment OV6: Counter-current, horizontal orientation, kerosene-water pair.

6.1.2.2 Co-current interaction

To have a better understanding of gravity effect, samples with two edges (top and bottom) contacting with water were also constructed. Co-current oil-water experiments are conducted in two different ways for each fluid pair. As similar to air-water experiments, the top edge is left open to atmosphere. These experiments are shown in **Figs. 6.13** and **Fig. 6.14** for mineral oil and kerosene, respectively.

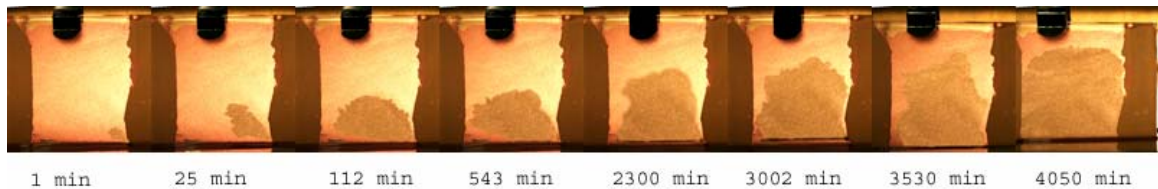


Figure 6.13 Experiment OV3-n : Co-current, vertical orientation, mineral oil-water pair.

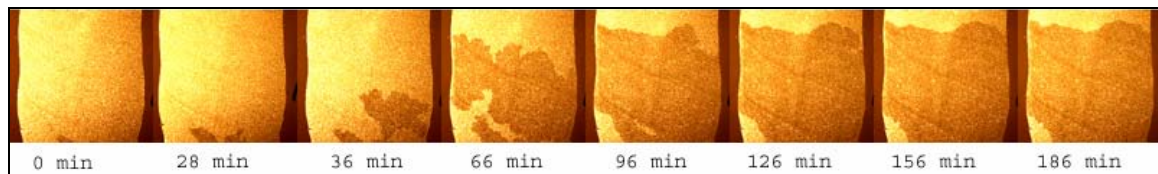


Figure 6.14 Experiment OV4-n : Co-current, vertical orientation, kerosene-water pair.

For the models with only bottom edges open to interaction, similar behaviour to their counter-current counterparts were observed. Mineral oil in case of co-current interaction (Fig 6.13) shows a frontal progress whereas the kerosene case (Fig. 6.14) represents a more random displacement front initially and it turns out to be frontal after while (66min case in Fig. 6.14) as similar to its counter-current counterpart. The upward movement of the

wetting phase, acting against gravity caused by the open top boundary, was faster for the kerosene case due to low viscosity ratio and this yielded more fingering. This was not the case for mineral oil. The imbibition process was so slow that the gravity suppressed the movement of the wetting phase inside the model and this resulted in much “smoother” and a more uniform displacement front. Note also that the process times were incomparably different in favor of kerosene.

To represent another common case that might be encountered in subsurface reservoirs, samples contacting water through both top and bottom edges were also constructed (Fig. 6.15 - 6.16). One can see a massive -viscous- fingering caused by gravity for the mineral oil case (Fig. 6.15). As the fluid front reaches down the bottom of the model, fingers start expanding horizontally.

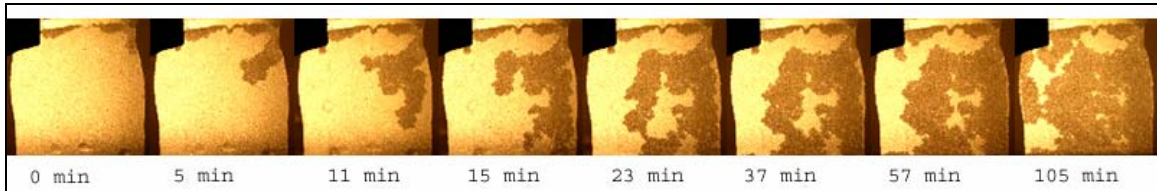


Figure 6.15 Experiment OV3-t : Co-current, vertical orientation, mineral oil-water pair.

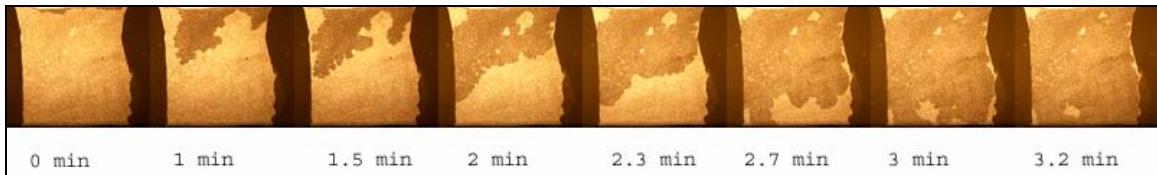


Figure 6.16 Experiment OV4-t : Co-current, vertical orientation, kerosene-water pair.

Both cases presented a steady period in early times where no interaction had occurred even though both sides were open to flow. Obviously, counteracting forces such as water head from top and capillarity forcing water in to the model from bottom and top parts were in balance in the beginning. Then the gravity and capillary forces acted on the top portion overcame and water entered into matrix from this side. Progress was in the downward direction mainly dominated by gravity. Note that no capillary interaction at the bottom of the sample was observed at all throughout the experiments for both cases.

6.1.2.3 Matrix shape

Two additional experiments were conducted to observe the effect of matrix shape. In parallel to the air-water cases, 2:1 and 1:2 aspect ratio models were prepared, and saturated with 100% mineral oil. Core representatives of these samples were not tested and the study was limited for only qualitative analysis. From the 2:1 aspect ratio model (**Fig. 6.17**) we observed that the process initially started as similar to the standard 1:1 ratio case (Fig. 6.9). Since the width of the sample was smaller compared to the length, which creates a highly unfavorable boundary condition, interaction edge started to cause bottlenecks within the system. In order to prove this theory, an experiment with 1:2 aspect ratio model was conducted (**Fig. 6.18**). Frontal progress was observed to be in good agreement with the standard 1:1 model. The very last shots of both cases taken at 18,621 minutes show approximately 50% and 20% areal sweep for the 1:2 and 2:1 cases, respectively. No bottlenecks were observed caused by water blocking the oil paths for 1:2 aspect ratio case given in Fig. 6.18 and the rate of recovery is very close to that of the standard model. Note that both models given in Figs. 6.17 and 18 have the same area and contain the same amount of non-wetting phase.

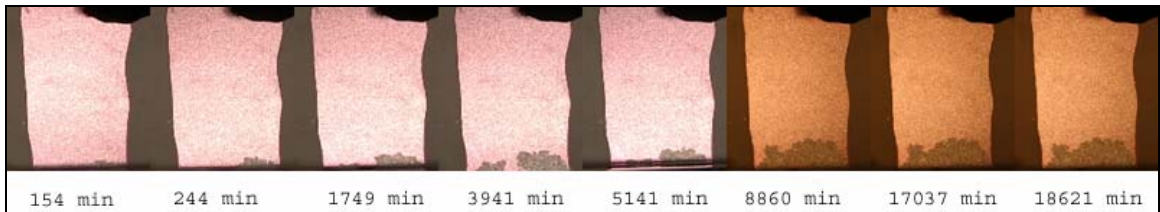


Figure 6.17 Experiment OV7: Counter-current, 2:1 aspect ratio, vertical orientation, mineral oil-water pair.

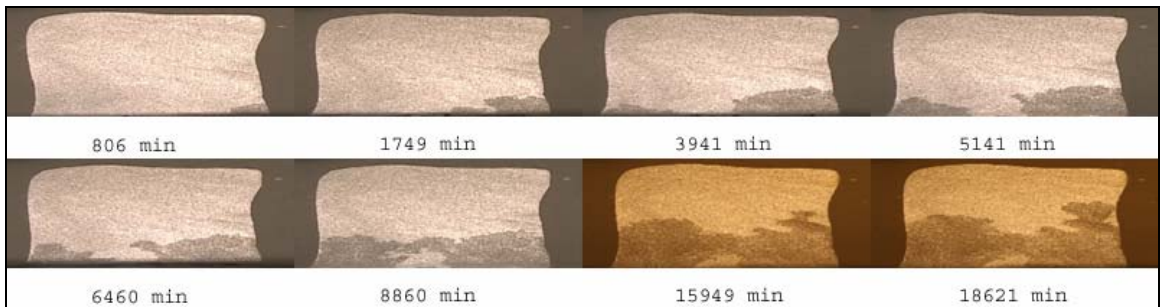


Figure 6.18 Experiment OV8: Counter-current, 1:2 aspect ratio, vertical orientation, mineral oil-water pair.

6.1.2.4 Aged samples

To change the wettability of the glass-beads to more oil wet, the models were kept in the oil phase after the saturation. Our previous experience had shown that this wettability alteration process works with mineral oil even though it is not as effective as with the crude oil which has strong polar groups. We were bound to transparent oil for the visualization experiments.

Water was observed to enter into matrix from a single point rather than a uniform frontal invasion as similar to the horizontal cases. Water invasion grew from a single point and progressed linearly for the counter-current case (**Fig. 6.19**). In a similar manner, the co-current case, with both sides in contact with water, also showed a similar “single point invasion” (this time starting from the top) behavior but with a thicker “single finger” (**Fig. 6.20**).

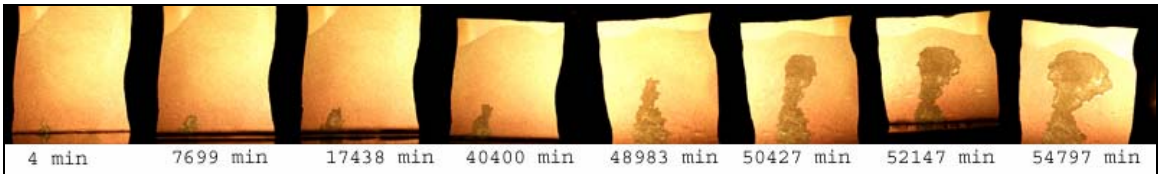


Figure 6.19 Experiment OWV1: Counter-current, vertical orientation, mineral oil-water pair, aged sample.

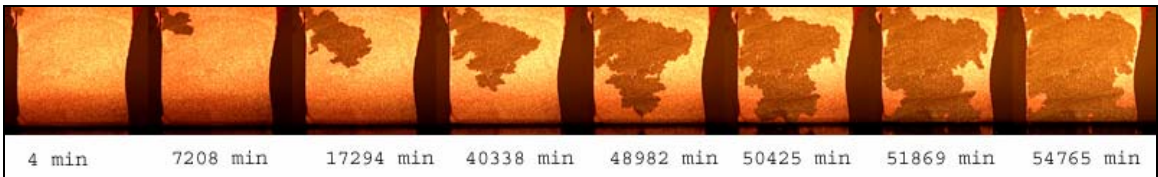


Figure 6.20 Experiment OWV3: Co-current, vertical orientation, mineral oil-water pair, aged samples.

6.2 Diffusion-dispersion experiments (miscible process)

The type of the displacement patterns and the progress of fronts as well as the residual oil saturation were the main concerns in the qualitative analysis. The fractal dimensions of the displacement fronts were obtained for the quantitative analysis. In addition to the fractal analysis of the whole front, a small portion of the front was extracted and a fractal analysis was performed on those parts as well for the horizontal direction experiments. The fractal

analysis was carried out using the program FracLac v2.0aF, a plug-in for ImageJ program. These quantified data were used in later sections for the comparison of the fluid front characteristics between experimental and stochastic model results.

Two different glass bead models were constructed. The first one was a three-sides-sealed model to obtain fully counter-current flow and the second one was two-sides-sealed model that provided a co-current flow. In addition to the horizontal configuration experiments were performed on vertically situated samples to account for the gravity effect as well as in a horizontal configuration. The effect of the viscosity ratio and density on the process was also considered using two different oil types.

6.2.1 Horizontal experiments: Counter-current interaction

For the counter-current models, horizontal orientation showed a steady and frontal displacement in all cases (**Figs 6.21** and **6.22**). Kerosene and mineral oil behaviour was very similar and the small fingers observed in the early stages of the process disappeared at later stages. Viscosity difference translated into experiments as time difference, less viscous kerosene having a faster process. The front progressed in the middle of the model was faster compared to the edges creating a “bullet” shape profile

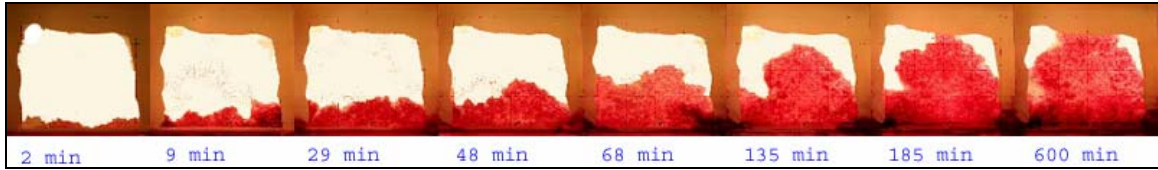


Figure 6.21 Experiment on 2-D glass bead model (white: kerosene, red: solvent (pentane)).

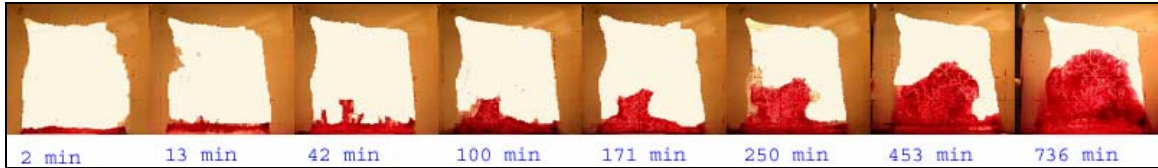


Figure 6.22 Experiment on 2-D glass bead model (white: mineral oil, red: solvent (pentane)).



Figure 6.23 Pattern captured in close-up of Fig. 6.22 at 42 min.

When we zoom in to the front of a pattern, we see DLA type fingers more clearly at smaller (micro) scale. A close-up for the case in 42 min is given in **Fig. 6.23**. This was the motivation for using DLA modeling of the experiments as will be discussed in Chapter 9.

6.2.2 Vertical experiments: Counter-current interaction

When the gravity becomes effective, more complex patterns were observed. Buoyancy drive caused a dispersion dominated miscible process to occur. The kerosene displayed a fast process caused by low resistance to flow due to low viscosity. Thinner fingers were observed in the kerosene experiments causing earlier arrival of the front at the top boundary (**Fig. 6.24**). Difference in viscosity is reflected as longer process times for the mineral oil case (**Fig 6.25**). Fingers were developed through the sides of the models due to less resistance to flow caused by the “inner” pressure distribution. After the arrival of the front

to the top boundary, a “convective” displacement due to the density difference between the distinguishable “phases”, i.e., original oil and oil mixed with pentane, began to dominate.

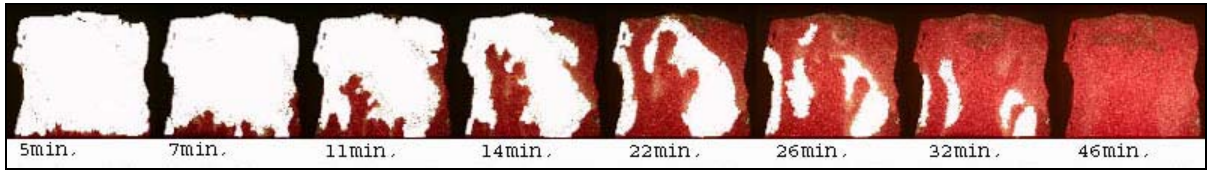


Figure 6.24 Experiment on 2-D glass bead model (white: kerosene, red: solvent (pentane)).



Figure 6.25 Experiment on 2-D glass bead model (white: mineral oil, red: solvent (pentane)).

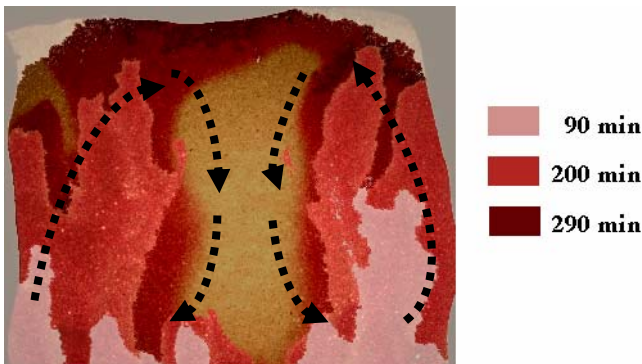


Figure 6.26 Convective behaviour observed in vertical oriented experiments.

The buoyant convection followed a path depicted in **Figure 6.26**. The fluid fronts tend to progress close to the boundaries where less resistance exists compared to the center (in 90 min). Once the front reached the top of the model (in 200 min), the un-swept oil in the middle portion was displaced predominantly by the “buoyant convection” where displacement develops through the sides of the sample and goes downward from the inner part as indicated by arrows. In other words, the convection took place from the outer sides of the model and as the lighter phase accumulates on top of the model it pushes the unmixed heavier oil down following a circular motion. That is an interesting characteristic of the diffusion phenomenon and it was more prominent for the lighter oil case (kerosene).

6.2.3 Vertical experiments: Co-current

The co-current models have one edge open to atmosphere which alters the “inner” pressure distribution in the model. This change in boundaries and thus the “inner” pressure distribution caused radical differences on the displacement patterns compared to the counter-current model.

The kerosene-pentane mixing showed a similar convection type displacement but with more distinctive fingered patterns (**Fig 6.27**). Open top edge causes a more tolerant behaviour in terms of oil back flow. This translates as higher intrusion rate for pentane phase and thus faster oil recovery. This yielded a faster convective displacement compared to the counter-current equivalent of the case.

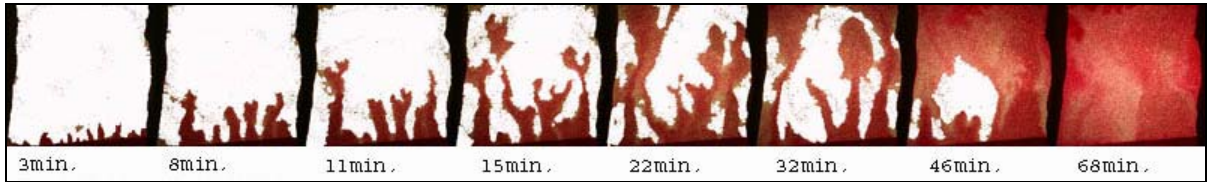


Figure 6.27 Experiment on 2-D glass bead model (white: kerosene, red: solvent (pentane)).

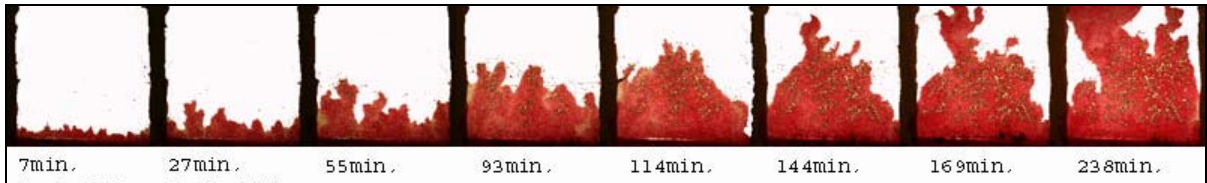


Figure 6.28 Experiment on 2-D glass bead model (white: mineral oil, red: solvent (pentane)).

The experiments done with the mineral oil showed a bullet shaped fluid front progressing centered along the model (**Fig. 6.28**) without any significant fingering. Once the lighter front reached the top of the model, accumulation as in counter-current cases is observed and convective displacement process started.

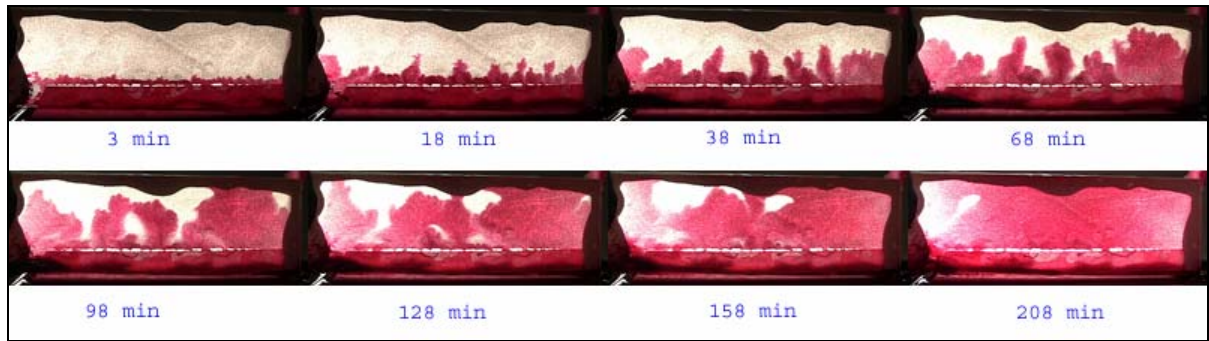


Figure 6.29 Experiment on 2-D glass bead model (2:1 aspect ratio, white: mineral oil, red: solvent (pentane)).

In all the cases above, a square shape model where the boundary conditions, i.e., edges close to flow, were highly in effect. To minimize this effect the shape and the dimensions of the model was altered slightly. **Fig. 6.29** shows the counter-current diffusion process on a rectangular shape model for mineral oil. In first 68 minutes fingers developed as similar to the square equivalent of this case (Fig. 6.25). Finger development through the sides was less compared to the square shape model but at later stages, the convective transport was also observed.

6.2.4 Quantitative analysis on finger development

Finally, in an effort to compare the samples, a finger displacement versus time plot is given (**Fig 6.30**). The slope of this plot would give the speed of the finger growth. Since most of the figures consisted two fingers that grow through each side of the model, both fingers are plotted. Two groupings are observed looking at the finger speeds. Different viscosity fluids are grouped as kerosene or mineral oil. Constant speed for fingers in kerosene is measured to be 0.127m/sec where for the higher viscosity mineral oil sample, velocity drops to 0.011m/sec. Boundary conditions are not observed to affect the finger speed.

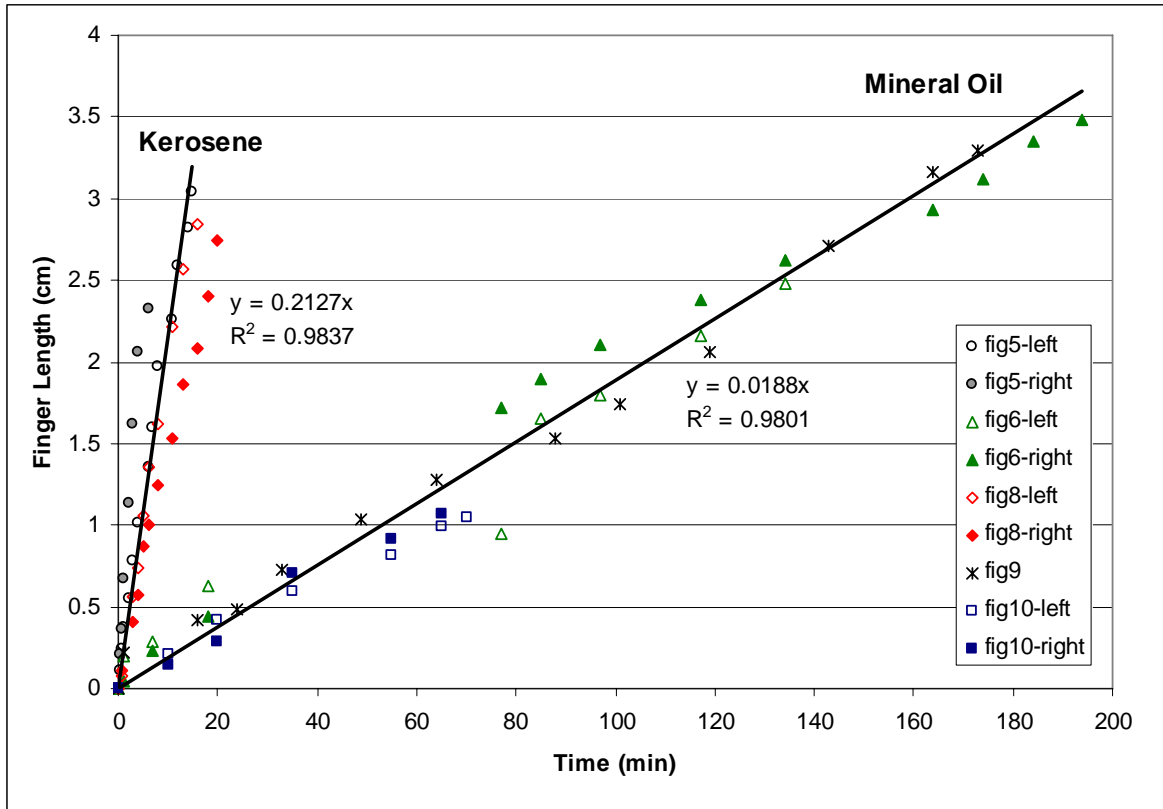


Figure 6.30 Displacement vs. time plot of observed fingers.

7 Silicon etched micro-models

Capillary imbibition process is highly sensitive to pore structure, i.e., size and distribution. To clarify this effect and observe the process at pore level, micro-models were used. Silicon etched micro-models provide high repeatability and full control over matrix properties. This aid is especially helpful in computational modelling comparisons as will be explained in Chapter 9.

The first generation micro-models were glass etched using HF. In those models, regular shaped patterns or channels were commonly applied. Though they were far from reflecting the complexity of natural porous media, these models became very useful in serving the importance of micro scale observation of the displacement process. With the advancements in technology, silicon-etching became viable and applicable for micro-model preparation and it was possible to replicate actual rock pore patterns on silicon wafer.

For glass micro-models, the reaction kinetics of acid etching makes it necessary to enlarge the pore sizes of typical sandstone by a factor of 5 to 50 compared to the original size. This turned out to be a limitation in studying processes that depend critically on capillary forces on remarked by Sagar and Castanier [1997].

The main mechanism of acid etching was simply to introduce chemicals to start a very fast erosion process to erode away the unprotected zones and to have the protected zones serve

as grains. This reaction also erodes the walls of grains and would introduce a degree of surface roughness to the pore walls.

The micro-models used in this study were manufactured at Stanford University, Department of Energy Resources Engineering, SUPRI-A group.

7.1 Model preparation

The silicon-etched micro-models do not bring acid into play, but uses UV rays to introduce erosion to silicon wafers. With this advancement, it is now possible to create accurate patterns on walls from original images with close to perfect 90 degree walls. These high resolution silicon micro-models offer 1:1 scaling of Berea sandstone pores and throats. Details on the preparation are given in Section 3.2.2 and are also summarized in Table 7.1.

Table 10 Micro-model properties.

	Pentane
Porosity	35%
Permeability	1 md
Pore Sizes	1-150 μ m
Throats	0.5-10 μ m
Etch Depth	15 to 35 μ m
Fracture width	2000 μ m

The construction involves four major steps. (Fig 7.1)

1. Deposit
2. Patterning
3. Etching
4. Glass to glass bonding

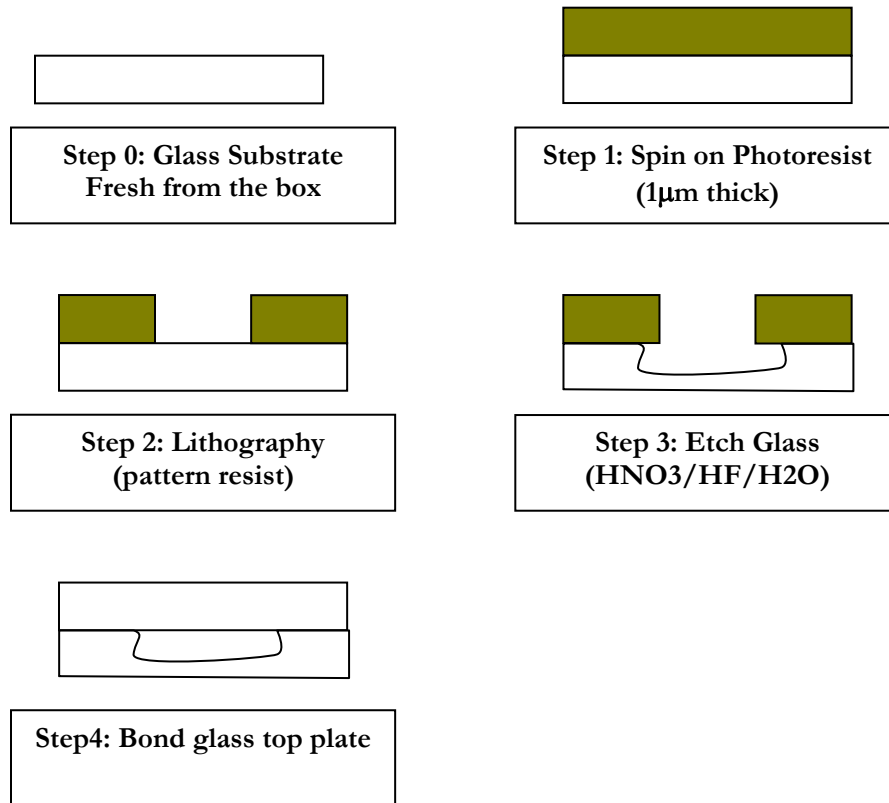


Figure 7.1 Glass etching process.

Figure 7.1 shows the basic steps (or the theory) of the process. Far from being ideal, the substrates, even fresh from the box could not attain the necessary cleanness level. Hence they have to be cleaned of particles, organic films, finger prints etc. In addition to this, Photoresist would be quickly attacked by a HNO₃ based etchant because of material science incompatibility. Photoresist would not stick well to glass and finally glass to glass bonding is tricky. The actual (or practical) process steps are listed as follows:

- 1-Glass substrates come stacked in together fresh from the box (coin rolled)
- 2-Piranha solution is used to remove particles and organic layers (H₂SO₄/H₂O₂ 3:1)
- 3-Gold thin layer is used as mask for HNO₃/HF/H₂O glass etch.
- 4-Spin on Photoresist
- 5-Lithography
- 6-Wet Etch Au and Cr masking layer
- 7-Strip Photoresist

8-Carefully clean glass surfaces

9-Bond glass substrates together

In real life procedure, Piranha solution is used to clean substrates. The solution self heats to 150°C and removes organic layers extremely well. At the 3rd step, gold would not stick onto the glass and therefore, we need to deposit a thin layer of Cr between the glass and Au to have the Au stick onto the glass. For the next step, Photoresist is applied. At the etching step, gold and chromium etches are different, KI/I₂ is used for gold, where HNO₃+additives are used for chromium. Glass surfaces have to be very clean for a successful bond. This is obtained by hand washing and using high pressure washer of distilled water.

Imaging of the model onto the silicon wafer involves the digitization of a rock section into a computer from a high quality photograph. The section, which is approximately 500µm in length, is replicated to fill an area of 5 cm² (**Fig 7.2**). After assuring two dimensional continuity, the image is reproduced on a chrome mask, the grains being opaque and the pores being transparent.

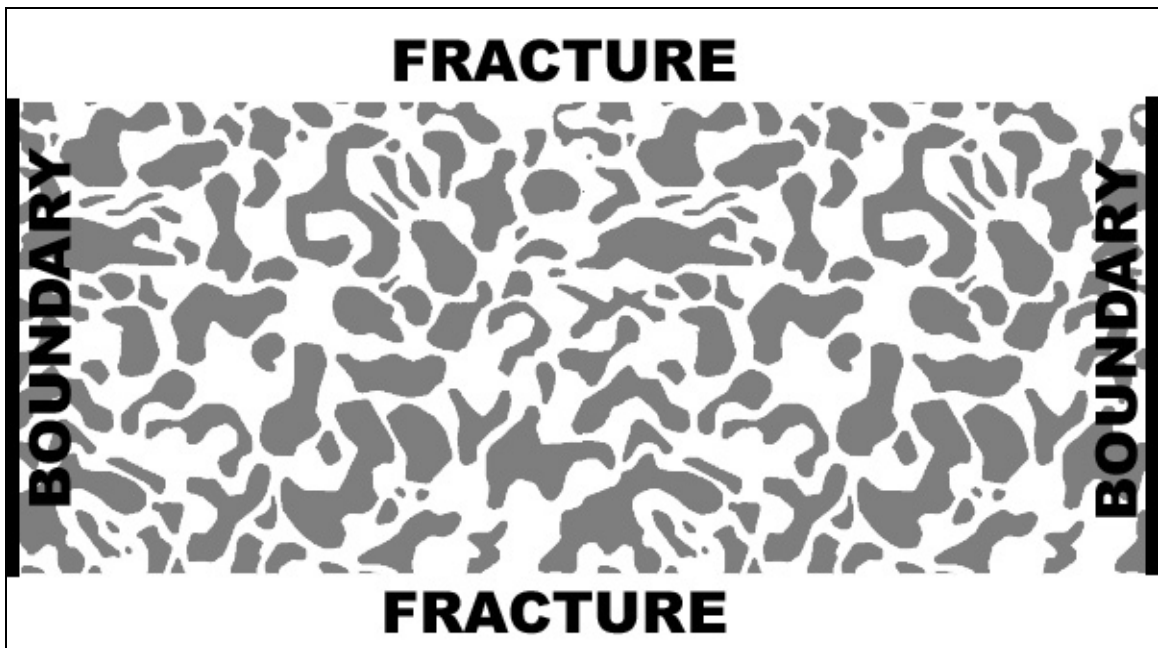


Figure 7.2 Repetitive pattern (2 patterns montaged side by side, fracture and boundaries are not to scale, fracture width: 2000 µm, average pore size: 75 µm)

7.2 Observations

Under the microscope, the progress of the fluid front was captured for the kerosene case (**Fig 7.3**). The same experiment was repeated with mineral oil and water pair (**Fig 7.4**). One can observe a frontal progress and a degree of oil entrapment (residual oil saturation) behind the front. Residual oil was observed to be strictly dependent on the pore and throat size and structure (**Fig 7.5a**). Note that the same experiment was repeated for mineral oil and it showed a very similar structure of residual oil saturation and front progress (**Fig 7.5b**).

The velocity of the displacement front (v) (to cover one repeated pattern length) was measured to be $500\mu\text{m} / 10 \text{ sec}$ for both mineral oil and kerosene. To have an understanding of the fluid properties and porous media implications, dimensionless numbers were calculated (Table 1). For the purpose of evaluating the effect of gravitational effects to capillary forces, the Bond number (B_o) (Dullien, 1992) was calculated as:

$$B_o = g(\rho_w - \rho_o)R / \sigma_{o-w} \quad \dots\dots\dots 20$$

where R denotes the characteristic pore radius; for simplicity this is taken as $75 \mu\text{m}$. Capillary number (C_a) is calculated to investigate the ratio of viscous and capillary forces as:

$$C_a = v * \mu / (\phi * \sigma_{o-w}) \quad \dots\dots\dots 21$$

v denotes the fluid speed, and Φ the porosity. The calculated numbers show that viscous forces are negligible compared to capillary forces for both oil types. The Reynolds number (R_e) would give further information by providing the ratio of inertial and viscous forces:

$$R_e = \rho * v * R / \mu\phi \quad \dots\dots\dots 22$$

Values are very small as expected, these dimensionless quantities confirm that capillary forces dominate the system.

To clarify the effect of pore structure on the process another test was performed using a perfectly uniform model (**Fig 7.6**). This type of models had one port for fluid input and a large reservoir to imitate the fracture between the port and the matrix part. The displacing phase was introduced at a very slow rate to simulate a low capillary number “quasi static”

displacement. The purpose was, once again, to test the effect of pore structure on the development of residual phase saturation. The process was in co-current fashion. The displacement was observed to follow a “perfect” front progressing in a bulk (or piston-like) fashion. No residual saturation was left behind.

Table 11 Fluid pairs used in experiments

	Water	Kerosene	Mineral oil
Density (g/cc)	0.99	0.79	0.83
Viscosity (cp)	1	2.9	36.32
Interfacial tension (dyne/cm) - with water -		46.1	33.2
Bond number -with water -		2.52E-4	2.84E-4
Capillary number		9.0E-6	1.57E-4
Reynolds number		2.92E-3	2.7E-4

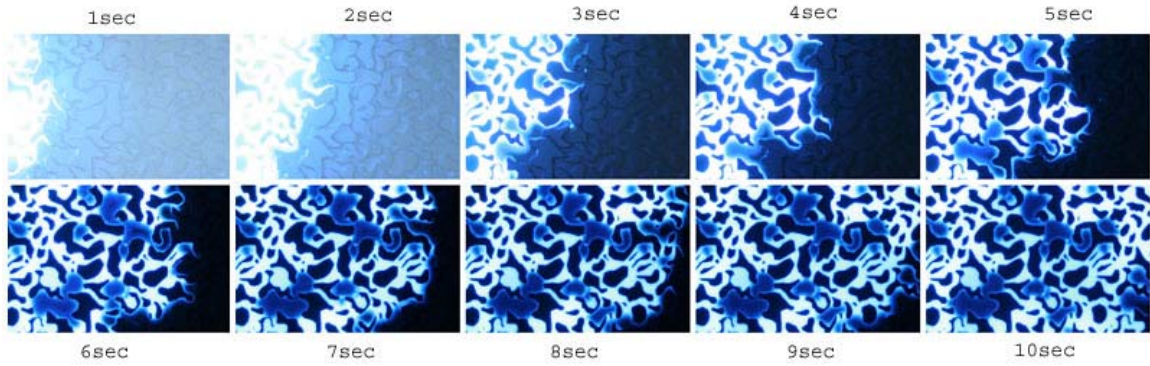


Figure 7.3 Time-lapse visualization of spontaneous imbibition on the micro-model. Water imbibes from left (white color) displacing kerosene (blue color). Each image is 500 μm wide and magnified 20X.

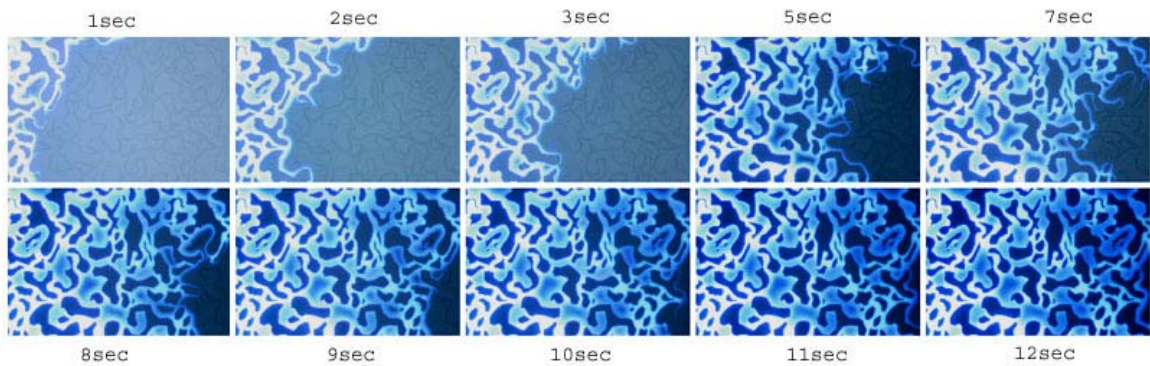


Figure 7.4 Visualization of spontaneous imbibition on the micro-model. Water imbibes from left (white color) displacing mineral oil (blue color). Each image is 500 μm wide and magnified 20X.

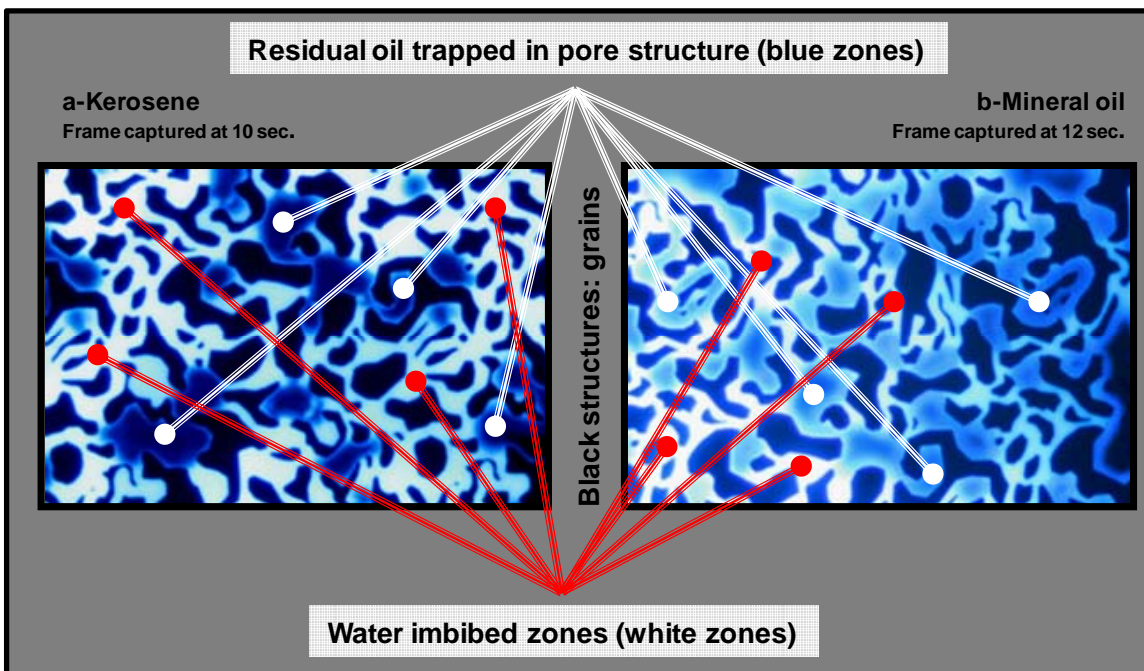


Figure 7.5 Residual oil saturation development for two different oil types. Water imbibes from left (white color) displacing oil phase (blue color). This experiment proves residual oil is directly related to pore structure. Image is 3000 μm wide

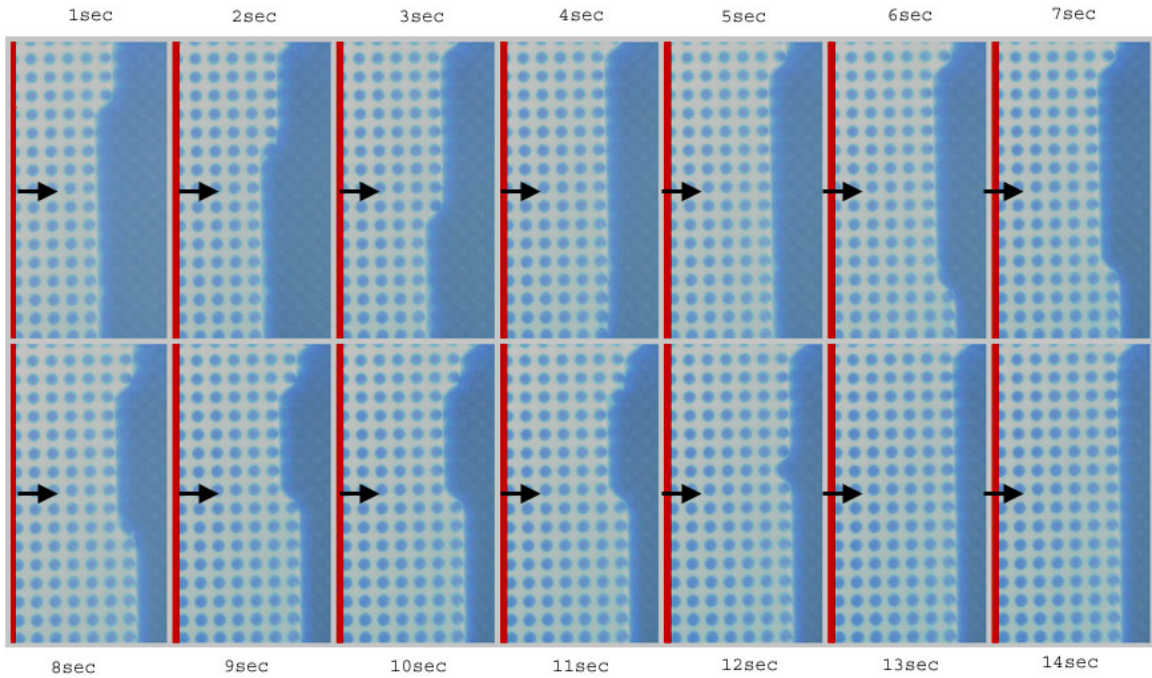


Figure 7.6 Visualization experiment on a micro-model with homogeneous pore structure. The displacing phase (white) is observed to be progressing in a frontal fashion. Fracture is positioned on the left side and imbibition front progress from left to right as indicated by the arrows. Displacement is in co-current manner. Oil is in blue color.




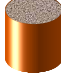




8 Results and interpretations

This section of the thesis consists of the interpretations of the experimental part by cross comparison of the core and 2D visualization experiments. For this effort, 2D visualization experiments equivalent of the core experiments (fluid types, matrix aspect ratios etc.) were performed. The results are presented in a way to demonstrate the relationship/similarities between the recovery curves from core experiments (quantitative data) and the images from 2D sand pack models (qualitative data). The processes are analyzed under two different sections for miscible and immiscible displacement.

8.1 Immiscible displacement between matrix and fracture

Table 8.1 displays the core and 2D sand pack experiments used in the cross-comparison analysis. Visual experiments are named as the same as in Chapter 6, and the core counterparts are named with “C” denoting the core. The visualization experiments were helpful in explaining many uncertainties reflected by the recovery curves obtained from the core experiments.

Table 12 Experiments conducted in this part of study. L: Length, D: Diameter.

Visual Model	Corresponding core shape		L	D	Heat		Viscosity		Wettability
					Air - Water (25C)	Air - Water (90C)	M. Oil - Water	Kerosene - Water	M. Oil - Water
		counter - current Vertical	2	2	aV1 aC1	aV2 aC2	OV1 OC1	OV2 OC2	OWV1 OWC1
		co-current Vertical	2	2	aV3 aC3	aV4 aC4	OV3n OV3t OC3	OV4n OV4t OC4	OWV3 OWC3
		counter - current Horizontal	2	2			OV5 OC5	OV6 OC6	
		counter - current Vertical	2	1	aV7	aV8			
		counter - current Vertical	1	2					

8.1.1 Air-water

Air-water experiments were conducted for vertical position only because of the difficulty in visualizing the horizontally situated model experiments at higher temperatures. Both three-sides-sealed (counter-current) and two-sides-sealed (co-current) models were used. For the counter-current sample, the only open edge was oriented to face down and immersed into water and progress was recorded using time-lapse photography. A similar procedure was applied to the co-current model, but the top edge was not in contact with the wetting phase.

8.1.1.1 Counter-current interaction

As the base case of counter-current imbibition (**Fig. 8.1 a**), the visual experiment (aV1 in **Fig. 8.1 c**) and corresponding core experiment recovery curve (aC1) are given in **Fig. 8.1 b** for low-temperature water (25 °C) – air. The results of high temperature water (90 °C) – air experiments are shown in Figs. 8.1 b and d, respectively. One can see through the snapshots in Fig. 8.1 c that fluid front shows a bullet-shape profile (Fig. 8.1 c), Low temperature case

showed slower recovery supported also by the visual experiment (see the time difference between the low and high temperature experiments in Figs. 8.1 c and d). Although visual models indicate very successful sweep, the core experiments showed low ultimate recovery (around 42% OOIP) for the low temperature case. This could be attributed to much more significant air entrapment in the cores compared to loose sand pack. It is also expected that the difference in the residual air saturation between the two cases is due to unswept region around the top corners of the sample (see the picture at 66second in Fig. 8.1 c)

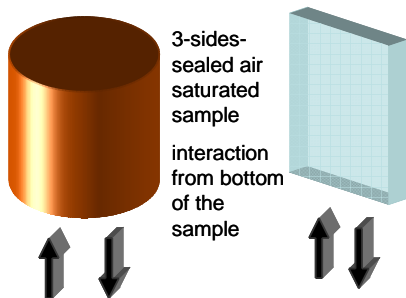


Figure 8.1 a-Model representation

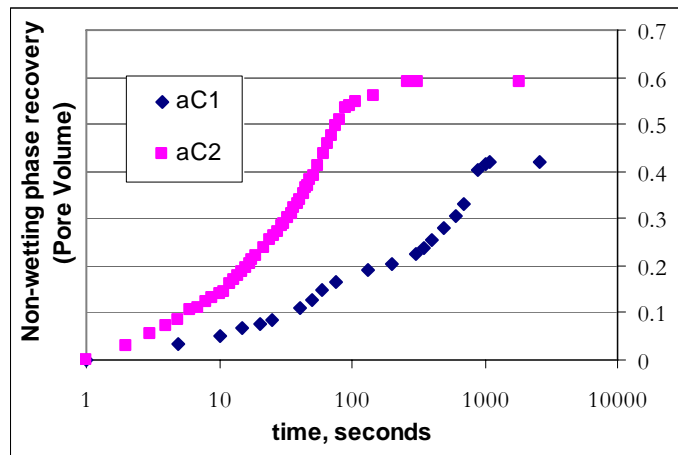


Figure 8.1b-Recovery curves obtained from core experiments

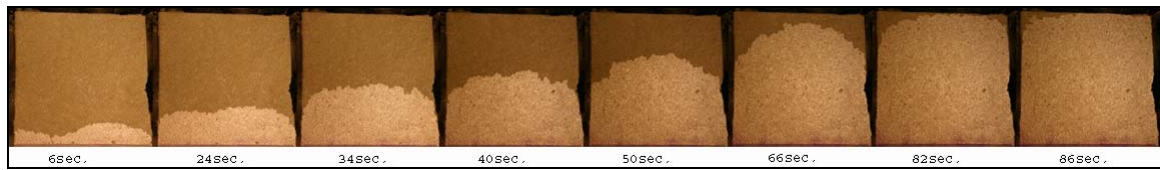


Figure 8.1 c- Experiment aV1: Counter-current, vertical orientation, air-water pair at 20 °C.

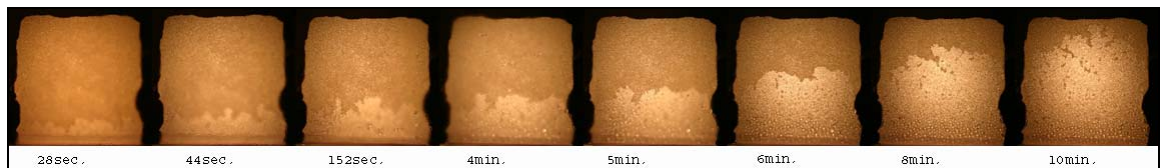


Figure 8.1 d- Experiment aV2: Counter-current, vertical orientation, air-water pair at 90 °C.

A very significant feature of the recovery curve is that the process slowed down drastically around 90seconds causing a bump on the curve for the low temperature case (Fig. 8.1 b). Knowing that the fluid front progresses in a bullet shaped profile, this reduction in speed is attributed to the fact that the front ran up against the top boundary. After this stage, the progress of the front continues in the horizontal direction and by gravity causing air displacement by water in downward direction.

When temperature is increased to 90 °C, the progress of the displacement front (aV2 in **Fig.8.1 d**) as well as the recovery curve (aC2 in Fig.8.1 b) changed. Fluid front is not stable anymore and the bullet-shape profile front was replaced by a more random interface. With the increase in temperature, the viscosity of water and IFT decrease yielding a faster displacement and instability at the interface compared to low-temperature experiments. Fingers accelerated the recovery as well as the removal of the bump that was previously observed in the recovery curve of low-temperature counterpart. Less residual saturation of the non-wetting phase in the case of high temperature experiment could be attributed to more “flat” front, rather than bullet shape, which results in no unswept regions around the corners of the top of the model.

8.1.1.2 Co-current interaction

With an open-top architecture (only two-sides-sealed as in **Fig. 8.2 a**) gas phase does not have to exit from the same edge that the liquid phase enters and gas escape at the top edge of the model is possible. Less resistance is enforced on imbibing water in the upward direction resulting in more fingering in the co-current cases (**Figs. 8.2 c and d**).

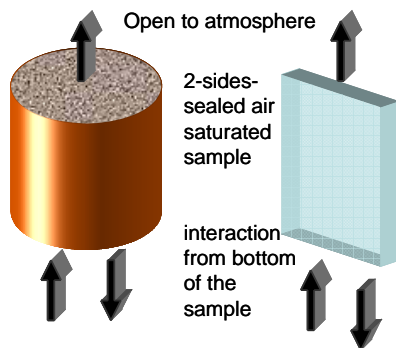


Figure 8.2 a-Model representation

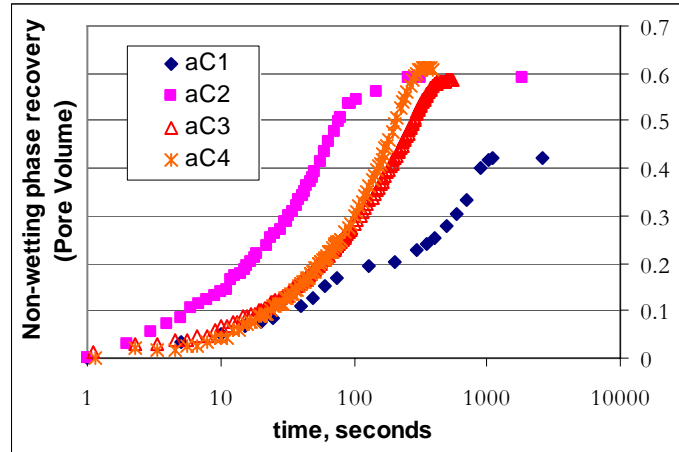


Figure 8.2 b-Recovery curves obtained from core experiments

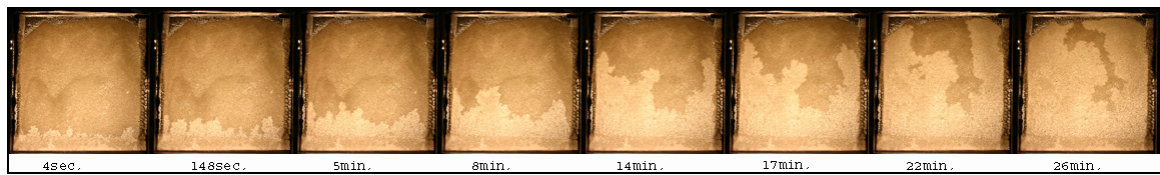


Figure 8.2 c- Experiment aV3: Co-current, vertical orientation, air-water pair at 20°C.

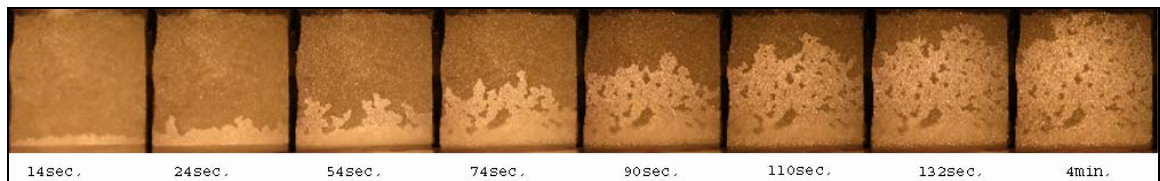


Figure 8.2 d- Experiment aV4 Co-current, Vertical oriented model for air-water pair at 90°C.

For low temperature case (aV3 in Fig. 8.2 c), random displacement pattern is easily identifiable. This type of displacement pattern is totally in disagreement with the counter-current counterpart (Fig. 8.1 c). The top boundary is no more interfering with the rate of recovery as in the previous counter-current case. No “bump” was observed on the recovery curve (Fig. 8.2 b) for low temperature case (aC3) which is in agreement with the visual experiments. This “bump” decelerated the imbibition, which had followed a similar trend as the co-current case up to the point (Fig. 8.1 b).

Both high temperature cases represented a frontal displacement but air entrapment behind the front is more obvious in co-current case (Fig. 8.2 d). Although the front progress was faster for the counter-current case (Fig. 8.1 d), the air entrapment behind the front prevented the recovery rate to be faster than the counter-current counterpart as also verified by the core experiments (compare aC2 and aC4 in Fig. 8.2 b). Ultimate recoveries for low-temperature (aC3 in Fig. 8.2 b) and high-temperature (aC4 in Fig. 8.2 b) co-current models

are very close, even though high-temperature case has a slight advantage in terms of the recovery rate. Interestingly, the high temperature case presented a displacement pattern with a systematic residual non-wetting phase entrapment reminiscent of invasion percolation type displacement.

8.1.2 Oil-water

It is expected that the dynamics of the imbibition of liquid-liquid and gas-liquid pairs would be different. Oil-water experiments were conducted to clarify these differences emerging mainly from lower viscosity ratio and less favorable wettability in the oil-water case. In addition to counter-current interaction, co-current interaction for oil-water experiments were studied in detail.

8.1.2.1 Counter-current interaction

Similar to air-water experiments, for counter-current interaction, three-sides-sealed models were prepared first (Fig. 8.3 a). The models were saturated 100% with the oleic phase (kerosene or mineral oil). Then, the samples were immersed into water to start the capillary imbibition process.

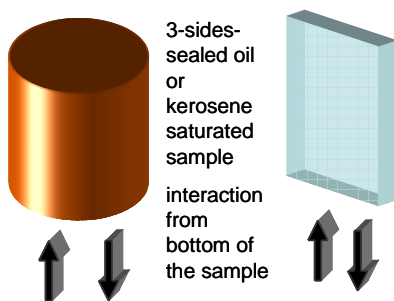


Figure 8.3 a-Model representation

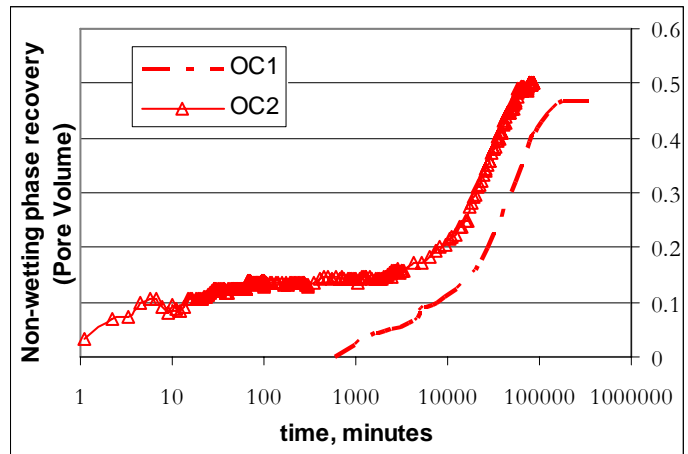


Figure 8.3 b-Recovery curves obtained from core experiments

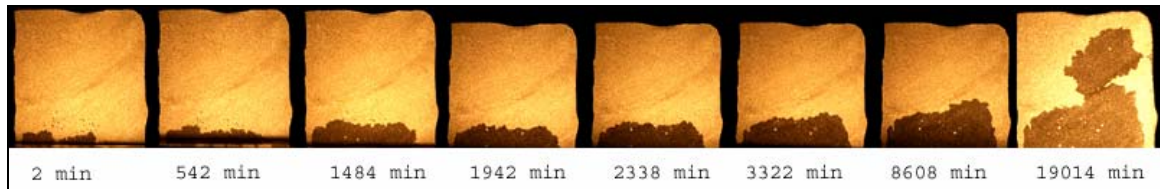


Figure 8.3 c- Experiment OV1: Counter-current, vertical orientation, mineral oil-water pair.

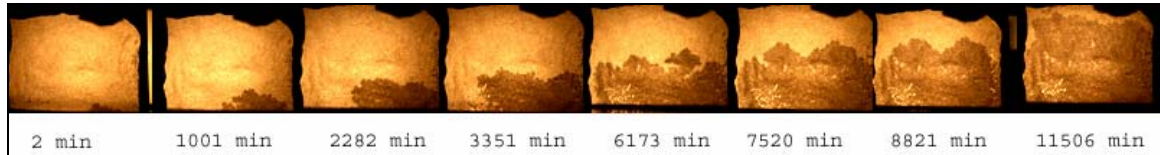


Figure 8.3 d- Experiment OV2: Counter-current, vertical orientation, kerosene-water pair.

For counter-current experiments (Figs. 8.3 c and 8.3 d) boundary effects were not felt since fluid front progressed in a bulk fashion regardless the type of the oleic phase for a while. The core experiments showed a slowing down period (between 100 and 1000 minutes for the kerosene case and between 1 and 1000 minutes for the mineral oil case) which could be caused by the closed top boundary. Once the front reached the top part of the model, gravity starts to dominate displacing the oil downward. This accelerates the process indicated by a higher slope of both recovery curves in late times (after 10,000 minutes -OC2 in Fig. 8.3 b). Less viscous kerosene was displaced faster than the mineral oil as inferred both from the visual observations and core experiments.

The experiments were also conducted for horizontal orientation (Fig. 8.4 a) to account for the gravity effect that was critically effective in the vertical experiments. In this case a random displacement was observed (Figs. 8.4 c and 8.4 d) as opposed to the vertical cases that exhibited more stable-frontal progress. The kerosene case (Fig. 8.4 d) sweep was inefficient initially, where fingers did not expand but proceed almost linearly until they reach the top boundary. It is very interesting that the imbibition started at a point and grew from this point (see the snapshot for the kerosene after 24 minutes) for both mineral oil and kerosene case. The process started from a point and the displacement was achieved by the growth of this “single finger” (Fig. 8.4 c) which is thicker in the mineral oil case compared to the kerosene counterpart. All other (vertical) cases, however, showed a trend of frontal progress which was identified by a uniform and frontal progress of the invading wetting phase.

Since there is no gravity effect, boundary effects were not as strong as in the vertical case and no bumps were observed in the recovery curves (**Fig. 8.4 b**). Because of the viscosity difference, kerosene showed a faster recovery. This is in agreement with both visual experiments and core recovery plots. For the mineral oil experiment (OV5), the dynamics was slightly different. Because of high oil viscosity, the movement of the fluid front was dampened in the mineral oil case (**Fig. 8.4 c**). Water tended to follow a laterally expanding branch pattern. Recovery was slow compared to kerosene case (OC5 in **Fig. 8.4 b**).

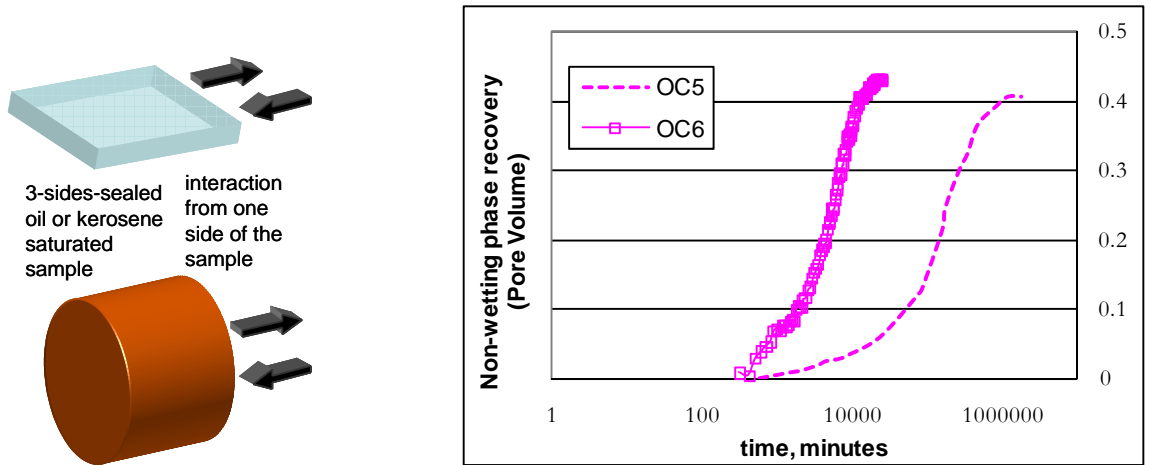


Figure 8.4 a-Model representation

Figure 8.4 b-Recovery curves obtained from core experiments

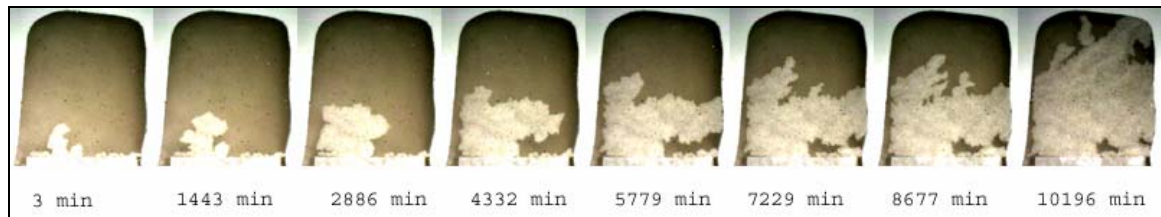


Figure 8.4 c- Experiment OV5: Counter-current, horizontal orientation, mineral oil-water pair.

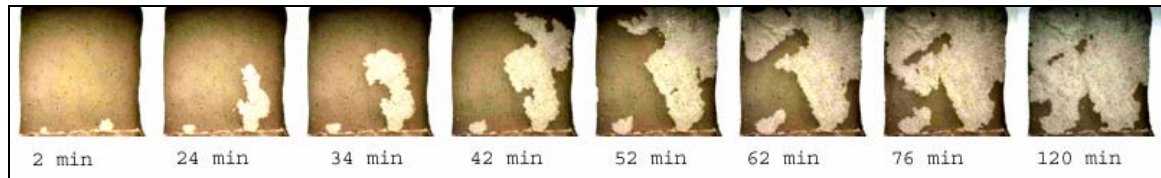


Figure 8.4 d- Experiment OV6: Counter-current, horizontal orientation, kerosene-water pair

8.1.2.2 Co-current interaction

Co-current oil-water experiments were conducted in two different ways for each fluid pair. In the first case, as similar to the air-water experiments, top edge was left open to the

atmosphere (**Fig. 8.5 a**). The cases for mineral oil (OV3-n) and kerosene (OV4-n) are given in **Figs. 8.5 b** and **c**, respectively.

For the models with only the bottom edge open to interaction, a similar behaviour to their counter-current counterparts was observed. Mineral oil showed a frontal progress in case of co-current interaction (**Fig. 8.5 b**) whereas kerosene (**Fig. 8.5 c**) displayed a more random displacement character with small fingers. Eventually, it turned out to be a frontal displacement following a similar pattern as its counter-current counterpart.

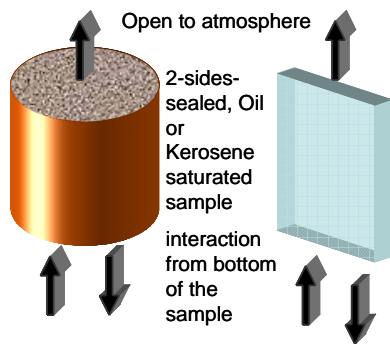


Figure 8.5 a-Model representation

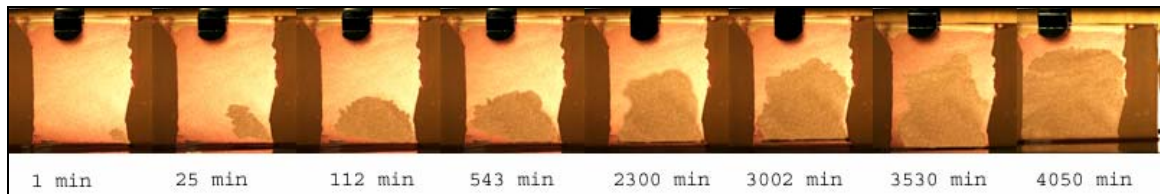


Figure 8.5 b- Experiment OV3-n Co-current, Vertical oriented model for Mineral Oil-water pair

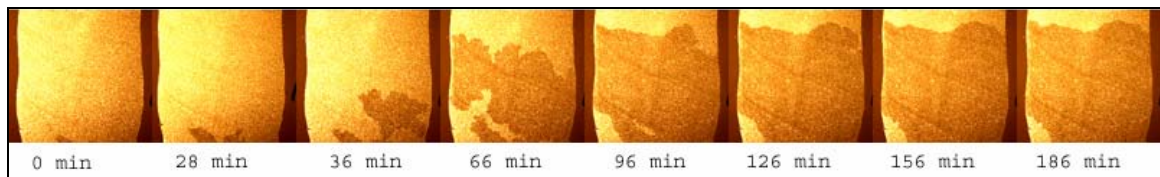


Figure 8.5 c- Experiment OV4-n Co-current, Vertical oriented model for Kerosene-water pair

More fingers (or a random front) were characteristically observed during co-current displacement for the lighter oil (kerosene) case. Because the upward movement of the wetting phase, acting against gravity caused by the open top boundary, was faster due to low viscosity ratio, more fingering was observed. This was not the case for the heavier oil case (mineral oil). The imbibition process was so slow that the gravity suppressed the movement of the wetting phase inside model and this resulted in much “smoother” and a more uniform displacement front. Note, however, that the process times were incomparably different in favor of kerosene.

To represent another common case that might be encountered in subsurface reservoirs, samples contacting water through both top and bottom edges were constructed (Fig. 8.6 a). One can see a massive -viscous- fingering caused by gravity for the mineral oil case (Fig. 8.6 c). As the fluid front reaches down the bottom of the model, fingers start expanding horizontally, but this causes a slowdown of the imbibition indicated as a bump in the recovery curve (OC3 in Fig. 8.6 b). For the kerosene case, no bumps were apparent in the recovery curve (OC4 in Fig. 8.6 b). This implies that fingering was not as severe as in the mineral oil case and this was verified by the visual experiment (Fig. 8.6 d). A much faster recovery was observed for the kerosene case due to more favorable mobility ratio and the ultimate recovery was reached in a very minimal time (Fig. 8.6 b).

Both cases presented a steady period in early times where no interaction had occurred (Fig. 8.6 b) even though both sides were open to flow. Obviously, counteracting forces such as water head from top and capillarity forcing water in to the model from bottom and top parts of the model were in balance in the beginning. Then the gravity and capillary forces acted on the top portion overcame and water entered into matrix from this side. Progress was in the downward direction mainly dominated by gravity. Note that no capillary interaction at the bottom of the sample was observed at all throughout the experiments for both cases.

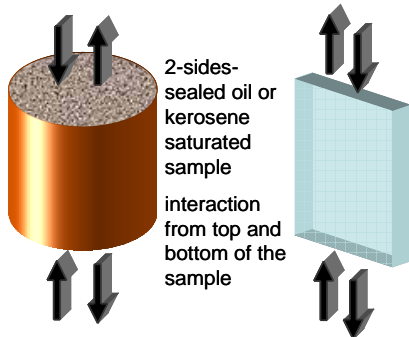


Figure 8.6 a-Model representation

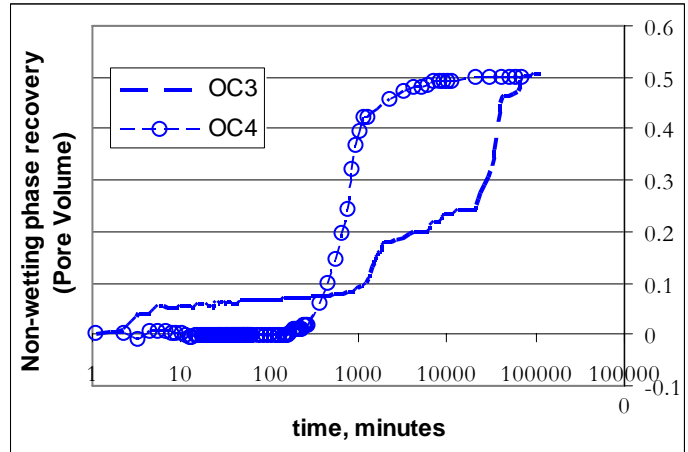


Figure 8.6 b-Recovery curves obtained from core experiments

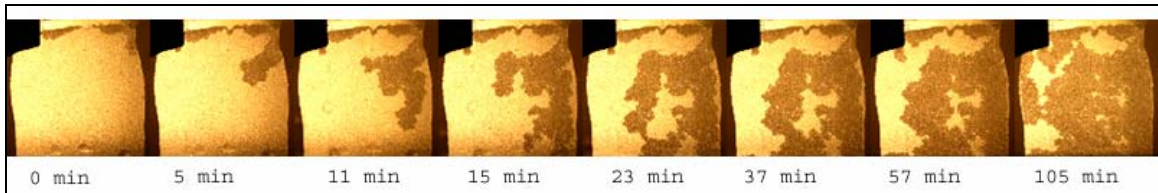


Figure 8.6 c- Experiment OV3-t Co-current, Vertical oriented model for Mineral Oil-water pair

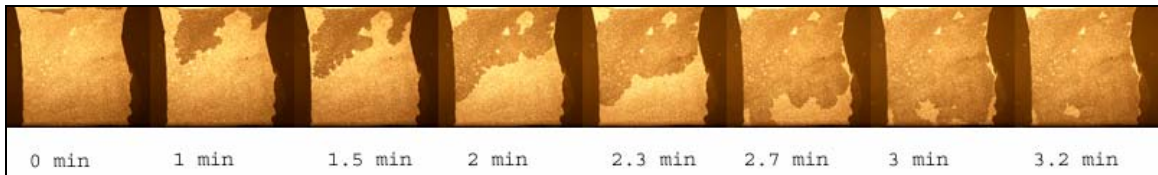


Figure 8.6 d- Experiment OV4-t Co-current, Vertical oriented model for Kerosene-water pair

8.1.2.3 Aging - wettability effect

2-D glass bead models and core samples were kept in oleic phase longer period of time (two weeks) after the saturation to alter the wettability. As expected, both visual experiments (Figs. 8.7 c and 8.7 e) and core recovery curves (OWC1, OWC3 in Fig. 8.7 b) showed slower recovery and less ultimate recovery due to reversal of wettability compared to the non-aged counterpart (Fig. 8.3 c).

Water was observed to enter into matrix from a single point rather than a uniform frontal invasion as similar to the horizontal cases. Water invasion grew from a single point and progressed linearly. In a similar manner, the co-current case also showed a similar single point invasion behavior (Fig.8.7 e). Under the influence of gravity, the recovery was

comparatively faster than the counter-current model, which was also verified by the recovery curves given in Fig. 8.7 b. Both aged samples, regardless of the interaction type, delivered less ultimate recovery compared to non-aged samples.

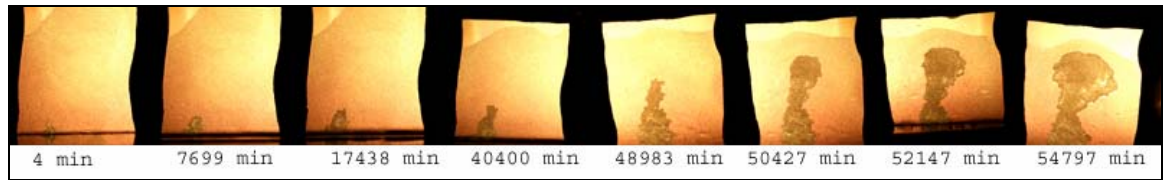
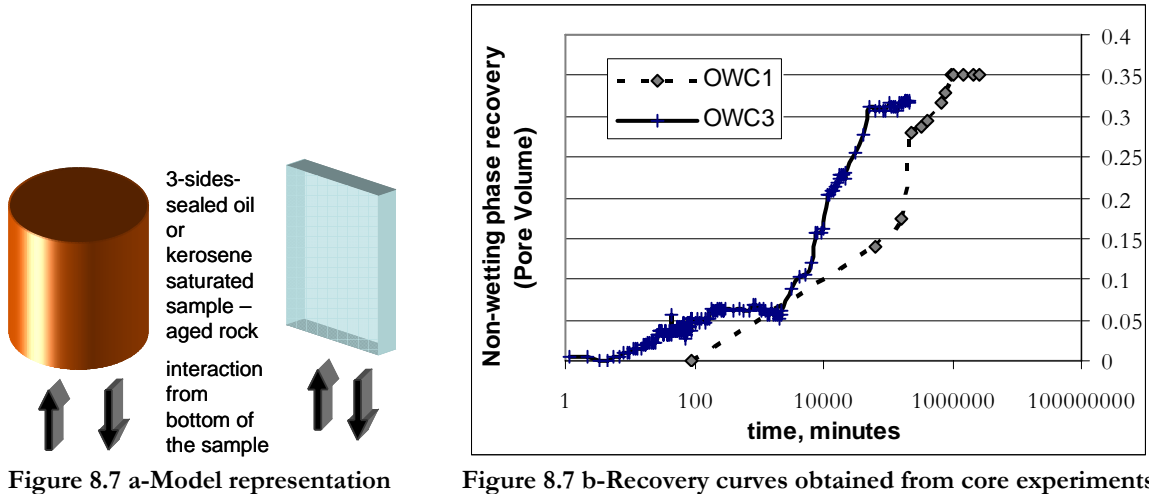


Figure 8.7 c- Experiment OWC1 Counter-current, Vertical oriented model for Mineral Oil-water pair-aged samples

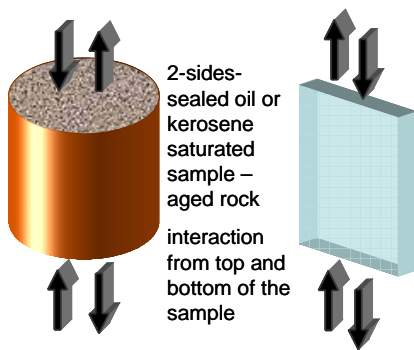


Figure 8.7 d-Model representation

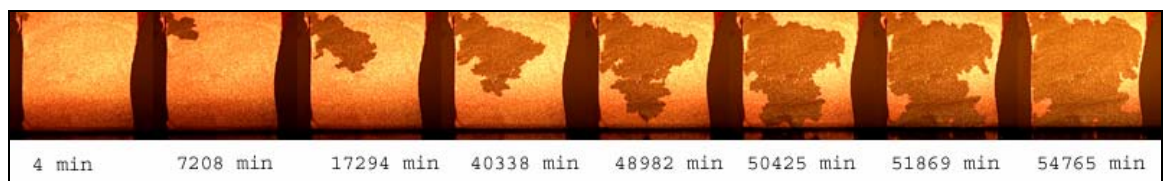







Figure 8.7 e- Experiment OWC3 Co-current, Vertical oriented model for Mineral Oil-water pair-aged samples

8.2 Miscible displacement between matrix and fracture

Visualization experiments were coupled with the core experiments to explain the dynamics of matrix fracture interaction for miscible processes. Displacement patterns and the progress of the front as well as oil recovery were the main concerns. The core experiments that are used for this part of the study is listed in Table 8.2.

Table 13 Updated diffusion experiment inventory.

	CoreShape					
	Length (inch)	2	2	6	2	6
	Diameter (inch)	1	1	1	2	2
Primary Diffusion	Berea SS	1	2U	3	4	5-5U
	Indiana LST	6	7U	8	9	10
	1-week aged Berea	11	12U	13	14	15
	1-month aged Berea	16	17U	18	19	20
Primary Imbibition Secondary Diffusion	Berea SS	21	22U	23	24	25-25U
	Indiana LST	26	27U	28	29	30
	1-week aged Berea	31	32U	33	34	35
	1-month aged Berea	36	37U	38	39	40

8.2.1 Vertical experiments: Counter-current interaction

Two different oil types, kerosene and mineral oil, were compared in **Figures 8.8** through **8.9** for counter-current experiments in vertical direction. Difference in aging was also considered in Figs 8.8 d.

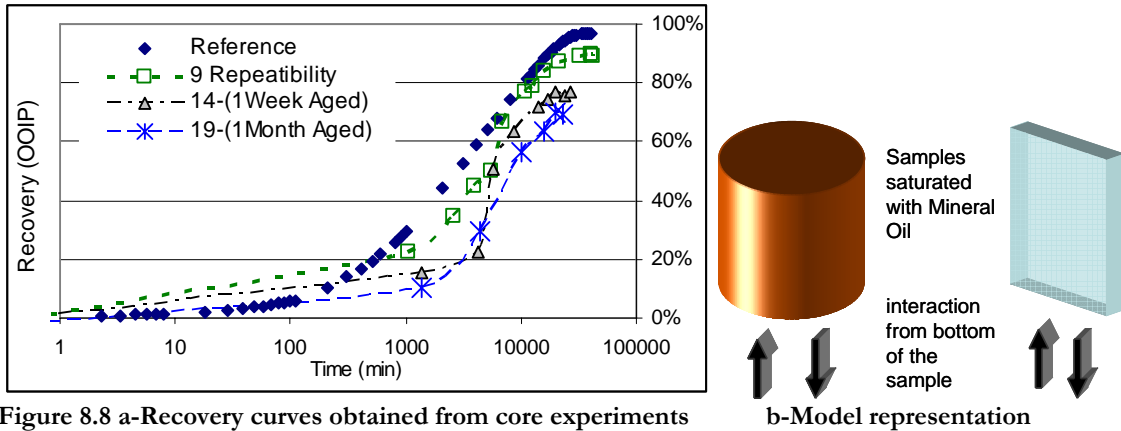


Figure 8.8 c-Experiment V1 (counter-current, mineral oil) 2D visualization experiment. (OOIP: Original Oil In Place)

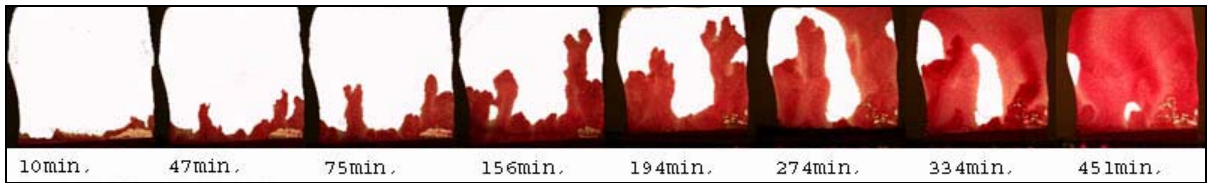


Figure 8.8 d-Visualization experiment for the aged (weakly water-wet) sample (counter-current, mineral oil).

Compared to the mineral oil case (Fig. 8.8 c), the kerosene experiment was much faster and generated slightly thinner fingers (Fig. 8.9c). The front reached the top boundary much earlier in case of kerosene. Then, the process was controlled predominantly by the gravity due to density difference between the original mineral oil (higher density) and mixture (pentane and mineral oil) which has lower density. This was reflected on the recovery curves (triangles in Fig. 8.9 a) as a bump (see the change in the slope of the recovery curve at 0.4 OOIP -original oil in place- recovery). Because of this, oil production was faster initially for the kerosene case.

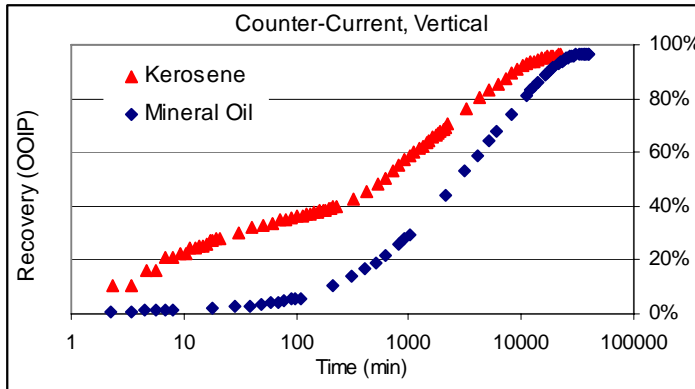
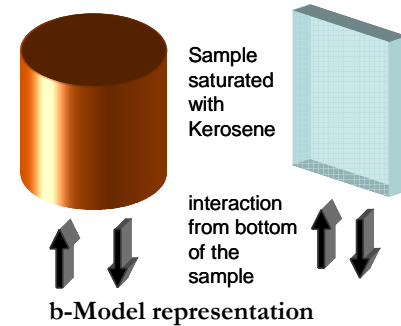


Figure 8.9 a-Recovery curves obtained from core experiments



b-Model representation

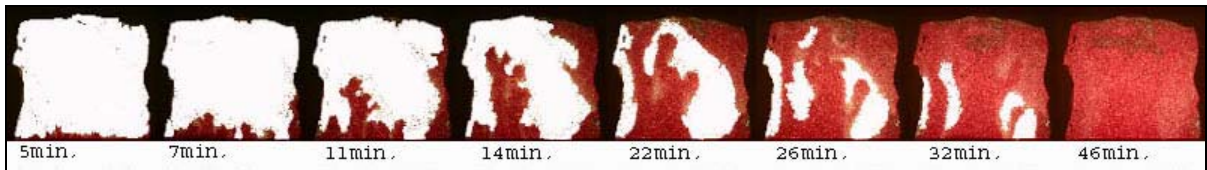


Figure 8.9 c-Experiment V2 (counter-current, kerosene) 2D visualization experiment. (OOIP: Original Oil In Place)

It was observed that the “inner” pressure distribution created by boundary conditions inside the porous medium model (inner pressure) and gravity played significant role on the displacement front. It is notoriously hard to construct a flat and homogeneous 2D glass-bead pack. We followed the same procedure in the model preparation and assumed that the beads are packed with similar efficiency. Vertically positioned models showed a “convective” displacement mechanism regardless of the oil type. The fluid fronts tend to progress through the sides of the model where less resistance exists compared to the center due to existing inner pressure distribution. Once the gravity driven front reaches the top of the model, lighter components start to accumulate over the heavier component, pushing the -heavier-oil-phase down. This can be called “buoyant convection” where displacement develops through the sides of the sample and goes downward from the inner part. Kerosene saturated sample has significant advantage in terms of the oil recovery rate even though the gravitational (buoyancy) force is expected to be much less (because of mineral oil and kerosene density difference); low viscous nature of the oleic-phase makes it easier for the solvent to disperse.

For the less viscous kerosene case this effect was more significant. Kerosene, lighter in terms of density and with a lower viscosity, showed more fingering but eventually a better sweep. The integrity within the fingers was preserved. Lower viscosity translates as better

dispersion of the solvent thru higher flow speed due to gravity. Note that the convective transport rising from the edges (due to gravity) of the model and descending from the middle portion caused re-production of the solvent. This could be a critical issue in the processes like CO₂ sequestration in oil reservoirs and contaminant transportation/waste disposal in which the matrix portion is desired to be the storage medium holding the solvent (or injected) phase.

An aged sample (Fig. 8.8 d) showed a similar behavior compared to the non-aged one (Fig. 8.8 c). The process time and dynamics were quite similar except that the unswept zones were slightly larger for a given time in the case of aged sample as also reflected by lower recovery at any time on the recovery curves (Exp 14 and 19 in Fig. 8.8 a). Note that the convective process was also observed and eventually the whole sample was swept in a longer time compared to the non-aged sample. The convective transport due to gravity was observed more prominent in the aged samples. The aged case (Fig. 8.8 d) presented smoother displacement fronts with less finger compared to the non-aged case (Fig. 8.8 c).

8.2.2 Vertical experiments: Co-current interaction

When the co-current models of vertical orientation were used, two distinctive patterns were obtained for the mineral oil and kerosene cases (**Fig. 8.10 c** and **8.10 d**). Pressure distribution altered with the top edge open to atmosphere and this caused different displacement fronts compared to the counter-current interaction. The kerosene case showed convection type displacement as similar to counter-current cases given above with more distinctive fingered pattern which translates into significant bumps on the recovery curve (triangles in Fig. 8.10 a, first bump at 0.45 OOIP and the second at 0.8 OOIP recovery). The fluid front progressed faster near the two edges and accumulation on top boundary started after 32 minutes for the kerosene case (Fig. 8.10 d). In the core experiments, the effect of buoyant convection (accumulation) starts to appear around 25 minutes (that is the point where the curve shows a bump and inclination starts). The light color in the center of the model indicates some residual oil saturation in the middle portion.

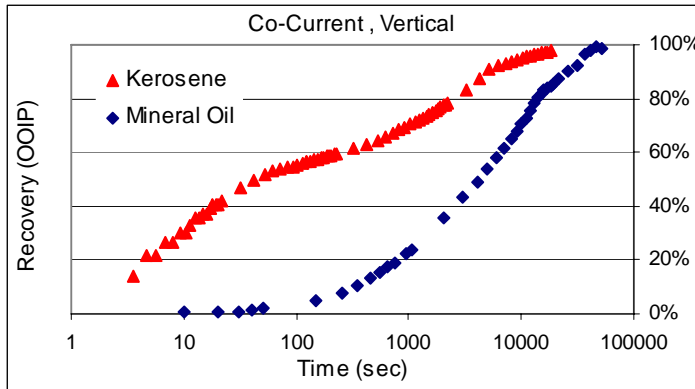
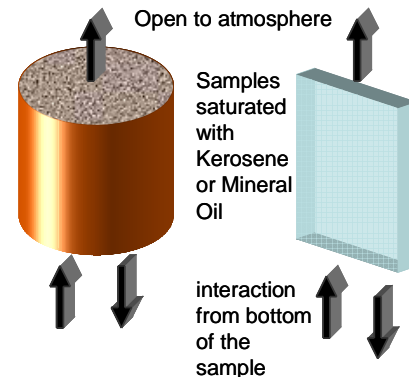


Figure 8.10 a-Recovery curves obtained from core experiments



b-Model representation

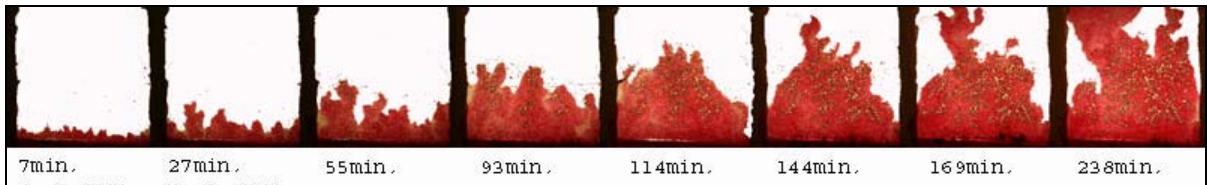


Figure 8.10 c-Experiment V3 (co-current, mineral oil) 2D visualization experiment. (OOIP: Original Oil In Place)

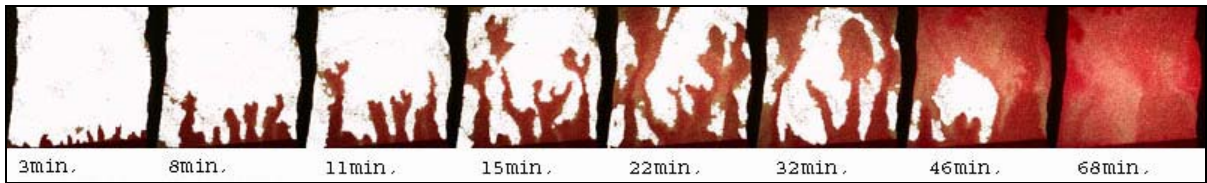


Figure 8.10 d-Experiment V4 (counter-current) - 2-D visualization experiment with kerosene.

The experiments done with the mineral oil showed a totally opposite behavior, where the “bullet shaped” displacement front is centered along the model without any significant fingering (Fig. 8.10 c). This showing viscosity is dominating over gravity effects. The front was much more stable than that of kerosene of the same model configuration. The higher viscosity of the oil phase discouraged the dispersion of the solvent closer to boundaries, despite the increased gravity effect due to higher density difference compared to kerosene. local pressure distribution (higher resistance to flow near the sides and less resistance in the middle portion of the model) and viscosity were the dominant factors controlling the process. Once the front reached the top, the gravitational forces started to become effective and the convective transport started. The displacement efficiency was much lower than that of the kerosene case yielding some unswept zones as can be seen through the comparison of Figs. 8.10 c and 8.10 d.

It was obvious that the dispersion of the solvent phase (due to gravity), was more prominent in the case of kerosene. This apparently caused more efficient displacement of oil compared to the mineral oil case. In other words, the dispersive flow is more pronounced in the case of kerosene due to low viscosity and less resistance to flow; causing more effective convective transport. This can be attributed to the lower viscosity of kerosene compared to mineral oil.

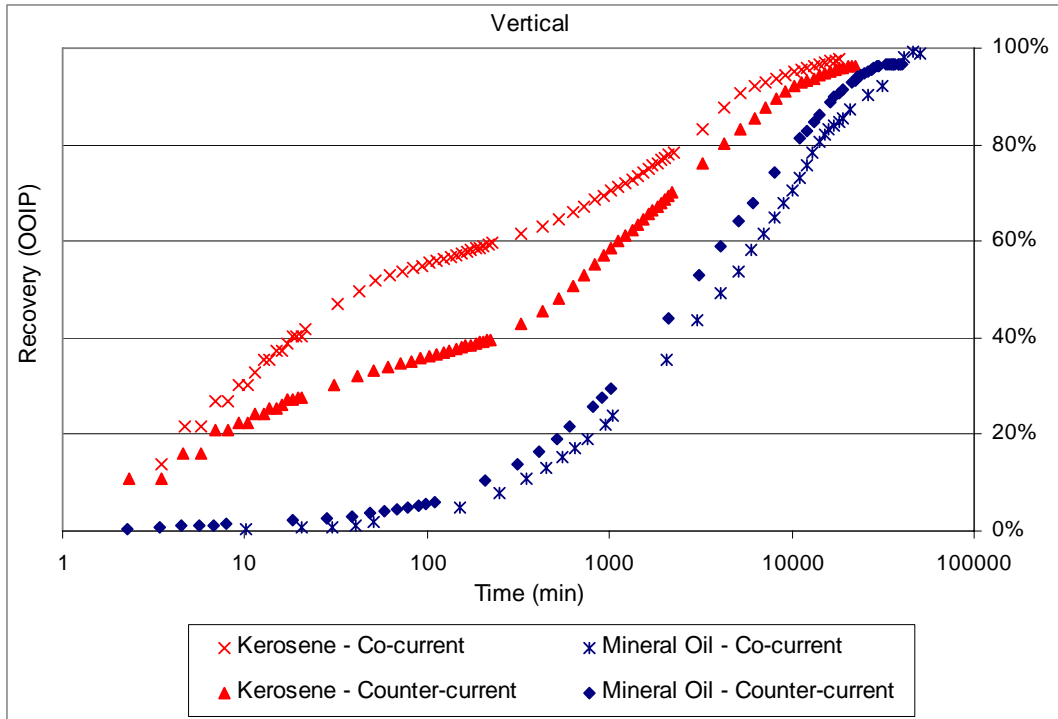


Figure 8.11: Comparison of the four experiments given in Figures 5 through 9. (OOIP: Original Oil In Place)

Four experiments comparing two different fluids and two different orientations are plotted in **Fig. 8.11**. Shape of the curves confirm that fingering is an indication of faster recovery. In fact, kerosene exhibited more fingering for all cases compared to mineral oil. This was more obvious for the co-current interaction (compare Figs. 8.9 c and 8.10 d). This is reflected as recovery on the recovery curve. Whereas for the mineral oil case, changing the boundary conditions from counter-current to co-current caused the fingers to disappear and process continued as bulk diffusion for long time, then converting to dispersive, convective flow. This behavior is also traceable from the recovery curves where the rate of oil recovery for mineral oil is lower. The bumps on the kerosene recovery curves are obvious and this is attributed to quicker arrival of the front to the top of the model due to severe fingering

8.2.3 Horizontal experiments: Counter-current interaction

Horizontal orientation showed a steady and frontal displacement for all cases (Figs. 8.12 and 8.13). Counter-current experiments yielded a bullet shaped front profile because of the fact that in the absence of gravity, no flow is occurring. At early stages, random process was observed in the shape of fingers confirming that the process is diffusion dominated for a short period of time. This indicates that the horizontal process is more of a stochastic process but the pattern would be highly dependent on pore structure and homogeneity rather than matrix boundary conditions and fluid type in the later stage. The development and progress of the front for the mineral oil and kerosene cases were quite similar. Obviously, the process of time for the mineral oil case was much longer as indicated in Figs. 8.12 and 8.13. This can be explained by slightly lower diffusion coefficient and higher viscosity of the mineral oil.

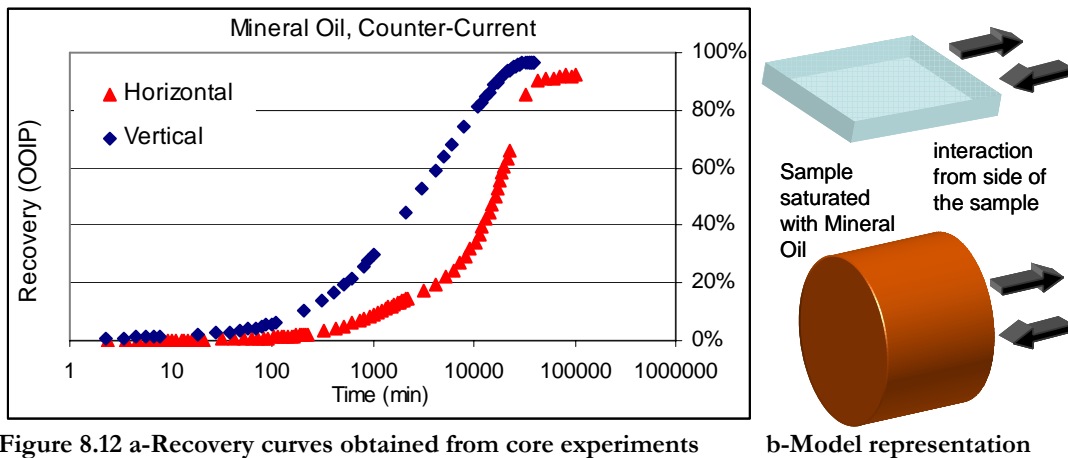


Figure 8.12 a-Recovery curves obtained from core experiments

b-Model representation

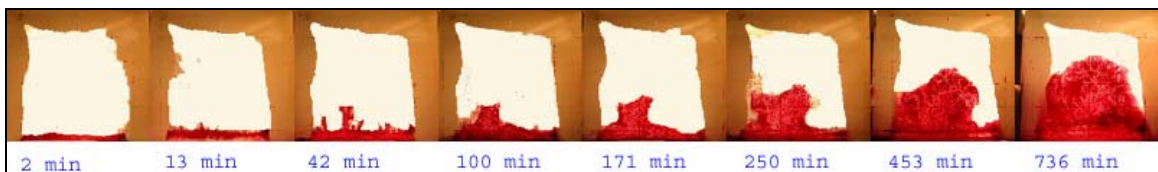


Figure 8.12 c-Experiment V5 (mineral oil) 2D visualization experiment. (OOIP: Original Oil In Place)

The comparison of the recovery curves for horizontal and vertical positioning indicated that the gravity driven vertical process is much faster (Fig. 8.12 a). Buoyancy caused by the density difference and gravity helps solvent phase disperse into the heavier oil phase, increasing the speed of recovery. This is especially significant for the low viscosity kerosene

case. It is interesting to note that the bumps on the curves were not observed in either case unlike the recovery curves for kerosene.

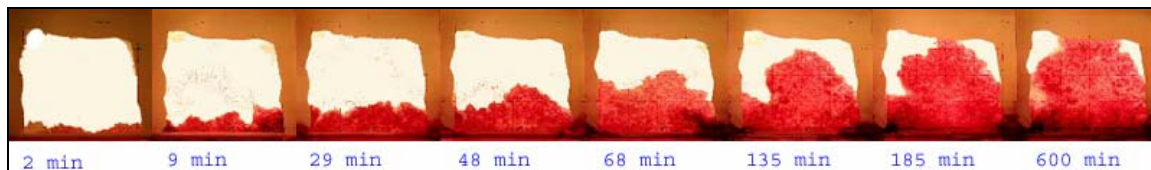


Figure 8.13: 2-D visualization experiment with kerosene (horizontal and counter-current case).

8.2.4 Horizontal experiments: Co-current interaction

Difficulties inherited due to the 3-D nature of the cores made it highly difficult to conduct accurate and identical core experiments to the 2-D visualization models. Therefore, it was only possible to provide visualization experiments for horizontal co-current models. Co-current experiments with one end open to atmosphere had different pressure distributions within the model (Figs. 8.14 and 8.15) compared to the counter-current case. The displacement front preferentially progressed near the sides of the model, but no convective behavior was observed due to lack of gravity and buoyancy effects for both cases. Mineral oil (Fig. 8.14) displayed more stable front compared to the kerosene case due to its higher viscosity (Fig. 8.15).

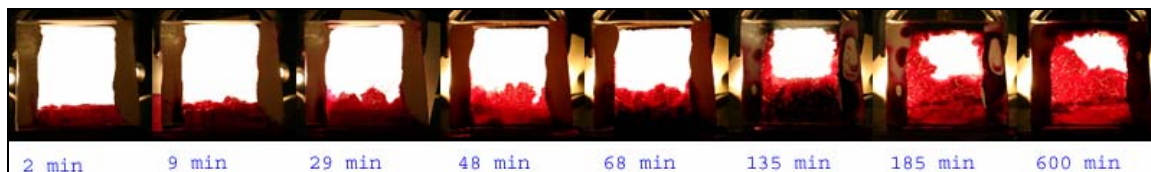


Figure 8.14: 2-D visualization experiment with mineral oil (horizontal and co-current case).

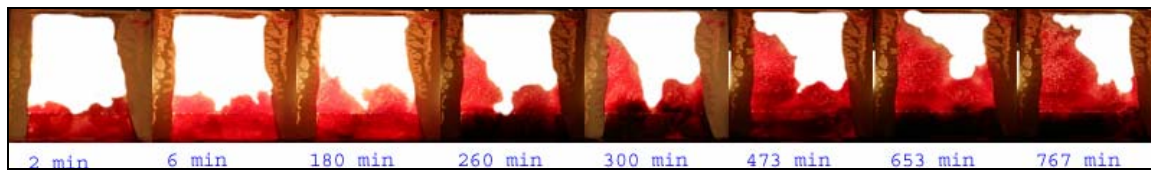


Figure 8.15: 2-D visualization experiment with kerosene (horizontal and co-current case).

8.2.5 Inclined experiments: Clarification on the effect of gravity

Visualization experiments slightly tilted (10 degrees) from the horizontal orientation were performed to observe the effect of gravity (Figs. 8.16 and 8.17). Although the angle of orientation was only 10° , it was sufficient to observe the dominance of the gravity effect and the transformation of the process to dispersion. Difference between the mineral oil and

kerosene cases for the vertical and inclined experiments is significant in both process time and fingering behavior. Shorter and thicker fingers are visible in both cases for the mineral oil case (Fig. 8.16) due to higher viscosity. As similar to the previous cases, kerosene yielded thinner and longer fingers and much faster process. Dispersive flow was observed more significant in the case of kerosene as similar to the vertical experiments.

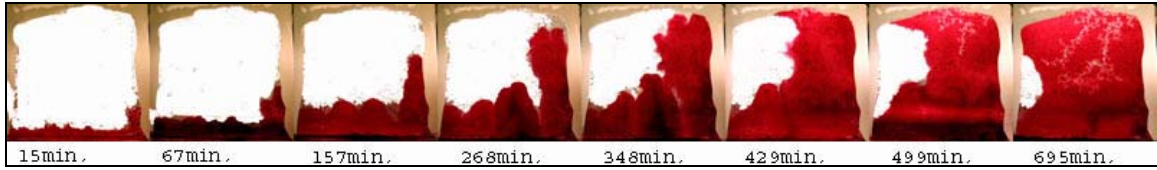


Figure 8.16: 2-D visualization experiment with mineral oil (inclined (10°) and counter-current case).

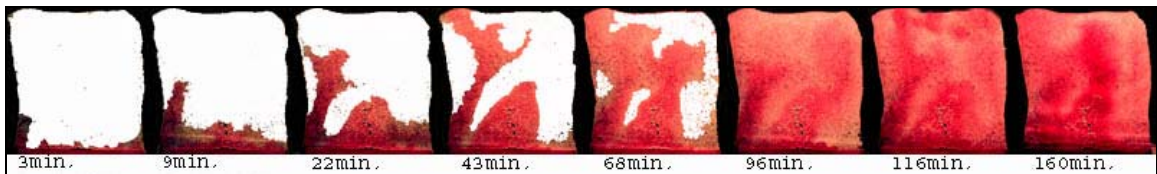


Figure 8.17: 2-D visualization experiment with kerosene (inclined (10°) and counter-current case).

8.3 Discussion

The purpose in this chapter was to explain some uncertainties we observed in the core experiments using 2-D visual models and it was done in qualitative basis. One-to-one match of these two different types of models would not be possible as they are not perfect representative of each other due to differences in the pore size, pore structure and permeability, and even wettabilities though they both are silica origin materials. On the other hand, the matrix boundary conditions and fluid type are identical in both experimental designs and we decided to utilize the experimental data of different sources collected throughout this study to explain some uncertainties.

One critical issue was fingering. It is controlled to great extent by viscosity ratios and the gravity forces. The latter is controlled by matrix boundary conditions and co- and counter-current representations do not reflect the same type of gravity effect on the process.

We were able to explain some uncertainties (e.g. hump in the recovery curves of the counter-current case) using visual models. Further studies could be done focusing on quantitative analysis of the data with more supportive experiments including defining time dependent

matrix diffusion coefficients and quantitative analysis of finger characteristics as functions of matrix boundary condition (interaction type, co-or counter-current) and fluid properties.

9 Modeling

Modelling part includes our efforts to model the matrix-fracture interaction phenomena we have previously observed experimentally. Early modelling efforts started with stochastic models and we are inspired from well known invasion percolation (IP) and diffusion limited aggregation (DLA) algorithms to model the diffusive matrix-fracture interaction first. This approach was observed to be partially successful responding well to the horizontal displacement cases where no convection due to gravity effect (buoyancy) was in effect. To develop a more universal model, the lattice Boltzmann methods (LBM) was adapted and the code is written for miscible process. Later the model is converted to handle immiscible processes. Then, the simulations are tested against glass-bead and micro-models.

9.1 Modified invasion percolation algorithm

The observations and the images obtained from the 2D glass bead models and a preliminary qualitative analysis were provided in Chapter 6 for miscible interaction. As those images were used in matching the simulation results for time scaling, we will begin with more detailed qualitative and quantitative analysis of those experiments in this section. The quantitative analysis comprises an estimation of the fractal dimension of the images and

comparing them with the ones obtained from the stochastic simulation. Therefore, the fractal dimensions of the displacement patterns were also provided here.

9.1.1 Vertical Experiments: Counter-current

Two different oil types, kerosene and mineral oil, were compared in **Figs. 9.1** and **9.2** for a counter-current experiment in vertical direction. Compared to the mineral oil case, the kerosene experiment was much faster and generated fronts with lower fractal dimensions initially. It was observed that the pressure distribution created by boundary conditions and gravity played significant role on the displacement front. It is a well established fact that it is notoriously hard to construct a flat and homogeneous 2D glass-bead pack. However, repeatability of the experiments indicated that the beads are packed relatively homogeneously and act in the same manner in all experiments. The closed boundaries of the sample from three sides created barriers that cause a different resistance to flow near the sides of the counter-current model. This is referred to “inner pressure distribution” as it controls the flow direction in the model. Obviously, the inner pressure distribution is different in the co- and counter-current cases.

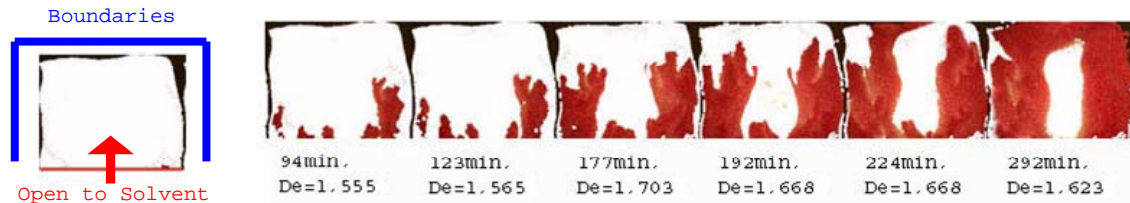


Figure 9.1: Pentane (red) mineral oil (white) experiment (counter-current interaction, vertical orientation). Thick (blue) lines in the model representation indicate the sides closed to flow.

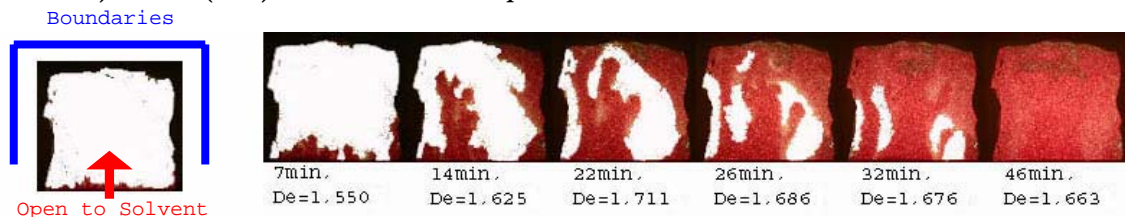


Figure 9.2: Pentane (red) kerosene (white) experiment (counter-current, vertical orientation). Thick (blue) lines in the model representation indicate the sides closed to flow.

Vertically positioned models showed a “convective” displacement mechanism regardless of the oil type. The fluid fronts tend to develop through the sides of the model where less resistance exists compared to the center due to existing -inner- pressure distribution within the model. Once the front reached the top of the model, the un-swept oil in the middle portion was displaced predominantly by the gravity forces. This can be called “buoyant

convection” or “free convection” where displacement develops through the sides of the sample and goes downward through the inner part. The lighter solvent-dispersed oil mixture develops through the boundaries and as it accumulates on the top of the model, it displaces the original (and heavier) matrix oil downward by gravity.

This effect was more significant for the less viscous kerosene case. During the process, the integrity within the fingers was preserved. Kerosene, lighter in terms of density and with a lower viscosity, showed more fingering but eventually a better sweep. Lower viscosity translates to stronger dispersion of the solvent by high flow velocity enhanced also by gravity. The fractal dimensions (D_e) did not give much clue about the overall process but the trend shows that the D_e becomes larger and begins to decrease by the end of the process. The kerosene experiment did not show any residual oil saturation due to unswept zone but the mineral oil experiment resulted in an unswept zone that is distinguished by white color in the middle portion of the last photo in Fig. 9.1. Note that the convective transport rising from the edges of the model and descending from the middle portion due to gravity caused re-production of the solvent. A one week aged sample, prepared to test model validity and experimental repeatability, showed a similar behavior to the non-aged one. The process time, progress of the front and fractal dimensions were all similar for the matching time values (Fig. 9.3).

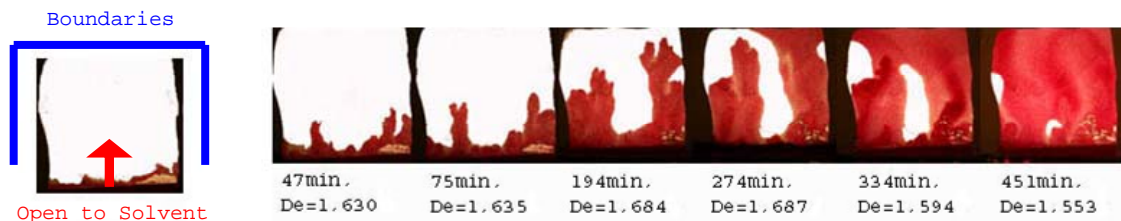


Figure 9.3: Pentane (red) mineral oil (white) experiment on an aged model (counter-current, vertical orientation). Thick (blue) lines in the model representation indicate the sides closed to flow.

9.1.2 Vertical Experiments: Co-current

When the co-current models of vertical orientation were used, two distinctive patterns were obtained for the mineral oil and kerosene cases (Figs. 9.4 and 9.5, respectively). The -inner- pressure distribution inside the model was altered by the open top edge and this caused different displacement patterns compared to counter-current models. The kerosene-pentane diffusion showed a convection type displacement that was similar to the counter-current cases (Figs. 9.1 and 9.2) but with a more distinctive fingered pattern (Fig. 9.5). The fluid

front progressed faster near the two edges and convective transport started after 32 minutes. This accelerated the displacement and eventually whole model was swept. The light color in the middle portion of the model indicates some residual kerosene saturation (Fig. 9.5).

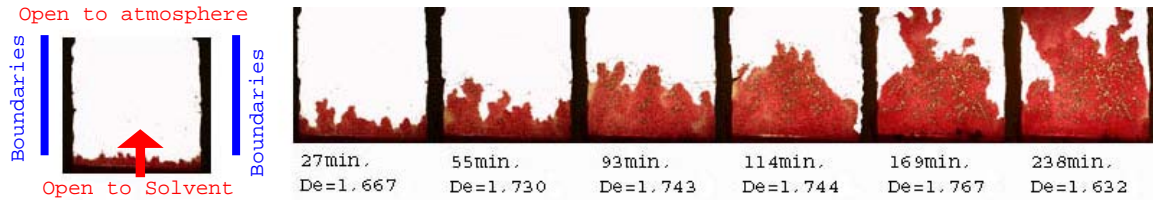


Figure 9.4: Pentane (red) mineral oil (white) experiment (co-current, vertical orientation). Thick (blue) lines in the model representation indicate the sides closed to flow.



Figure 9.5: Pentane (red) kerosene (white) experiment (co-current, vertical orientation). Thick (blue) lines in the model representation indicate the sides closed to flow.

The experiments with mineral oil showed a totally opposite behavior, where the bullet shaped fluid front is centered along the model (Fig. 9.4) without any significant fingering. The higher viscosity of the oil phase discouraged the dispersion of the solvent closer to the boundaries, despite the increased gravity effect due to higher density difference compared to the kerosene case. Local pressure distribution (high pressure near the sides and lower pressure in the middle portion of the model) was the dominant factor controlling the process. Once the front reached the top, the gravitational forces started to become effective and the convective behavior started. The displacement efficiency was much lower than that with the kerosene case yielding some un-swept zones as can be seen through the comparison of Figs. 9.4 and 9.5.

9.1.3 Horizontal Experiments: Counter-current

Horizontal orientation showed a steady and frontal displacement in all cases (Figs. 9.6 and 9.7). Without the gravity effect, pressure distribution, which is controlled by boundary conditions, was the dominating factor in the distribution of the fluids. The counter-current experiments yielded a bullet shaped front profile because of the fact that the lowest -inner- pressure was obtained at the center of the model due to the boundary conditions. The development and progress of the front for the mineral oil and kerosene cases were quite

similar. Obviously, the process of time for the mineral oil case was much longer as can be inferred from Figs. 9.6 and 9.7. The difference between the fractal dimensions of the fronts was also insignificant.

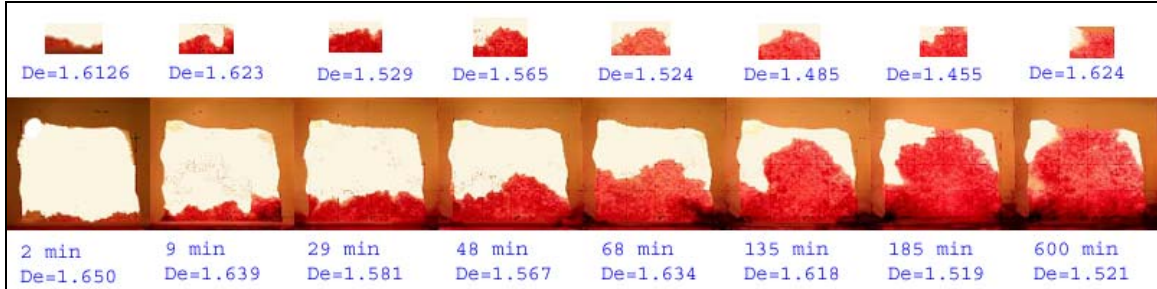


Figure 9.6: Pentane (red) kerosene (white) experiment (counter-current, horizontal orientation). Top values represent the fractal dimension of a small portion from the front (smaller scale).

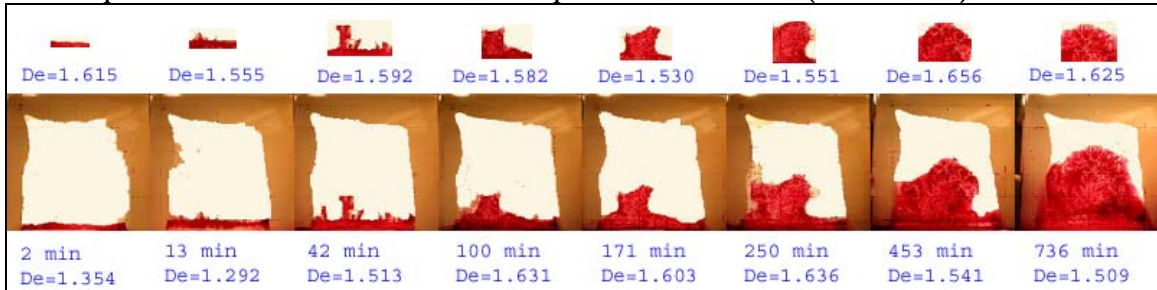


Figure 9.7: Pentane (red) mineral oil (white) experiment (counter-current, horizontal orientation). Top values represent the fractal dimension of a small portion from the front (smaller scale).

9.1.4 Horizontal Experiments: Co-current

Co-current experiments with one end open to atmosphere had totally -inner- different pressure distributions within the model (Figs. 9.8 and 9.9). The open ends (the bottom and top of the model) had the lowest pressure, causing a characteristic pressure distribution given in Fig. 9.10 (the highest -inner- pressure is at the center for the co-current and at the upper corners for the counter-current). The fluid front preferentially progressed near the sides of the model, as similar to the vertical experiments, but no convective behavior was observed due to lack of gravity and buoyancy effects for both cases as shown in Figs. 9.8 and 9.9.

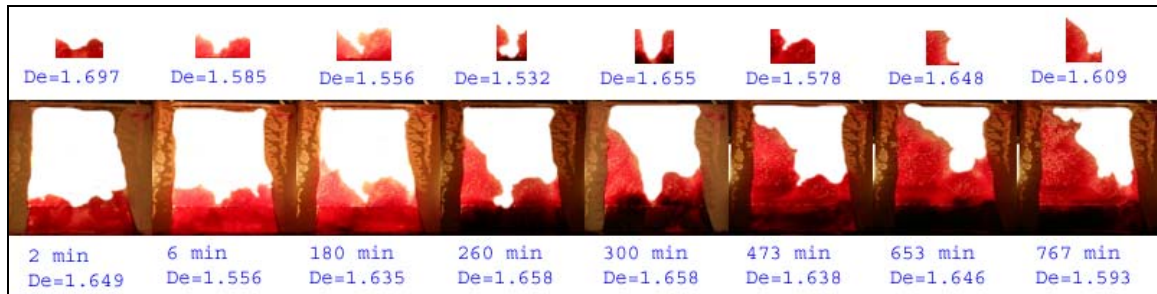


Figure 9.8: Pentane (red) kerosene (white) experiment (co-current, horizontal orientation). Top values represent the fractal dimension of a small portion from the front (smaller scale).

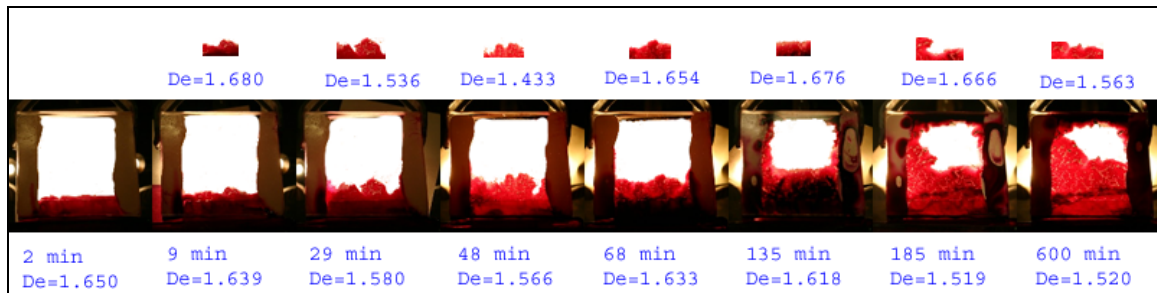


Figure 9.9: Pentane (red) mineral oil (white) experiment (co-current, horizontal orientation). Top values represent the fractal dimension of a small portion from the front (smaller scale).

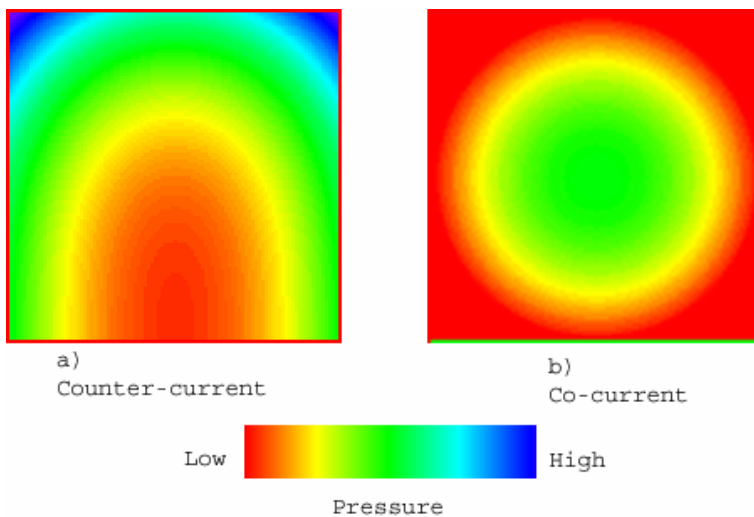


Figure 9.10: Initial -inner- pressure distribution in the model, caused by the boundary conditions of the model, for a) counter-current and b) co-current cases. These distributions were based on the experimental observations and used as the initial data in the stochastic simulation

A stochastic modeling technique was proposed using the well known invasion percolation (IP) and diffusion limited aggregation (DLA) algorithms to model the process. In this “hybrid” model, unlike in the conventional IP method, front does not advance by filling one pore at a time depending on the pore size. The modified algorithm uses the pressure

distribution as the basis for the front progress. All the cells that are in contact with the solvent phase (or any density values lower than the original oil density) are excited in a random sequence. All cells are assumed to be in contact with neighbours (a square lattice model) as depicted in Fig. 9.11. The cell sizes are assumed to be the same in accordance with the experimental model as the same size glass beads were used.

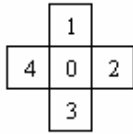


Figure 9.11: Invasion probability sketch for the stochastic model. In this square lattice model, “0” represent the pore and “1”, “2”, “3”, and “4” are the possible pores to which the fluid in “0” to diffuse.

Initially, the oil (displaced) phase is virtually saturated through all the cells assigning its original density value. As experimentally observed, the progress of the front would be controlled by the pressure distribution in the model created by the boundary conditions, at the end of each loop, pressure distribution is reconstructed. To define the initial pressure distribution values, minimum and maximum limiting pressures were defined and the pressure was distributed gradually according to Fig. 9.11, which was created based on the experimental observations.

Decision of which cell would be chosen to diffuse into first is made by comparing the pressure values of the neighboring cells. Eq.23 shows the probability of diffusing into Cell #1 (C_1) from Cell #0(C_0):

$$\frac{\left(\frac{C_1}{C_0}\right)^{Power}}{\left(\frac{C_1}{C_0}\right)^{Power} + \left(\frac{C_2}{C_0}\right)^{Power} + \left(\frac{C_3}{C_0}\right)^{Power} + \left(\frac{C_4}{C_0}\right)^{Power}} \dots\dots\dots 23$$

where C_0 is the pressure value of the cell that we focus on, C_1 , C_2 , C_3 , and C_4 are the values for the neighboring cells (Fig. 9.11). This equation gives the normalized value, i.e., the sum of the values calculated for the four cells would be unity. The same calculation is performed for the other three cells and the randomness was introduced by assigning random numbers to each cell that are proportional to the magnitude of the pressure. The term power in Eq. 23 is a constant value varied between 10 and 100 in different runs. It enhances

the effect of pressure distribution in the selection of the cell to be diffused into and eventually controls the front of the displacement as will be discussed later. The cell with the highest number among the four cells is selected to be diffused from the Cell #0.

Once the decision of which cell will be diffused into is made, the density value of the two cells (diffusing and being diffused) are found. To obtain the new density value, an exponential relationship given below was used:

$$\rho v_c = 0.5 * (\text{mixing time})^{-0.23} \dots\dots\dots 24$$

This relationship was based on an approach proposed by Wen et al. [2005]. According to this approach the amount of fluid exchange between two nodes decreases with time. Time here represents the duration of interaction between the two nodes which is named mixing time. Initially, the amount of fluid that will diffuse between two nodes is at its maximum. As the mixing time progresses and the densities of the cells becomes closer to each other, the diffusion between the two nodes will slow down until it reaches the density value of pentane following the exponential trend given in Eq. 24. Mixing time and number of iterations (real-time) are discrete and are held in different arrays. Each node keeps (or stores) its own mixing time value, this value is increased only if a mixing occurs between another node. Number of iterations are increased when a process occurs in any of the nodes within the model

The real time values, that represent the progress of the simulation was a linear function of the total number of iterations. For clarification, real-time represented by the model is named process time for this study. As more cells were invaded by the solvent, there is a less chance of mixing for a specific node with the same rate of frequency. In other words, for a specific node; the probability to mix is always higher in the early process times. This is, in a sense, assigning a residence time in each grid [Olayinka and Ionnidis, 2004]. The values yielding the best matches for the kerosene and mineral oil cases are given in **Fig. 9.12** and **9.13**. For example, 100x100 and power=100 (Eq. 23) case gave the best match to the experimental (real) time values of the counter-current kerosene case (Fig. 9.12). The time values (process time) obtained through this procedure from the stochastic modeling were used to match the corresponding experimental time values as explained in the next section.

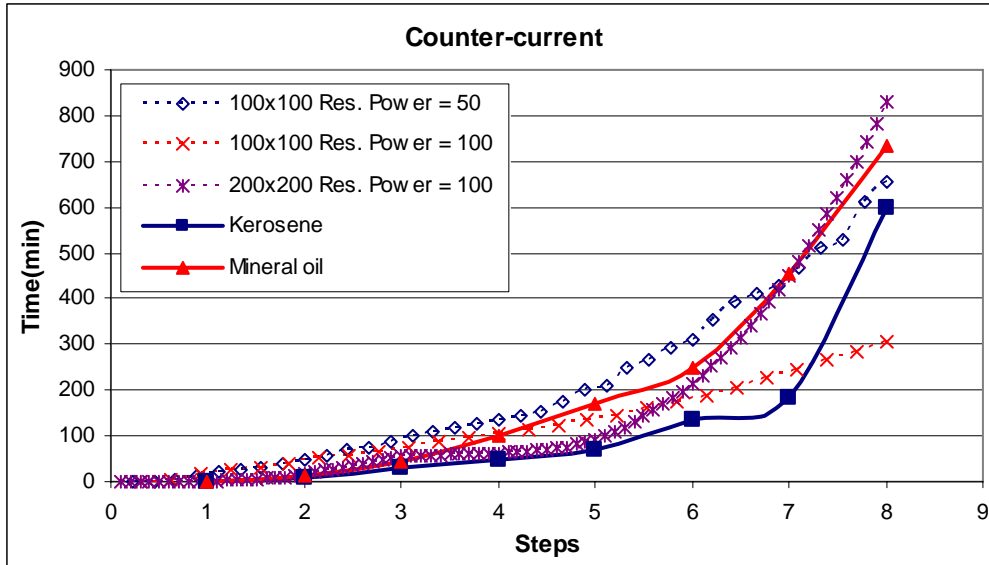


Fig. 9.12: Timing comparison between selected simulations and experiments (countercurrent cases).

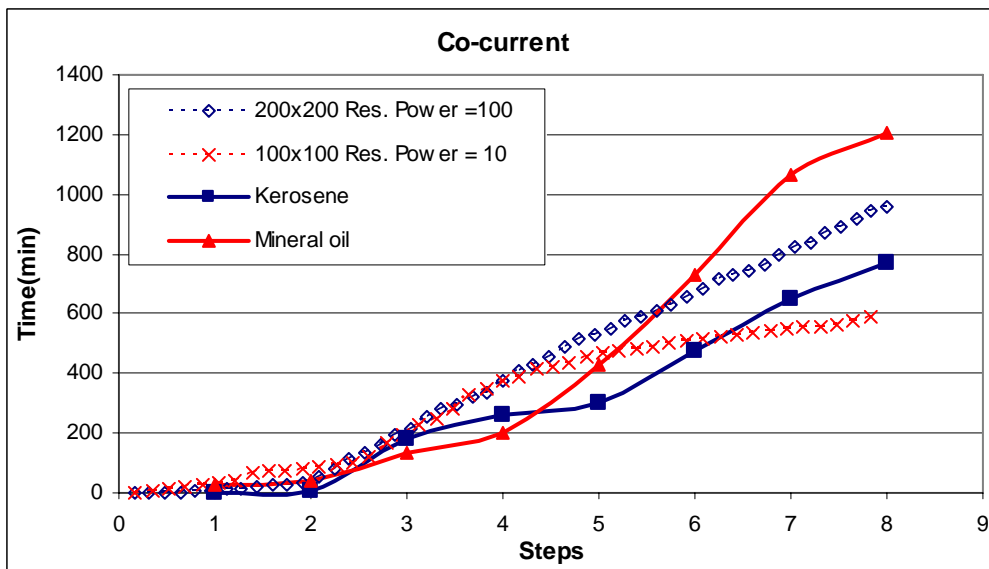


Fig. 9.13: Timing comparison between selected simulations and experiments (co-current cases).

9.1.5 Analysis of the results

The fractal dimension values of the whole front and small portion of the front (smaller scale) obtained from the simulation and experimental patterns were compared in Figs. 9.14 and 9.15. In addition to the fractal values (quantitative analysis), a visual inspection was

performed for the same time values of the experimental and stochastic models (qualitative) to obtain the best grid size and power value yielding the best match.

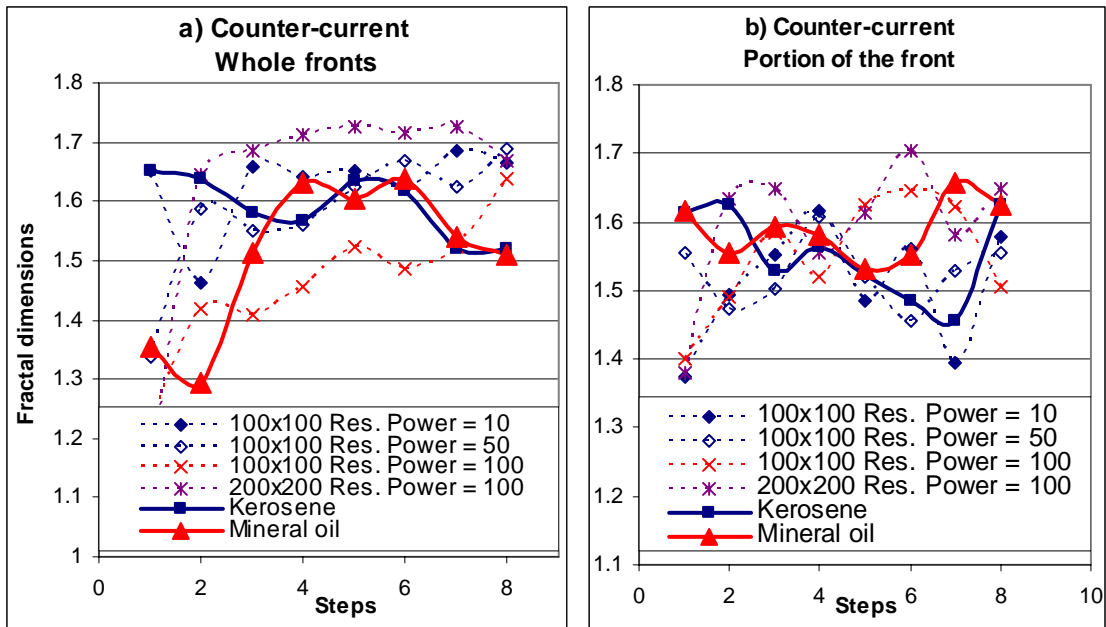


Fig. 9.14: Fractal dimensions of fronts obtained from the simulations and experiments a) whole front b) portion of the front.

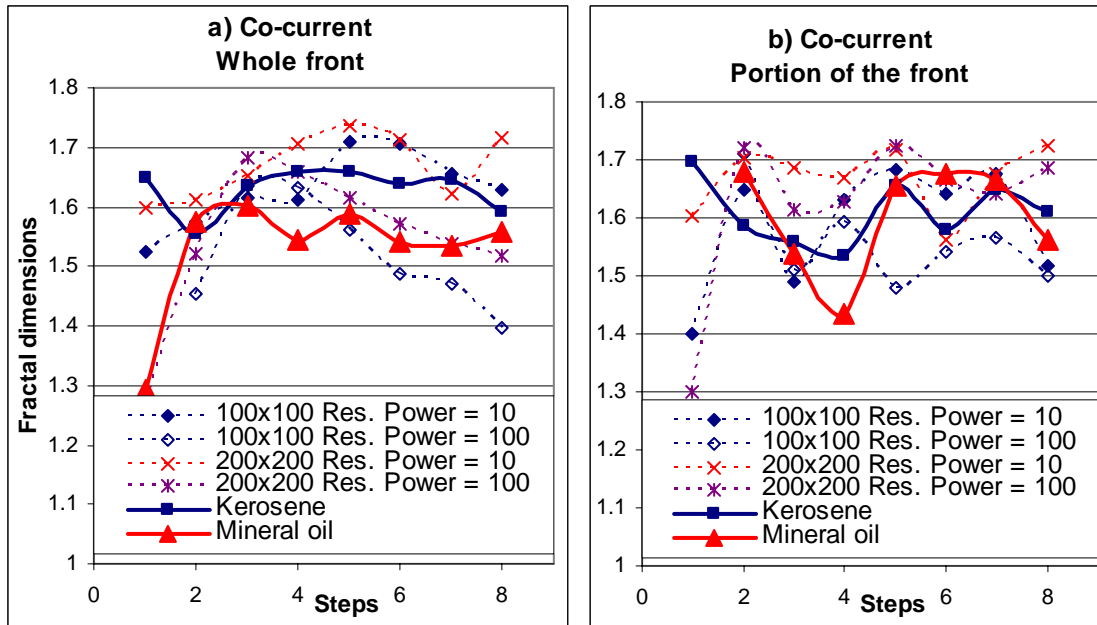


Fig. 9.15: Fractal dimensions of fronts obtained from the simulations and experiments a) whole front b) portion of the front.

Simulations performed using varying resolutions showed that it is possible to scale the process by adjusting power value and thus the effect of pressure. **Figs. 9.16 to 9.18** represent three simulations using the same resolution (100x100) but varying power values. Increasing the power value (given in Eq. 23) resulted in more fingered displacement front, less iteration and thus completion of the simulation in less time. Similarly, low power value resulted in more frontal displacement and higher iteration and longer duration. There is an optimum number of grids and power value in between to match with the experimental values. Increasing resolution dramatically increases processing time, where it takes 24 hours for a 300x300 lattice to be simulated on a Pentium 4, 3.4 GHz computer. Besides processing time, increasing resolution decreases the effect of power value. Comparing two different resolutions having the same power value, one will get more frontal displacement on the high resolution simulation. Comparisons can be seen through **Figs. 9.16 through 9.23** for the co- and counter-current interaction types. The time values given for each snapshot were obtained from the procedure explained above and given in Figs. 9.14 and 9.25.

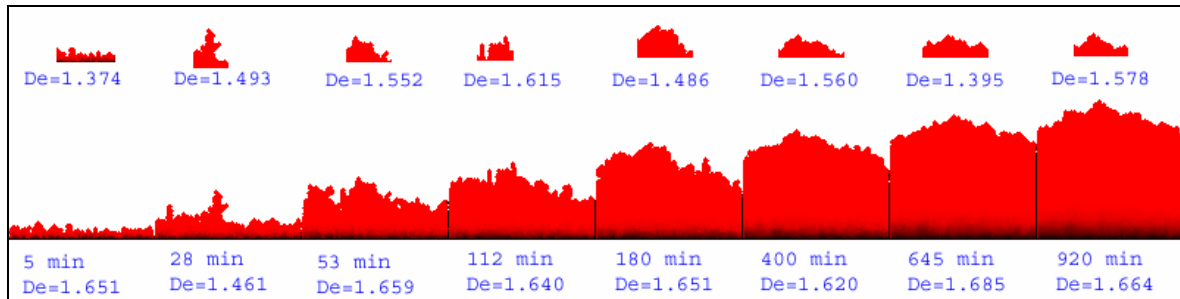


Fig. 9.16: Simulation of kerosene (white) pentane (red) diffusion (counter-current, 100x100 matrix, probability power=10). Top values represent the fractal dimension of a small portion from the front (smaller scale).

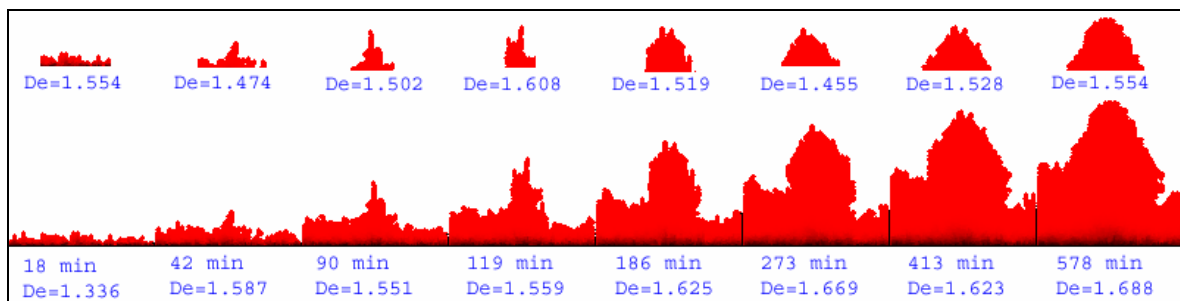


Fig. 9.17: Simulation of kerosene (white) pentane (red) diffusion (counter-current, 100x100 matrix, probability power=50). Top values represent the fractal dimension of a small portion from the front (smaller scale).

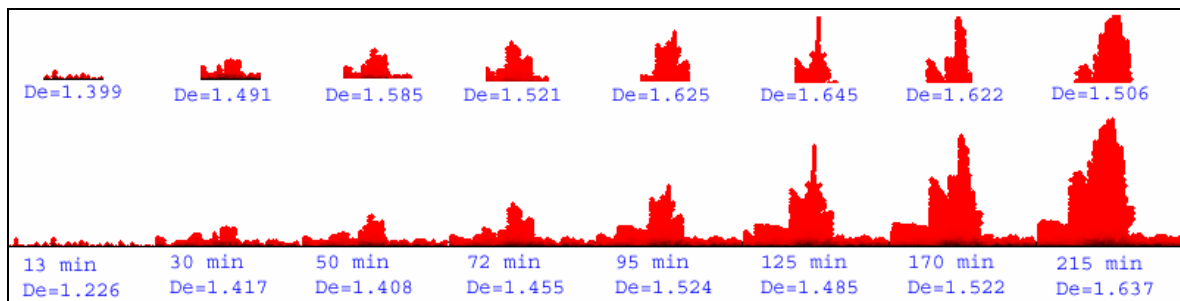


Fig. 9.18: Simulation of kerosene (white) pentane (red) diffusion (counter-current, 100x100 matrix, probability power=100). Top values represent the fractal dimension of a small portion from the front (smaller scale).

The fractal dimensions measured for the simulation images were observed as dependent on the power value and grid size. For the whole image front fractal dimensions, high power values yielded lower fractal dimensions, which are applicable for both co-current and counter-current simulations (Figs.9.14 a and 9.15 a). No particular trend was observed within fractal dimensions of the portion of the image front (Figs. 9.14 b and 9.15 b). Since the

fractal dimension is a function of resolution, it is expected to change with the number of grids. Increasing resolution also increased the fractal dimensions, comparing same power value but varying resolution size simulations.

Based on the fractal dimensions and visual observation of the snapshots of the same time points of the experiments and simulation results, a matching exercise was performed. It was observed that, for the counter-current kerosene case, 100x100 simulation with a power value of 50 and for the mineral oil case, 100x100 resolution with a power value of 10 showed the best match. Co-current experiment matches are observed to be 100x100, power=10 for kerosene case and 200x200 power=100 for mineral oil case.

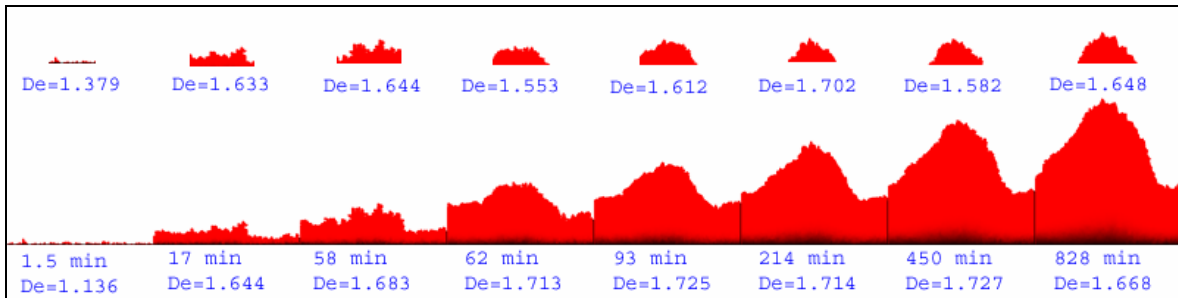


Fig. 9.19: Simulation of mineral oil (white) pentane (red) diffusion (counter-current, 200x200 matrix, probability power=100). Top values represent the fractal dimension of a small portion from the front (smaller scale).

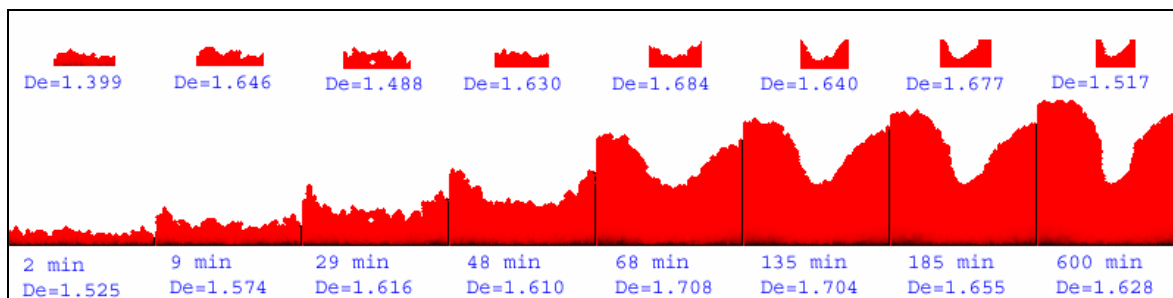


Fig. 9.20: Simulation of kerosene (white) pentane (red) diffusion (co-current, 100x100 matrix, probability power=10). Top values represent the fractal dimension of a small portion from the front (smaller scale).

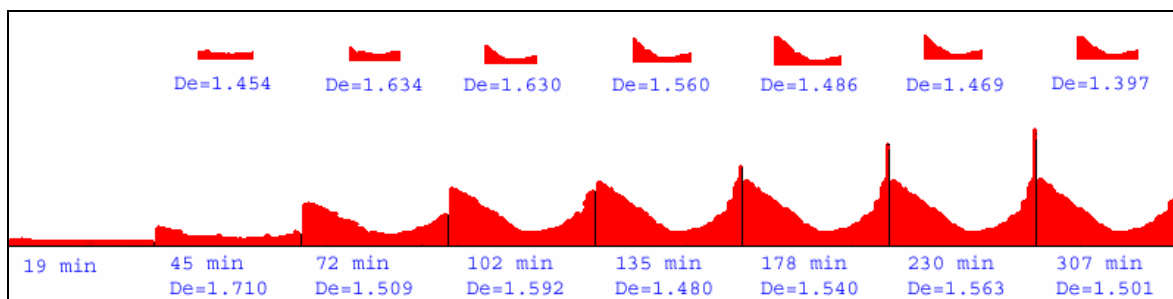


Fig. 9.21: Simulation of kerosene (white) pentane (red) diffusion (co-current, 100x100 matrix, probability power=100). Top values represent the fractal dimension of a small portion from the front (smaller scale).

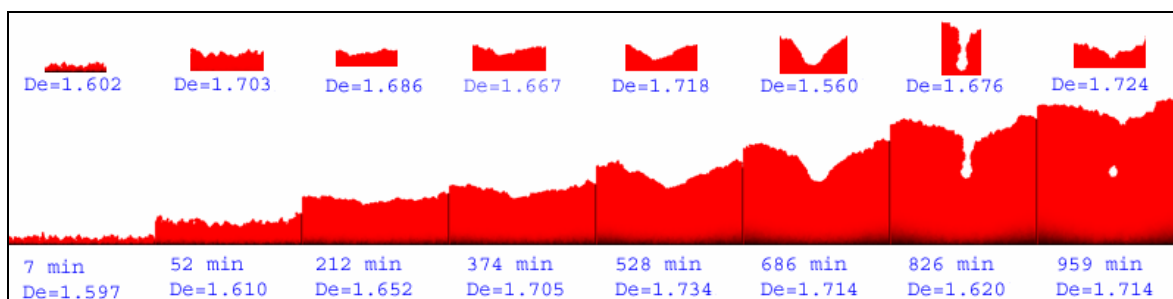


Fig. 9.22: Simulation of mineral oil (white) pentane (red) diffusion (co-current, 200x200 matrix, probability power=10). Top values represent the fractal dimension of a small portion from the front (smaller scale).

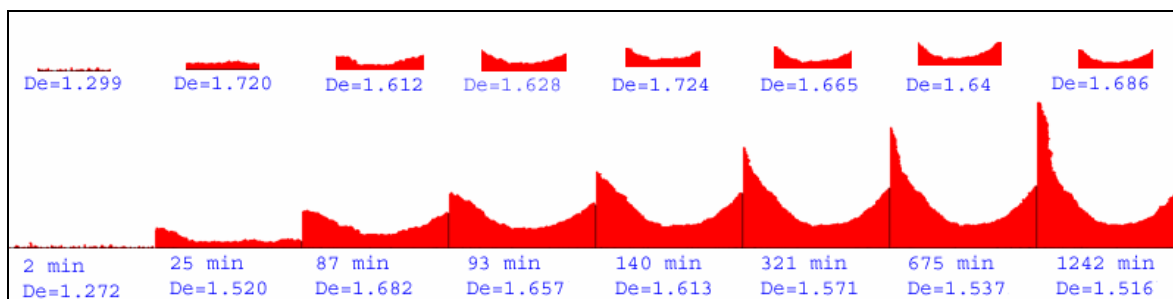


Fig. 9.23: Simulation of mineral oil (white) pentane (red) diffusion (co-current, 200x200 matrix, probability power=100). Top values represent the fractal dimension of a small portion from the front (smaller scale).

Visual comparison of experimental and stochastic patterns revealed that the model has given better results for the counter-current type interaction, where fractal dimensions and time values yielded close numbers to experimental results. The co-current model simulations were able to capture the shape of the front and the displacement pattern. But the fractal dimensions and time values obtained from the experiments and simulations were not as close as the counter-current simulation cases.

9.2 Diffusion Limited Aggregation (DLA)

The diffusion limited aggregation (DLA) method is a stochastic model which assumes the solvent particles forming the structure wander around randomly before attaching themselves to the structure. One important assumption for this model is that the particles are considered to be in low concentrations so they do not come in contact with each other and the structure grows one particle at a time rather than by chunks of particles.

The basic DLA algorithm was first described by Witten and Sander [1981] and is simple enough to be described informally. Given a discrete 2D grid, a single particle representing the crystal (or aggregate) is placed in the center. This acts as an attraction zone. A particle called the walker is then placed at a random location along the grid perimeter. The particle walks randomly along the adjacent grid cells until it either is adjacent to the chunk or falls off the grid. If it is adjacent to the chunk, it sticks and becomes part of the chunk, thus increasing the size of the attraction zone. A new walker is then inserted at the perimeter and the random walk is repeated.

In order to represent the experimental runs realistically, the attraction zone is assigned to be the lower end of the grid. In real-life this would represent the open edge of the model, where solvent is introduced. This is a diversion from the Witten-Sander's case, where they modelled diffusion into a particle, and in our case diffusion is through the edge. The rest of the algorithm is loyal to its roots, where probability may be manipulated using following modifications.

The first modification applied to this algorithm was to incorporate a sticking probability term to be able to increase or decrease the chance of sticking where particle densities are higher. The method is to introduce probability where sticking process would normally occur, this increases the chance of sticking for denser zones, where there are more than one adjacent particles, thus more than one chance to stick.

Two other modifications have been applied to take flow and gravity into consideration. Basic principle is to add a velocity vector to the random movement of the walker. In case of gravity, this is done by adding 1 unit of velocity that points to earth. Similarly in case of flow, the effect can be simulated by adding a velocity vector that is opposite to flow direction.

Time values were obtained from the total number of iterations. The simulations are visually matched with experiments and values yielding the best matches for the kerosene and mineral oil cases are given in Fig. 9.14 and 9.15.

Simulations are color coded in order to make it easier for the reader to distinguish the nodes that have mixed more. As the nodes go through more mixing process, the color changes from red to green to blue.

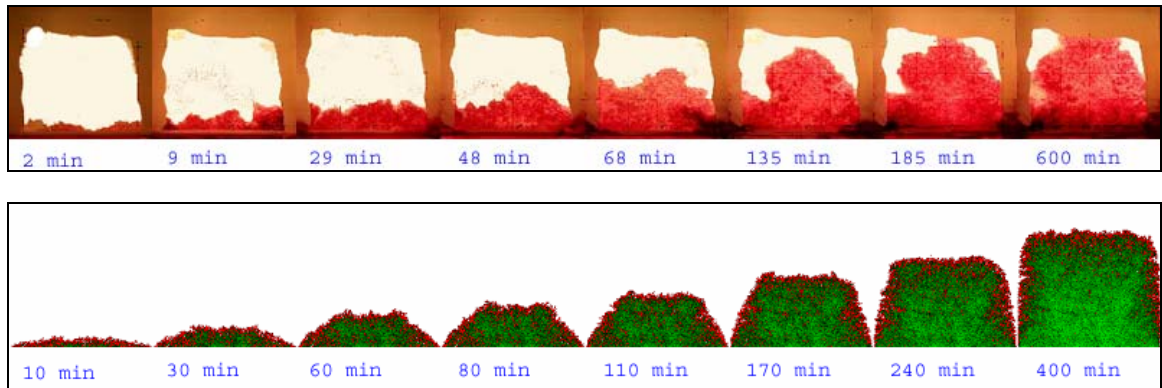


Figure 9.24 Kerosene-pentane diffusion for counter-current, horizontal case (a) experimental observations, (b)DLA simulation of the process.

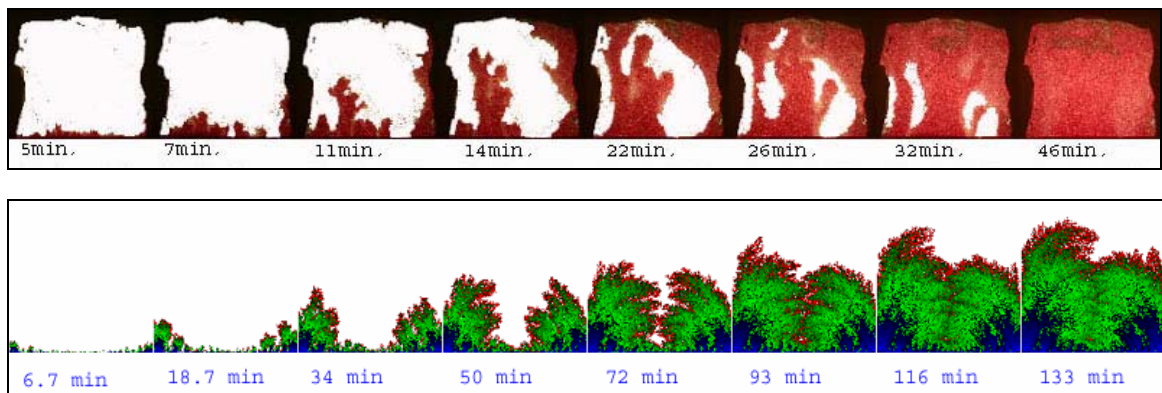


Figure 9.25 Kerosene-pentane diffusion for counter-current, vertical case (a) experimental observations, (b)DLA simulation of the process.

Complexity carried over by probability, diffusion coefficient and viscosity terms make it harder to obtain a direct relation for the time value. A curve fitting approach is applied for the solution. By plotting the number of iterations to achieve an instant of the simulation at matching images with experiments, one can obtain a curve that has the same exponentially increasing behavior as real time values, to obtain the best match; one only has to multiply with a constant number. In this case, the constant has to be calculated for each experiment done for accurate results. Instead we plotted matching image number versus time values for horizontal and vertical cases. The number of iterations were multiplied by the constant and then plotted. Then, the constant value is changed until a good match is obtained.

Note that the time conversion value based on the number of iterations was obtained using only the horizontal case of the mineral oil for counter-current transfer. This number was

then applied in the all the other cases for visual experiments. Reasonable matches for the times of the experimental results were obtained as shown in those figures indicating the usability of the conversion factor.

DLA was observed to be a powerful tool for modelling diffusion dominated phenomena. This was not the case for vertical oriented samples where the buoyancy (natural convection) caused a dispersive transport dominated by convection.

9.3 Lattice Boltzmann Method (LBM)

The LBM is simply composed of a set of non-linear partial differential equations, i.e., the Navier-Stokes equations, which are ultimately a statement of mass and momentum conservation. The abilities of the method attracted attention not only because it can simulate fluid flow through complex boundaries and interfacial dynamics but also it can easily be programmed for the parallel computers. A pioneering work by Kadanoff [1986] justified the use of simplified kinetic-type methods for macroscopic fluid flows. It was shown that the macroscopic dynamics of a fluid is the result of the collective behavior of many microscopic particles in the system and that the macroscopic dynamics of a fluid is the result of the collective behaviour of many microscopic particles in the system and that the macroscopic dynamics is not sensitive to the underlying details in microscopic physics.

Several review papers described the basics and evolution of the method over time [Kadanoff, 1986; Doolen and Chen, 2001; Rothman and Zaleski, 1994; Benzi et al. 1992]. Some researches focused on phase separation fluids [Rothman and Zaleski, 1994; Gunstensen et al. 1991; Rothman and Keller, 1988], others dealt with miscible processes [Stockman et. al., 1988; Cali et al., 1992; Flekkoy, 1993; Martys and Chen, 1996; Chen et al. 1996; Yeo and Ge, 2001].

Since the LBM is composed of distribution functions, physical interactions of the fluid particles (either one-phase or multi-phase) can be conveniently incorporated. In case of complex fluid flows with interfaces between multiple phases and phase transitions, the complex macroscopic behaviour is the result of the interaction of the fluid particles in a

microscopic level. Rothman and Keller [1988] was the first to develop the first lattice gas model for two immiscible fluids. The Boltzmann approach was later applied by Gunstensen et al. [1991]. This approach used rearranging of particle distributions of the two species in the interfacial region depending on concentrations. Miscible fluid model is first proposed by Flekkoy [1993] and Flekkoy et al. [1995] in which the sum of the distribution functions of the two components and the difference between them are made to relax at difference rates. Relaxation rate is dependent on kinematic viscosity for one of the distribution functions and diffusion coefficient for the other. Since different rates are used for relaxation, the diffusivity is independent of the viscosity of the fluid mixture.

9.3.1 Miscible model

Evolution of the LBM was observed as well over the last decade. Research was focused on improving the algorithm to simulate fluids both miscible and immiscible, as well as more efficient algorithms to lighten the heavy computing requirements. Bouzidi et al. [2001] studied the velocity boundary condition for curved boundaries in an effort to improve the simple bounce-back boundary condition. They worked on LBM boundary conditions for moving boundaries by combination of the “bounce-back” scheme and spatial interpolations of first and second order. Flekkoy [1993] was the first to introduce Bhatnagar-Gross-Krook model for miscible fluids. He derived the convection-diffusion equation and the Navier-Stokes equation describing the macroscopic behaviour using Chapman-Enskog expansion. Stockman et al. [1998] focused on enhancing the algorithm and making it more efficient for practical use and used the code to model dispersion in rough fractures and double-diffusive fingering.

The LBM proposed in this study uses a 9-speed structure, in a square lattice which is widely expressed as D2Q9 (2 dimensions, 9 velocities). The fluids are distinguished using Flekkoy proposed method [1993] as either “red” or “blue”. The basic variables of the models are the distribution functions. Where R_i is red (solvent) and B_i is blue (oil) fluid densities.

$$N_i = R_i + B_i \quad \dots\dots\dots 25$$

$$\Delta_i = R_i - B_i \quad \dots\dots\dots 26$$

Where R_i (B_i) is the mean occupation number for red (blue) fluid particles in direction i at a given node. By choosing the variables, in this manner, it is possible to decouple the information of flow (N_i) from the information of amount of solvent (Δ_j). The particles on each node have 9 velocities (Fig 9.26).

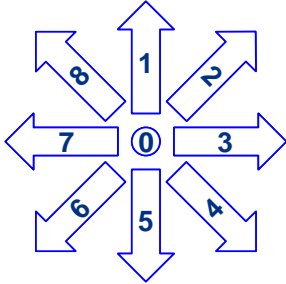


Figure 9.26 Speed vectors used in the LBM simulations.

According to the kinetic equation of lattice-gas automata (LGA), particles in one node with a velocity e_i after a timestep Δt would be conserved unless, some collision occurs, which is depicted with the Ω function. Ω is called the collision operator. As a derivative method of the LGA, the LBM incorporates the same equation which is:

$$N_i(x + c_i, t + 1) = N_i(x, t) + \lambda_v N_i^{neq}(x, t) \dots\dots\dots 27$$

$$\Delta_i(x + c_i, t + 1) = \Delta_i(x, t) + \lambda_D \Delta_i^{neq}(x, t) \dots\dots\dots 28$$

where this represents the particles at node (x, t) move with the unit speed c_i . Here λ_v and λ_D are the relaxation parameters which determine the kinematic viscosity ν and the diffusion coefficient D respectively. The relationship between those parameters is given as

$$\nu = \frac{1}{3} \left(\lambda_v - \frac{1}{2} \right) \dots\dots\dots 29$$

$$D = \frac{1}{3} \left(\lambda_D - \frac{1}{2} \right) \dots\dots\dots 30$$

The non-equilibrium distributions are given as

$$N_i^{neq} = N_i - N_i^{eq} \dots\dots\dots 31$$

$$\Delta_i^{neq} = \Delta_i - \Delta_i^{eq} \dots\dots\dots 32$$

where (for 9 speed architecture)

$$N_i^{neq} = w\rho(1 + 3c_i \cdot u + 9/2(c_i \cdot u)^2 - 3/2(u \cdot u)) \dots\dots\dots 33$$

$$\Delta_i^{neq} = w\rho(1 + 3c_i \cdot u) \dots\dots\dots 34$$

The mass density per site is defined as follows:

$$\rho = \sum_i N_i \dots\dots\dots 35$$

Then, the momentum density can be written as

$$\rho u = \sum_i c_i N_i \dots\dots\dots 36$$

The density difference ($\Delta\rho = \rho_r - \rho_b$ - ρ_r and ρ_b are the site densities) of red (blue) particles is defined as

$$\Delta\rho = \sum_i \Delta_i \dots\dots\dots 37$$

The vectors c_i are velocity vectors on the lattice connecting neighboring nodes. On the square lattice one of these c_i 's have zero length, four of them have unit length (vertical and horizontal vectors), and the rest four has $\sqrt{2}$ length (diagonals) as depicted in Fig. 9.26. The weight factors (w_i) are chosen to obtain isotropy of velocity moments and depend only on the lengths of the c_i 's.

$$w_i = \begin{cases} \frac{4}{9} & \text{for } i = 0 \\ \frac{1}{9} & \text{for } i = (1,3,5,7) \\ \frac{1}{36} & \text{for } i = (2,4,6,8) \end{cases} \dots\dots\dots 38$$

From Eq. 36, the flow is defined as

$$u = \frac{1}{\rho} \sum_i N_i c_i \quad \dots\dots\dots 39$$

Until now the basic equations of the LBM are given. These equations are not designed to handle external body forces, such as gravity. The gravity term has long been a discussion subject in this field. Some researchers modified the velocity vector [Martys and Chen, 1996; Shan and Doolen, 1995], others have incorporated as an additional term to Boltzmann equation (into the collision function to be more specific [Ginzbourg and Adler, 1994; He et al., 1997]). Composite-hybrid models have also been proposed [Buick and Greated, 2000].

This study uses the method proposed by Van der Sman [2006] where the moments of the equilibrium distributions equal to those of the Maxwell Boltzmann distribution.

The Boussinesq approximation is used to model the natural convection caused by the density differences. Additional term, F , is added to the velocity vector as:

$$u = \frac{1}{\rho} \sum_i N_i c_i + F \quad \dots\dots\dots 40$$

$$F = \rho_f g (1 - C_j) \left(\frac{\partial \rho_f}{\partial C_j} \right) \quad \dots\dots\dots 41$$

where q_f denotes the occupation number for the carrier fluid (oil), g is gravity, and C_j is solvent concentration. Collision step (Eqs. 33 and 34) is also changed to conform the Maxwell Boltzmann constants:

$$N_i(x + c_p t + 1) = N_i(x, t) + \lambda_v N_i^{neq}(x, t) + J \quad \dots\dots\dots 42$$

$$J = -\rho_f g w_i \frac{c_i}{c_s^2} \Delta t \quad \dots\dots\dots 43$$

where c_s is the speed of sound and c_i/c_s^2 equals 3 for D2Q9 geometry.

Because of the numerical constraints of the LBM, it is not possible to directly input the variables and therefore, scaling has to be applied. It is known that the Rayleigh and Schmidt numbers (the Prandtl number for heat convection) are the controlling parameters for natural convection. The variables are scaled to match Rayleigh and Schmidt numbers for real life values.

The Rayleigh number for this study is defined as:

$$Ra = \left(\left(\frac{\partial \rho_f}{\partial C_j} \right) C_j (g \sin \theta \left(\frac{b^2}{12} \right) L \right) / D.v \dots\dots\dots 44$$

and the Schmidt number is

$$Sc = \frac{\nu}{D} \dots\dots\dots 45$$

Since we are modelling a 3-dimensional phenomenon on a 2-dimensional model, we accepted *b* as 1 for LBM, this parameter translates as the model thickness. *L* is the length term.

The real values of oil viscosity, diffusion coefficient for solvent and oil, and gravity term were used to calculate the *Ra* and *Sc* numbers. Experimental values of the Rayleigh and Schmidt numbers were calculated to be 224.67, and 28.6 respectively. After entering the constraints in Solver option in MS Excel, scaled values of those three parameters were computed and used in the simulation.

Time values are obtained from number of iterations since each iteration step reflects an incremental time increase. To obtain the time values, for a healthy comparison, it has to be scaled back using the equation previously proposed by Stockman, et al. [1998] and Van Der Sman [2006] :

$$time = 12L.v / (b^2 g) \dots\dots\dots 46$$

Following the initialization step, particles are streamed for the next step. Completion of streaming requires the calculation of new density, flow speed and particle distribution values. Density and flow values are used to get the distribution in equilibrium.

The last step of the loop is the collision step, where particles are collided depending on their relaxation parameter. Relaxation parameter for each phase is different and they are obtained from viscosity and diffusion coefficient values. Instead of using simple bounce-back, the scheme that is proposed by Bouzidi et al. [2001] is utilized for this study. This scheme is more appropriate for curved boundaries since it uses linear or quadratic interpolation formulas involving values at two or three nodes (Fig 9.27).

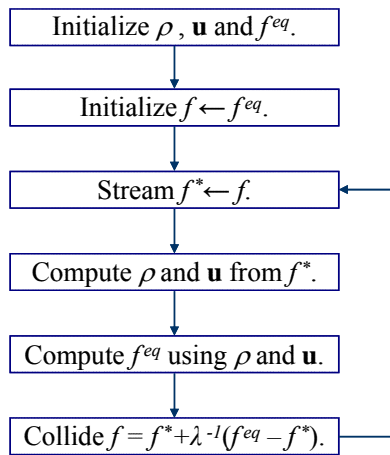


Figure 9.27 Flowchart of loop section.

To model the continuous solvent feed of the experimental model, the solvent feed is incorporated as a static reservoir at the bottom of the model. A small amount of pressure difference had to be incorporated into the model caused by the way the experimental set-up was constructed. Pressures are represented as densities in the LBM, so a slight density difference is accepted to mimic the behaviour. Boundaries of the model are adjusted to ensure counter-current or co-current displacement as desired. It was decided to assign the nodes as initial solvent feed or boundary using an image file that was obtained from the corresponding experiment at initial time. The image is modified in order to represent 3-node types; the black pixels would translate as solvent feeding nodes, the gray nodes are the boundaries, and white nodes are the oil saturated nodes. For the co-current models open-top architecture was simulated as constant pressure (density) on top nodes. The relaxation

parameters of the two phases are controlled by oil viscosity and diffusion coefficient of the solvent respectively.

9.3.1.1 Simulation results

The LBM was observed to be highly applicable and flexible for modeling the miscible interaction between fracture and matrix. The ability to handle complex boundaries was a big advantage of this model. This feature made it possible to simulate co-current and counter-current behaviour, as well as the change in transfer mechanism when changing orientation. In the LBM, no user interference to dictate the behaviour is present. Instead the user is required to input fluid properties, initial solvent occupied nodes and boundary conditions. The model was able to capture the diffusive flow and buoyant convection behavior for vertical (Figs. 9.30 b, 9.31 b, 9.32 b and 9.33 b) and bulk diffusion for horizontally oriented samples (Figs. 9.28b and 9.29b) successfully.

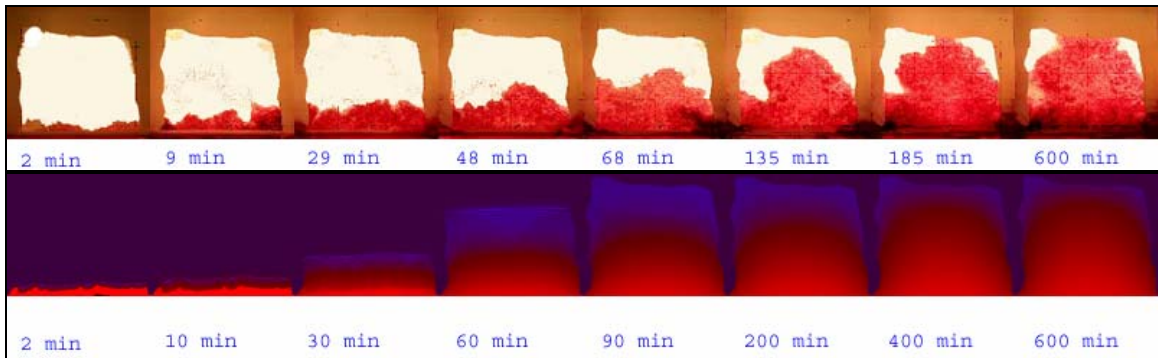


Figure 9.28 Kerosene-pentane diffusion for counter-current, horizontal case (a) experimental observations, (b) LBM simulation

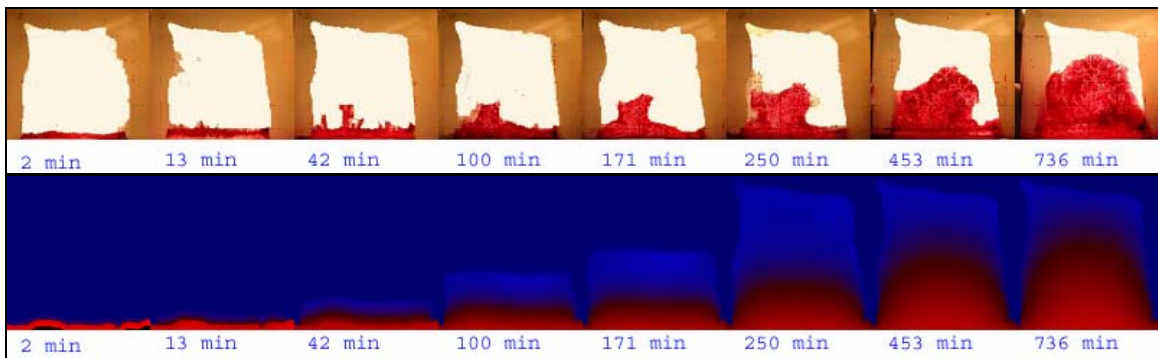


Figure 9.29 Mineral oil-pentane diffusion for counter-current, horizontal case (a) experimental observations, (b) LBM simulation of the process

The finger growth after 10min in case of counter-current diffusion for kerosene was observed in the LBM simulations (Fig. 9.30). Two big fingers growing through the sides were prominent and the convective transport was captured in the LBM runs. As for the co-current cases, the LBM model for the mineral oil case showed a good match with the experimental observation reflecting the frontal displacement with less fingers (Fig. 9.33). The finger growths and the buoyant convective transport were captured successfully. In the kerosene case, however, thin fingers were not observed in the LBM simulations (between 11 and 32 min in Fig. 9.32 a) but the convective transport was reflected well and the time matches were successful (Fig. 9.32).

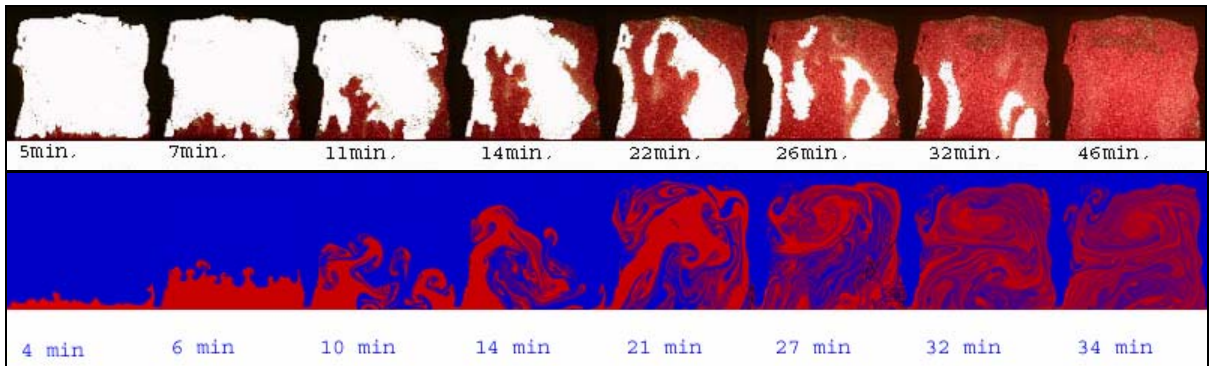


Figure 9.30 Kerosene-pentane diffusion for counter-current, vertical case (a) experimental observations, (b) LBM simulation

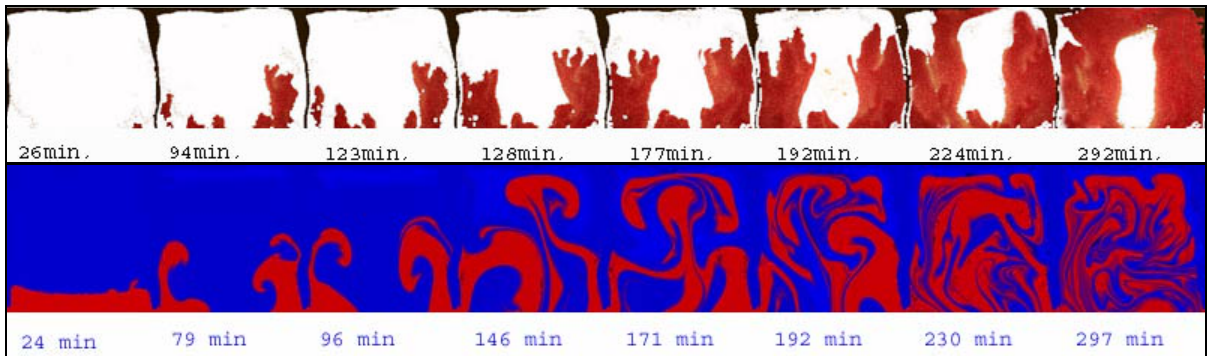


Figure 9.31 Mineral oil-pentane diffusion for counter-current, vertical case (a) experimental observations, (b) LBM simulation of the process.

Square shaped models were used in all experiments. In order to minimize the boundary effects that caused a faster movement of the front through the less resistant portion (the two sides of the models) on the process, a different model dimension was applied. An extreme

case with 2:1 aspect ratio was also included (Fig. 9.34 a) in an effort to see the adaptability of the LBM proposed in this study (Fig. 9.34 b). No input parameters were changed except the dimensions of the model. This turned out to be a test of the algorithm and time conversion factor presented in this paper on a different shape/dimension model. In this case the effect of boundaries were suppressed because of the width of the model. Initial fingering caused by initial random walk of diffusion was obvious before the gravity effect starts to become dominant. The process was observed to be similar to double diffusive fingering. At the later stages, the buoyant convection for the unswept parts was also visible. Despite high aspect ratio (or shorter size) of the sample, the accumulation of the lighter phase on top of the model causing buoyant convection was observed after 76 minutes (Fig. 9.34). The LBM model proposed was able to simulate the process successfully as can be seen through the comparison of the simulation and experimental runs.

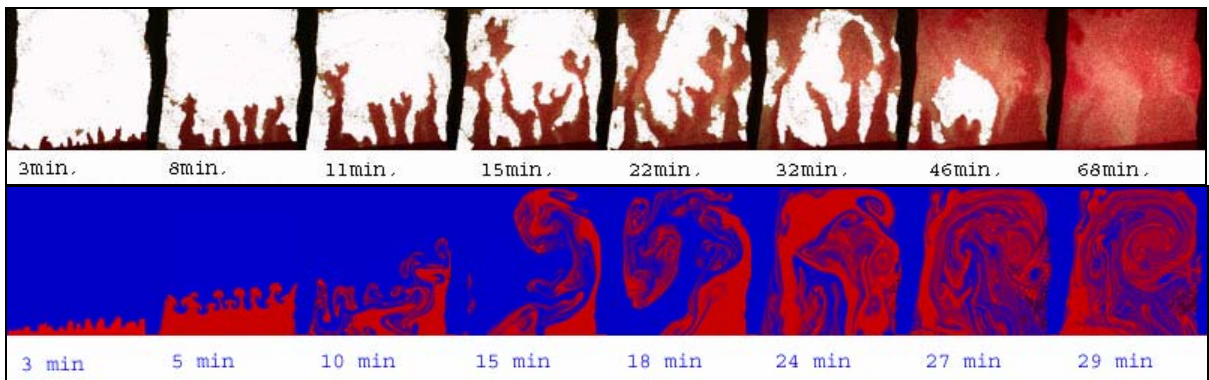


Figure 9.32 Kerosene-pentane diffusion for co-current, vertical case (a) experimental observations, (b) LBM simulation of the process.

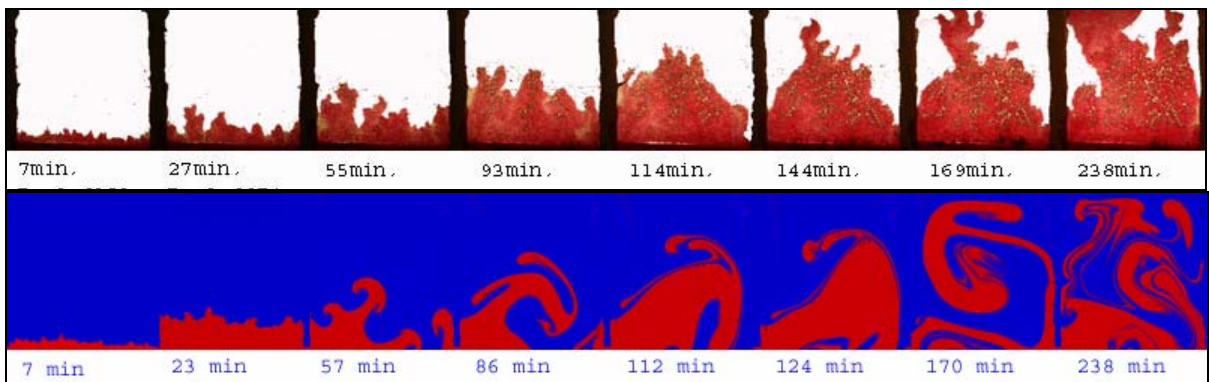


Figure 9.33 Mineral oil-pentane diffusion for co-current, vertical case (a) experimental observations, (b) LBM simulation of the process.

Note that the porous media characteristics of the model have not been taken into account in this study. The relatively simple design of the model, i.e., homogeneous and unconsolidated design of the same size of standard glass beads, made this assumption to be valid. Inclusion of the characteristics of natural porous medium is still a challenge for the LBM modeling. There are studies to include the effect of porous media, in a manner that low resolution, low grid size simulations can be run [Yoshino and Inamuro, 2003; Dardis and McCloskey, 1998]. Although these studies are useful at macro scale, it would not be possible to model fingering behaviour observed in the experimental part of this study using grain size grids. It is possible to run LBM model through real pore structure, however vast computing power and real digitized rock structure is required.

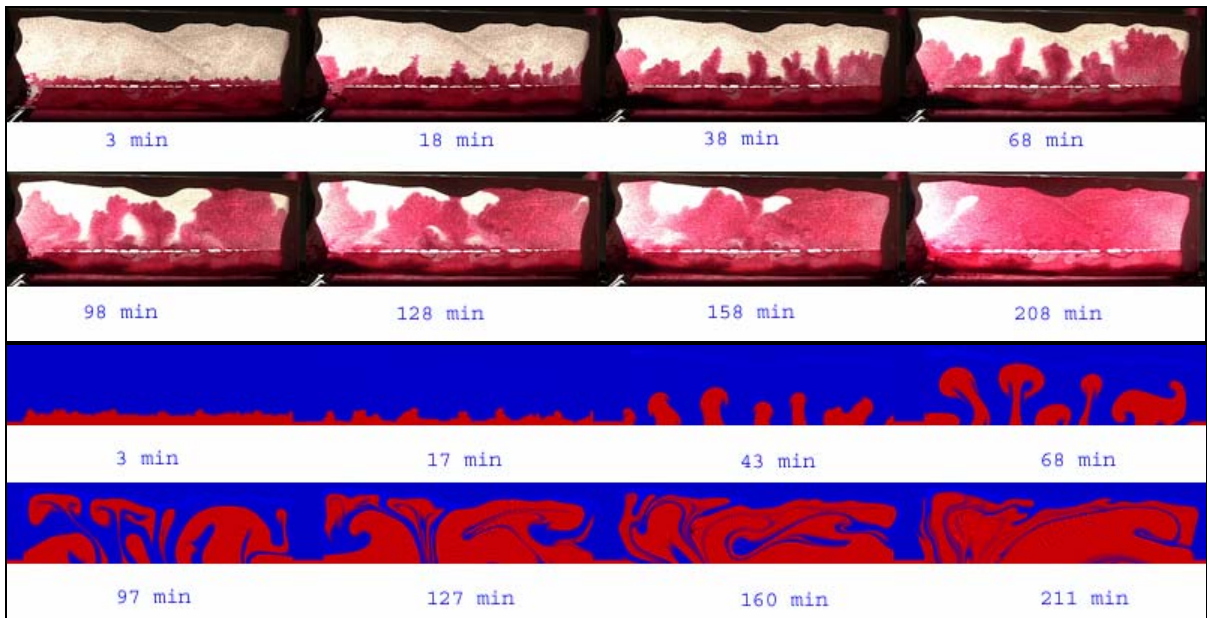


Figure 9.34 Mineral oil-pentane diffusion for counter – current, vertical case with 2:1 aspect ratio (a) experimental observations, (b) LBM simulation of the process.

The LBM is well suited to model dispersion, particularly in the intermediate Peclet (defined as $W.U/D_m$ where W is the width, U is the velocity and D_m is the diffusion coefficient) number range. This corresponds to the region where neither diffusion nor fluid flow dominates the spreading of solute. It is time dependent, and viscosity and diffusion coefficient changes can be accurately reflected in this model. Since the LBM is required to be scaled accordingly for the constraints of the algorithm, time has to be scaled back to real time simulation values. This is done using Eq. 46.

Experiments in the horizontal orientation and the initial stage for vertical oriented samples were purely diffusion dominated. The random behaviour observed in these processes was captured to some extent as can be seen through the comparison of the experimental and stochastic images. This was achieved by capturing the random walk stage at the early times of the process visually, and the LBM was applied just at the end of this step. This typically corresponds to the first few minutes of each experiment. Solvent was fed through these nodes initially to create the disturbance, which is believed to be affecting the overall behaviour. As diffusion loses its dominant power, the nodes previously invaded by random walk became the paths for solvent feed.

Finally, the major assumptions, limitations, and strengths of the modeling study presented in this part are listed below:

1. No characteristics of porous medium were included in the modeling study. The process time and type are dependent on the pore structure and heterogeneity and this constitutes the next phase of the study,
2. The transfer process starts as a random - diffusion – process. The LBM is not so strong to model this process. To preserve accuracy at later stages, solvent is fed into model through the randomly invaded nodes. After filling a few layers of pores through this process with a random displacement process, the LBM algorithm is started.
3. The finger development at early stages and the dispersive flow (natural convection due to gravity and diffusion) process were captured in all co- and counter-current interaction cases regardless the orientation and fluid viscosity.
4. The DLA modeling was limited to horizontal case and the model was not capable of reflecting the gravity and viscosity effects. It, however, successfully captured the random fingering process and later diffusion for the horizontal cases.
5. The time conversion value was observed quite universal.
6. Using microscale phenomena the macroscale behaviour was captured by the LBM modeling. Note that the LBM approach presented a modeling technique that does

not require any further input based on experimental observations and/or semi-empirical correlations. In the modeling study, only the viscosity term and the boundary conditions were input and the gravity term was added if it is vertical displacement.

9.3.2 Immiscible Model

The immiscible model follows a similar basic algorithm as given before for the miscible case. The main difference is that it is required to create cohesion between fluids. The LBM proposed in this study uses a 9-speed structure, in a square lattice which is commonly expressed as D2Q9 (2 dimensions, 9 velocities). The adapted Shan-Chen [1993] method (also known as pseudo-potential) in which the basic variables of the models are the distribution functions, where R_i is red (water) and B_i is blue (oil) fluid densities. Shen and Chen introduced this model for immiscible displacement in porous media. We, in this research, adapted this model for spontaneous imbibition (quasi static displacement) which requires a very low capillary number range.

The collision functions as in Eqs. 27 and 28 in miscible model are replaced with

$$R_i(x + c_p t + 1) = R_i(x, t) + \lambda_{vR} R_i^{neq}(x, t) \dots\dots\dots 47$$

$$B_i(x + c_p t + 1) = B_i(x, t) + \lambda_{vB} B_i^{neq}(x, t) \dots\dots\dots 48$$

These two equations represent the particles at node(x,t) move with the unit speed c_i . Here λ_{vR} and λ_{vB} are the relaxation parameters which determine the kinematic viscosity ν of each phase respectively. The relationship between those parameters is given as

$$\nu_R = \frac{1}{3} \left(\lambda_{vR} - \frac{1}{2} \right) \dots\dots\dots 49$$

$$\nu_B = \frac{1}{3} \left(\lambda_{vB} - \frac{1}{2} \right) \dots\dots\dots 50$$

The non-equilibrium distributions are given as

$$R_i^{neq} = R_i - R_i^{eq} \quad \dots\dots\dots 51$$

$$B_i^{neq} = B_i - B_i^{eq} \quad \dots\dots\dots 52$$

where (for 9 speed architecture)

$$R_i^{neq} = w\rho(1 + 3c_i \cdot u + 9/2(c_i \cdot u)^2 - 3/2(u \cdot u)) \dots\dots\dots 53$$

$$B_i^{neq} = w\rho(1 + 3c_i \cdot u + 9/2(c_i \cdot u)^2 - 3/2(u \cdot u)) \dots\dots\dots 54$$

The mass density per site is defined as follows

$$\rho = \sum_i R_i + B_i \quad \dots\dots\dots 55$$

Then, the momentum density can be written as

$$\rho u = \sum_i c_i (R_i + B_i) \quad \dots\dots\dots 56$$

The vectors c_i are velocity vectors on the lattice connecting neighboring nodes. On the square lattice one of these c_i 's have zero length, four of them have unit length (vertical and horizontal vectors), and the rest four has $\sqrt{2}$ length (diagonals) as depicted in Fig. 9.26. The weight factors (w_i) are chosen to obtain isotropy of velocity moments and depend only on the lengths of the c_i 's.

$$w_i = \begin{cases} \frac{4}{9} & \text{for } i = 0 \\ \frac{1}{9} & \text{for } i = (1,3,5,7) \\ \frac{1}{36} & \text{for } i = (2,4,6,8) \end{cases} \quad \dots\dots\dots 57$$

From Eq. 56, the flow is defined as

$$u = \frac{1}{\rho} \sum_i (R_i + B_i) * c_i \quad \dots\dots\dots 58$$

It should be noted that for immiscible fluids where the fluids are separated by a thin line, one of the phases (red or blue) is going to be zero.

Until now the basic equations of the LBM are given. These equations are not designed to handle external body forces, such as gravity, solid adhesion (wettability) or fluid cohesion (interfacial tension). The additional forces, namely wettability (solid adhesion), IFT (fluid-fluid cohesion) and gravity are added to velocity vector as follows:

$$u = \frac{1}{\rho} \sum_i (R_i + B_i) * c_i + F_g + F_c + F_a \dots\dots\dots 59$$

$$F_g = \rho_f g * \Delta m \dots\dots\dots 60$$

where ρ_f denotes the occupation number for the carrier fluid (oil), g is gravity, and is scaled mass. F_a and F_c is not equal to zero only when the neighbour is not the same as the occupied node. Simply the solid adhesion (F_a) is only applicable when the neighbour of the target cell is a solid node. Similarly, fluid-fluid cohesion (F_c) is non-zero when the neighbour node is occupied with the fluid of different type. Value of F_a and F_c are assigned empirically and would change as the viscosities (relaxation parameters) of the fluids change.

Because of the numerical constraints of the LBM, it is not possible to directly input the variables and therefore, scaling has to be applied. Since IFT and wettability is viscosity dependent, fluid viscosities have to be scaled first.

Having in hand the real values of fluids and model we need to define:

1. the viscosities of the fluid phases ν [m/s^2]
2. the surface tension σ [N/m]
3. the strength of external force (gravity) g [m/s^2]
4. the densities of fluids ρ [kg/m^3]
5. the size of an LBM cell Δx [m] (resolution dependent)

These parameters are used to set a reasonable time step size Δt [s] and limit the mass difference in the simulation Δm [kg]. Values of lattice boltzmann simulation are dimensionless, they are calculated as:

1. lattice viscosity = $\nu * (\Delta t / \Delta x^2)$
2. lattice surface tension = $\sigma * (\Delta t^2 / \Delta m)$
3. lattice force = $g * (\Delta t^2 / \Delta x)$
4. lattice density = $\rho * (\Delta x^3 / \Delta m)$

Here, the lattice density is used while calculating the external force (gravity). Occupation numbers for simulation of both phases are taken as unity. The value of Δt [s] will be used in matching the real experimental time values.

To define IFT and wettability, empirical constants F_a and F_c have to be calibrated for the desired fluids. To define these constants, virtual experiments were performed in different studies [Christensen. 2006; Chin et al., 2002]. A commonly used method to define fluid-cohesion parameter is to simulate varying sizes of droplets and check their compliance with the Laplace's law [Shan and Chen, 1993; Pan et al, 2004]. According to this, pressure difference within the droplet has to be larger than the surrounding fluid pressure.

Similarly solid adhesion F_a is defined using simulations. Both a droplet on a solid surface, and also virtual capillary tubes are used to calibrate the parameter as suggested by Christensen et al. [2006]. Since a strongly water wet media is desired, zero contact angle is assigned for F_a .

The parameters should be chosen within the algorithm constraints. The fluid viscosity ν is scaled, where this is used to calculate relaxation parameter (λ_{rR} and λ_{rB}). The way relaxation parameter is defined (Eq. 51 and 52) puts restriction to relaxation parameter; which is defined as: $0.51 < \text{relaxation parameter} < 2.5$. Therefore, the scaling of the viscosity and definition of lattice time scale is chosen accordingly.

Apart from theoretical ones, practical constraints also limit the range of viscosity. Our simulation runs showed that the interface between two phases becomes fuzzy for viscosity ratios four and higher. In an effort to make the interface sharper, fluid-fluid cohesion (F) constant was increased and this caused instabilities in the runs. Similar limitations of the method were also reported by different researchers [Thurey, 2005; Chin et al., 2002]

The results of kerosene-water simulations are given in **Fig. 9.35** for the counter-current model of vertical orientation. Fig 9.36 displays the horizontal orientation. The gravity is apparently effective for the co-current model (Fig 9.37). Good time and behaviour match was obtained even though the heterogeneity of the glass-bead models was thought to be a critical issue. The time match is not as high quality as for the co-current simulation compared to the counter-current equivalent (Fig. 9.37). This is probably due to problems in the representation of the experimental model characteristics in exact manner on the LBM. Note that the gravity apparently controls the flow strongly on the top portion of the model as captured also captured well on the LBM simulation. But, the LBM simulations showed some small amount of intrusion from the bottom portion totally controlled by capillary forces and this was not observed in the experimental case.

The model was also tested at micro-model scale. The model pattern was digitized and the simulation was run on this image (**Fig. 9.39**). The displacement is controlled by counter-current action even though the other end is open to flow. The portion of the micro-model shown in Figs. 9.38 and 9.39 and its LBM equivalent given in Fig. 9.39 covers a very small part of the model and we observed during the experimentation that the effect of open – opposite- boundary has not been felt yet. Therefore, the displacement occurred totally by capillary forces.

Comparing the two cases given in Figs. 9.28 and 9.29, one can observe that the development of residual phase saturation and the progress of the front are in a very similar fashion in both simulation and experiment. For the strongly water-wet medium the process is controlled by the pore structure (or pore scale heterogeneity). This can be seen in Fig. 9.28 by a rapid movement of the wetting phase in the smaller pores compared to bigger size pores. In other words, the process follows the general rule of capillarity, i.e., the smaller size pores are occupied first by the wetting phase. The same was captured in the simulation as marked by

dotted arrows on the first three images of Fig. 9.39. Obviously, in case of less favourable wettability (mixed or intermediate wet) rather than strongly water-wet medium, the wettability will start playing a role on the dynamics of the process in addition to the pore size and heterogeneity. One can also observe that the experimental and simulation results exhibit a good match for the time values and the frontal progress observed in the experiments was captured successfully in the simulation.

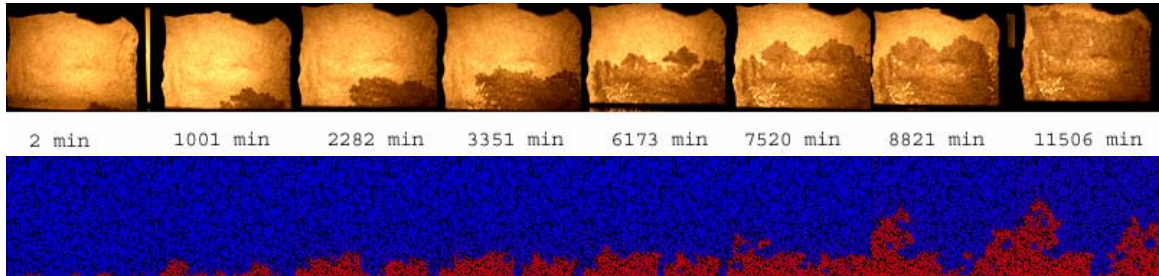


Figure 9.35 Kerosene - water counter-current imbibition a)experiment b)simulation using LBM. Time values are same with experimental values. (Vertical orientation)

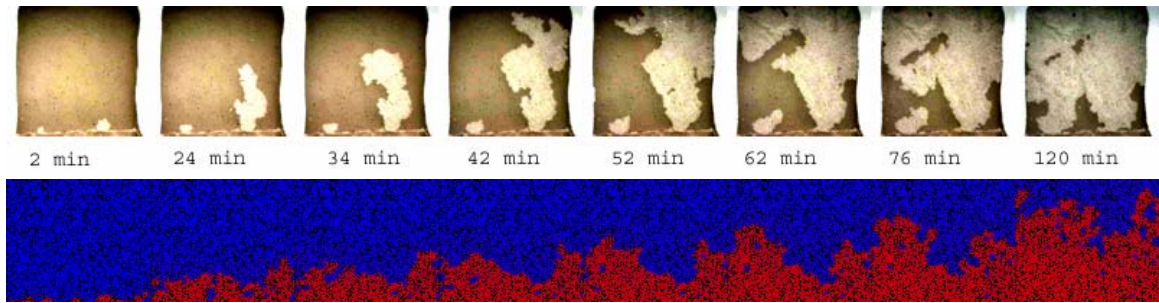


Figure 9.36 Kerosene - water counter-current imbibition a)experiment b)simulation using LBM. Time values are same with experimental values. (Horizontal orientation)

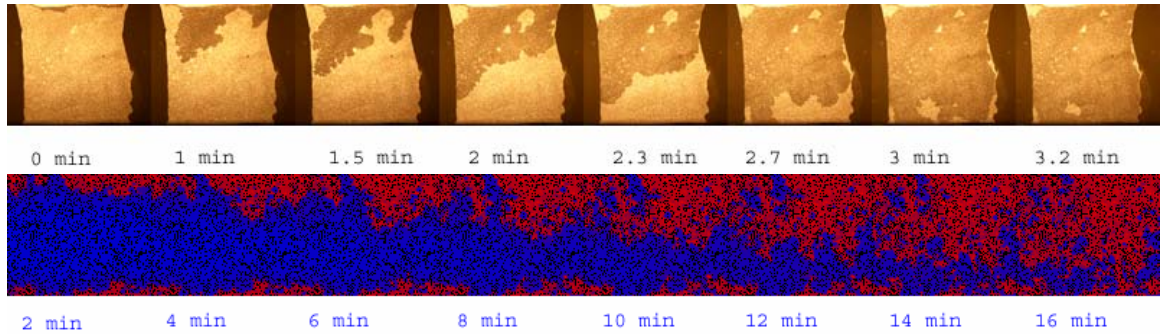


Figure 9.37 Kerosene - water co-current imbibition a)experiment b)simulation using LBM. (Vertical orientation)

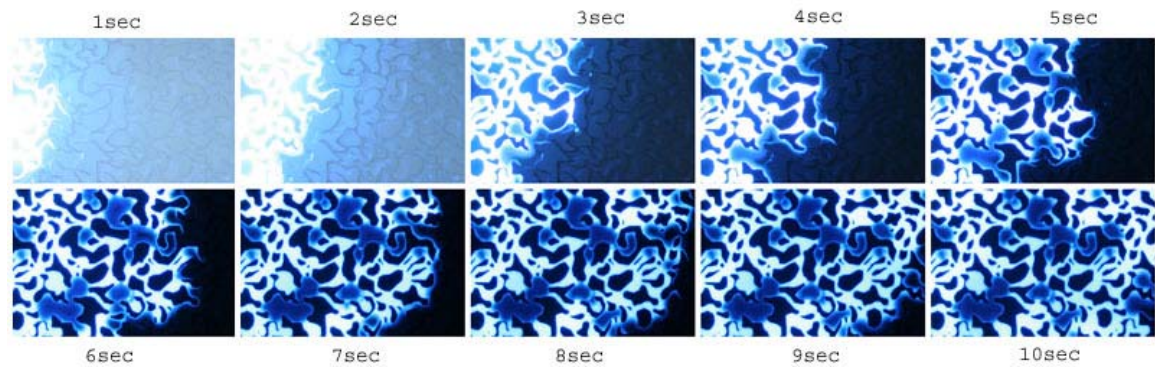


Figure 9.38 Time-lapse visualization of spontaneous imbibition on the micro-model. Water imbibe from left (white color) displacing kerosene (blue color). Each image is 500 μm wide and magnified 20X.

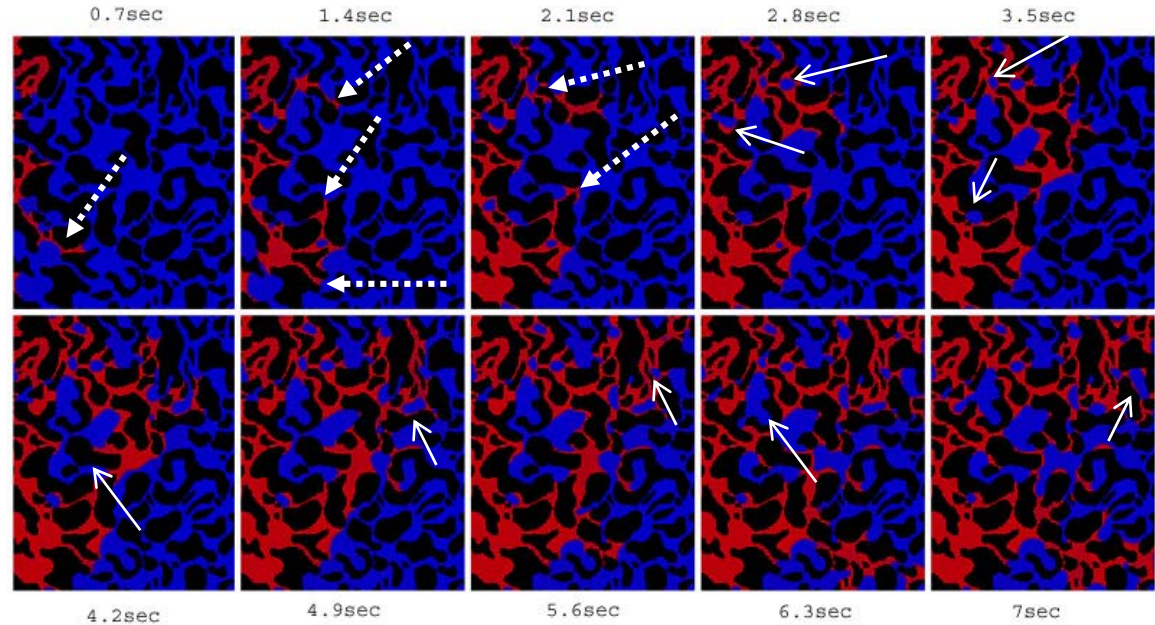


Figure 9.39 Simulation results of spontaneous imbibition at micro scale. Water imbibe from left (red color) displacing oil (blue color). Dotted arrows on the first three images indicate the invasion of the smallest size pores first. Solid arrows on the rest of the images point the residual saturation development. Displacement is controlled by counter-current action even though the other end is open to flow. This portion covers a very small part of the model and the effect of open –opposite- boundary has not been felt yet. Therefore, the displacement occurs in counter-current manner during the time period covered in this figure.

10 Conclusion

10.1 Accomplishments

Miscible and immiscible transfer of liquid-liquid and gas-liquid pairs between matrix and fracture under static conditions are modeled and analyzed. Although they are studied separately, the experimental program followed is similar for both immiscible and miscible experiments. To clarify the dynamics of the process, core experiments are performed first. The recovery curves (quantitative data) coupled with visual experimentation (qualitative data) provided a methodology to identify the dynamics of the processes, i.e., the progress of the fluid front and the distribution of the phases in the matrix that results in the development of residual oil (or gas) saturation. Both mechanisms are modeled using the Lattice Boltzmann Method (LBM), owing to its ability to adapt different parameters and to be able simulate complex boundary conditions.

The following are the conclusions withdrawn from the research work presented in this dissertation:

10.1.1 Immiscible interaction: Core studies.

10.1.1.1 Gas – liquid (water displacing gas in the matrix by capillary imbibition)

1. It has been observed that oil-water pair dynamics are remarkably different than air-water pair imbibition. For the air-water pair experiments, as the temperature is increased from 20°C to 90°C, more fingering occurs. But this does not translate into an increase in recovery rate. For the counter-current interaction of low temperature case, it is observed that the fluid front shows a bullet profile, and is affected by the matrix shape factor. In case of the co-current interaction, a more random front was obtained and the recovery was observed to be faster than counter-current interaction.
2. The optimum core size in gas-water case was observed to be 0.5 inch diameter and 6 inches of length, both in terms of the recovery rate and ultimate recovery for low temperature air - water imbibition experiments.
3. Residual gas saturation is sensitive to the matrix shape factor (or core dimensions) for the counter-current imbibition of water into gas saturated systems.
4. The effect of surface tension on the recovery rate and ultimate recovery in the counter-current type interaction is critical. Although the horizontal cases did not show any significant change in terms of the recovery trend (but showed an increase in the ultimate recovery), the vertical cases yielded different recovery rates and ultimate recoveries with increasing temperature. Lower residual gas saturation was obtained only for certain core sizes (typically high diameters) with increasing temperature. That was attributed to the reduction in surface tension.
5. Four different scaling groups were tested. Eqs. 6, 7, and 9 (horizontal only) were observed useful for scaling for low temperature experiments. High temperature cases were more difficult to obtain a scaling behavior. Only Eq. 5 and 7 showed a grouping indicating that they further can be considered for improvement.

10.1.1.2 Liquid – liquid (water displacing oil in the matrix by capillary imbibition)

1. Oil-brine cases did not show any scaling when the recoverable oil was plotted against the classical dimensionless group (Eq. 11) for horizontal cases. Vertical cores for oil-brine cases, however, showed that a scaling behavior could be obtained if the wettability factor is also included. Although no significant difference in the ultimate recoveries was observed among all the samples, 1” diameter cores yielded the fastest recovery rate indicating the existence of an optimum rate.
2. Despite the viscosity difference, mineral oil yielded a faster recovery rate for a larger diameter and longer cores compared to the kerosene case. This indicates that the matrix shape factor is a dominant factor over the viscosity assuming that both kerosene and mineral oil have similar wettability characteristics. By introducing an empirical shape factor (Eq. 19), classical (Eq. 11) and two other scaling equations (Eqs. 14 and 17) were tested. It was shown that better results could be obtained with a careful calibration of the shape factor. The effect of the new shape factor (characteristic length) given in Eq. 19 on the improvement of the correlations was more remarkable for the residual oil saturation relationship compared to the scaling.
3. The effect of IFT on the recovery rate and ultimate recovery in the counter-current type interaction was very critical. Surfactant concentrations above the CMC yielded a very inefficient imbibition for smaller diameter cores. For the larger cores, no effect of surfactant concentration was observed.
4. To clarify the effect of wettability on the process, limestone and aged Berea sandstone samples were tested. Under the assumption of Berea sandstone samples either aged or non-aged accommodates the same pore structure, the rate of recovery is observed to be slower, yet the ultimate recoveries stayed unaffected. This indicates that the wettability effect is critical on the recovery rate and pore structure is dominant over ultimate recovery for counter-current interaction.

10.1.2 Immiscible interaction: Visualization studies

1. Significant differences were observed between oil-water and air-water capillary imbibition dynamics and phase distribution in the matrix. For the air-water pair it was noticed that more fingering was observed as the temperature is increased. But this does not translate into an increase in the rate of non-wetting phase recovery. For counter-current interaction, it was observed that fluid front shows a bullet profile at low temperature, and the matrix shape factor (aspect ratio) significantly controls the phase distribution in the matrix. For co-current interaction, more random progress of the front was observed. High temperature cases yielded more air entrapment behind the front.
2. For the counter-current experiments of oil-water pair, the fluid front progressed in a bulk fashion regardless of the viscosity difference in vertical cases. For horizontal orientation, in the absence of gravity effect, the wetting phase invasion developed from a single point as a “single finger” and displacement was achieved by the growth of this finger, which was much thicker in case of mineral oil compared to the kerosene case
3. For co-current interaction, when the two (bottom and top parts) sides are in contact with the wetting phase, fingering was remarkable for the high viscosity oil. The kerosene case represented a better sweep caused by more favorable mobility. If the top part is not in contact with the wetting phase, more fingering was observed in case of kerosene.
4. Aged sample showed significant change in the dynamics. The invasion of wetting phase into matrix was observed to occur from a single point and grew from this point instead of uniform frontal progress as similar to the displacement pattern observed for the horizontal cases.

10.1.3 Immiscible interaction: Modeling by the Lattice Boltzmann method

1. The LBM was able to capture the physical mechanism, and was accurate enough to display a similar residual oil saturation patterns as in the experimental case performed on the micro-model.
2. The same model was applied to glass-bead experiments in an effort to model kerosene-water interaction. Similar fingering behaviour, the effect of gravity, and lattice time-real time conversion were successfully captured.
3. The previous finding on application limits of the LBM technique for immiscible displacement, i.e., the maximum allowable viscosity ratio is four, was also verified.

10.1.4 Miscible interaction: Liquid-liquid pair (solvent displacing oil in the matrix by diffusion and convection)

10.1.4.1 Core experiments

1. Though it is not feasible in terms of the recovery time and potentially the cost of the process, oil recovery by diffusion only is the most effective way of producing oil. Its recovery can go up to 95% OOIP for uncoated samples but the process was observed to be slow.
2. When the recovery was normalized by dividing ultimate recoveries by the duration of recovery, it was observed that the primary imbibition followed by diffusion is more efficient process compared to starting the project with diffusion process. This is more prominent for strongly water wet cases.
3. For unaged samples, diffusion alone is not effective since substantial recovery could be obtained from capillary imbibition. But as the wettability changes, oil production by imbibition turns out to be slower, and in long term ultimate recovery would be less compared to diffusion. As the matrix becomes more oil-wet, primary diffusion becomes more competitive and feasible.

4. In case of counter-current diffusion, the pore structure of matrix plays a more critical role in comparison to the fluid properties and the wettability of matrix does not seem to affect diffusion mechanism.
5. For practical applications, optimal strategy should be determined based on the conditions and matrix characteristics including wettability, size and interaction type. For certain circumstances, starting the enhanced oil recovery process by solvent injection instead of waterflooding might be competitive and in return would increase the ultimate recovery significantly in naturally fractured reservoirs.

10.1.4.2 Visualization study

1. Vertically positioned models showed a “convective” displacement characteristics caused by the gravity effect, which alters the pressure distribution created by the boundary condition of matrix block. This buoyancy effect transforms the slow diffusion process to a faster convection process. Depending on the fluid properties, especially viscosity, the displacement process might diverge from convective dispersion to frontal diffusion, i.e., a displacement front progressing in a stable manner without eminent fingers. The mineral oil-pentane diffusion case of co-current interaction (Fig. 9.23) was the typical example for this situation.
2. Viscosity and displacement direction were observed critical on fingering. The most significant fingering was obtained in case of kerosene-pentane displacement in the vertical direction, especially for the co-current models. Co-current models yielded more fingering initially. For the counter-current cases, “buoyant convection” was more significant.
3. The oil displacement experiments for the vertical displacement cases had two stages. Initially solvent disperses up in the shape of fingers by diffusion. As the lighter component reaches the upper boundary, it accumulates on the top part and then a – free- convection due to density difference caused by mixing starts dominating the displacement process.

4. Horizontal experiments were diffusion dominated, that was dependent on the boundary conditions of the model. The fronts proceeded randomly through the “easy flow zones” (edges of the model) for co-current interaction. In case of counter-current interaction, bulk diffusion type displacement yielding a frontal progress was obtained. Oil recovery was slower compared to the vertical orientation and no fingers were observed especially in the later stages of the process.

10.1.4.3 Stochastic and Lattice Boltzmann models

1. A stochastic model reminiscent of the invasion percolation and diffusion limited aggregation algorithms was developed to model horizontal displacement. Time spent during the displacement process was calculated using an empirical correlation (a relationship between time and diffusion coefficient), number of iterations and residence time in each grids. The values obtained from the simulations were in good agreement with the experimental values. The fractal dimensions of the experimental and simulation fronts were compared and reasonable matches between the experiments and simulations were observed, especially for the counter-current cases.
2. The DLA type modeling was quite suitable for the horizontal (bulk) diffusion process since this is a diffusion dominated process. Controlling parameter for this process is observed to be diffusion coefficient. Once the iteration-time relationship was established, it was applied successfully for the horizontally oriented samples. For the vertically oriented samples however, a more powerful tool is required. The LBM was chosen due to its capability in handling complex boundaries and accuracy for the processes near the intermediate Peclet number region. Although the model was not as accurate in terms of capturing the randomness and small fingers on horizontal orientation, it showed reasonable match for the later stages of the process (Figs. 9.18b and 9.19b). The LBM was also successful in capturing the, convective type process and the immediate change from diffusion to dispersion (natural convection and diffusion) was achieved just with the introduction of gravity term (Figs. 9.20b, 9.21b, 9.22b, 9.23b).

3. For the kerosene cases, less gravity effect was applied compared to mineral oil due to lower density difference. Less gravity effect and less viscous oil phase translate into more fingering and faster transfer by convection for both co-current and counter-current cases (Figs. 9.20b and 9.23b). Difference between the mineral oil and kerosene cases can be successfully reflected by changing the viscosity and gravity terms.
4. The co-current cases were simulated by assigning constant pressure at the top of the model and this was achieved by assigning the top nodes to constant density. Low pressure zone at the top of the models magnified the effect of gravity especially for mineral oil. The mechanism was not convection for the whole life of the process. It starts as diffusion initially for a short time, then converts into dispersive flow (natural convection due to gravity and diffusion) (Figs. 9.22b and 9.23b).

10.2 Future Work

1. Experimental procedure is observed to be very beneficial to model matrix-fracture interaction for immiscible and miscible cases. More universal models can be developed by including wider scales of viscosity, more heterogeneous pore size distributions, and more oil wet systems.
2. Due to preparation restrictions, initial water in the models were ignored. Its effect especially in the miscible interaction with oil-wet and water-wet matrix needs visual (2D and micro model) studies.
3. Micro-models were not tested for miscible displacement and the priority was given to immiscible interaction. The effect of pore structure could be investigated on not only sandstone pore structures but also more complex carbonate replicas.
4. It was observed that LBM is a very powerful tool in modeling both miscible and immiscible interaction, especially in capturing the boundary condition and pore distribution effects. The model is fairly new and it attracts great attention from many disciplines. In its current form it can model fluid flow as long as constraints are met

(viscosity ratio between fluids – fluid velocities – model scales etc.). It will not take much time for this model to be perfected, and be applied for the oil industry. The achievements can be implemented within reservoir simulation software (especially discrete fracture network simulators) to model large scale reservoirs.

5. The LBM model developed can be improved to generate relative permeability curves for modeling co-and counter-current matrix-fracture transfer in naturally fractured reservoirs.

11 Bibliography

Austad T., Matre B., Milner J., Saelig vareid A., and Oslashyno L., 1998. Chemical Flooding of Oil Reservoirs. Spontaneous Oil Expulsion From Oil- and Water-Wet Low-Permeable Chalk Material by Imbibition of Aqueous Surfactant Solutions. *Coll. and Surf. A: Phys. and Eng. Aspects*. 137: 117-129.

Austad T., Milner J., 1997. Spontaneous Imbibition of Water Into Low Permeable Chalk at Different Wettabilities Using Surfactants. SPE 37146, Int. Symp. on Oilfield Chem., Houston, TX.

Babadagli T., 1992. Aspects of Counter-Current Imbibition on Two-Phase Flow in Fractured Rocks. Ph.D. Thesis, University of Southern California, Department of Chemical Eng., Petroleum Eng.

Babadagli T., 1996. Temperature Effect on Heavy-Oil Recovery by Imbibition in Fractured Reservoirs. *J. of Petroleum Science and Eng.*, 14 (3/4): 197.

Babadagli T., 2000. Efficiency of Capillary Imbibition Dominated Displacement of Non-Wetting Phase by Wetting Phase in Fractured Porous Media. *Transport in Porous Media*, 40(3): 323-344.

Babadagli T., 2001. Scaling of Cocurrent and Countercurrent Capillary Imbibition for Surfactant and Polymer Injection in Naturally Fractured Reservoirs. *SPE Journal* (Dec. 2001) 465-478.

Babadagli T., 2002. Dynamics of Capillary Imbibition When Surfactant, Polymer, and Hot Water Are Used as Aqueous Phase for Oil Recovery. *J. Coll. and Int. Sci.* 156: 203-213.

Babadagli T., 2003. Analysis of Oil Recovery by Spontaneous Imbibition of Surfactant Solution. SPE 84866, Asia Pac. Imp. Oil Rec. Conf., Kuala Lumpur, Malaysia.

Babadagli T., 2006. Evaluation of Critical Parameters in Oil Recovery from Fractured Chalks by Surfactant Injection. *J. Pet. Sci. and Eng.* 54(1-2): 43-54.

Babadagli T. and Ershaghi I., 1992. Imbibition Assisted Two-Phase Flow in Natural Fractures. SPE 24044, Western Reg. Meet., Bakersfield, CA.

Babadagli T. and Hatiboglu C.U., 2005. Analysis of Counter-Current Gas-Water Capillary at Different Temperatures" SPE 93882, Western Regional Meeting, Irvine, CA.

- Babadagli T. and Hatiboglu C.U., 2007. Analysis of Counter-Current Gas-Water Capillary Imbibition at Different Temperatures. *J. Pet. Sci. and Eng.* 55: 277-293
- Babadagli T., Hatiboglu C. U. and Hamida, T., 2005. Evaluation of Matrix-Fracture Transfer Functions for Counter-Current Capillary Imbibition. SPE 92111, Asia Pacific Oil & Gas Conf. and Exh., Jakarta, Indonesia.
- Benzi R., Succi S. and Vergassola M., 1992. The Lattice Boltzmann Equation: Theory and applications. *Phys. Rev. E* 222(3): 145-197.
- Birkholzer J., 2003. Penetration of Liquid Fingers into Superheated Fractured Rock. *Water Res. Res.*, 39(4): 1102.
- Birovljev A., Furuberg L., Feder J., Jssang T., Mly K. J., and Aharony A., 1991 Gravity Invasion Percolation in Two Dimensions: Experiment and Simulation. *Physical Review Letters*, 67 (5):584-587.
- Blunt M., King M. J., Scher H., 1992. Simulation and theory of two-phase flow in porous media, *Phys. Rev. A*, 46(12): 7680-7699.
- Bourbiaux B. J., Kalaydjian F. J., 1988. Experimental Study of Cocurrent and Countercurrent Flows in Natural Porous Media. SPE 18283, Annual Tech. Conf. and Exh., Houston, Texas.
- Bouzidi M., Firdaouss M. and Lallemand P., 2001. Momentum Transfer of a Boltzmann-Lattice Fluid with Boundaries. *Physics of Fluids*, 13(11): 3452-3459
- Buick J. M. and Greated C. A., 2000. Gravity in a lattice Boltzmann model. *Physical Review E*, 61 (5): 5307-5319
- Cali A., Succi S., Cancelliere A. and Benzi R., 1992. Gramignani M. Diffusion and Hydrodynamic Dispersion with the Lattice Boltzmann Method. *Phys. Rev. A* 45(8): 5771-5775
- Chen S., Dawson S. P., Doolen G. D., Jannecky D. R. and Lawniczak A., 1996. Lattice Methods and Their Applications to Reacting Systems. *Computers Chem. Eng.* 19(6/7): 617-646.
- Chin J., Boek E. S., and Coveney P. V., 2002. Lattice Boltzmann Simulation of the Flow of Binary Immiscible Fluids with Different Viscosities Using the Shan-Chen Microscopic Interaction Model. *Proc. R. Soc. London. A.* 360: 547
- Christensen B. S. B., 2006., Using X-ray Tomography and Lattice Boltzmann Modeling to Evaluate Pore-scale Processes in Porous Media. PhD Thesis, Institute of Environment & Resources, Technical University of Denmark.
- Civan F. and Rasmussen M.L., 2003. Modeling and Validation of Hindered-Matrix-Fracture Transfer for Naturally Fractured Petroleum Reservoirs. SPE 80918, SPE Mid-Continent Oper. Symp., Oklahoma City, OK.
- Civan F. and Rasmussen M.L., 2005. Determination of Parameters for Matrix-Fracture Transfer Functions from Laboratory Data. SPE 94267 Prod. and Oper. Symp., Oklahoma City, OK.
- Da Silva F. V. and Belery P., 1989. Molecular Diffusion in Naturally Fractured Reservoirs: A Decisive Recovery Mechanism. SPE 19672 Annual Technical Conf. and Exh., San Antonio, TX.

- Dardis O. and McCloskey J., 1998. Lattice Boltzmann Scheme With Real Numbered Solid Density for the Simulation of Flow in Porous Media. *Phys. Rev. E*. 57 (4): 4834-4837.
- Doolen G. D. and Chen S., 2001. Lattice Boltzmann Method for Fluid Flows. *Annu. Rev. Fluid Mech.* 30: 329-364.
- Dullien F. A. L., 1992. *Porous Media: Fluid Transport and Pore Structure*. Academic Press, San Diego, California.
- Ferer M., Bromhal G. S., Smith D. H., 2003. Pore-Level Modeling of Immiscible Drainage: Validation in the Invasion Percolation and DLA Limits. *Physical Review E*, 67: 051601.
- Fernandez J. F., Rangel, R., and Rivero J., 1991. Crossover Length from Invasion Percolation to Diffusion-Limited Aggregation in Porous Media. *Physical Review Letters*, 67(21): 2958-2961
- Flekkoy E. G., 1993. Lattice BGK models for Miscible Fluids. *Physical Review E*, 47: 4247-4258.
- Flekkoy E. G., Oxaal U., Feder J. and Jossang. T., 1995. Hydrodynamic Dispersion at Stagnation Points. *Phys. Rev. E*. 52(5): 4952-4962
- Frisch U. Hasslacher B. and Pomeau Y., 1986. Lattice-Gas Automata for the Navier-Stokes Equation. *Phys Rev Lett*. 56:1505
- George D. S., and Kovscek A. R., 2001. Visualization of Solution Gas Drive in Viscous Oil. Technical report, Stanford University, California..
- Ginzbourg I., Alder P. M., 1994. Boundary Flow Condition Analysis For the Three-Dimensional Lattice Boltzmann Model. *J. Phys. II* (4) 191-214.
- Gunstensen A. K., Rothman D. H., Zaleski S. and Zanetti G., 1991. Lattice Boltzmann Model of Immiscible Fluids. *Phys. Rev. A* 43 (8): 4320-4327.
- Handy L.L., 1960. Determination of Effective Capillary Pressure for Porous Media from Imbibition Data. *Trans. AIME*, 219: 75.
- Hamon G. and Vidal J., 1986. Scaling-Up the Capillary Imbibition Process from Laboratory Experiments on Homogeneous and Heterogeneous Samples. SPE 15852 European petroleum conf., London, UK.
- Hatiboglu C. U., Babadagli T., 2007-a. Oil Recovery by Counter-Current Spontaneous Imbibition: Effects of Matrix Shape Factor, Gravity, IFT, Oil Viscosity, Wettability, and Rock Type. *Journal of Petroleum Science and Engineering*. 59: 106-122
- Hatiboglu C. U. and Babadagli T., 2007-b. Primary and Secondary Oil Recovery From Different-Wettability Rocks by Countercurrent Diffusion and Spontaneous Imbibition. SPE 94120 accepted for publication in *SPE Reservoir Evaluation and Engineering*.
- Hatiboglu C. U. and Babadagli T., 2007-c. Lattice-Boltzmann Simulation of Solvent Diffusion into Oil Saturated Porous Media. Submitted to *Physical Review E* (in review).
- Hatiboglu C. U. and Babadagli T., 2007-d. Diffusion Mass Transfer in Miscible Oil Recovery: Visual Experiments and Simulation. Submitted to *Transport in Porous Media* (in review).

- Hatiboglu C. U. and Babadagli T., 2007-e. Experimental and Visual Analysis of Matrix-Fracture Interaction by Spontaneous Imbibition. Submitted to Water Resources Research (in review).
- Hatiboglu C. U. and Babadagli T., 2007-f. Experimental and Visual Analysis of Mass Transfer into Porous Media. Submitted to American Institute of Chemical Engineers (AIChE) (in review).
- Hatiboglu C. U. and Babadagli T., 2007-g. Lattice-Boltzmann Simulation of Spontaneous Imbibition into Oil Saturated Porous Media. Submitted to Physical Review E (in review).
- Hatiboglu C. U. and Babadagli T., 2005a. Visualization Studies on Matrix-Fracture Transfer Due to Diffusion. CIPC 2005-077, Canadian Int. Petr. Conf., 7-9 June, Calgary, Alberta, Canada.
- Hatiboglu C. U. and Babadagli T., 2005-b. Experimental and Stochastic Modeling of Diffusion Controlled Matrix-Fracture Transfer in Naturally Fractured Reservoirs. SPE 95474, Annual Technical Conference and Exh., 9-12 Oct, Dallas, TX.
- Hatiboglu C.U., Babadagli T., 2004-a. Experimental Analysis of Primary and Secondary Oil Recovery from Matrix by Counter-Current diffusion and Spontaneous Imbibition. Paper SPE 90312, Annual Technical Conference and Exh., 26-29 Sept, Houston, TX.
- Hatiboglu C.U., Babadagli T., 2004-b. Dynamics of Spontaneous Counter-Current Imbibition for Different Matrix Shape Factors, Interfacial Tensions, Wettabilities and Oil Types. CIPC 2004-091, CIM 55th Annual Technical Meeting, Canadian Int. Petroleum Conf., 8-10 June, Calgary, Canada.
- Hazi G., Imre A. T., Mayer G., and Farkas I., 2002. Lattice Boltzmann Methods for Two-Phase Modeling. Ann. Nuclear Energy, 29: 1421-1453.
- He X., Zou Q., Luo L.S. and Dembo M., 1997. Analytic Solutions of Simple Flows and Analysis of Nonslip Boundary Conditions for the Lattice Boltzmann BGK Model. J. Stat. Phys 87 (1/2): 115-136.
- Hornbrook J. W., Castanier L. M., and Pettit P., 1992. Visualization of Foam/Oil in a New High Resolution Sandstone Replica Micro-Model. Report SUPRI TR-86, Stanford University,
- Hughes R.G., Blunt M. J., 2001. Network Modeling of Multiphase Flow in Fractures. Advances in Water Resources 24: 409-421.
- Hughes R.G., Blunt M. J., 2000. Pore Scale Modeling of Rate Effects in Imbibition. Transport in Porous Media 40: 295-322.
- Indelman P. V., and Katz R. M., 1980. On Counter-Current Capillary Imbibition in a Hydrophilic Porous Medium. Izvestiya Akademii Nauk SSSR, Mekhanika Zhidkosti I Gaza, 2: 141-144. (translated from Russian).
- Kadanoff L., 1986. On Two Levels. Phys. Today 39: 7-9.
- Kantzas A., Pow M., Allsopp K., and Marenette D., 1997. Co-Current and Counter-Current Imbibition Analysis for Tight Fractured Carbonate Gas Reservoirs. paper 97-181, CIM Petroleum Conf. of the South Saskatchewan Section, the Petroleum Society of CIM, Regina, Saskatchewan, Canada.

- LaBolle E. M., Quastel J., Fogg G.E., and Gravner J., 2000. Diffusion Integration by Random Walks: Generalized Stochastic Differential Equations with Discontinuous Coefficients. *Water Resources Research*, 36: 651.
- Le Romancer J.F., Defives D. F., and Fernandes G., 1994. Mechanism of Oil Recovery by Gas Diffusion in Fractured Reservoir in Presence of Water. SPE 27746 SPE/DOE 9th Symposium on Improved Oil Recovery, Tulsa, April 17-20.
- Lenormand R., Zarcone C., Sarr A., 1983. Mechanism of the displacement of one fluid by another in a network of capillary ducts. *J. Fluid Mech.* 189: 165-187.
- Lenormand R., 1989. Flow Through Porous Media: Limits of Fractal Patterns. *Proc. R. Soc. Lond. A*, 423:159-168.
- Lenormand R., 1990. Liquids in Porous Media. *J.Phys, Condens. Matter*, 2:79-88.
- Lenormand R., Le Romancer J.F., Le Gallo Y. and Bourbiaux B., 1998. Modelling the Diffusion Flux Between Matrix and Fissure in a Fissured Reservoir. SPE 49007, Annual Technical Conf. and Exh., New Orleans.
- Li K. and Horne R.N., 2002. Scaling of Spontaneous Imbibition in Gas-Liquid Systems. SPE 75167, SPE/DOE Imp. Oil Rec. Symp., Tulsa, OK.
- Li K., and Horne R. N., 2000. Characterization of Spontaneous Water Imbibition Into Gas-Saturated Rocks. SPE 74703, SPE/AAPG Western Regional Meeting, Long Beach, California.
- Lolomari T.O., 1996. Micromodel Studies of Three Phase Flow in Porous Media. MS Thesis, Stanford University, CA.
- Ma S., Morrow N.R. and Zhang X., 1995. Generalized Scaling of Spontaneous Imbibition Data for Strongly Water Wet Systems. paper 95-138, 6th Petroleum Conference of the South Saskatchewan Section, the Petroleum Society of CIM, held in Regina, Saskatchewan, Canada.
- Martys N. S. and Chen H., 1996. Simulation of Multicomponent Fluids in Complex Three-Dimensional Geometries by the Lattice-Boltzmann Method. *Phys. Rev. E* 53(1): 743-751
- Mattax C. C. and Kyte J. R., 1962. Imbibition Oil Recovery from Fractured, Water-Drive Reservoir, *SPE Journal*, June:177-184.
- Medina A., Perez-Rosales C., Pineda A., and Higuera F. J., 2001. Imbibition in Pieces of Paper with Different Shapes. *Revista Mexicana De Fisica*, 47(6): 537-541.
- Medina A., Pineda A. and Trevino, C., 2003. Imbibition Driven by a Temperature Gradient. *J. of the Physical Soc. of Japan*, 72(5): 979.
- Milner J., and Austad T., 1996. Chemical Flooding of Oil Reservoirs, Evaluation of the Mechanism for Oil Expulsion by Spontaneous Imbibition of Brine With and Without Surfactant in Water-Wet, Low-Permeable, Chalk Material. *Coll. and Surf. A: Phys. and Eng. Aspects*, 113: 269-278.
- Morel D. D., Bourbiaux B., Latil, M. and Thiebot, B., 1990. Diffusion Effects in Gas-Flooded Light Oil Fractured Reservoirs. SPE 20516 Annual Technical Conf. and Exh., New Orleans.

- Morrow N.R. and Mason, G., 2001. Recovery of Oil by Spontaneous Imbibition. *Current Opinion in Coll.&Int. Sci.*, 6:321.
- Nourgaliev R. R., Dinh T. N., Theofanous T. G., and Joseph D., 2003. The Lattice Boltzmann Equation Method: Theoretical Interpretation, Numerics and Implications. *Int. J. Multiphase Flow*, 29: 117-169.
- Olayinka S. and Ionnidis, M. A., 2004. Time Dependent Diffusion and Surface-Enhanced Relaxation in Stochastic Replicas of Porous Rock. *Transport in Porous Media*, 54: 273-295.
- Pan C., Hilbert M., and Miller C. T., 2004. Lattice Boltzmann Simulation of Two-Phase Flow in Porous Media. *Water Resour. Res.*, 40: W01501, doi:10.1029/2003WR002120
- Polak A., Grader A. S., Wallach R. and Nativ R., 2003. Chemical Diffusion between a Fracture and the Surrounding Matrix: Measurement by Computed Tomography and Modelling. *Water Resources Research*, 39:1106.
- Pow, M., Kantzas A., Allan V., and Mallmes R., 1999. Production of Gas from Tight Naturally Fractured Reservoirs with Active Drive JCPT, 38(7): 38.
- Pringle S. E., Glass R. J., and Cooper C. A., 2002. Double-Diffusive Finger Convection in a Hele-Shaw Cell: An Experiment Exploring the Evolution of Concentration Fields, Length Scales and Mass transfer. *Trans. in Porous Media* 47: 195-214
- Raiskinmaki P., Shakib-Manesh A., Jasberg A., Koponen A., Merikoski J., and Timonen J., 2002. Lattice Boltzmann Simulation of Capillary Rise Dynamics. *J. Stat. Phys.*, 107:143-158.
- Rangel-German E. and Kovscek A.R., 2002. Experimental and Analytical Study of Multidimensional Imbibition in Fractured Porous Media. *J. of Pet. Sci. and Eng.* 36:45.
- Rangel-German E., Kovscek A.R., 2003. Time Dependent Matrix-Fracture Shape Factors for Partially and Completely Immersed Fractures. SPE 84411 Annual Tech. Conf. and Exh., Denver, CO.
- Rasband, W.S., ImageJ, U. S. National Institutes of Health, Bethesda, Maryland, USA, <http://rsb.info.nih.gov/ij/>, 1997-2005.
- Rothman D. H. and Keller J. M., 1988. Immiscible Cellular-Automaton Fluids. *J. Stat. Phys.* 52 (3/4): 1119-1127.
- Rothman D. H. and Zaleski S., 1994. Lattice-Gas Models of Phase Separation: Interfaces, Phase Transitions, and Multiphase Flow. *Rev. Mod. Phys.*, 66 (4): 1417-1481.
- Sagar, N. S., and Castanier, L. M., 1997. Oil-Foam Interactions in a Micro-Model. Technical Report, Stanford University, California, USA.
- Schechter D.S., Zhou D., Orr F.M., 1994. Low IFT Drainage and Imbibition. *J. Pet. Sci. and Eng.*, 11: 283-300.
- Schembre J. and Kovscek A.R., 2003. A Technique for Measuring Two-phase Relative Permeability in Porous Media via X-ray CT Measurements. *J. of Pet. Sci. and Eng.*, 39:159.

- Schembre J. M., Akin S., Castanier L. M., and Kovscek A. R., 1998. Spontaneous Water Imbibition into Diatomite. SPE 46211 Western Regional Meeting held in Bakersfield, California.
- Shan X. And Chen H., 1993. Lattice Boltzmann Model for Simulating Flows with Multiple Phases and Components. *Phys. Rev. E*, 47 (3): 1815-1819
- Shan X., and Doolen G., 1995. Multicomponent Lattice-Boltzmann Model with Interparticle Interaction. *J. Stat. Phys.* 81 (1/2): 379-393.
- Standnes D. C., Nogaret L. A. D., Chen H., and Austad T., 2002. An Evaluation of Spontaneous Imbibition of Water into Oil-Wet Carbonate Reservoir Cores Using a Nonionic and a Cationic Surfactant. *Energy and Fuels*. 6: 1557-1564.
- Stockman H.W., Glass R.J., Cooper C.A., and Rajaram H., 1998. Accuracy and Computational Efficiency in 3D Dispersion via Lattice-Boltzmann: Models for Dispersion in Rough Fractures and Double-Diffusive Fingering. *International Journal of Modern Physics*, 9(8):1-13.
- Strand S., Standnes D. C., and Austad T., 2003. Spontaneous Imbibition of Aqueous Surfactant Solutions into Neutral to Oil-Wet Carbonate Cores: Effects of Brine Salinity and Composition. *Energy and Fuels*, 17: 1133- 1144.
- Stubos A. K. and Poulou S., 1999. Oil Recovery Potential from Fractured Reservoirs by Mass Transfer Processes. SPE 56415 Annual Technical Conf. and Exh., Houston, TX.
- Sukop M. C., and Or D., 2004. Lattice Boltzmann Method for Modeling Liquid-Vapor Interface Configurations in Porous Media. *Water Resour. Res.*, 40: w01509, doi: 10.1029/2003WR002333.
- Sukop M.C., and Thorne D. T., 2006. Lattice Boltzmann Modeling, An Introduction for Geoscientists and Engineers Springer-Verlag Berlin Heidelberg, ISBN: 978-3-540-27981-5
- Suzanne K., Hamon G. and Billiotte J., 2003. Experimental Relationship between Residual Gas Saturation and Initial Gas Saturation in Heterogeneous Sandstone Reservoirs. SPE 84038 Annual Technical Conference and Exh., Denver, CO.
- Swift M. R., Osborn W. R., and Yeomans J. M., 1995. Lattice Boltzmann Simulation of Non-Ideal Fluids. *Phys. Rev. Lett.*, 75 (5), 830-833
- Takada N., Misawa M., Tomiyama A. and Hosokawa S., 2001. Simulation of Bubble Motion Under Gravity by Lattice-Boltzmann Method. *J. Nuc. Sci. Tech.*, 38(5): 330-341.
- Thurey N., 2005. A Single-Phase Free-Surface Lattice Boltzmann Method. MSc Thesis. Friedrich-Alexander-Universitat Erlangen-Nurnberg
- Tidwell V. C., and Glass R. J., 1995. Laboratory Investigation of Matrix Imbibition from a Flowing Fracture. *Geop. Res. Letters*, 22(11): 1405-1408.
- Udell K.S., 1985. Heat Transfer in Porous Media Considering Phase Change and Capillarity – The Heat Pipe Effect. *Int. J. Heat and Mass Transfer*. 28(2): 485.
- Van Der Smán R. G. M., 2006. Galilean Invariant Lattice Boltzmann Scheme for Natural Convection on Square and Rectangular Lattices. *Physical Review E*, 74 (026705): 1-17.

- Wagner G., Meakin P., Feder J., and Jossang, T., 1999. Invasion Percolation in Fractal Fractures. *Physica A*, 264: 321-337.
- Wardlaw N.C., Stein G. and Mckellar M., 1993. Countercurrent Imbibition in Glass Sells of Variable Roughness. *In Situ* 17(3): 311-329.
- Wen Y., Bryan J., Kantzas A., 2005. Estimation of Diffusion Coefficients in Bitumen Solvent Mixtures as Derived from Low Field NMR Spectra. *JCPT*, 44(4): 29-34
- Wilkinson D., 1984. Percolation Model of Immiscible Displacement in the Presence of Buoyancy Forces. *Physical Review A*, Vol 30(1).
- Witten T. and Sander L., 1981. Diffusion-Limited Aggregation, a Kinetic Phenomenon. *Phys. Rev. Lett.* 47 (19): 1400-1403.
- Wooding R. A., 1960. Instability of a Viscous Liquid of Variable Density in a Vertical Hele-Shaw Cell. *J. Fluid Mech.* 7: 501-515
- Woody F.; Blunt M.; Castanier L.M., 1995. Pore Level Visualization of Foam Flow in a Silicon Micromodel. SUPRI TR-100, Stanford University.
- Xie X. and Morrow N.R., 2000. Oil Recovery by Spontaneous Imbibition from Weakly Water-Wet Rocks. SCA-2000-27, Int. Symp. of the Soc. of Core Analysis, Abu Dhabi, UAE.
- Xu B., Yortsos Y. C., and Salin D., 1998. Invasion Percolation with Viscous Forces. *Physical Review E*, Vol 57(1).
- Yeo I.W. and Ge S., 2001. Solute Dispersion in Rock Fractures by Non-Darcian flow. *Geop. Res. Lett.*, 28(20): 3983-3986.
- Yildiz H.O., Gokmen M., Cesur Y., 2006. Effect of Shape Factor, Characteristics Length, and Boundary Conditions on Spontaneous Imbibition. *J. of Pet. Sci. and Eng.* 53: 158-170.
- Yortsos Y. C., Xu B., 1997. Phase Diagram of Fully Developed Drainage in Porous Media. *Physical Review Letters*, Vol 79 (23).
- Yoshino M. and Inamuro T., 2003. Lattice Boltzmann Simulations for Flow and Heat/Mass Transfer Problems in a Three-Dimensional Porous Structure. *Int. J. Numer. Meth. Fluids*, 43: 183-198.
- Zakirov S. N., Shandrygin A. N. and Segin T. N., 1991. Miscible Displacement of Fluids Within Fractured Porous Reservoirs. SPE 22942 66th Annual Technical Conf. and Exh., Dallas.TX.
- Zhang X., Bengough A. G., Deeks L. K., Crawford J. W., and Young I. M., 2002. A Novel Three-Dimensional Lattice Boltzmann Model for Solute Transport in Variably Saturated Porous Media. *Water Resources. Res.*, 38 (9): 1167. doi:10.1029/2001WR000982.
- Zhang X., Morrow N.R., and Ma S., 1996. Experimental Verification of a Modified Scaling Group for Spontaneous Imbibition. *SPERE*, 280.
- Zhou D., Jia L., Kamath J. and Kovscek A.R., 2002. Scaling of Counter-Current Imbibition Processes in Low-Permeability Porous Media. *J. of Pet. Sci. and Eng.*, 33: 61.

12 Appendix A

Derivation of the new shape factor

Cores with nine different shape factors were tested for the vertically (Exps. 1 to 9) and horizontally (Exps 10 to 18) situated samples. Using the recovery curves obtained for those systematically designed length and diameter, a new characteristic length was obtained through reverse engineering of the problem.

A “pseudo characteristic length” is assigned for each of the experiments. Sensitivity analysis is done for each of the recovery curve, changing the assigned pseudo characteristic length. Values are changed until visually a good match is obtained.

Once the “pseudo characteristic length” values were obtained for each dimensionless group, they were plotted on a 3-D plot against the diameter and length. All 3 scaling groups are used for this method. For the vertical cases it was significant that for all three methods, a similar trend was captured. For the horizontally oriented samples trend was not significant, but the optimum around 1 inch diameter and 4 inch length core was still noticeable.

Looking at the averaged values (Figs. A1-a and A1-b), the equation for the “pseudo characteristic length” is decided to be parabolic. The difference between the two orientations was due to the dependency on the length term. Hence the center of the parabolic shifts to 0 length for the vertical and to 4 inches length for the horizontal. By including the gravity

effect in terms of angle with the horizontal, the “pseudo characteristic length” equation was obtained to be:

$$L_c^2 = (Length - 4 \cos \theta)^2 + (Diameter - 1)^2$$

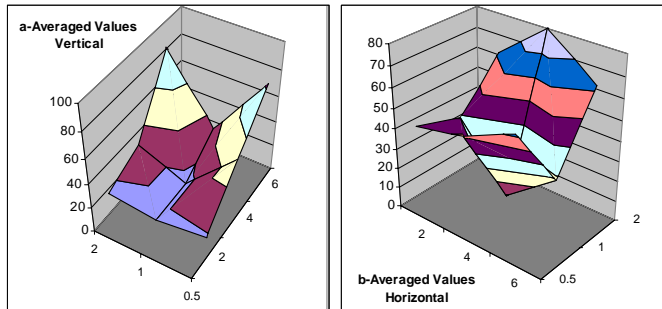


Fig. A1: Surfaces created by Pseudo Shape factor values with respect to Length and Diameter for vertically oriented core samples (Averaged Values) (a) Vertical, (b) Horizontal.

13 Appendix B

The Properties of Rock Samples Used in the Experiments

Two types of rock samples with different permeability and porosity values and lithologies were selected for the experiments. Berea sandstone was used as typical homogeneous porous media in laboratory experiments. Indiana limestone experiments were also included to see the contrast between the two types of rocks in terms of pore structure and wettability as well as permeability and porosity.

The porosities were measured during the saturation process by weighting the sample before and after the saturation and dividing the difference by the density of the fluid. Permeabilities were measured once and compared to the value provided by the supplier of the rock samples. The average porosity and permeability of the rock samples were previously given as:

$$\phi_{\text{bera}}=0.21$$

$$\phi_{\text{Indiana}}=0.16$$

$$k_{\text{bera}}=500\text{mD}$$

$$k_{\text{Indiana}}=15\text{mD}$$

The samples were selected from the same block so that they are believed to be consistent in terms of petrophysical properties. Core properties for selected Berea samples are presented in Table B1 to show the range of consistency.

Table B1 Properties of select Berea sandstone samples.

Diameter (in)	Length (in)	Pore Volume (cc)	Porosity
0.5	2	1.33	0.21
0.5	4	2.95	0.23
0.5	6	3.57	0.18
1	2	4.54	0.18
1	4	11.00	0.21
1	6	21.23	0.27
2	2	20.73	0.20
2	4	42.68	0.21
2	6	60.98	0.20

Same procedure is repeated for Indiana limestone samples. The results are given in Table B2.

Table B2 Properties of select Indiana limestone samples.

Diameter (in)	Length (in)	Pore Volume (cc)	Porosity
1	2	3.92	0.15
1	2	4.30	0.17
1	6	10.97	0.14

One of the most important characteristic properties of the rocks is the capillary pressure that represents the wettability and pore size characteristics of sedimentary rocks. In reservoir conditions, wettability is not a simply defined property. The contact angle is the only parameter that can represent the wettability characteristics of the rock surface for a given fluid pair. Dynamic capillary pressure measurements will reflect the wettability properties if the same fluid pair is used in the experiments and capillary pressure measurements. To quantify wettability the procedure defined by Babadagli [1996] was adapted instead of contact angle measurement. Calculations and plots are given in chapter 4.1.4 (Fig. 4.16) for the rock samples used in this study.

Another indirect way of measuring is to use the drainage capillary pressure for the same fluids. The capillary pressure for Berea sandstone sample is shown in Fig. B1 to give an idea about the wettability and pore size characteristics.

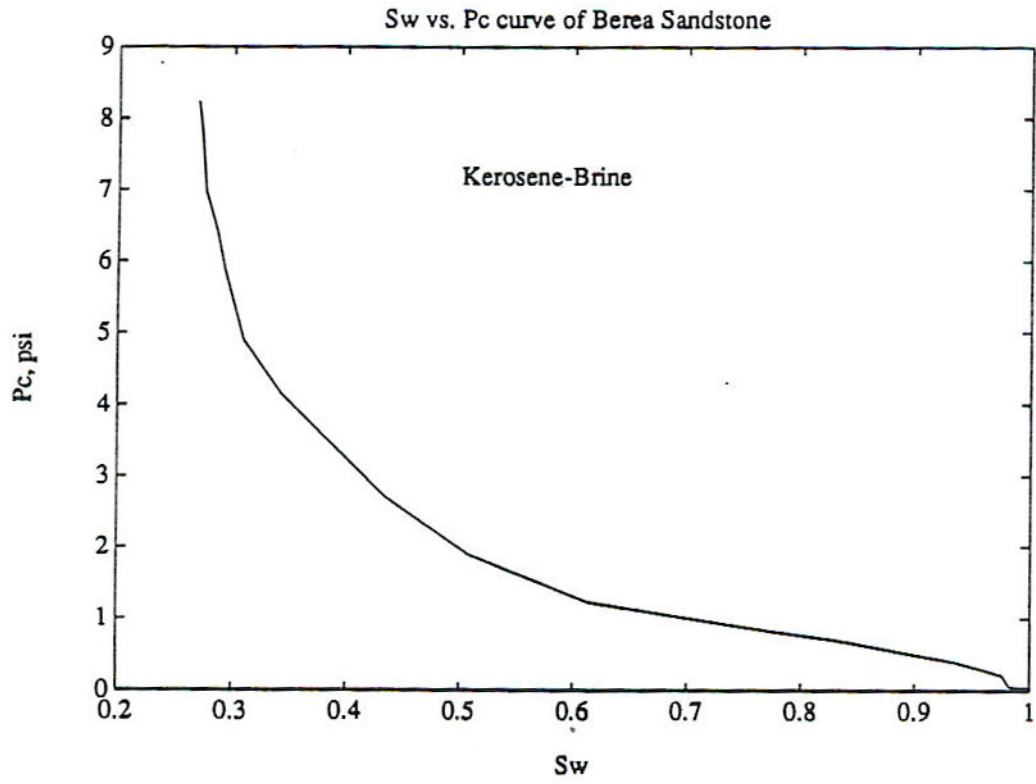


Figure B1. P_c for drainage, Berea sandstone sample (Babadagli [1992]).